ABSTRACT

Title of Dissertation:	TAILORING LOCALIZED SURFACE PLASMON RESONANCES IN METALLIC NANOANTENNAS
	Kunyi Zhang, Doctor of Philosophy, 2020
Dissertation Directed By:	Professor Oded Rabin, Department of Materials Science and Engineering

The strong localized electromagnetic field achievable with metallic nanoantennas provides new opportunities for harmonics generation and label-free chemical sensing. In this work, the localized surface plasmon resonances (LSPRs) of metallic nanoarcs on dielectric substrates have been systematically investigated with visible and infrared spectroscopy, with the goal of elucidating the relationship between the structural and material parameters of the nanoarcs and their resonances. The transmission spectra provide rich information regarding the fundamental and higher order LSPR modes. Experimental results and numerical simulations demonstrate that the LSPR wavelengths are governed by the mid-arc length of the nanoarcs, and the extinction cross-sections of the different order modes are controlled by the central angle of the nanoarc and the symmetry of the mode. The fundamental and second order LSPR wavelengths can be tuned independently through the design of a non-uniform arc-width profile. Several relationships between features of the LSPR modes and the geometric

parameters of nanoarcs are also confirmed by transformation optics analysis. The newly found relationships are then utilized as guidelines for the realization of plasmonic nanoarc antennas exhibiting efficient second harmonic generation (SHG). In another application, strong coupling between LSPRs and molecular vibrations is evident in the IR spectra of plasmonic nanoarcs placed in contact with a thin film of polymer, a native oxide layer or a thiol monolayer, enhancing the vibrational mode signals. This observation suggests that by appropriately tuning the frequency of the LSPR modes, the localized electromagnetic field around nanoarcs can resonantly couple to another emitter to boost its far-field radiation, which could benefit applications requiring highly localized, sensitive and selective chemical detection.

TAILORING LOCALIZED SURFACE PLASMON RESONANCES IN METALLIC NANOANTENNAS

by

Kunyi Zhang

Dissertation submitted to the Faculty of the Graduate School of the
University of Maryland, College Park, in partial fulfillment
of the requirements for the degree of
Doctor of Philosophy
2020

Advisory Committee:
Professor Oded Rabin, MSE, Chair/Advisor
Professor Thomas E. Murphy, ECE, Dean's representative
Professor Mohamad Al-Sheikhly, MSE
Professor Yifei Mo, MSE
Professor Edo Waks, ECE

Dedication

To my family

Acknowledgements

I owe my gratitude to all the people who have made this thesis possible. This work and the wonderful academic time in the University of Maryland would not have been possible without the help and the support of many people. In particular I would like to thank:

My advisor, Prof. Rabin, for his truly infectious enthusiasm for science accompanied with many inspiring ideas and the possibility to discuss scientific problems at any time.

Prof. Murphy for providing guidance and support for research, and the mentoring and encouragement that are inestimable.

Prof. Al-Sheikhly, Prof. Mo, and Prof. Waks for kindly serving as my thesis committee.

Dr. Matthew Davis for the collaboration on the numerical simulations.

Dr. Gyan Prakash for his help in setting up the nonlinear optical measurements.

Dr. Karen Gaskell for the training and the help on atomic force microscopy and Raman spectroscopy.

Dr. SC Liou and Dr. Jiancun Rao for providing technical support for scanning electron microscopy and focused ion-beam milling.

Dr. Hans Bechtel for providing technical support for FTIR measurement at Lawrence Berkeley National Laboratory.

Dr. Xiaoxiao Ge and Chris Klingshirn from Prof Riba's group, and Dr. John Howard for useful discussions about research and the suggestions on English writing.

Members of Prof. Murphy's group for their support and the great working atmosphere.

Members of Prof. Waks's group for sharing their experience of experiments.

My parents and grandparents for their loving support during the time of my whole PhD, their constant encouragement, and their unshakable believe in the success of my work. Jitao for his enduring support and understanding, and for making every day beautiful. Lovable friends for their wide-opened door, their wholehearted support and all the food.

Table of Contents

List of Tables

List of Figures

Chapter 1: Introduction

Plasmonic nanoarc antennas are curved metal strips with nanometer-sized dimensions on dielectric substrates that can interact with light and produce strongly enhanced and highly localized electromagnetic (EM) fields. In contrast to uniaxial nanorods (D_{2h} point group) that support only odd-order longitudinal plasmon modes, nanoarcs (C_{2v} point group) can support both even- and odd-order longitudinal plasmon modes, which is an advantageous feature for nonlinear optics applications and ultrasensitive sensing techniques. However, the plasmon features of plasmonic nanoarcs are not yet fully understood. To systematically explore the plasmon resonances of nanoarcs, this work focuses on the design, fabrication, and characterization of a variety of metallic nanoarcs. The goal of this work is twofold: to establish the relationship between the plasmon resonances and the geometric parameters of nanoarcs; and to apply nanoarcs for improving the efficiency of harmonics generation and the sensitivity of optical spectroscopy, using the established relationship as a guide. Before we go any further, the remainder of this chapter will provide an overview of the basic principles of localized surface plasmon resonances in nanoantennas (Section 1.1), and introduce two representative applications of plasmonic nanoantennas, namely, second-harmonic generation (SHG) (Section 1.2), and surface-enhanced infrared absorption spectroscopy (SEIRA) (Section 1.3). Section 1.4 outlines the scope of this Dissertation.

1.1 Localized Surface Plasmon Resonances in Plasmonic Nanoantennas

Plasmonic nanoantennas have been an active research topic in the last two decades due to their highly promising applications in molecular spectroscopy [1-3], photocatalysis

[4], nonlinear integrated optics [5-8], and near-field optical microscopy [9, 10]. The novel optical properties of plasmonic nanoantennas arise from the interaction between light and surface plasmons. When the nanoantennas are illuminated by light at the resonance frequency with proper polarization, the collective oscillation of the free electrons on the surface of the metal particle will be largely enhanced in response to the electromagnetic field of the incoming light (Figure 1.1.1). This phenomenon is known as the excitation of the localized surface plasmon resonance (LSPR). Meanwhile, a highly enhanced electromagnetic field is generated around the nanoantenna. The negative permittivity values of metals, which are wavelength-dependent, allow the metals to support surface plasmon resonances. The metals that have been most commonly applied as antenna materials include gold, silver [11, 12], aluminum [13], and platinum [14]. The LSPR effect leads to unprecedented phenomena including the formation of hot spots [15], directional scattering [16], and nonlinear light-matter interaction over a broad spectral range [5]. Moreover, LSPRs can couple to the EM field of other emitters placed in the vicinity of the nanoantenna, modifying the radiative (elastic and inelastic scattering) and nonradiative (absorption) properties of the emitters [1, 17]. These novel optical properties make plasmonic nanoantennas an ideal building block for light manipulation at the nanoscale.

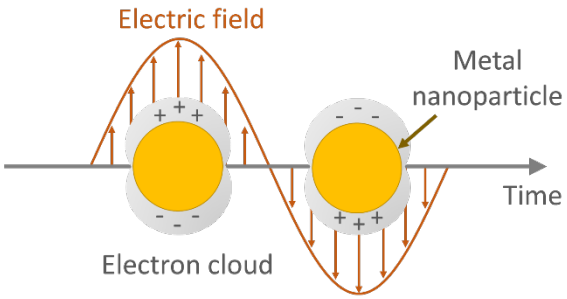

Figure 1.1.1 Schematic of the oscillating electron cloud in metallic nanoparticles under illumination.

To accommodate a wide range of applications, the ability to tune the resonance wavelengths/frequencies of nanoantennas is of great importance. Previous studies [2, 3] have demonstrated that the LSPR frequency depends strongly on the plasmonic particle shape, size and material, as well as the dielectric environment. Plasmonic effects have been investigated with various metallic nanostructures (Figure 1.1.2), including centrosymmetric nanodisks [14] and nanorods [18-20], and non-centrosymmetric nanocrescents [21, 22], nanoarcs [23-26], split-ring resonators [27-30], V-shaped, L-shaped and U-shaped antennae [31-33], and multimers [34-36]. Methods for predicting the frequencies of LSPRs of plasmonic nanoantennas and design rules for tuning these frequencies are of general interest.

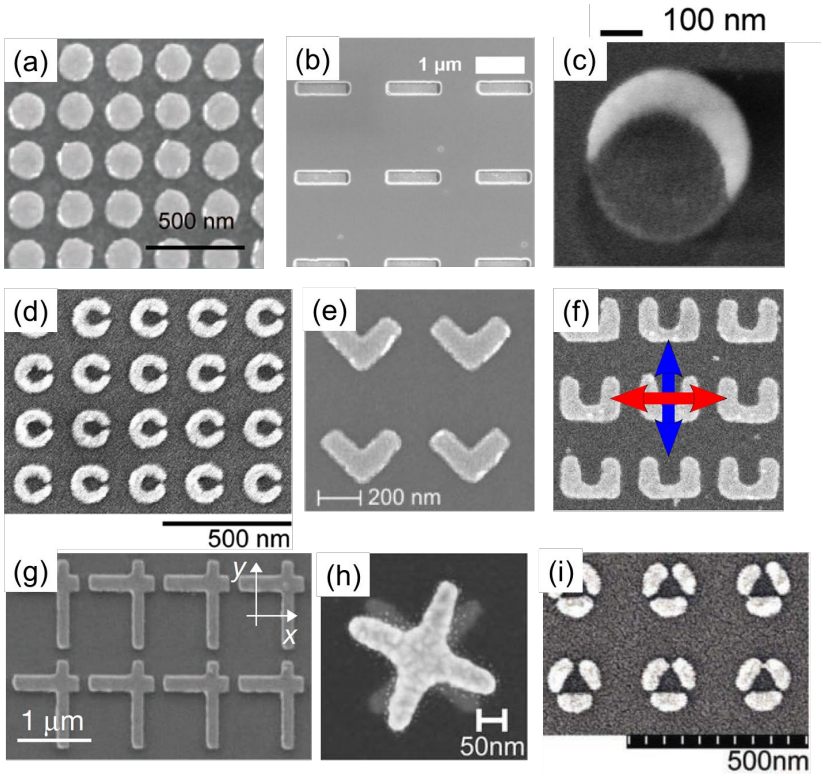

Figure 1.1.2 Scanning electron microscopy (SEM) images of plasmonic nanostructures: (a) nanodisks [37], (b) nanorods [38], (c) nanocrescent [39], (d) nanoarc [24], (e) V-shaped nanostructures [40], (f) U-shaped nanostructures [29], (g) L-shaped nanostructures [32], (h) double-layer twists [35], and (i) three-segment split-rings [25].

Among all the nanoantenna geometries, plasmonic nanorods have attracted significant research interest [18-20]. Plasmonic nanorods (Figure 1.1.3 (a)) are uniaxial nanostructures that absorb, scatter, and emit electromagnetic radiation preferentially at the LSPR frequencies. The ease of nanorod fabrication, via chemical synthesis [19, 41-44], electrochemical assembly [45] or lithography (Figure 1.1.3 (b)-(d)), [46-50] and the ability to modify their optical properties by adjusting their aspect ratios [46, 51, 52] have motivated numerous studies that focus on nanorods and their use as building blocks for more complex plasmonic structures and metamaterials. [18, 53-56]

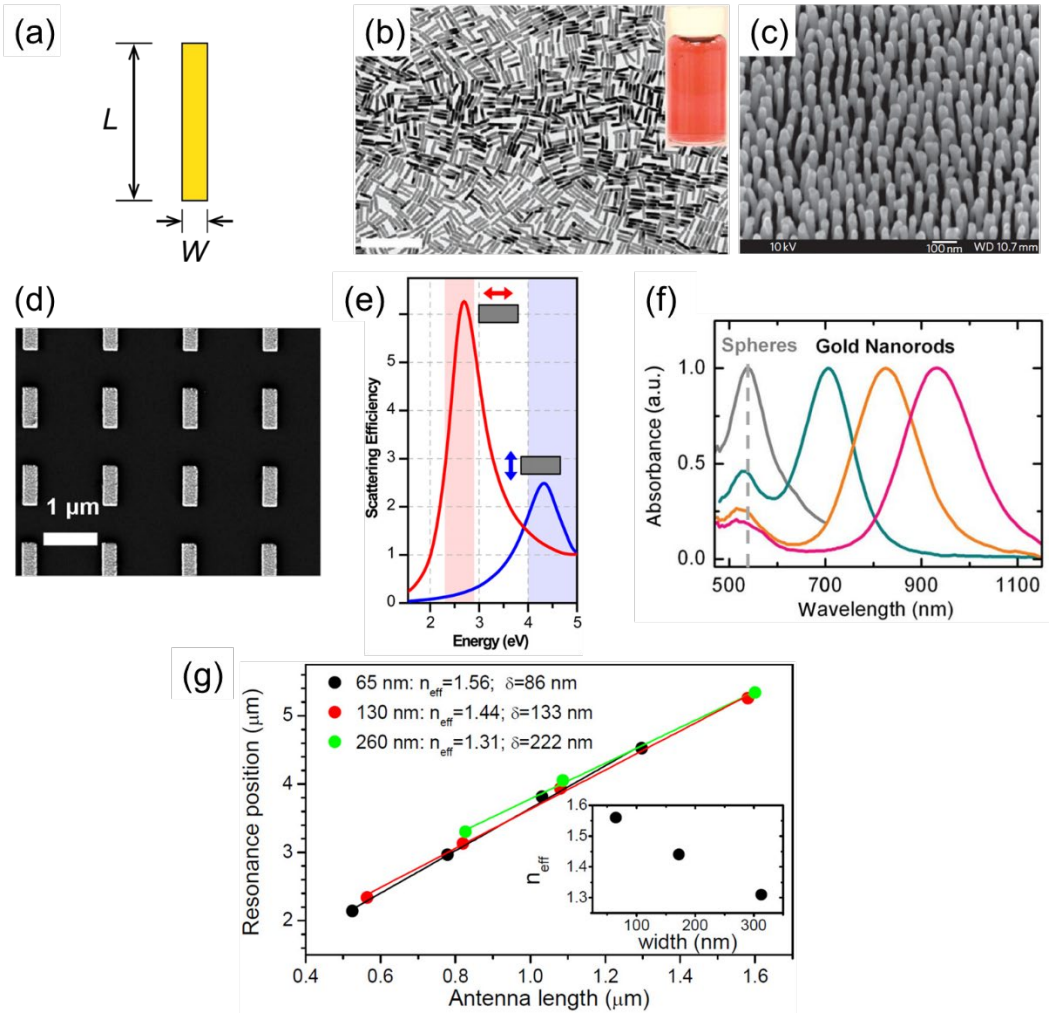

Figure 1.1.3 (a) Schematic of a nanorod geometry with definitions for the rod length *L* and rod width *W*. (b-d) Nanorods fabricated by different methods. (b) Chemically synthesized gold nanorods, reprinted from Ref. [43]. Scale bar 200 nm. (c)

Electrochemically grown nanorod assembly, reprinted from Ref. [45]. (d) Lithographically fabricated gold nanorods, reprinted from Ref. [38]. (e) Calculated scattering spectra of an aluminum nanorod with L = 100nm and W = 40 nm, illustrating the longitudinal (red) and transverse (blue) LSPR modes, reprinted from Ref. [13]. (f) Measured absorbance spectra of gold nanospheres and nanorods with different rod lengths, reprinted from Ref. [57]. The dash line marks the center of the LSPR peak of nanospheres. (g) The LSPR wavelength of gold nanorods with different lengths and widths on sapphire substrates. Adapted from Ref. [50].

Polarization-dependent spectroscopy studies and related numerical simulations of nanorods have identified longitudinal and transverse LSPR modes with oscillating electric dipoles oriented along the long and short axes of the nanorod, respectively (Figure 1.1.3 (e)). The longitudinal LSPRs in plasmonic nanorods are highly tunable by adjusting the nanorod length (L in Figure 1.1.3 (a)) [48, 58] while the transverse LSPRs typically resonate at significantly higher frequencies and their tunability is negligible for high aspect ratio nanorods (Figure 1.1.3 (f)). [52, 59] A linear relationship was observed between the longitudinal LSPR wavelength and the length of the nanorods (Figure 1.1.3 (g)) [48, 50, 60]. For Au and Ag nanorods, the longitudinal LSPRs are tunable across the visible and infrared (IR) bands of the electromagnetic spectrum [12, 52, 59]; for Al nanorods, they are tunable from the ultraviolet to the infrared [13, 61]. Due to symmetry, the even-order LSPR modes in nanorods are dark modes, meaning they do not exhibit a dipole moment therefore cannot be directly excited through normally-incident plane-wave illumination.

To enable the excitation of both even- and odd-order LSPRs in plasmonic nanoantennas, the symmetry of the plasmonic system needs to be broken through tilted illumination or the design of non-centrosymmetric nanoantennas. Plasmonic nanoarcs and nanocrescents (Figure 1.1.4) are examples of nanoantennas with broken inversion symmetry, whose optical attenuation spectra exhibit twice the number of longitudinal

LSPR signatures compared to nanorods. In nanoarcs and nanocrescents, the even- and odd-order LSPR modes correspond to orthogonal polarization states (Figure 1.1.4 (b), (e)), resulting in coupling to radiation with polarization in all in-plane directions, with potential implications for filtering and polarization conversion effects. [62, 63] The LSPR frequencies/wavelengths of nanoarcs and nanocrescents are highly tunable across the visible and infrared regime ((Figure 1.1.4 (c), (f)). A linear trend in the resonance wavelength of nanocrescents with respect to the crescent diameter has been observed, similar to the trend found in nanorods. [64] However, the attribution of these LSPR wavelengths/frequencies is often carried out on a case-by-case basis via numerical simulations or trial-and-error experimentation, and there is no universal rule for predicting these resonance wavelengths – a deficiency that this Dissertation seeks to address.

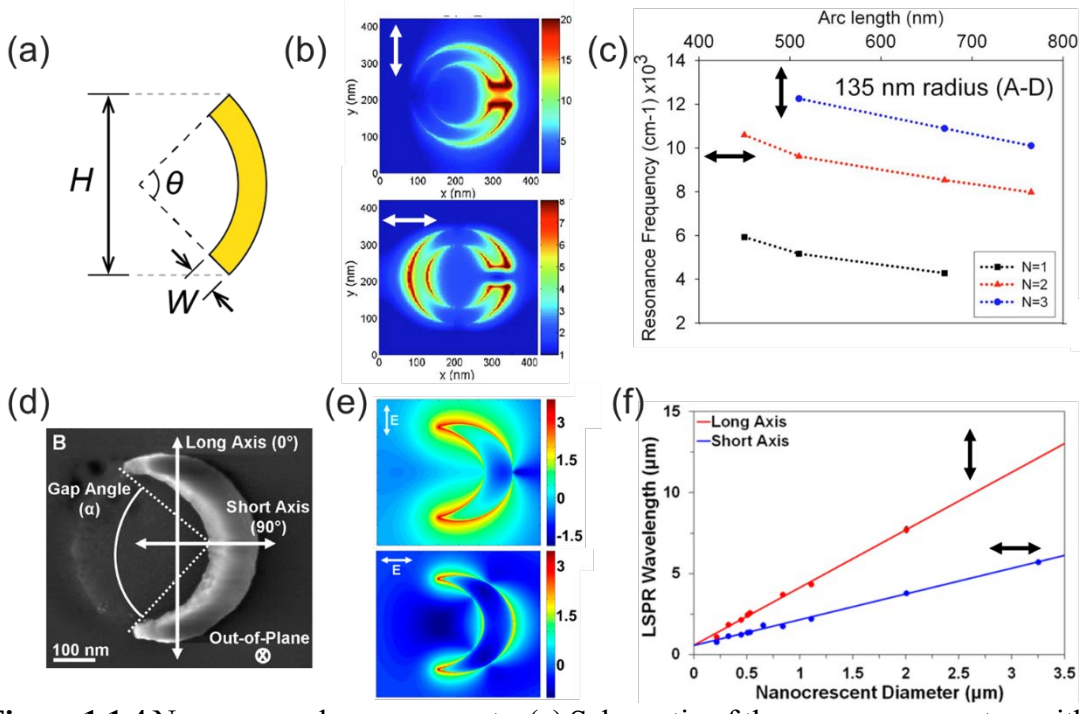

Figure 1.1.4 Nanoarcs and nanocrescents. (a) Schematic of the nanoarc geometry, with definitions for the arc height H, arc width W, and central angle θ. (b) Calculated electric field enhancement of gold nanoarcs at resonances. (c) LSPR frequencies of gold

nanoarcs with different arc lengths. (d) SEM image of a gold nanocrescent. (e) Calculated electric field enhancement of nanocrescents at resonances. (f) LSPR wavelengths of gold nanocrescents with different diameters. Arrows show the polarization orientation of the linearly polarized incoming light. (b, c) are adapted from Ref. [23]. (d)-(f) are adapted from Ref. [64, 65].

1.2 Second-Harmonic Generation in Plasmonic Nanoantennas

Second-harmonic generation (SHG) is a nonlinear optical process in which incoming light with frequency ω is converted into radiation with a doubled frequency [66, 67] upon the interaction between light and a medium with a non-zero second-order susceptibility $\chi^{(2)}$ (Figure 1.2.1). Since the first observation of this phenomenon in a crystalline quartz sample in 1961 [68], numerous efforts have been devoted to the advancement of theoretical models and experimental designs for SHG. Beyond frequency-doubling crystals, SHG has been realized photonic crystals [69, 70], and more recently, in plasmonic nanoantennas [5, 71]. The strong light-plasmon interaction in the near-field of the plasmonic nanoantennas gives rise to efficient nonlinear conversions, opening new realms for nonlinear plasmonics. Plasmonic nanostructures have the advantages of low cost, size compatibility with micro electro-optical devices, and material compatibility for integration in biodevices.

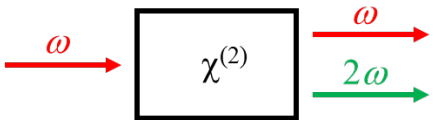

Figure 1.2.1 Diagram of second-harmonic generation.

SHG has been investigated in a variety of plasmonic nanoantennas, ranging from U- and V-shaped nanoantennas to plasmonic dimers and multimers with nanometer-size gaps [27, 31, 72, 73]. The highest SHG efficiency in nanoantennas is predicted when the LSPR wavelengths of the fundamental and second-order modes have a ratio of 2

[72]. However, the role of the two LSPRs in enhancing SHG is not yet fully elucidated. In this context, plasmonic nanoantennas with two strong LSPRs whose resonance wavelengths and oscillator strengths can be tuned independently are important for the study of SHG in plasmonic systems. Plasmonic nanoarcs are an ideal platform for realizing this tunability. The study of plasmonic nanoarcs can provide insights into the role of the two LSPRs in enhancing SHG.

1.3 Surface-Enhanced Infrared Absorption

Molecular vibrational spectroscopy is often used to identify molecules because the molecular vibrations frequencies and signal amplitudes are characteristic "fingerprints" of chemical bonds and molecular configurations. [1, 74, 75]. As summarized in Figure 1.3.1 (a), the frequencies of most molecular vibrational modes are in the infrared (IR) region, making IR spectroscopy an informative and powerful tool for routine investigations of chemical compounds [76]. However, ultrasensitive IR detection remains a challenge due to the low absorption cross-section of molecular vibrations ($\sigma_{abs} \approx 10^{-20}$ cm^2) [1]. The vibrational signal of molecules can be detected only in samples with high concentrations. To improve the detection sensitivity, innovative techniques such as surface-enhanced infrared absorption (SEIRA) have been developed [75]. SEIRA takes advantage of the strong electromagnetic field generated in the near-field of the plasmonic nanoantennas, especially at the hot spots, [77] to locally enhance molecular signals. When the analyte is placed in the vicinity of a nanoantenna, its molecular vibrations couple to the surface plasmons of the antenna, resulting in enhanced light absorption/scattering by the molecules. The enhanced signal of the molecules typically presents in the linear optical attenuation spectrum as a Fano-type

signal (Figure 1.3.1 (b)) with an enhancement factor of ~10 – 10^5 [1, 78], or a transparency window (Figure 1.3.1 (c)) if multiple energy levels associated with different molecular vibrations are involved in the near-field interactions [79]. The SEIRA effect has been investigated with different types of analyte/emitters including molecules[80], quantum dots [81] and thin films [82, 83].

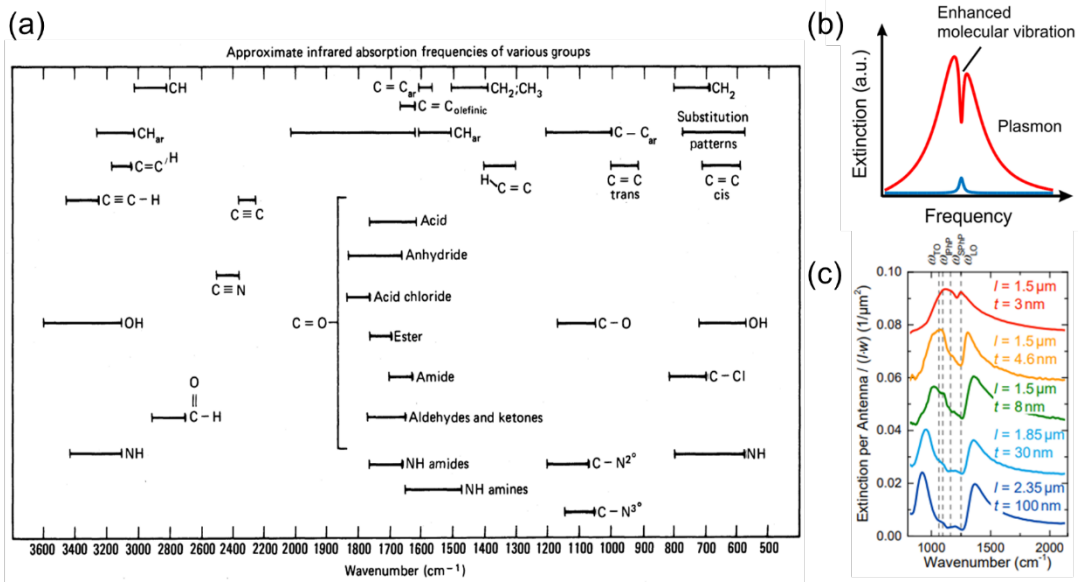

Figure 1.3.1 (a) Characteristic infrared vibrational frequencies of organic functional groups. Adapted from Ref. [84]. (b) Schematic of an extinction spectrum of nanoantennas with surface plasmons coupled to a molecular vibration (red) compared to the spectrum of the molecular vibrational mode (blue). Adapted from Ref. [1]. (c) Extinction cross-section of gold nanorods coupled to thin film of SiO_2, adapted from Ref.[85].

The design of nanoantennas is crucial for improving the SEIRA enhancement factor and remains an active area of research. The maximum enhancement in experiment was often observed when the LSPR frequency of the nanoantennas matched the molecular vibration frequency [86]. As shown in Figure 1.1.4, the different-order LSPR wavelengths of nanoarcs can be continuously tuned in the infrared regime by adjusting the arc dimensions, therefore, plasmonic nanoarcs are a highly promising candidate for

SEIRA applications. In addition, nanoarcs allow selective detection of molecular vibrations at different spectral bands because their 1st and 2nd LSPRs corresponds to orthogonal polarizations. Furthermore, a chiral multimer of nanoarcs may rotate the polarization of the incoming light [87] and generate a localized electromagnetic field with enhanced chirality [88], making it possible to probe the absolute configuration of molecules [89].

1.4 Scope of Doctoral Dissertation

The objectives of this Dissertation are to establish the relationship between the localized surface plasmon resonances and the geometric/material parameters of plasmonic nanorods, nanoarcs, nanocrescents and nanospheres, with a focus on nanoarcs, and to utilize nanoarcs in the investigation of SHG and SEIRA. The ultimate goal is to optimize the nonlinear conversion efficiency in plasmonic systems and improve sensitivity of optical spectroscopies in the infrared.

Chapter 2 focuses on interpreting the tunability of LSPRs in plasmonic nanorods and nanoarcs. It introduces the design, fabrication and characterization of these nanostructures, and the experimental design allowing for the systematic variation of individual geometric parameters, including length and central angle. Through transformation optics analysis, numerical simulations, and spectroscopy measurements, we establish the relationship between features of the LSPR spectra and the geometric parameters of nanorods and nanoarcs. The effect of antenna materials (Au and Al) and substrate materials (Si and fused quartz) on the plasmon resonance wavelengths are also explored.

Chapter 3 concentrates on tuning the wavelength interval between the fundamental and 2nd order LSPRs in nanoarcs. It is demonstrated that the relative wavelength of the LSPRs can be controlled through the design of nanoarcs with a non-uniform width profile. With two LSPRs tuned independently by adjusting the width profile and the mid-arc length of the nanoarc, it is feasible to design nanoarcs with LSPR wavelengths separated by precisely one octave.

The relationships established in Chapters 2 and 3 are then used as a guide to design nanoarcs for specific applications in the later portion of this Dissertation. Chapter 4 discusses SHG in plasmonic nanoarcs. With the LSPR wavelengths and oscillator strengths engineered by the geometric parameters of the nanoarcs, and the excitation laser tuned to match either LSPR wavelength, the contribution of the 1st and 2nd LSPRs in enhancing SHG is studied. Chapter 5 explores the coupling between nanoarcs and nearby emitters, i.e., a thin film of photoresist, a silicon oxide layer, or thiol molecules. Chapter 6 discusses the dipolar coupling between adjacent plasmonic nanorods/nanoarcs fabricated as dimers, tetramers, and a fiber-coupled remote Raman sensor. Chapter 7 provides a summary of the Dissertation and outlook for future research in this field.

Chapter 2: Tunability of Localized Surface Plasmon Resonances in Plasmonic Nanoarcs

2.1 Introduction

Nanoarcs can be considered as an intermediate geometry linking straight nanorod antennae and nanoscale split-ring resonators (SRR) through the process of bending. [90] A series of nanoarcs with varying central angles is ideal for the study of the emergence of the magnetic character of the surface plasmon mode, which is a strong and useful feature in SRRs. [91-93] The simultaneous presence of oscillating electric and magnetic dipoles upon excitation of the fundamental longitudinal LSPR mode makes the nanoarc an ideal building block for nonlinear optical and chiroptical metamaterials. [5, 94] Although plasmonic nanoarcs have the advantages listed above, it is highly challenging to design plasmonic nanoarcs with desired optical properties due to the lack of universal rules for predicting their localized surface plasmon resonances (LSPRs). Here, we report a study of LSPRs in plasmonic nanoarcs employing transformation optics (TO) design (Section 2.2), numerical simulations (Section 2.3), and Fourier-transform infrared (FTIR) spectroscopy measurements (Section 2.5).

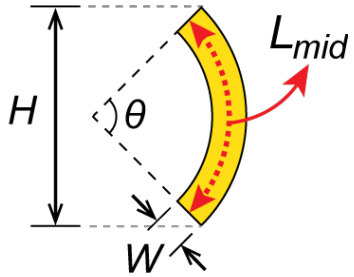

Figure 2.1.1 Schematic of the nanoarc geometry, top view, with definitions for the arc height H, arc width W, central angle θ and mid-arc length L_{mid}.

The nanoarcs investigated in this chapter are sectors of circular rings with a rectangular cross-section. As such, their geometry is fully described by 4 parameters, i.e., height H, width W, thickness t and central angle θ (Figure 2.1.1). This family of structures was chosen because their fabrication is feasible by means of standard electron-beam lithography (EBL) and metal film lift-off processes, their shape parameters can be tuned systematically, and straightforward comparisons with rectangular cross-section nanorods can be made. Related structures, namely V-shaped nanoantennas [95-97] and nanocrescents, [98, 99] have been previously made by direct lithography and template shadow evaporation, respectively. In contrast to the nanoarcs reported here, each of those nanostructures has 2 sharp corners that under proper illumination conditions are associated with the sub-wavelength localization of the optical field (i.e. hot spot). [99] Unfortunately, these sharp features make the optical response of the nanostructure strongly dependent on the resolution and uniformity of the fabrication process. [100] Furthermore, overlapping peaks from tip-localized modes and inhomogeneous broadening due to spatial variations in the dielectric constants of the matrix complicate the interpretation of the optical spectra. [62, 97] Nano-crescents pose the additional challenge of having a non-uniform width and thickness, making them difficult to model and difficult to study systematically. The goal of this chapter is to provide a blueprint for predicting the infrared spectra of plasmonic nanoarcs.

2.2 The Conformal Transformation Linking Nanorods and Nanoarcs

To elucidate which nanoarc dimensions are important for controlling the resonance wavelength, we employ the method of transformation optics [101, 102] to map a

nanoarc into a nanorod (and vice versa) using a two-dimensional (2D) conformal transformation.

Transformation optics is a mathematical technique for designing novel electromagnetic (EM) media [102]. It is based on the concept that Maxwell's equations can be written in a form that is invariant under coordinate transformations. Maxwell's equations are satisfied in both the original and transformed spaces if properly modified values of the permittivity (ε) and permeability tensors (μ) are used. [101-103] Under a general 2D coordinate transformation (x', y') = f (x, y) the permittivity tensor ε' and permeability tensor μ' in the transformed space (x', y') are related to the permittivity (ε) and permeability (μ) tensors in the original space (x, y) as [102-104]

$$\varepsilon' = \frac{\Lambda \cdot \varepsilon \cdot \Lambda^T}{\det(\Lambda)} \quad (2.2.1)$$

$$\mu' = \frac{\Lambda \cdot \mu \cdot \Lambda^T}{\det(\Lambda)} \quad (2.2.2)$$

where

$$\Lambda = \begin{bmatrix} \partial x'/\partial x & \partial x'/\partial y \\ \partial y'/\partial x & \partial y'/\partial y \end{bmatrix} \quad (2.2.3)$$

is the Jacobian matrix of the coordinate transformation.

Conformal mapping (or conformal transformation) is an analytical transformation that preserves local angles. [103, 105, 106] 2D conformal transformations are recognized by their Jacobian matrix taking the form

$$\Lambda = \begin{bmatrix} a & -b \\ b & a \end{bmatrix}, (a \neq 0) \quad (2.2.4)$$

While conformal transformations have various applications in physics [107-109], this section focuses on its role in transformation optics in 2D. By substituting (2.2.4) in

equations (2.2.1) and (2.2.2) one can demonstrate that 2D conformal transformations preserve the in-plane components of the permittivity ε and permeability μ tensors, i.e.

$$\varepsilon_x{}' = \varepsilon_x;\ \varepsilon_y{}' = \varepsilon_y \qquad (2.2.5)$$

$$\mu_x{}' = \mu_x;\ \mu_y{}' = \mu_y \qquad (2.2.6)$$

for isotropic and non-magnetic materials. [101, 103] In other words, 2D conformal transformations are a subset of geometric transformations that map the solutions of Maxwell's equations from one geometry to another without requiring a concomitant change of materials. When the field pattern of the plasmon mode is dominated by in-plane electric fields, as is the case for the longitudinal LSPR modes in nanorods and nanoarcs studied here, the objects with the original-space geometry and the transformed-space geometry share the same surface plasmon resonance conditions. [110, 111]

Since the LSPRs of plasmonic nanorods are well-understood, a 2D conformal transformation can help predict the LSPRs of nanoarcs by relating them to nanorods. However, it should be noted that a 2D conformal transformation does not conserve the values of the out-of-plane components of the permittivity and permeability (ε_z and μ_z) [105, 112, 113]. When the effect of the z-component of the fields needs to be considered, an alternative model must be sought.

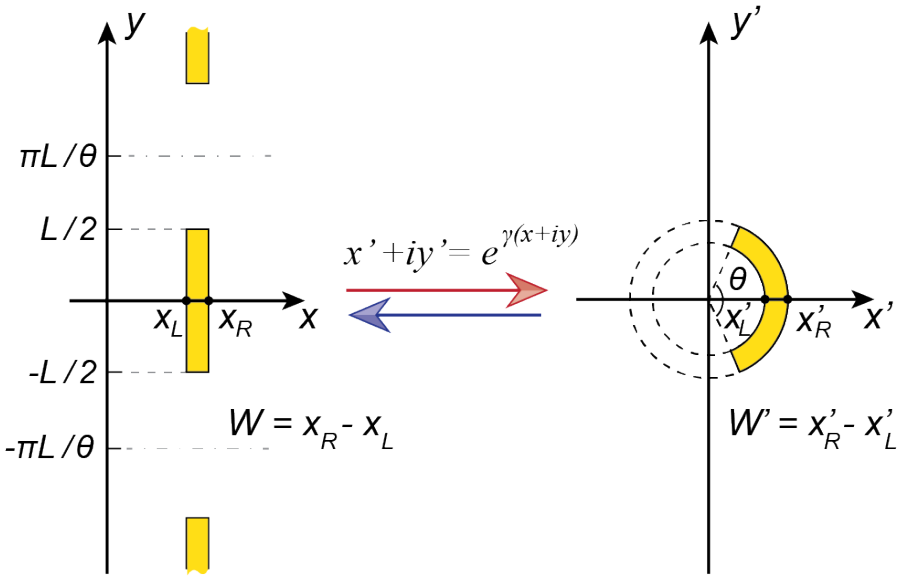

Figure 2.2.1 The 2D conformal transformation that maps a periodic array of rods to an arc, and vice versa. The coordinates in the transformed plane are primed to distinguish them from those in the original plane.

The shape parameters of the nanorod-to-nanoarc transformation in 2D are depicted in Figure 2.2.1. We mapped a nanorod of length L and width W to a nanoarc through the conformal transformation [110]

$$\zeta' = e^{\gamma\zeta} \qquad (2.2.7)$$

with the usual complex number notations $\zeta = x + iy$ for the original (rod) space and $\zeta' = x' + iy'$ for the transformed (arc) space. The mathematical proof showing that Eq. (2.2.7) is a conformal transformation can be found in Appendix 8.1.

The parameter γ sets the central angle θ (in radians) subtended by the resulting arc via the relation

$$\gamma = \frac{\theta}{L} \qquad (2.2.8)$$

where L is the length of the rod and γ is real. By selecting different values of γ, the same nanorod of length L can be mapped into a set of different nanoarcs with central angle of γL. Eq. (2.2.7) can be equivalently written as

$$x' = e^{\gamma x}\cos(\gamma y) \qquad (2.2.9)$$

$$y' = e^{\gamma x}\sin(\gamma y) \qquad (2.2.10)$$

From Eqs. (2.2.9) and (2.2.10), it is evident that the parameter γ sets a periodic boundary condition in the original space: the permittivity values need to display a periodicity of $2\pi/\gamma$ along the *y*-axis, $\varepsilon(x, y) = \varepsilon(x, y + 2\pi/\gamma)$, i.e. the nanorod is an element in a one-dimensional (1D) array.

The inverse conformal transformation maps an individual nanoarc onto an array of nanorods of dimensions L-by-W if the following two conditions are satisfied:

(I) The origin of the nanoarc radii (i.e, the ring center) is placed at $\zeta' = 0$. Placing the nanoarc in any other location on the plane will result in a transformed object whose contour is not rectangular. Note that the arc may be placed in any orientation with respect to the origin within a ring, as long as this condition is satisfied.

(II) The mid-arc length of the nanoarc (L_{mid} in Figure 2.1.1), defined as the length of the line contour stretching along the middle of the width of the arc from one tip to the other, and computed using Eq. (2.2.11), and the nanoarc width ($W' = x'_R - x'_L$) relate to L, W and θ according to Eq. (2.2.12)

$$L_{mid} = \left(\frac{x'_R + x'_L}{2}\right)\theta \qquad (2.2.11)$$

$$\frac{\theta W'}{L_{mid}} = \frac{2(\exp(\frac{\theta W}{L}) - 1)}{\exp(\frac{\theta W}{L}) + 1} \qquad (2.2.12)$$

Eq. (2.2.12) is derived as follows:

Condition (I) makes the coordinates x_R' and x_L' in Figure 2.2.1 correspond to the outer and inner radii of the arc, respectively. Therefore, x_L' and x_R' relate to the mid-arc length and the width *W'* of the nanoarc

$$x_L' = \frac{L_{mid}}{\theta} - \frac{W'}{2} \quad (2.2.13)$$

$$x_R' = \frac{L_{mid}}{\theta} + \frac{W'}{2} \quad (2.2.14)$$

In the conformal transformation (Eqs. (2.2.7), (2.2.8)) the inner and outer contours of the nanoarc correspond to the left and right contours of the rod, respectively, thus the coordinates x_L', x_R', x_L and x_R are related through

$$x_L = \frac{1}{\gamma}\ln(x_L') \quad (2.2.15)$$

$$x_R = \frac{1}{\gamma}\ln(x_R') \quad (2.2.16)$$

The width of the rod *W* is determined by x_L and x_R as

$$W = x_R - x_L = \frac{1}{\gamma}\ln\left(\frac{x_R'}{x_L'}\right) \quad (2.2.17)$$

By substituting Eqs. (2.2.8), (2.2.13) and (2.2.14) into Eq. (2.2.17), one obtains

$$\frac{\theta W}{L} = \ln\left(\frac{2L_{mid} + \theta W'}{2L_{mid} - \theta W'}\right) \quad (2.2.18)$$

which is another form of Eq. (2.2.12).

Condition (II) defines the geometric parameters of the nanoarc (L_{mid} and *W'*) in the arc space based on the shape (length *L* and width *W*) of the nanorod in the rod space and θ. To maintain the geometric dimensions of the nanoarcs within narrow bounds, we chose $L_{mid} = L$, and computed the value for *W'*. The difference between *W* and *W'* ($\Delta W = W - W'$) calculated using Eq. (2.2.18) is shown in Figure 2.2.2 for nanoarcs with

different L_{mid} and central angle θ. The maximum ΔW in the patterns in this work is 3.6 nm (for L = 180 nm and W = 50 nm), which is comparable to the length uncertainty in the EBL pattern generation process. For most of our structures L > 500 nm, ΔW < 0.5 nm and this difference is inconsequential. Effectively, the above discussion identifies a conformal transformation that maps a 1D array of rods with length L to an individual arc with mid-arc length $L_{mid} = L$, and vice versa, independent of the curvature, with the width and thickness unaltered.

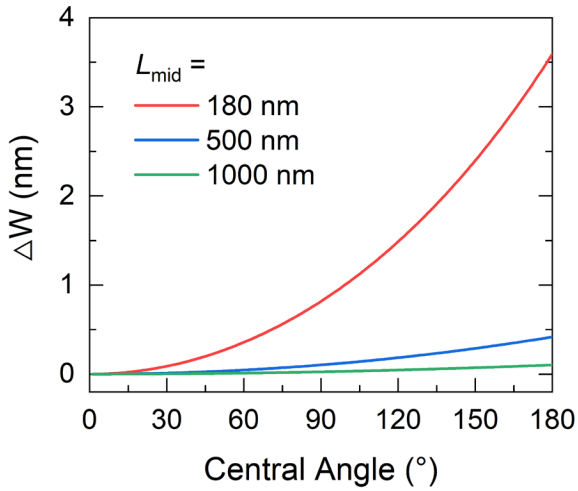

Figure 2.2.2 Difference between the width of the transformed nanorods (W) and the width of the original nanoarcs (W') computed using Eq. (2.2.18). $\Delta W = W - W'$ is plotted as a function of central angle θ for nanoarcs with different L_{mid}. The nanorods have a fixed width W = 50 nm.

Nanoarcs with small central angles ($\theta < 145°$) correspond to nanorod arrays with elements far enough apart (gap > 1.48L) so that plasmonic interactions (e.g. dipolar coupling) between adjacent elements can be neglected [90]. In this scenario, the conformal transformation analysis suggests that nanoarcs with different curvatures share the same LSPR spectra as long as they have the same L_{mid}, W and t. Furthermore, the variation of the resonance wavelength (λ_{res}) with L_{mid} in nanoarcs should track the variation of λ_{res} with L in nanorods. Overall, this analysis suggests that the vast

knowledge available for plasmonic nanorods and nanorod arrays can be readily utilized to predict the properties of plasmonic nanoarcs. Care must be taken when the central angle exceeds approximately 145°, since increasing the arc curvature should cause a blue-shift in the resonance (see Sections 2.5.2 and 2.5.3), in line with LSPR spectra of arrays of plasmonic nanorods coupled via short tip-to-tip gap distances (gap < 1.48*L*). [49, 50]

In summary, we have set up a method for predicting the spectra of plasmonic nanoarcs using the conformal transformation of Eq. (2.2.7) and the well-established optical spectra of plasmonic nanorods.

2.3 Numerical Simulations of Nanoarcs

The transformation optics analysis in Section 2.2 predicts that nanoarcs with the same L_{mid}, W' and t have the same LSPR wavelengths, regardless of the curvatures. To verify this prediction, we performed numerical simulations to calculate the scattering/absorption cross-section and the resonance wavelengths of the nanoarcs. In addition, the electric field profiles of the 1st and 2nd LSPR modes were extracted to study the electric dipole orientations at the two resonances.

2.3.1 Simulation Method

Numerical calculations were performed using 3D finite-difference-time-domain (FDTD) simulations with the *Lumerical* software package (v8.21.1882) by Dr. Matthew Davis. The model used in each simulation consisted of a single nanoarc placed on the surface of a semi-infinite substrate, as illustrated in Figure 2.3.1.1. The nanoarc was illuminated by a plane wave. The light scattering and absorption by the nanoarc

were monitored while sweeping the excitation wavelength. The electric near-field distributions at resonance conditions were also calculated. We have chosen to address exclusively gold nanoarcs on quartz substrates in order to circumvent including a surface oxide layer at the interface, as would be needed in a model that includes nanoscale objects made of Al or Si.

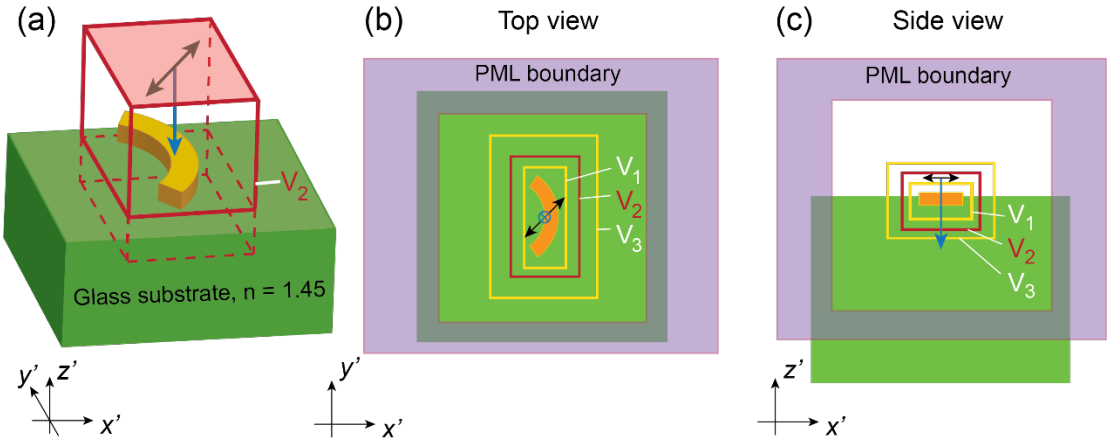

Figure 2.3.1.1 Schemes of the simulation region. A gold nanoarc (orange) placed on a dielectric substrate (green) is enclosed in a perfectly matched layer (PML) absorbing boundary (purple). The source field is injected through the total-field-scattered-field (TFSF) source denoted by the red box V_2. The TFSF source produces within V_2 an electric field that is equivalent to that of a linearly-polarized plane wave with the polarization aligned in the $x'y'$-plane at 45° with respect to the x'-axis, as indicated by the black double-headed arrow. The plane wave propagates along the negative z'-direction, as indicated by the blue arrow. The smaller yellow box V_1 represents the absorption monitor, while the larger yellow box V_3 represents the scattering monitor. (a) A 3D illustration of the region around the TFSF source. (b) The top view and (c) the side view of the simulation region.

The simulation region with volume V consisted of a single Au nanoarc with a width of W = 62 or 40 nm and a thickness of t =50 or 20 nm placed on the surface of a semi-infinite fused quartz substrate. The mesh size within the volume V was set to 2×2×2 nm^3. A perfectly matched layer (PML) boundary condition was applied to all sides of the simulation region (Figure 2.3.1.1) in order to minimize Fresnel reflections into the simulation space. The scattering cross-section σ_{scat} and the absorption cross-section

σ_{abs} of an isolated nanoarc as a function of frequency – quantities that are parallel to the plasmon extinction spectrum – were calculated using the Huygens surface method [114] which is also referred to as the total-field-scattered-field (TFSF) method. [115]

In the TFSF method, the investigated plasmonic nanoarc is placed inside a TFSF source, a near-field rectangular volume V_2 contained within the simulation region V with boundary electric and magnetic current sheets chosen to produce a normally incident plane wave in the interior of V_2, but to cancel the incident, transmitted and reflected plane waves in the exterior of V_2. Therefore, the nanoarc responds as if it is excited by a plane wave while the regions exterior to V_2 contain only the portion of light that was scattered by the nanoarc.

In these simulations, the TFSF plane wave propagated towards the substrate surface and the nanoarc at normal incidence (along negative *z'*-direction) and was linearly polarized with the electric field component oriented 45° with respect to the *x'*-axis of the nanoarc (same *x'*-axis as defined in Figure 2.2.1). The scattering cross-section σ_{scat} was defined as $P_{scat} = \sigma_{scat} I$, where I is the intensity given by the magnitude of the time-averaged Poynting vector of the excitation source and P_{scat} is the scattered power calculated as $P = \oint \vec{S}_{\text{avg}} \cdot d\vec{A}$, where $\vec{S}_{\text{avg}}$ is the time averaged Poynting vector of the scattered field outside of V_2 and the numerical integration was performed over a closed area with surface elements $d\vec{A}$ and enclosing a volume V_3 that contains both the nanoarc and TFSF source ($V_2 < V_3 < V$). Similarly, the absorption cross-section σ_{abs} was defined as $P_{abs} = \sigma_{abs} I$, where P_{abs} is the power removed from the incident plane wave by absorption, calculated using six rectangular surface monitors enclosing the nanoarc and a volume V_1 within the TFSF source ($V_1 < V_2 < V$). The extinction cross-

section was defined as the sum of the scattering and absorption cross-sections [116], $\sigma_{ext} = \sigma_{scat} + \sigma_{abs}$. The dielectric properties of the gold used in the simulations were taken from independent ellipsometry measurements from a 90-nm thick Au film thermally evaporated on a quartz substrate (Figure 2.3.1.2). A refractive index of 1.45 is used for the fused quartz substrate. [117]

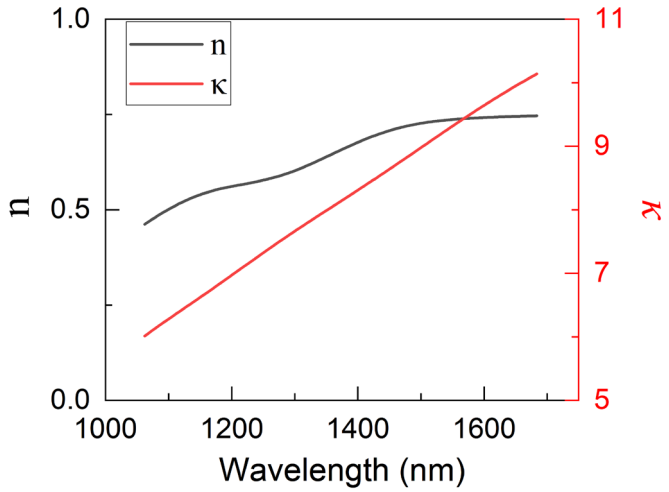

Figure 2.3.1.2 The real and imaginary components of the refractive index of a 90 nm gold film on a quartz substrate.

2.3.2 Effect of the Central Angle on the Scattering and Absorption Cross-section of Gold Nanoarcs

The dependence of the scattering cross-section spectra $\sigma_{scat}(\lambda)$, the absorption cross-section spectra $\sigma_{abs}(\lambda)$ and the extinction cross-section spectra $\sigma_{ext}(\lambda)$ on the central angle subtended by the nanoarc was studied in simulations of gold nanoarcs with mid-arc length L_{mid} = 395 nm, width W = 62 nm, thickness t = 50 nm and central angles in the range of θ = 0 – 180° on quartz substrates. The absorption, scattering and extinction cross-section spectra were calculated over the wavelength range of 600 – 2600 nm to discern the position and intensity of the fundamental and 2nd order LSPR peaks. The simulation results were analyzed with respect to experimental FTIR and visible

transmission spectra collected from gold nanoarcs with similar dimensions (L_{mid} = 395 nm, W = 60 nm, t = 55 nm, and θ = 0° – 180°) fabricated on a fused quartz substrate (methods in Section 2.4.1 – 2.4.5). In order to compare the experimental transmission data to the simulated σ_{scat}, σ_{abs} and σ_{ext} spectra, the transmission spectra were converted point-wise to extinction spectra using the relation: extinction $(\alpha(\lambda))$ = $-log_{10}[T(\lambda)]$.

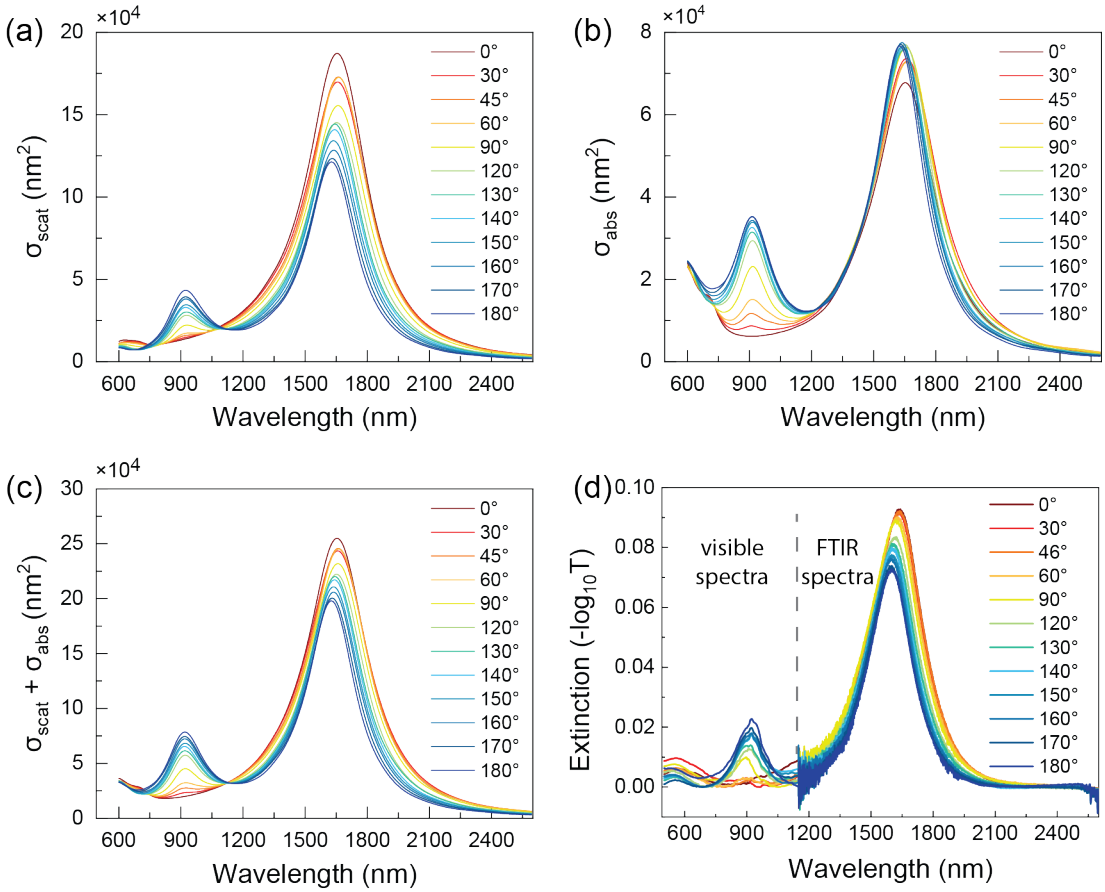

Figure 2.3.2.1 (a,b) Simulated scattering cross-section spectra $\sigma_{scat}(\lambda)$ and absorption cross-section spectra $\sigma_{abs}(\lambda)$ of gold nanoarcs on quartz with L_{mid} = 395 nm, W = 62 nm, t = 50 nm, and θ = 0° – 180°. (c) Simulated extinction cross-section spectra $\sigma_{ext}(\lambda)$. (d) Visible extinction spectra and FTIR extinction spectra of gold nanoarcs on quartz with L_{mid} = 395 nm, W = 60 nm, t = 55 nm, and θ = 0° – 180°.

The scattering cross-section spectra (Figure 2.3.2.1 (a)) and the absorption cross-section spectra (Figure 2.3.2.1 (b)) display two peaks at 1626-1664 nm and 913-930

nm. The main difference between the two sets of spectra is in the intensity of the peaks. The values of the scattering cross-section are larger than the values of the absorption cross-section, by up to a factor of approximately 3. At the fundamental resonance wavelength, the intensity of the scattering cross-section decreases with central angle, as was observed in experimental extinction data of nanoarcs. In contrast, the intensity of the absorption cross-section increases with central angle. Thus, the simulations indicate that in these gold nanoarcs the dominant light-surface plasmon interaction is light scattering. The sum of the scattering and absorption cross-section (Figure 2.3.2.1 (c)) adequately predicts the wavelength and intensity of the extinction peaks due to the longitudinal LSPRs in nanoarcs, including the impact of the central angle on these properties (Figure 2.3.2.1 (d)). Specifically, the variations of the LSPR peak intensities in panel (c) are in good agreement with the peak intensity variations in panel (d), i.e. the intensity (peak height) of the 1st LSPR mode deceases as the central angle increases, while that of the 2nd LSPR mode shows the opposite trend. The LSPR wavelengths (λ_1 and λ_2) obtained from the calculated $\sigma_{ext}(\lambda)$ spectra using a Gaussian-Lorentzian fit (Section 2.4.6) agree well with the experimental results, as summarized in Figure 2.3.2.2 (data tabulated in Appendix 8.2). The calculated spectra of σ_{ext} show two peaks at λ_1 = 1626 – 1660 nm and λ_2 = 917 – 921 nm. As the central angle (θ) changes from 0° to 60°, λ_1 slightly increases from 1653 nm to 1660 nm, and as θ increases from 60° to 180°, λ_1 decreases from 1660 nm to 1626 nm. The overall variation is 2.1%. For the 2nd LSPR mode, as θ increases from 60° to 180°, λ_2 varies from 921 nm to 919 nm. The variation of λ_2 is negligibly small. The experimental data (Figure 2.3.2.1 (d)) shows similar features: the two LSPR peaks in the measured extinction spectra are at

λ_1 = 1597 – 1639 nm and λ_2 = 894 – 925 nm. λ_1 in the extinction spectra is nearly constant when the central angle increases from 0° to 45° and decreases as the angle increases from 45° to 180°. The variation of λ_1 is 2.6%. λ_2 increases as the central angle increases from 60° to 180°. The variation of λ_2 is 3.5%. The maximum difference between the experimental data and the calculated data is less than 2.7%.

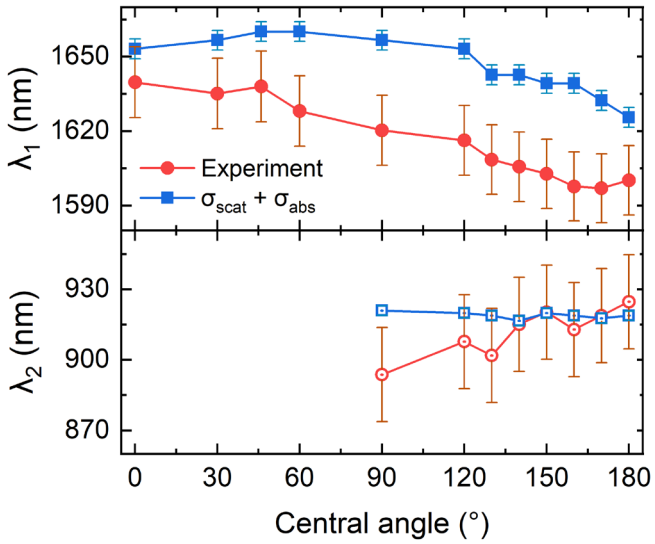

Figure 2.3.2.2 The 1st and 2nd LSPR wavelength (λ_1 and λ_2) of nanoarcs with L_{mid} = 395 nm. Data were obtained from the spectra in Figure 2.3.2.1 (c) and (d). For λ_1 obtained from experimental data, the error bar ± 0.87% is determined using the statistical deviation of the resonance wavelengths of nanostructures fabricated on quartz (see Section 2.5.1). For λ_2 obtained from experimental data, the error bar ±20 nm is estimated as twice the variation of λ_2 observed in repeated measurement of visible spectra from the same array. For λ_1 and λ_2 obtained from simulation, the error bar is ± 4 nm and ± 2 nm, respectively, which is determined based on the wavelength spacing in the cross-section simulation.

Importantly, both the simulation (i.e. σ_{ext}) and experimental results (i.e. extinction spectra) show that the central angle has a minor effect on the peak position in the spectra (variation ≤ 3.5%), in line with the conclusions of the TO analysis (section 2.2) that the resonance wavelengths of nanoarcs are primarily determined by L_{mid}. We note that a previous computational study reported on the minor blue-shift in λ_1 as the curvature

increases in nanoarcs subtending large central angles, from 90° up to at least 270°, until the onset of capacitive coupling between the tips of the arc dramatically red-shifts the resonance. [90]

In summary, simulated spectra of σ_{scat}, σ_{abs} and σ_{ext} of nanoarcs were compared to the experimental extinction spectra, and this analysis confirms that nanoarcs with the same L_{mid}, W' and t have the same LSPR wavelengths regardless of central angle, one of the predictions of the conformal transformation analysis.

2.3.3 Near-field Electric Field Profile around a Gold Nanoarc

This set of simulations was performed to calculate the electric field profile in the near field of a gold nanoarc on a quartz substrate, with the purpose of investigating the electric dipole orientations of the 1st and 2nd LSPR modes.

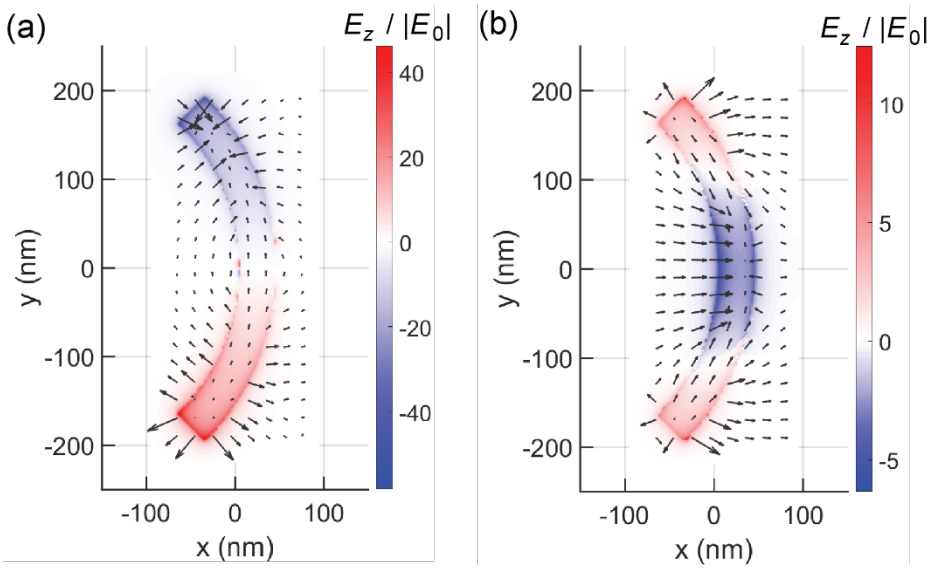

Figure 2.3.3.1 Calculated surface plasmon mode profiles displayed as the magnitude of the *E*-field components, in the vicinity of an L_{mid} = 395 nm, W = 40 nm, t = 20 nm, θ = 90° gold nanoarc on quartz, for excitation wavelengths (a) λ = 2200 nm and (b) λ = 1100 nm. Arrows represent the normalized in-plane components (E_x / $|E_0|$, E_y / $|E_0|$) of the electric field. Color represent the normalized out-of-plane component (E_z / $|E_0|$) of the electric field. $|E_0|$ is the magnitude of the incident *E*-field.

The electric near-field distribution around a gold nanoarc on a quartz substrate was simulated for a nanoarc with a mid-arc length of 395 nm and subtending a central angle of 90°. The nanoarc width (W = 40 nm) and thickness (t = 20 nm) in these simulations were selected to be smaller than the experimental values, as a means of reducing the calculation time while still achieving the goals of this investigation. First, a coarse-grid scattering cross-section spectrum was simulated, in order to identify the wavelengths of the LSPR peaks. For this geometry, the resonances occur at $\lambda_1 \approx 2200$ nm and at $\lambda_2 \approx 1100$ nm. At these wavelengths, the electric field distribution within the simulation volume $\bar{E}(\bar{r})$ was calculated and normalized to the magnitude of the electric field of the incident plane wave $|E_0|$. In the simulation of the field distribution, the incident light was linearly polarized at 45° with respect to the *x'*-axis. This polarization angle was chosen to ensure that electric dipoles along both the *x'* and *y'*-axis could be excited. The normalized electric near-field vector-field at each resonance condition was analyzed to extract the orientation of the electric dipole, the location of field enhancement sites and their relative enhancement efficiency. Figure 2.3.3.1 shows two profiles of the calculated electric field amplitude in the vicinity of the nanoarc at resonance. The data corresponds to a plane normal to the *z*-axis situated in air, 2 nm above the gold surface. The in-plane components of the normalized electric field, E_x / $|E_0|$ and E_y / $|E_0|$, are represented by the arrows, whereas the out-of-plane component E_z / $|E_0|$ is represented by color. In Figure 2.3.3.1 (a), corresponding to the 1st LSPR mode of the nanoarc, the maxima in the electric field amplitude are found at the tips of the nanoarc. The electric field distribution (and the surface charge density) is anti-symmetric with respect to the *x*-axis, suggesting an LSPR mode with an instantaneous

electric dipole oriented parallel to the *y*-axis (and an out-of-plane magnetic dipole, not shown). The electric field intensity is largest by the corners of the arc tips due to the lighting-rod effect and the field enhancement factor $(|E_x|^2 + |E_y|^2 + |E_z|^2) / |E_0|^2$ is up to 4.0×10^3. This strong electric field at the tips of the nanoarc is beneficial for surface enhancement effects including surface enhanced Raman scattering (SERS) and surface enhanced infrared absorption (SERIA; see Section 5.4). Figure 2.3.3.1(b) corresponds to the 2nd LSPR mode of the nanoarc. Here, the electric field distribution is symmetric with respect to the *x*-axis. For the 2nd LSPR mode, the electric field intensity (and the surface charge density) is high at the two arc tips and around the middle of the arc, with an enhancement factor $(|E_x|^2 + |E_y|^2 + |E_z|^2) / |E_0|^2$ of up to 170, showing additional potential for surface enhanced spectroscopy applications. The centers of mass of the instantaneous positive and negative surface charge are offset, suggesting a mode with an instantaneous electric dipole parallel to the *x*-axis, which increases with central angle. The simulation results indicate that the electric dipoles of the 1st and 2nd LSPR modes are orthogonal to each other. The two modes could therefore be excited individually by *y'*- or *x'*-linearly polarized light. This attribute of the resonance modes was utilized in the design of the polarization-dependent spectroscopy measurements reported in Section 2.5.3.

2.4 Sample Fabrication and Characterization Methods

Nanorod and nanoarc arrays were fabricated by electron-beam lithography, metal film thermal evaporation, and lift-off procedures. The samples were characterized by spectroscopy and microscopy tools as described below.

2.4.1 Pattern design

The patterns in this thesis were designed in a CAD (computer-aided design) software *LayoutEditor*. A typical pattern consists of four parts as shown in Figure 2.4.1.1: the label, the corner marks, the alignment marks (not shown) and the nanostructure arrays. The label is a text (line width of each letter > 3 μm) that provides information regarding the dimensions of the nanostructures and/or the lattice parameters of the arrays. For example, the label "L1000W50A0 – fix y" in Figure 2.4.1.1 indicates that the arrays in this pattern consist of nanoarcs with dimensions of $L(L_{mid})$ = 1000 nm, W = 50 nm, and central angle θ = 0°, and the lattice parameter along the y-axis is fixed.

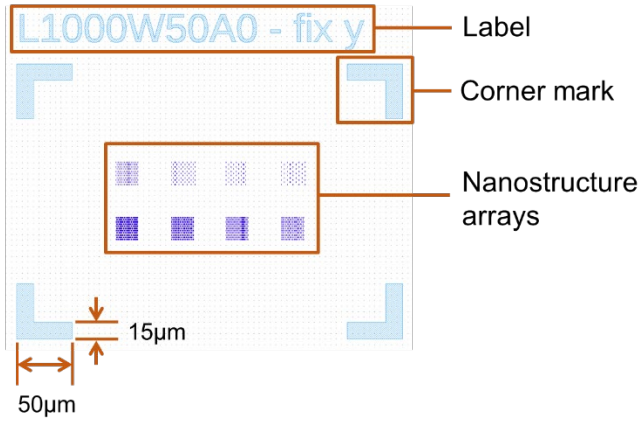

Figure 2.4.1.1 A CAD pattern with a label, 4 corner marks and 8 nanostructure arrays. The alignment marks are not shown here due to their large size.

The alignment marks and corner marks are used to assist in locating the nanostructure arrays by eye or under the optical microscope and SEM. The alignment marks are squares with a size of 250 μm by 250 μm and crosses with four arms 150 μm or 400 μm long. When fabricated on a substrate, these large marks can be observed with the naked eye therefore they are used for quality control. When the sample is observed under an optical microscope or SEM, the alignment marks and the corner marks help to align the axes of the sample to the horizontal and vertical axes of the field of view.

Due to the diffraction limit, it is hard to observe the nanostructures under a standard optical microscope, while the corner marks are sufficiently large (each 50 μm by 15 μm in size as illustrated in Figure 2.4.1.1) and can be easily observed. In the pattern design, one or more nanostructure arrays are placed in rectangular regions enclosed by four corner marks, with known distances between the corners of the corner marks and the center of the nanostructure arrays. When observing the pattern under a microscope, the region of the nanostructure arrays is reached by first locating the label and a corner mark nearby and then moving the sample stage by the known distance, so that the center of the array is aligned to the center of the field of view.

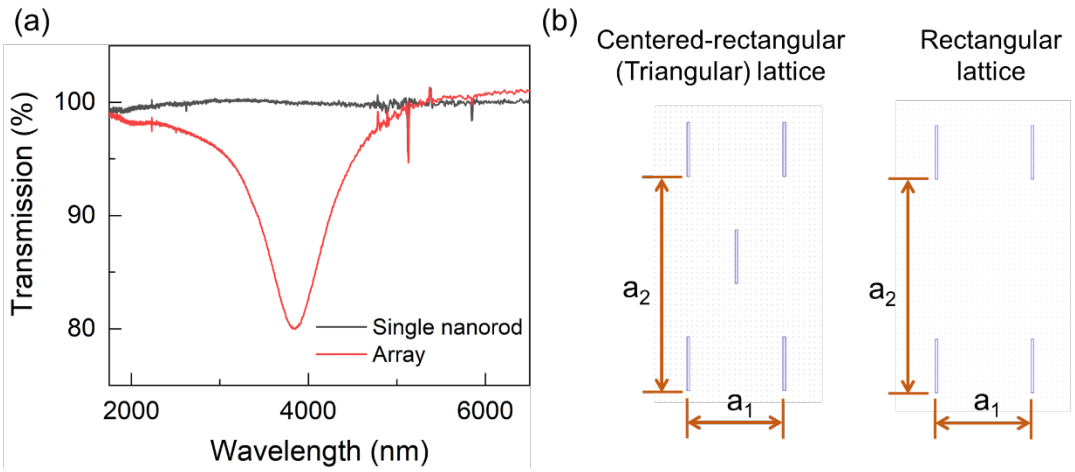

Figure 2.4.1.2 (a) FTIR transmission spectra of a single nanorod and a nanorod array. The dimensions of the nanorod are $L = 600$ nm, $W = 50$ nm, and $t = 55$ nm. The nanorod array has a rectangular lattice with (a_1, a_2) = (1.0, 1.6) μm. (b) Two lattices of nanostructures: centered-rectangular (triangular) lattice and rectangular lattice, with the definitions of the lattice parameters (a_1, a_2).

In our experiments, the FTIR spectrum is collected from an array of identical nanostructures instead of a single nanostructure because the light scattering of the latter is too weak to be detected by the spectrometer, while the light scattering of an array is contributed by all elements that have been illuminated, therefore it is more intense and

can be easily detected. An example of the spectra of a single nanorod and a nanorod array is shown in Figure 2.4.1.2 (a). About 60 nanorods in the array were illuminated by the light spot resulting in a LSPR peak with an attenuation (1-T) of 20%, while the LSPR peak of the single nanorod is indistinguishable from the baseline.

The elements in the arrays are arranged in either a center-rectangular lattice (which we also call a triangular lattice) or a rectangular lattice, as shown in Figure 2.4.1.2 (b). In most cases, the arrays have a triangular lattice to benefit from its higher density of nanostructures. The nanoarc arrays in this work were each 20 × 20 μm^2, 80 × 80 μm^2 or 150 × 150 μm^2 in area. The elements in an array needs to be sufficiently far apart such that there is no dipolar coupling between adjacent element, in order for the spectrum of the array to be representative of the spectrum of the individual elements. The effect of the lattice parameters on the LSPR wavelength will be discussed in Section 2.5.2.

2.4.2 Electron-Beam Lithography

Nanoarc arrays were fabricated on double-side polished single-crystal silicon (0.38 mm thick, n-type, 20-30 ohm-cm, Silicon Inc.) or high-purity fused quartz substrates (0.5 mm thick, Ted Pella, #26016) using electron beam lithography (EBL). First, the substrate (silicon or quartz) was cleaned by acetone, isopropanol, and distilled water, and was dried by baking at 180°C for 2 min. Next, two layers of photoresists, ~100 nm thick P(MMA (8.5) MAA) (6% in ethyl lactate, MicroChem) and ~80 nm thick PMMA (950k molecular weight, 2% in anisole, MicroChem), were spin-coated onto the substrate with a spin-rate of 4000 rpm, and were baked at 180 °C for 1 min and 10 min, respectively. For quartz substrates, an additional conductive polymer (aquaSAVE) was

spun on top of the bi-layer photoresist to avoid charge accumulation during the e-beam exposure. The pattern files for e-beam exposure were prepared in *LayoutEditor* (Section 2.4.1) and were converted to machine code by *WecaS* CAD software. EBL pattering was performed in an Elionix G100 system with an accelerating voltage of 100kV and an e-beam current of 1 nA for nanoarc arrays, or 20 nA for marks and labels. The electron-beam dose depended on the photoresist used and the substrate material and was determined through a series of trial experiments. After e-beam exposure, the aquaSAVE layer on quartz substrates was removed by soaking the substrate in distilled water for 3s. The samples were developed in 1:3 methyl isobutyl ketone:isopropanol (1:3 MIBK:IPA) for 50s at room temperature to remove the photoresists from the exposed regions.

2.4.3 Thermal Evaporation and Lift-off

After development, a 20nm or 50-55 nm-thick metal film (gold 99.995% or aluminum 99.999% from Alfa Aesar) was thermally evaporated onto the patterned sample (without adhesion layers) using a custom-made vacuum chamber with base pressure of 10^{-6} Torr (Blue Wave Semiconductors Inc.). Lift-off was completed by submerging the sample in acetone at room temperature for about 1 hour until the metal film in the un-exposed regions fully detached from the substrate surface. After lift-off, the sample was cleaned by soaking in isopropanol and distilled water and was dried under a flow of nitrogen. The sample was then inspected using optical microscopy to check the quality of the pattern.

2.4.4 Fourier Transform Infrared Spectroscopy

Infrared reflection and transmission spectra of gold nanoarcs on silicon were acquired with a synchrotron-based system (LBNL ALS beamline 1.4 combined with a Nicolet FTIR spectrometer and a Nicolet Nic-Plan IR microscope) as illustrated in Figure 2.4.4.1. The incident light was focused using a 32x Schwarzschild objective lens, and the diameter of the focused incident light was diffraction-limited at ~10 μm. The light spot was aligned with the center of the nanoarc array for each measurement using the corner marks and a motorized sample stage. Additional measurements were performed using a Nicolet Continuum IR microscope coupled to a Nicolet iS50 FTIR spectrometer. This benchtop spectrometer employs a tungsten-halogen white light source in the NIR and a Thermo Scientific Polaris source in the mid-IR. A 15x objective lens and an image-plane aperture were used to selectively probe a single array of nanoarcs. The nanoarc arrays in this work were each 20 × 20 μm^2, 80 × 80 μm^2 or 150 × 150 μm^2 in area. The aperture size was set to be 30 × 30 μm^2 for small-area arrays, and 70 × 70 μm^2 for large-area arrays.

The background spectra were typically collected with 256 scans and a resolution of 0.482 cm^{-1}. The sample spectra were collected with same spectral resolution and 32-256 scans in the wavelength range of 650 – 10000 cm^{-1} (1000 – 15350 nm) excluding ranges of high attenuation by the substrates. For polarization-dependent FTIR spectroscopy, a wire-grid linear polarizer (WP25M-UB, Thorlabs) was placed between the light source and the sample. Alignment of the polarizer axis with respect to the sample axes was achieved by minimizing the FTIR signal from the odd-order LSPR modes. In all the FTIR measurements light was incident normally on the sample plane

and was detected with a liquid nitrogen cooled MCT (mercury cadmium telluride) detector. These spectroscopic measurements identified one or more LSPRs for each array of nanostructures as peaks in the reflectance spectra and corresponding dips in the transmission spectra. The LSPR wavelengths of the nanoarcs are widely tunable throughout the infrared spectral range by adjusting shape parameters (H, W, t or θ) or changing the materials used.

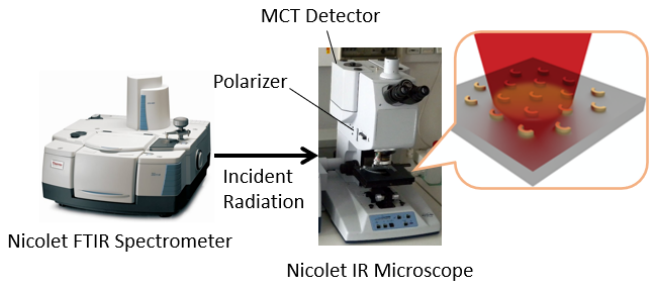

Figure 2.4.4.1 Schematic of the FTIR setup. The inset is an illustration of the IR beam illuminating a nanoantenna array.

2.4.5 Visible and Near-IR Spectroscopy

UV-Visible-NIR transmission spectra of gold nanoarcs on quartz were acquired using a Microspectra 121 microspectrometer (CRAIC Technologies) coupled to an AXIO microscope (ZIESS) by Dr. Oded Rabin at the Air Force Research Laboratory (Dayton, OH). The spectrometer employs a tungsten lamp to produce light in the NIR and a thermal source to produce UV-visible light. The combined spectral range is 300 – 1700 nm. A 15x objective lens and an image-plane aperture (30 × 30 μm^2) were used to selectively probe a single array of nanoarcs. The Image UV software was used for imaging and the CRAIC Minerva software was used for spectroscopy.

2.4.6 Determination of the LSPR wavenumber and the LSPR wavelength

The frequencies/wavelengths of the LSPR peaks in each FTIR spectrum were determined using a MATLAB-based peak-fitting software [118]. Each peak in an FTIR spectrum was modeled as the sum of a Gaussian function and a Lorentzian function,

$$T_{LSPR}(\nu) = f_{Gaussian}(\nu) + f_{Lorentzian}(\nu) \qquad (2.4.6.1)$$

where T_{LSPR} is the curve fitted to the FTIR transmission spectrum, ν is wavenumber (unit: cm^{-1}), $f_{Gaussian}$ is given by

$$f_{Gaussian}(\nu) = A_1 e^{-\frac{(\nu-\mu_1)^2}{(\Gamma_1/2\sqrt{\ln 2})^2}} \qquad (2.4.6.2)$$

and $f_{Lorentzian}$ is given by

$$f_{Lorentzian}(\nu) = \frac{A_2}{1 + (2/\Gamma_2)^2(\nu - \mu_2)^2} \qquad (2.4.6.3)$$

A_1, μ_1 and Γ_1 are the peak amplitude, peak center and the full width at half maximum (FWHM) of the Gaussian function, respectively, and A_2, μ_2 and Γ_2 are the peak amplitude, peak center and FWHM of the Lorentzian function, respectively. The peak-fitting Matlab program employed the least-squares method to fit T_{LSPR} to the FTIR data. The fit is performed over a limited range of wavenumbers that contains the resonance peak, and which may be discontinuous due to exclusion of data ranges affected by molecular signals (e.g. atmosphere gases). The wavenumber corresponding to the minimum of the fitting curve ($\frac{dT_{LSPR}(\nu)}{d\nu}\Big|_{\nu_{res}} = 0$) was recognized as the LSPR frequency. For consistency, data values and plots are displayed in terms of wavelength in this thesis. Thus, after fitting, data was converted from wavenumbers to wavelengths via $\lambda = 10^7/\nu$ (the unit of λ is nm). An example of a curve fitted to a measured FTIR spectrum by this method is shown in Figure 2.4.6.1. The fitting procedure was applied

to the data in the range of 2400 – 3100 cm^{-1}, containing the 1st LSPR peak. After unit conversion, the fitting curve is reported as spanning the range of 3225 – 4166 nm.

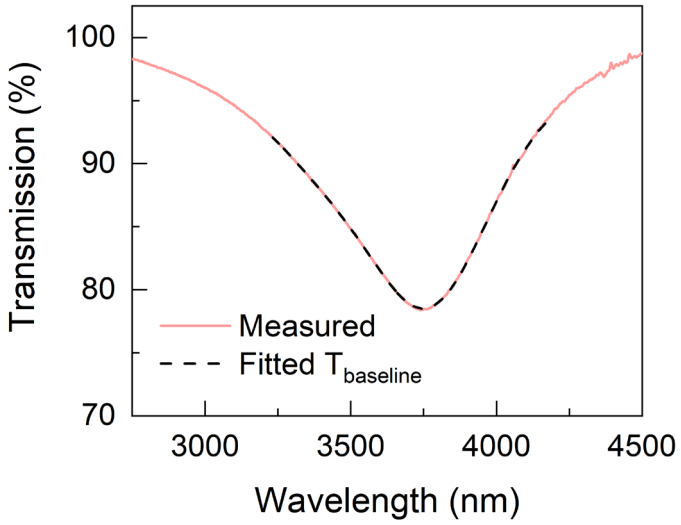

Figure 2.4.6.1 A portion of the FTIR spectrum of gold nanorods on a quartz substrate (L = 1000 nm, W = 50 nm and t = 55 nm) and the curve fitted to the 1st LSPR peak.

2.4.7 Scanning Electron Microscopy

Scanning electron microscopy (SEM) was performed in a Hitachi SU-70 system with an accelerating voltage of 10 kV and a working distance of 5 mm. Electron microscopy was used to determine the physical length L of nanorods, height H of nanoarcs, and width W of the nanostructures in each array. SEM imaging indicates that the corners of the nanostructures are rounded with a characteristic radius of approx. 10 nm. Examples of the SEM images are shown in Figure 2.4.7.1.

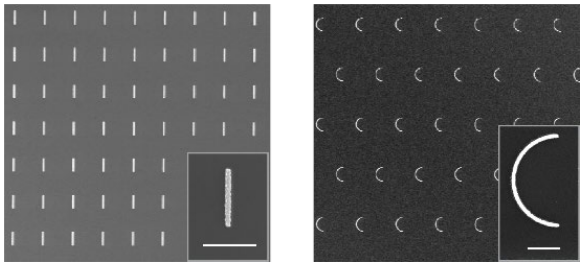

Figure 2.4.7.1 SEM images of gold nanorods and nanoarcs on silicon substrates. Insets are corresponding high magnification images. The inset scale bars are 500 nm long.

2.4.8 Atomic Force Microscopy

Atomic force microscopy (AFM) was performed in tapping mode using an Asylum Research Cypher ES system for substrates smaller than 1.5 × 1.5 cm^2, and an Asylum MFP-3D system for larger substrates. In the Cypher ES system, Arrow^{TM} UHF probes (NanoWorld; f = 755 kHz, k = 1N/m) were employed. In the MFP-3D system, Arrow NCR probes (NanoWorld; f = 285 kHz, k = 42 N/m) were utilized. AFM height profiling was used to determine the thickness *t* of the nanostructures. For patterns on quartz substrates, AFM imaging was utilized to obtain an estimate of the length *L* and width *W* of the nanostructures because quartz is non-conductive and SEM cannot provide high-resolution images of the nanostructures on quartz due to sample charging.

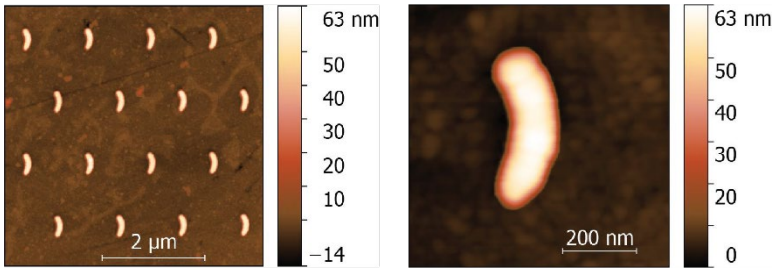

Figure 2.4.8.1 AFM images of gold nanoarcs on a quartz substrate.

2.5 Localized Surface Plasmon Resonances in Nanoarcs with Uniform Width Profile

2.5.1 Statistical Analysis of the Variation of the Resonance Wavelengths due to Fabrication Flaws

The lithography techniques and the photoresist quality limit the spatial resolution of the fabricated nanostructures. Fabrication flaws, including rounding at the corners, waviness on the edges, and non-uniform metal thickness, make the physical dimensions of the nanostructures different from their nominal dimensions listed in the design in the CAD file. As a result, repeating the fabrication of a single pattern for multiple times

may lead to slightly different outcomes even though the same fabrication protocol was followed. Therefore, before investigating the optical properties of different nanostructures, it is necessary to quantify the variation range of the LSPR wavelengths of nominally identical nanostructure, i.e., find out the extent of spectral shifts induced by fabrication flaws. This quantification was done by replicating small arrays of nanoarcs multiple times on a single substrate and measuring the FTIR spectra of the small arrays to find the maximum (λ_{max}), minimum (λ_{min}) and the average (λ_{avg}) of the LSPR wavelengths. These values were used to determine the deviation of the resonance wavelength, defined as ((λ_{max} - λ_{min})/ λ_{avg}).

The deviation of the LSPR wavelength induced by fabrication flaws was studied using gold nanoarcs on silicon and quartz substrates. The two substrates have different refractive indices which substantially impacts the LSPR wavelengths. The dimensions of the nanoarcs are summarized in Table 2.5.1.1. The nanoarcs on quartz have three different central angles θ = 0°, 46° and 180° and constant H, W and t. The nanoarcs on silicon have two different widths W = 50 nm and 100 nm, and constant H, θ and t. Each nanoarc array was replicated 49 times using the fabrication methods described in Section 2.4.1 – 2.4.3. FTIR spectra were collected from each array using the methods described in Section 2.4.4. For the nanoarcs on quartz, the LSPR wavelengths and intensities were determined using the Gaussian-Lorentzian fit described in Section 2.4.6. For nanoarcs on silicon, the LSPR wavelengths and intensities were determined by a fit to a 7th degree polynomial function

$$f(\nu) = b_7\nu^7 + b_6\nu^6 + \cdots + b_2\nu^2 + b_1\nu + b_0 \qquad (2.5.1.1)$$

where ν is the wavenumber, and $b_0,\ldots,b_7$ are the coefficients of the polynomial. The Gaussian-Lorentzian fit was not used for these data because these LSPR peaks were weak and noisy (Figure 2.5.1.3 (a) and (b)). The Gaussian-Lorentzian fit (with 6 fitting parameters) occasionally recognized erroneously a spike in the noise as the LSPR peak, while the polynomial function (with 8 parameters) could match the LSPR peaks more reliably. The polynomial fitting was accomplished using the "fit" function in Matlab. The wavenumber corresponding to the minimum of the polynomial function $\left(\frac{dT_{LSPR}(\nu)}{d\nu}\Big|_{\nu_{res}} = 0\right)$ was recognized as the LSPR peak position, and the result was reported as wavelength in nms.

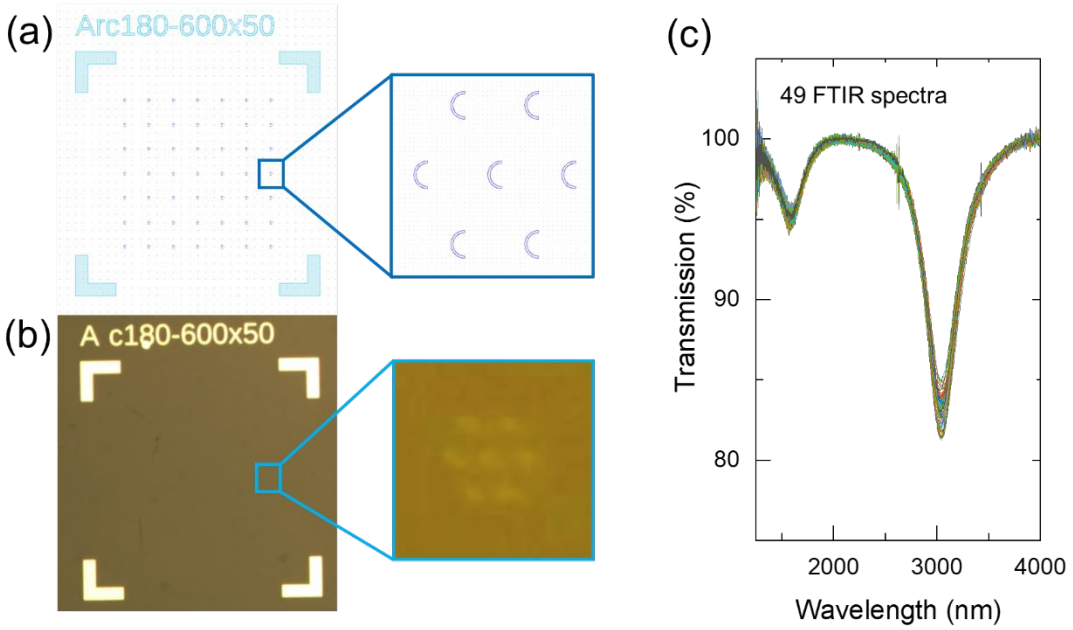

Figure 2.5.1.1 (a) A CAD pattern that includes 49 arrays as a square matrix. Each spot in the matrix represents an array containing 7 nanoarcs with H = 600 nm, W = 50 nm and θ = 180° as shown in the inset. This pattern was fabricated using gold on a quartz substrate. (b) Low and high magnification optical images of the fabricated pattern. (c) The FTIR transmission spectra obtained from the 49 nanoarc arrays in the pattern shown in (b).

An example of gold nanoarcs on quartz with $\theta = 180°$ is shown in Figure 2.5.1.1. Panels (a) and (b) shows the design and the optical microscopy images of the pattern, respectively. The FTIR transmission spectra of all 49 arrays are shown in panel (c).

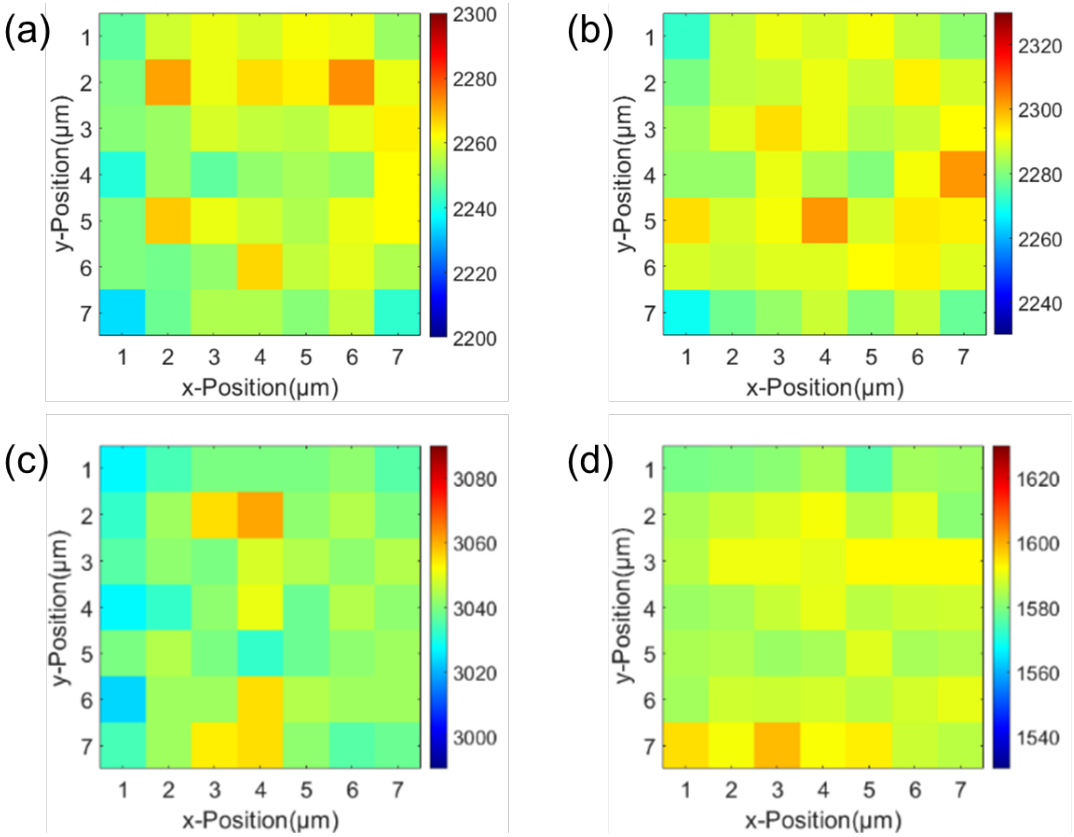

Figure 2.5.1.2 The 1st and 2nd LSPR wavelengths of gold nanoarcs on quartz. Each plot shows a 7-by-7 matrix. Each square in the matrix represents a small nanoarc array containing 7 or 9 elements. The color of the square corresponds to the wavelength of the 1st or 2nd LSPR of the nanoarcs. The nanoarcs have dimensions of $H = 600$ nm, $W = 50$ nm, $t = 55$ nm and (a) $\theta = 0°$ (nanorod), (b) $\theta = 46°$, or (c, d) $\theta = 180°$. The data in (a), (b) and (c) are for the 1st LSPR wavelength. The data in (d) is for the 2nd LSPR wavelength.

Figure 2.5.1.2 presents the LSPR wavelengths of gold nanoarcs on quartz. The LSPR wavelength of each array replicate is represented by color. Panels (a) – (c) show the 1st LSPR wavelengths of nanoarcs with $\theta = 0°$, 46° and 180° (nominal $L_{mid} = 600$, 606 and 903 nm), respectively, and panel (d) shows the 2nd LSPR wavelength of nanoarcs with $\theta = 180°$. The LSPR wavelengths in each panel vary, despite all 49 arrays being replicas.

These variations provide us a measure of the uncertainty caused by the fabrication flaws and likely affecting all the experiments in this work. In each panel of Figure 2.5.1.2, the nanoarc arrays whose LSPR wavelength deviates far from the mean value appear in random positions (bluer or redder squares), suggesting there is no systematic error in the fabrication process or data processing. The maximum (λ_{max}), minimum (λ_{min}), average value (λ_{avg}) and the deviation ((λ_{max} - λ_{min})/ λ_{avg}) are summarized in Table 2.5.1.1. Longer nanoarcs show smaller deviations in λ_1, which is expected because the fabrication flaws lead to similar amount of change in the physical dimensions of different nanoarcs. The longer the nanoarc, the smaller the percentage change in the arc dimension, therefore, the deviations in its LSPR wavelength (which depends on arc dimensions) are smaller. The nanorod arrays with $\theta = 0°$ display the largest deviation at 1.73%. This value was utilized when setting the statistical deviation of the resonance wavelength from the mean due to fabrication flaws in our experiments on quartz as ± 0.87%.

Table 2.5.1.1 The maximum, minimum, average, and maximum deviation of the LSPR wavelengths of gold nanoarcs on quartz and silicon substrates (based on 49 replicas).

Antenna/ Substrate Material	Rod/Arc Dimensions * (LSPR order)	λ_{max} (nm)	λ_{min} (nm)	λ_{avg} (nm)	Deviation (λ_{max} - λ_{min})/ λ_{avg}
Au/SiO_2	*H*600*W*50*t*55 *L*600, $\theta = 0°$ (λ_1)	2273	2234	2256	**1.73%**
	*H*600*W*50*t*55 *L*606, $\theta = 46°$ (λ_1)	2303	2268	2288	1.53%
	*H*600*W*50*t*55 *L*903, $\theta = 180°$ (λ_1)	3061	3023	3041	1.25%
	*H*600*W*50*t*55 *L*903, $\theta = 180°$ (λ_2)	1599	1576	1587	1.45%
Au/Si	*H*600*t*55θ90 *W* = 50nm (λ_1)	4409	4257	4336	**3.50%**
	*H*600*t*55θ90 *W* = 100nm (λ_1)	3904	3864	3889	1.03%

*H: height, L: length of nanorod or mid-arc length of nanoarc, W: width, t: thickness, unit: nm. θ: central angle, unit: °.

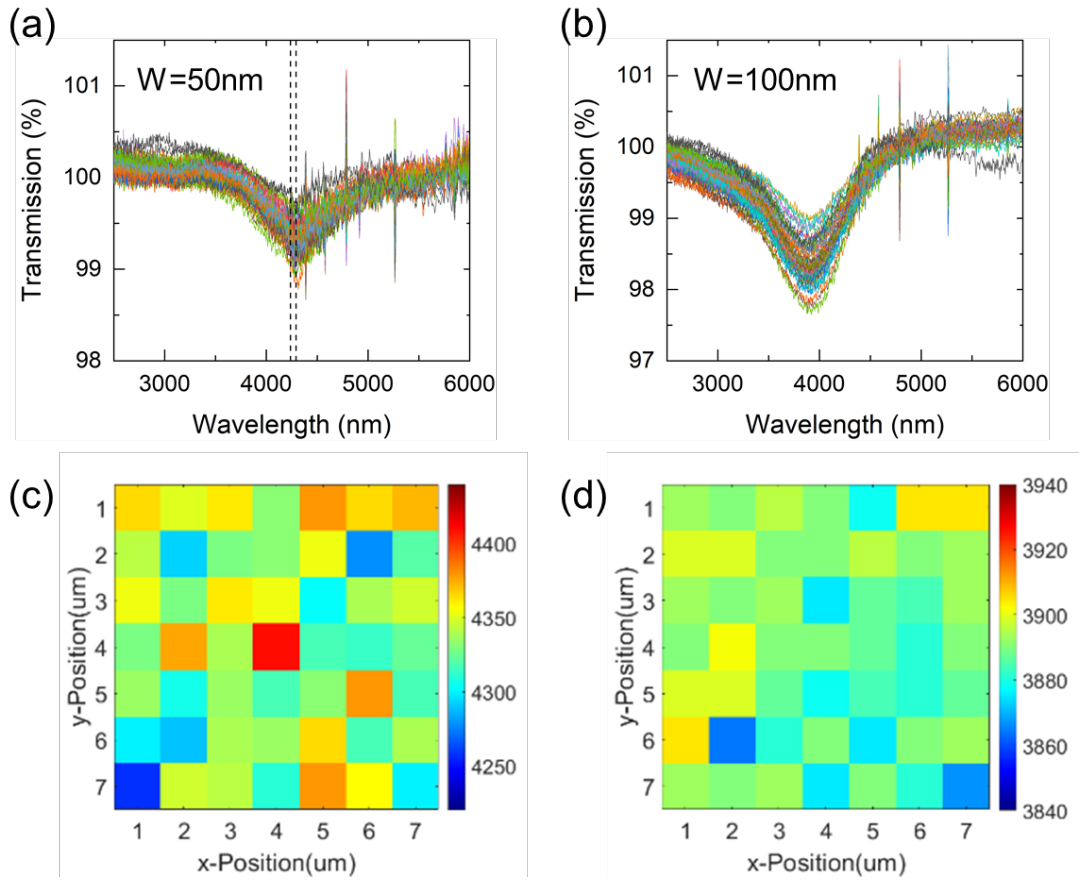

Figure 2.5.1.3 (a, b) 49 FTIR transmission spectra of gold nanoarcs on silicon. The nanoarcs have dimensions of H = 600 nm, θ = 90°, t = 55 nm and (a) W = 50 nm, or (b) W = 100 nm. The two dashed lines in panel (a) mark the positions of the CO_2 signal at 4292 nm and 4237 nm. (c, d) The 1st LSPR wavelength of the nanoarcs shown in (a) and (b), respectively. Each plot shows a 7-by-7 matrix. Each square in the matrix represents a small nanoarc array containing 9 elements. The color of the square corresponds to the wavelength of the 1st LSPR of the nanoarcs.

Figure 2.5.1.3 presents the FTIR transmission spectra (panel (a) and (b)) and the LSPR wavelengths (panel (c) and (d)) of gold nanoarcs with two widths (W = 50 nm and 100 nm) on silicon. The set of narrow nanoarcs (W = 50 nm) shows larger deviations in the LSPR wavelength than the set of wide nanoarcs (W = 100 nm) because the fabrication flaws affect the physical dimensions of different nanoarcs by similar amounts. While the L_{mid} of the narrow nanoarcs are affected by the fabrication flaws (rounding at the

corners of the two tips), the L_{mid} of the wide nanoarcs are less impacted. Furthermore, for the narrow nanoarcs there are two complications in the data processing: the weak LSPR peak with a peak height of less than 1% transmission (Figure 2.5.1.3 (a)), comparable to the noise level (~0.6% transmission), and the overlap of the 1st LSPR peak with the CO_2 signal at 2330 cm^{-1} (4292 nm) and 2360 cm^{-1} (4237 nm) [119]. During the fitting process, data points affected by the CO_2 signal were excluded to minimize their impact on the peak shape analysis. The weak LSPR peak and the lack of data for a certain wavenumber range within the peak linewidth increase the uncertainty in the LSPR wavelength of narrow nanoarcs. The set of narrow nanoarcs displays the largest deviation at 3.50%. This value was utilized when setting the statistical deviation of the resonance wavelength from the mean due to fabrication flaws in our experiments on silicon as ± 1.75%.

In summary, using the deviation of the resonance wavelengths ($(\lambda_{max} - \lambda_{min})/ \lambda_{avg}$), the statistical deviation of the LSPR wavelengths due to fabrication flaws was determined for nanoarcs fabricated on silicon (± 1.75%) and quartz (± 0.87%). These values were used when setting the anticipated variation range of the resonance wavelengths.

2.5.2 Determination of the Thresholds of the Lattice Parameters

As was illustrated in Figure 2.4.1.2 (a), the extinction of light by a single nanorod is too weak to be detected by the spectrometer used in the experiment. According to the Beer-Lambert law, the extinction signal intensity ($-\log_{10}T$) increases linearly with the number of nanostructures in the field of view. Therefore, in this work, the FTIR spectra were collected from arrays composed of identical nanoarcs to study the LSPR wavelengths of a single element, with the assumption that the nanoarcs in an array share

the same LSPR wavelength with a single nanoarc. However, previous studies [50, 120-122] have demonstrated that if the distance between elements in an array is below a threshold value, the dipolar coupling between adjacent elements will shift the LSPR wavelengths of the nanoparticles, making them different from those of a single nanoparticle. Consequently, the above assumption is only valid when the elements in an array are sufficiently far apart from each other. Hence, it is important to determine the threshold values of the lattice parameters of the nanoarc arrays that maximize the array density and avoid the dipolar coupling interactions. In this section, the threshold values of the lattice parameters are determined from spectroscopic measurements on nanoarc arrays with different lattice structures as a function of arc size and substrate material.

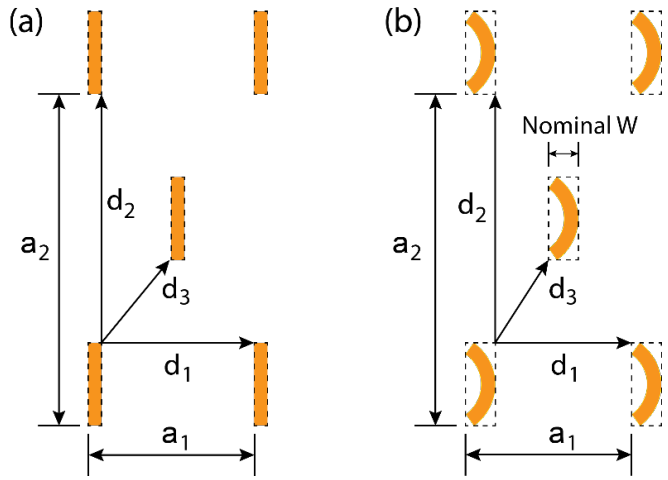

Figure 2.5.2.1 Definitions of the lattice parameters (a_1, a_2), and distance parameters (d_1, d_2, d_3) for (a) a nanorod array and (b) a nanoarc array. Two elements are contained within a unit cell area of $a_1 \cdot a_2$.

The nanorods and nanoarcs arrays studied here have a centered-rectangular lattice (referred to as a triangular lattice in this thesis) with lattice parameters (a_1, a_2), as shown in Figure 2.5.2.1. Three distance parameters (d_1, d_2, d_3) represent the shortest distance between the bounding box of a rod/arc (dashed rectangles in Figure 2.5.2.1) and those

of its neighboring elements along three different directions. The width of the bounding box of a nanoarc is defined as the nominal width (W_{nom}) of the arc. (d_1, d_2, d_3) are fully determined by (a_1, a_2) and the nanoarc dimensions as

$$d_1 = a_1 - W_{nom} \quad (2.5.2.1)$$

$$d_2 = a_2 - H \quad (2.5.2.2)$$

$$d_3 = \frac{1}{2}\sqrt{(a_1 - 2W_{nom})^2 + (a_2 - 2H)^2} \quad (2.5.2.3)$$

It is convenient to compare arrays with different lattice structures by the metal coverage rate R_m, which is defined as the ratio of the area of a single nanoarc A_{arc} to the area of the primitive cell of the triangular lattice A_{cell} (Eq. 2.5.2.4).

$$R_m = \frac{A_{arc}}{A_{cell}} = \frac{A_{arc}}{0.5a_1 \cdot a_2} \quad (2.5.2.4)$$

In the pattern design, the lattice parameters of the arrays were tuned in three ways: fixing a_1 and varying a_2, fixing a_2 and varying a_1, and varying both a_1 and a_2. These experiments were designed to study the dipolar coupling effect along the vertical and horizontal directions in the arrays and to check if there were mixed dipolar coupling interactions. When one of the lattice parameters (a_1 or a_2) was fixed, it was assigned a large enough value to avoid any coupling along that direction. When both a_1 and a_2 were varied, their ratio was kept constant. In all the three ways of tuning the lattice parameter, the metal coverage rate R_m was varied from 0.5% to 4.2%. This range of R_m was sufficiently large to determine spectroscopically that for the arrays with the largest lattice parameters ($R_m = 0.5\%$) the elements were uncoupled and for the arrays with the smallest lattice parameters ($R_m = 4.2\%$), the elements were coupled along at least one direction.

According to previous studies [122], the threshold values of the lattice parameters of nanorod arrays are rod-length-dependent. Therefore, the threshold values should be determined as a function of L (L_{mid}). We studied nanorods and nanoarcs with two lengths L (L_{mid}) = 400 and 1000 nm, and the other dimensions are fixed (W = 50 nm, t = 55 nm and θ = 0° or 150°). The two lengths were chosen because the LSPR peaks of these nanorods/nanoarcs are far away from the FTIR signals of the atmosphere and the substrate material (Section 2.5.4).

Twelve groups of nanoarc arrays (Table 2.5.2.1) were fabricated using the methods described in Section 2.4.1 – 2.4.3. Each group consists of 8 arrays of nanorods and 8 arrays of nanoarcs, with their lattice parameters (and R_m) varied systematically. Within each group, the nanoarcs were fabricated on the same substrate material, using the same values of L (L_{mid}), W, t and two values of θ (0° and 150°). The different groups correspond to different substrate materials (Au/Si or Au/SiO_2), different rod/arc length (L (L_{mid}) = 400 or 1000 nm), or different ways the lattice parameters are tuned (varying a_1, a_2 or both).

Table 2.5.2.1 Structural and material parameters of the 12 groups of nanoarc arrays

Group	Antenna/Substrate Material	Rod/Arc Dimensions *	Lattice Parameters
S1	Au/Si	***L*400*W*50*t*55 θ(0°, 150°)	vary a_2
S2			vary a_1
S3			vary a_1 & a_2
S4		***L*1000*W*50*t*55 θ(0°, 150°)	vary a_2
S5			vary a_1
S6			vary a_1 & a_2
Q1	Au/SiO_2	***L*400*W*50*t*55 θ(0°, 150°)	vary a_2
Q2			vary a_1
Q3			vary a_1 & a_2
Q4		***L*1000*W*50*t*55 θ(0°, 150°)	vary a_2
Q5			vary a_1
Q6			vary a_1 & a_2

**H*: height, *L*: length of nanorod or mid-arc length of nanoarc, *W*: width, *t*: thickness, unit: nm. θ: central angle, unit: °.

The dependence of the 1st LSPR wavelength (λ_1) on the lattice parameters is investigated through spectroscopic studies of the 12 groups of nanoarc arrays. FTIR spectra were collected from the nanoarc arrays using the methods described in Section 2.4.4 and the LSPR wavelengths were determined using the Gaussian-Lorentzian fit described in Section 2.4.6.

The dependence of λ_1 on the lattice parameters (a_1, a_2) is shown in the plots in Figures 2.5.2.2, 2.5.2.3, 2.5.2.5, and 2.5.2.6, where common trends are observed across the different groups. As the lattice parameters (a_1, a_2 or both) increase λ_1 approaches an asymptotic value. Below a threshold value of the lattice parameters (a_1, a_2 or both) the slope of the plotted data is significantly higher than above this threshold value. These trends are consistent with trends observed in a previous study on nanorod arrays. [50] These trends suggest that (i) the nanorods/nanoarcs in an array are coupled when the lattice parameters are small and the dipolar coupling between adjacent elements blue-

shifts the LSPR wavelength, and (ii) the nanorods/nanoarcs in an array are not coupled when the lattice parameters are large and the measured LSPR wavelength corresponds to that of an isolated nanorod/nanoarc. The threshold values of the lattice parameters were defined based on the asymptotic behavior of the data. A reference value λ_1^{ref} was set using the 1st LSPR wavelength of nanoarcs in the array with the lowest metal coverage rate ($R_m = 0.5\%$) in each group. The anticipated variation range of λ_1^{ref} was determined by the statistical deviation caused by fabrication flaws (+/- 1.75% for nanoarcs on silicon, and +/- 0.87% for nanoarcs on quartz, see Section 2.5.1). When an array displayed a resonance wavelength λ_1 outside of the anticipated variation range of λ_1^{ref}, the nanorods/nanoarcs in the array were considered as coupled. The minimum value of each lattice parameter (i.e. a_1 or a_2) obtained from arrays with no coupling was identified as the threshold value.

Example: Figures 2.5.2.2 shows the data of the spectroscopic study of nanorods/nanoarcs in Groups S1 – S3. Panel (a) shows that for arrays with $a_2 \geq 1.0$ μm, λ_1 falls within the anticipated variation range of λ_1^{ref} (delimited by dash lines), therefore these arrays are considered as free of coupling. The lattice parameters (a_1, a_2) = (1.2, 1.0) μm are temporarily set as the threshold values for nanorods/nanoarcs with $L(L_{mid})$ = 400 nm. In panel (b), it is observed that nanorod/nanoarc arrays with $a_1 \geq 0.8$ μm and a_2 = 2.4 μm are free of coupling, therefore, the threshold values are corrected as (a_1, a_2) = (**0.8, 1.0**) μm. These values are compared to the lattice parameters in panel (c) to confirm there is no contradiction, i.e., arrays with lattice parameters larger than these two values do not exhibit dipolar coupling. The thresholds of the three distance parameters (d_1, d_2, d_3) were calculated based on the thresholds of (a_1, a_2) of nanorods.

The same analysis procedure was followed to determine the threshold values for nanorods/nanoarcs in Groups S4 – S6 with $L(L_{mid})$ = 1000 nm, and the results are shown in Figure 2.5.2.3. The threshold values are (a_1, a_2) = **(1.8, 4.0) µm**.

Since the threshold values are $L(L_{mid})$-dependent, it is necessary to estimate the thresholds for nanorods/nanoarcs with other $L(L_{mid})$. We used a linear inter/extrapolation of the threshold values of (a_1, a_2) and (d_1, d_2, d_3) obtained from nanorods/nanoarcs with $L(L_{mid})$ = 400 nm and 1000 nm, as shown in Figure 2.5.2.4. This figure was used to guide the design of nanoarc arrays: to avoid the effects of dipolar coupling between array elements, the lattice parameters (a_1, a_2) and distance parameters (d_1, d_2, d_3) should all be above the corresponding threshold, i.e. fall in the shaded areas in Figure 2.5.2.4.

By comparing data in Figures 2.5.2.2 and 2.5.2.3 from nanorods vs. nanoarcs (central angle of 0° vs. 150°), we have determined that the threshold values of (a_1, a_2) are not affected by the central angle. Similar determinations were made with regards to the data in Figures 2.5.2.5 and 2.5.2.6, indicating that the central angle has a minor impact on the dipolar coupling in a lattice.

The same analysis was applied to nanorods/nanoarcs on quartz in Groups Q1 – Q6, and the results are shown in Figure 2.5.2.5 – Figure 2.5.2.7. For nanorods/nanoarcs on quartz substrates with $L(L_{mid})$ = 400 nm, the thresholds of (a_1, a_2) are **(1.2, 1.6) µm**, larger than the threshold values for the nanorods/nanoarcs with the same nominal dimensions on silicon; for nanorods/nanoarcs with $L(L_{mid})$ = 1000 nm, the thresholds of a_1 is **1.8 µm,** while the threshold of a_2 should be slightly larger than **4.0 µm** and less than 7.9 µm. The values are similar to those for nanorods/nanoarcs on silicon.

In summary, the effect of dipolar coupling in nanoarcs is to shift the fundamental LSPR to shorter wavelengths regardless of the orientation of the position-vector connecting the interacting nanostructures, as reported previously for nanorods. [50, 122] The larger L_{mid} is, the larger are the lattice parameters needed to prevent the effects of dipolar coupling on the resonance position. The threshold values of the lattice parameters (a_1, a_2) and distance parameters (d_1, d_2, d_3) for nanoarcs with different L_{mid} were determined on two substrates (Si and quartz). The arrays are free of dipolar coupling if the values of all 5 parameters are larger than the corresponding thresholds. When not specified otherwise, the data presented in the remainder of this thesis were collected from arrays of uncoupled nanoarcs, which ensured that the LSPR wavelengths of nanoarc arrays were identical to those of a single nanoarc.

(a) Varying a_2

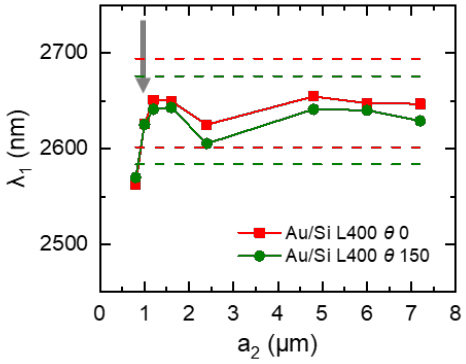

R_m (%)	a_1 (μm)	a_2 (μm)	d_1 (μm)	d_2 (μm)	d_3 (μm)
4.2	1.2	0.8	1.15	0.40	0.55
3.5	1.2	**1.0**	1.15	0.60	0.56
2.8	1.2	1.2	1.15	0.80	0.59
2.1	1.2	1.6	1.15	1.20	0.68
1.4	1.2	2.4	1.15	2.00	0.97
0.7	1.2	4.8	1.15	4.40	2.07
0.6	1.2	6.0	1.15	5.60	2.66
0.5	1.2	7.2	1.15	6.80	3.25

(b) Varying a_1

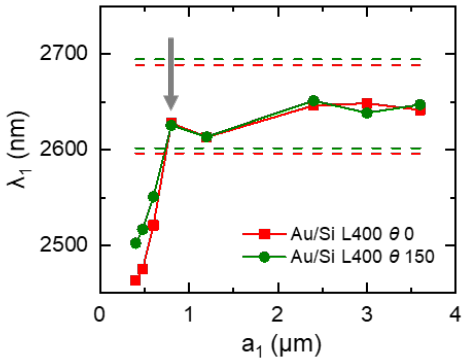

R_m (%)	a_1 (μm)	a_2 (μm)	d_1 (μm)	d_2 (μm)	d_3 (μm)
4.2	0.4	2.4	0.25	2.05	0.86
3.5	0.5	2.4	0.33	2.05	0.86
2.8	0.6	2.4	0.45	2.05	0.87
2.1	**0.8**	2.4	0.65	2.05	0.89
1.4	1.2	2.4	1.05	2.05	0.97
0.7	2.4	2.4	2.25	2.05	1.36
0.6	3.0	2.4	2.85	2.05	1.60
0.5	3.6	2.4	3.45	2.05	1.86

(c) Varying both a_1 and a_2

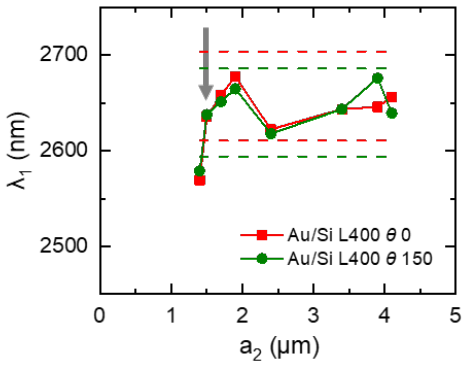

R_m (%)	a_1 (μm)	a_2 (μm)	d_1 (μm)	d_2 (μm)	d_3 (μm)
4.2	0.7	1.4	0.55	1.05	0.41
3.5	**0.8**	1.5	0.65	1.15	0.48
2.8	0.8	1.7	0.65	1.35	0.56
2.1	1.0	1.9	0.85	1.55	0.70
1.4	1.2	2.4	1.05	2.05	0.97
0.7	1.7	3.4	1.55	3.05	1.53
0.6	1.9	3.9	1.75	3.55	1.79
0.5	2.1	4.1	1.95	3.75	1.93

Figure 2.5.2.2 Dependence of λ_1 on the lattice parameters (a_1, a_2) for the nanorods/nanoarcs in Groups S1 – S3. The dimensions of the gold nanostructures on silicon are L_{mid} = 400 nm, W = 50 nm, t = 55 nm and θ = 0° (red), 150° (green). (a) Fixing a_1 and varying a_2. (b) Fixing a_2 and varying a_1. (c) Varying both a_1 and a_2. The dash lines indicate the anticipated variation range of λ_1 due to fabrication flaws. In each plot, the arrow indicates the smallest lattice parameter for which λ_1 is not affected by dipolar coupling. The values of the parameters are listed in the table. d_1, d_2, d_3 values are calculated for nanorods.

(a) Varying a_2

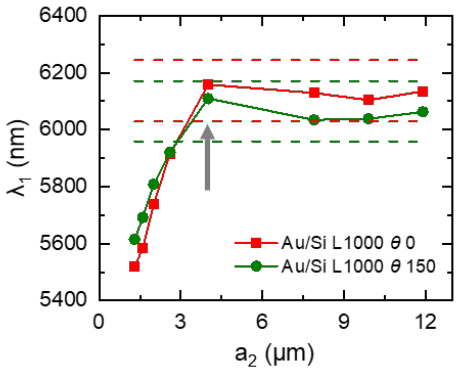

R_m (%)	a_1 (μm)	a_2 (μm)	d_1 (μm)	d_2 (μm)	d_3 (μm)
4.2	1.8	1.3	1.75	0.30	0.92
3.5	1.8	1.6	1.75	0.60	0.87
2.8	1.8	2.0	1.75	1.00	0.85
2.1	1.8	2.6	1.75	1.60	0.90
1.4	**1.8**	**4.0**	1.75	3.00	1.31
0.7	1.8	7.9	1.75	6.90	3.07
0.6	1.8	9.9	1.75	8.90	4.04
0.5	1.8	11.9	1.75	10.90	5.02

(b) Varying a_1

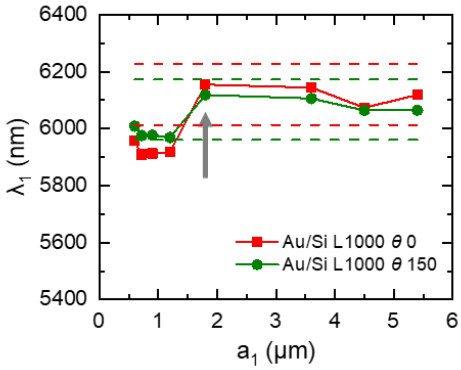

R_m (%)	a_1 (μm)	a_2 (μm)	d_1 (μm)	d_2 (μm)	d_3 (μm)
4.2	0.6	4.0	0.55	3.00	1.03
3.5	0.7	4.0	0.67	3.00	1.05
2.8	0.9	4.0	0.85	3.00	1.08
2.1	1.2	4.0	1.15	3.00	1.14
1.4	**1.8**	**4.0**	1.75	3.00	1.31
0.7	3.6	4.0	3.55	3.00	2.02
0.6	4.5	4.0	4.45	3.00	2.42
0.5	5.4	4.0	5.35	3.00	2.83

(c) Varying both a_1 and a_2

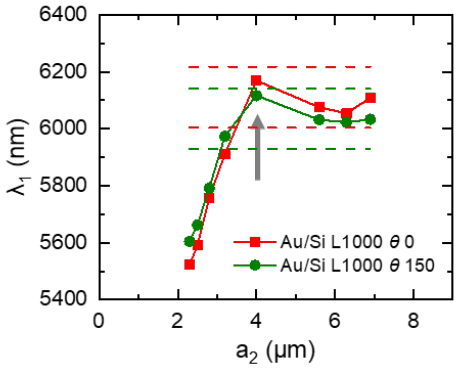

R_m (%)	a_1 (μm)	a_2 (μm)	d_1 (μm)	d_2 (μm)	d_3 (μm)
4.2	1.0	2.3	0.95	1.30	0.47
3.5	1.1	2.5	1.05	1.50	0.56
2.8	1.3	2.8	1.25	1.80	0.72
2.1	1.5	3.2	1.45	2.20	0.92
1.4	**1.8**	**4.0**	1.75	3.00	1.31
0.7	2.6	5.6	2.55	4.60	2.19
0.6	2.8	6.3	2.75	5.30	2.54
0.5	3.1	6.9	3.05	5.90	2.87

Figure 2.5.2.3 Dependence of λ_1 on the lattice parameters (a_1, a_2) for the nanorods/nanoarcs in Groups S4 – S6. The dimensions of the gold nanostructures on silicon are L_{mid} = 1000 nm, W = 50 nm, t = 55 nm and θ = 0° (red), 150° (green). (a) Fixing a_1 and varying a_2. (b) Fixing a_2 and varying a_1. (c) Varying both a_1 and a_2. The dash lines indicate the anticipated variation range of λ_1 due to fabrication flaws. In each plot, the arrow indicates the smallest lattice parameter for which λ_1 is not affected by dipolar coupling. The values of the parameters are listed in the table. d_1, d_2, d_3 values are calculated for nanorods.

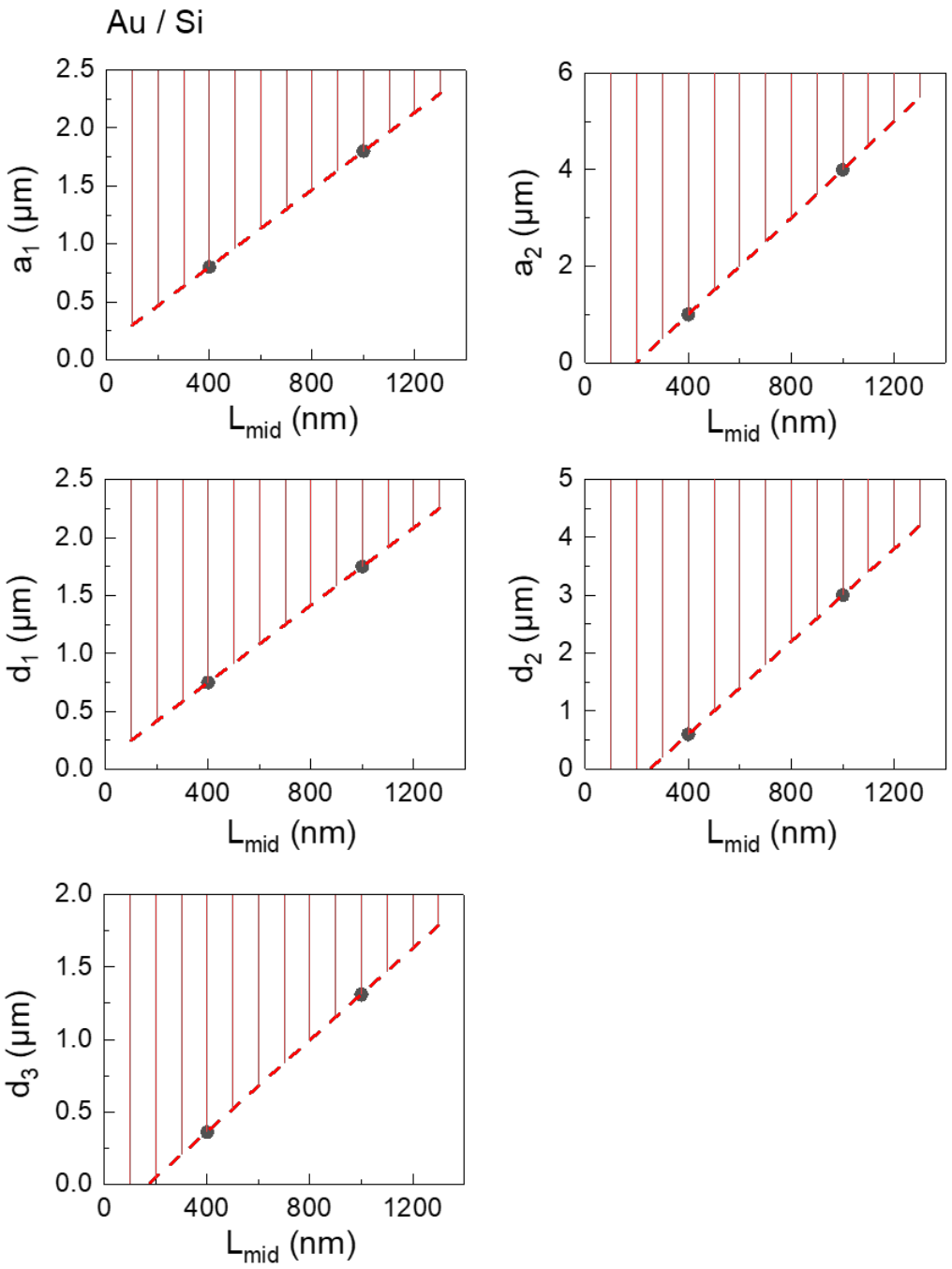

Figure 2.5.2.4 The threshold values of lattice parameters (a_1, a_2), and distance parameters (d_1, d_2, d_3) for gold nanoarcs on silicon substrates (Au/Si). The shaded areas indicate the region where the parameters must fall into to avoid dipolar coupling.

(a) Varying a_2

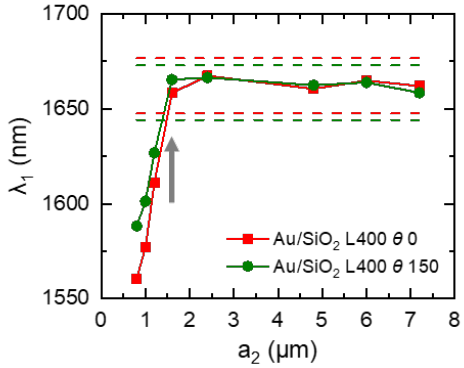

R_m (%)	a_1 (μm)	a_2 (μm)	d_1 (μm)	d_2 (μm)	d_3 (μm)
4.2	1.2	0.8	1.15	0.40	0.55
3.5	1.2	1.0	1.15	0.60	0.56
2.8	1.2	1.2	1.15	0.80	0.59
2.1	**1.2**	**1.6**	1.15	1.20	0.68
1.4	1.2	2.4	1.15	2.00	0.97
0.7	1.2	4.8	1.15	4.40	2.07
0.6	1.2	6.0	1.15	5.60	2.66
0.5	1.2	7.2	1.15	6.80	3.25

(b) Varying a_1

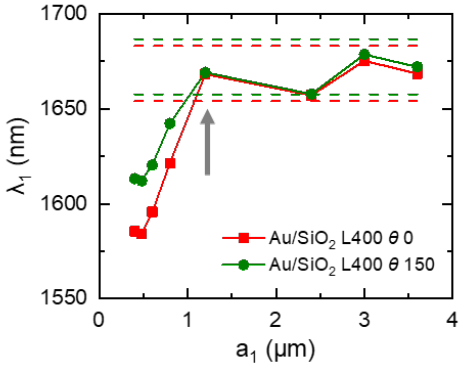

R_m (%)	a_1 (μm)	a_2 (μm)	d_1 (μm)	d_2 (μm)	d_3 (μm)
4.2	0.4	2.4	0.35	2.00	0.81
3.5	0.5	2.4	0.43	2.00	0.82
2.8	0.6	2.4	0.55	2.00	0.84
2.1	0.8	2.4	0.75	2.00	0.87
1.4	**1.2**	2.4	1.15	2.00	0.97
0.7	2.4	2.4	2.35	2.00	1.40
0.6	3.0	2.4	2.95	2.00	1.66
0.5	3.6	2.4	3.55	2.00	1.92

(c) Varying both a_1 and a_2

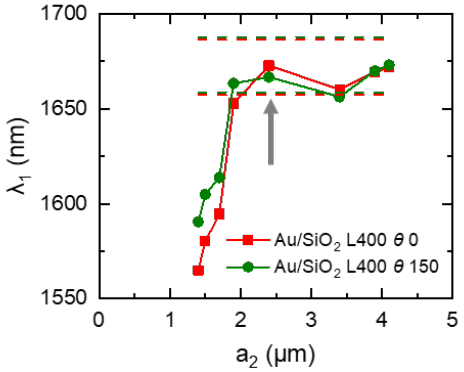

R_m (%)	a_1 (μm)	a_2 (μm)	d_1 (μm)	d_2 (μm)	d_3 (μm)
4.2	0.7	1.4	0.65	1.00	0.42
3.5	0.8	1.5	0.75	1.10	0.49
2.8	0.8	1.7	0.75	1.30	0.57
2.1	1.0	1.9	0.95	1.50	0.71
1.4	**1.2**	2.4	1.15	2.00	0.97
0.7	1.7	3.4	1.65	3.00	1.53
0.6	1.9	3.8	1.85	3.40	1.75
0.5	2.1	4.1	2.05	3.70	1.93

Figure 2.5.2.5 Dependence of λ_1 on the lattice parameters (a_1, a_2) for the nanorods/nanoarcs in Groups Q1 – Q3. The dimensions of the gold nanostructures on fused quartz are L_{mid} = 400 nm, W = 50 nm, t = 55 nm and θ = 0° (red), 150° (green). (a) Fixing a_1 and varying a_2. (b) Fixing a_2 and varying a_1. (c) Varying both a_1 and a_2. The dash lines indicate the anticipated variation range of λ_1 due to fabrication flaws. In each plot, the arrow indicates the smallest lattice parameter for which λ_1 is not affected by dipolar coupling. The values of the parameters are listed in the table. d_1, d_2, d_3 values are calculated for nanorods.

(a) Varying a_2

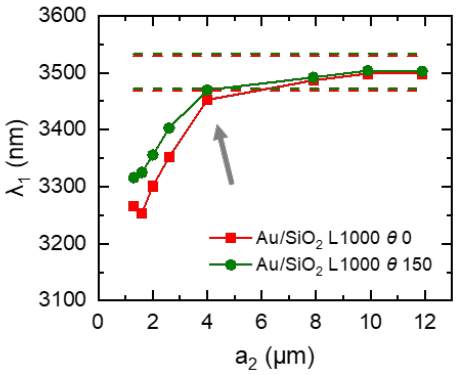

R_m (%)	a_1 (μm)	a_2 (μm)	d_1 (μm)	d_2 (μm)	d_3 (μm)
4.2	1.8	1.3	1.75	0.30	0.92
3.5	1.8	1.6	1.75	0.60	0.87
2.8	1.8	2.0	1.75	1.00	0.85
2.1	1.8	2.6	1.75	1.60	0.90
1.4	1.8	**4.0**	1.75	3.00	1.31
0.7	1.8	**7.9**	1.75	6.90	3.07
0.6	1.8	9.9	1.75	8.90	4.04
0.5	1.8	11.9	1.75	10.90	5.02

(b) Varying a_1

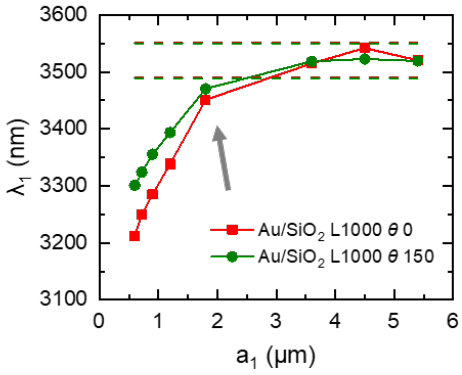

R_m (%)	a_1 (μm)	a_2 (μm)	d_1 (μm)	d_2 (μm)	d_3 (μm)
4.2	0.6	4.0	0.55	3.00	1.03
3.5	0.7	4.0	0.67	3.00	1.05
2.8	0.9	4.0	0.85	3.00	1.08
2.1	1.2	4.0	1.15	3.00	1.14
1.4	**1.8**	4.0	1.75	3.00	1.31
0.7	**3.6**	4.0	3.55	3.00	2.02
0.6	4.5	4.0	4.45	3.00	2.42
0.5	5.4	4.0	5.35	3.00	2.83

(c) Varying both a_1 and a_2

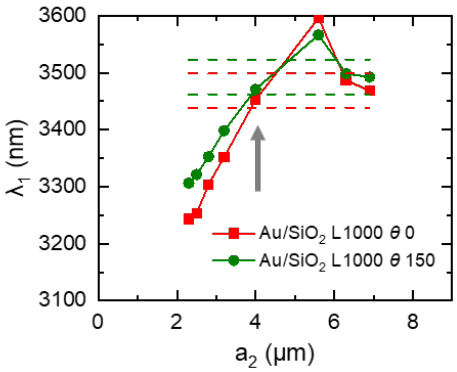

R_m (%)	a_1 (μm)	a_2 (μm)	d_1 (μm)	d_2 (μm)	d_3 (μm)
4.2	1.0	2.3	0.95	1.30	0.47
3.5	1.1	2.5	1.05	1.50	0.56
2.8	1.3	2.8	1.25	1.80	0.72
2.1	1.5	3.2	1.45	2.20	0.92
1.4	**1.8**	**4.0**	1.75	3.00	1.31
0.7	2.6	5.6	2.55	4.60	2.19
0.6	2.8	6.3	2.75	5.30	2.54
0.5	3.1	6.9	3.05	5.90	2.87

Figure 2.5.2.6 Dependence of λ_1 on the lattice parameters (a_1, a_2) for the nanorods/nanoarcs in Groups Q4 – Q6. The dimensions of the gold nanostructures on fused quartz are L_{mid} = 1000 nm, W = 50 nm, t = 55 nm and θ = 0° (red), 150° (green). (a) Fixing a_1 and varying a_2. (b) Fixing a_2 and varying a_1. (c) Varying both a_1 and a_2. The dash lines indicate the anticipated variation range of λ_1 due to fabrication flaws. In each plot, the arrow indicates the smallest lattice parameter for which λ_1 is not affected by dipolar coupling. The values of the parameters are listed in the table. d_1, d_2, d_3 values

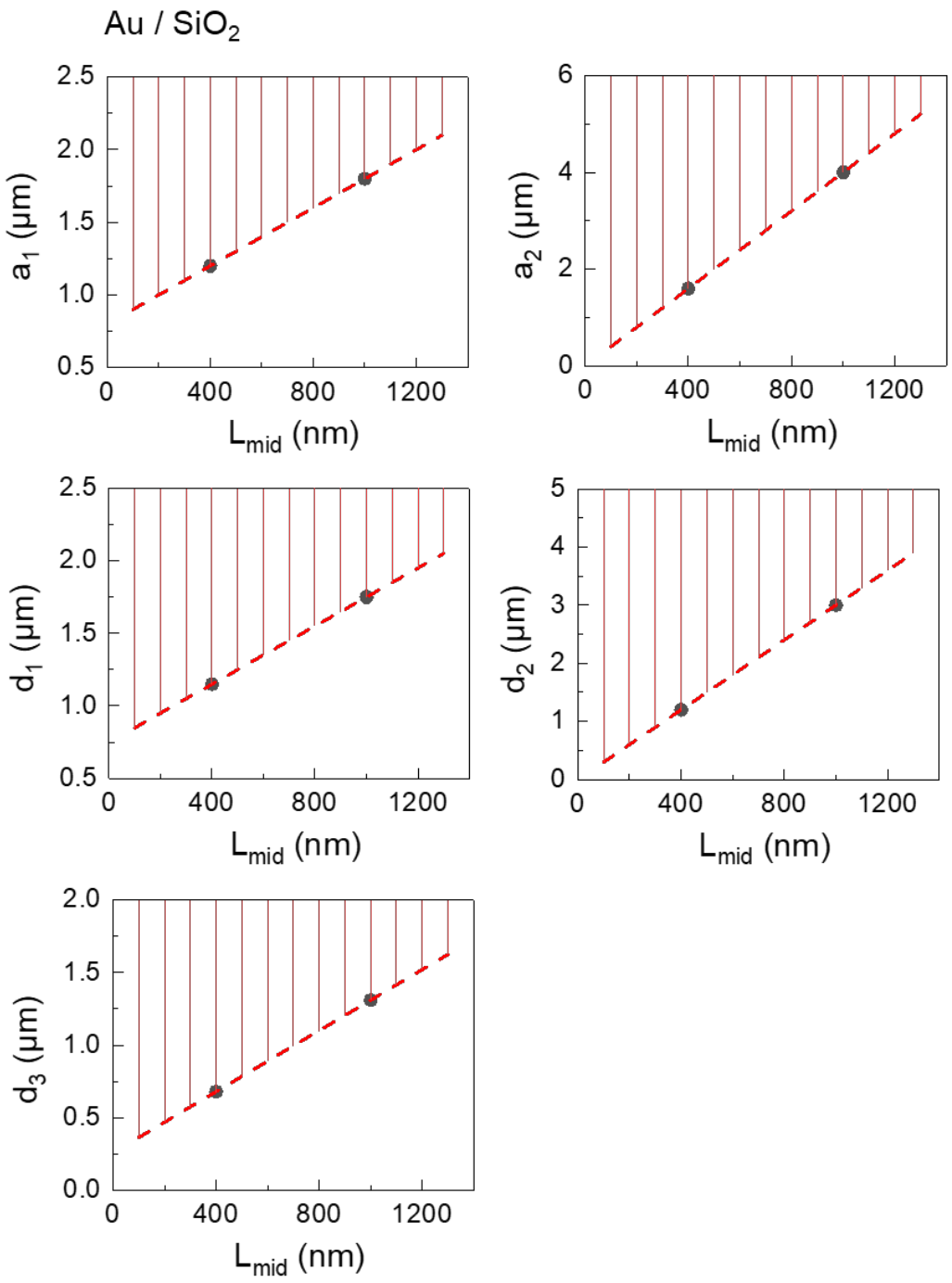

Figure 2.5.2.7 The threshold values of lattice parameters (a_1, a_2), and distance parameters (d_1, d_2, d_3) for gold nanoarcs on quartz substrates (Au/SiO_2). The shaded areas indicate the region where the parameters must fall into to avoid dipolar coupling.

2.5.3 Effect of the Central Angle on the LSPR Wavelengths and Peak Attenuations of Nanoarcs

The transformation optics analysis in Section 2.2 predicted that nanoarcs with the same L_{mid}, W' and t have the same LSPR wavelengths, regardless of the curvatures. To corroborate this prediction, we performed numerical simulations to estimate the LSPR wavelengths (λ_1 and λ_2) of nanoarcs with different central angles θ, and the results were discussed in Section 2.3.2. It was found that the LSPRs of nanoarcs with the same L_{mid} and different central angles θ spectrally overlap, and the peak intensities of the LSPR modes of nanoarcs were θ-dependent. In this section, we investigate the experimental spectra of plasmonic nanoarcs with various central angles, with the goal of quantifying the effect of the central angle θ on the wavelengths and intensities of the LSPRs of the nanoarcs.

A series of nanoarcs was designed with fixed L_{mid} = 600 nm, W = 55 nm, t = 55 nm, and subtending various central angles (θ ranged from 0° to 180° with 14 angles in total). The nanoarcs were patterned into rectangular lattice arrays with (a_1, a_2) = (1.3, 1.6) μm. The gold nanoarc arrays were fabricated on a silicon substrate using the methods described in Sections 2.4.1 – 2.4.3. FTIR transmission spectra were collected from the nanoarcs arrays using the methods described in Section 2.4.4, and wavelengths and intensities of the LSPR peaks were determined using the Gaussian-Lorentzian fit described in Section 2.4.6. SEM imaging (method in Section 2.4.7) was performed to check the dimensions of the nanoarcs. SEM images of nanoarcs with various central angles are shown in Figure 2.5.3.1.

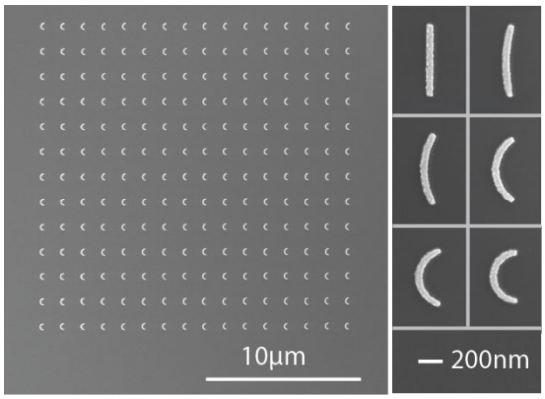

Figure 2.5.3.1 SEM images of gold nanoarcs on silicon with L_{mid} = 600 nm, W = 55 nm and t = 55 nm. Left: An array of nanoarcs with θ = 180°. Right: Individual nanoarcs with θ = 0°, 30°, 60°, 120°, 150°, 180°.

The experimental FTIR transmission spectra of the nanoarc arrays (including one nanorod array) are shown in Figure 2.5.3.2 (a), displaying 2 or 3 attenuation peaks in the infrared due to the longitudinal surface plasmon resonances. The 1st and 2nd LSPR modes of the nanorod (θ = 0°) in Figure 2.5.3.2 (a) are centered at 3850 nm and 1989 nm, respectively. Theoretically, the 2nd LSPR mode of the nanorod cannot be excited by a plane wave at normal incidence because the electric dipole moment of the 2nd LSPR mode in a nanorod (θ = 0°) vanishes due to the symmetry. In the experiment, a very weak attenuation at the wavelength corresponding to the 2nd LSPR mode was observed with nanorods. This is because of the conical illumination generated by the Schwarzschild objective lens in the experiments and symmetry-breaking defects introduced by imperfect lithography [47, 123, 124].

The FTIR spectra in Figure 2.5.3.2 (a) demonstrate that the resonance wavelengths (λ_{res}) of these nanoarcs are insensitive to the central angle of the nanoarcs or the radii of curvature. λ_1 of the 13 nanoarcs is found in the range of 3818 – 3878 nm, and λ_2 ranges from 1979 nm to 2007 nm (Figure 2.5.3.2 (b)). These wavelength variations are smaller than the shifts attributed to the statistical deviation induced by fabrication flaws

(±1.75%, shown by the error bars in Figure 2.5.3.2) determined independently in Section 2.5.1. The ranges of resonance wavelength variation are also significantly narrower than the linewidth of the resonance (~20%λ_{res}). This experiment shows that the resonance wavelengths of nanoarcs are almost fixed when L_{mid}, W, and t are kept constant, in accordance with the transformation optics analysis in Section 2.2 and the numerical simulation results in Section 2.3.2.

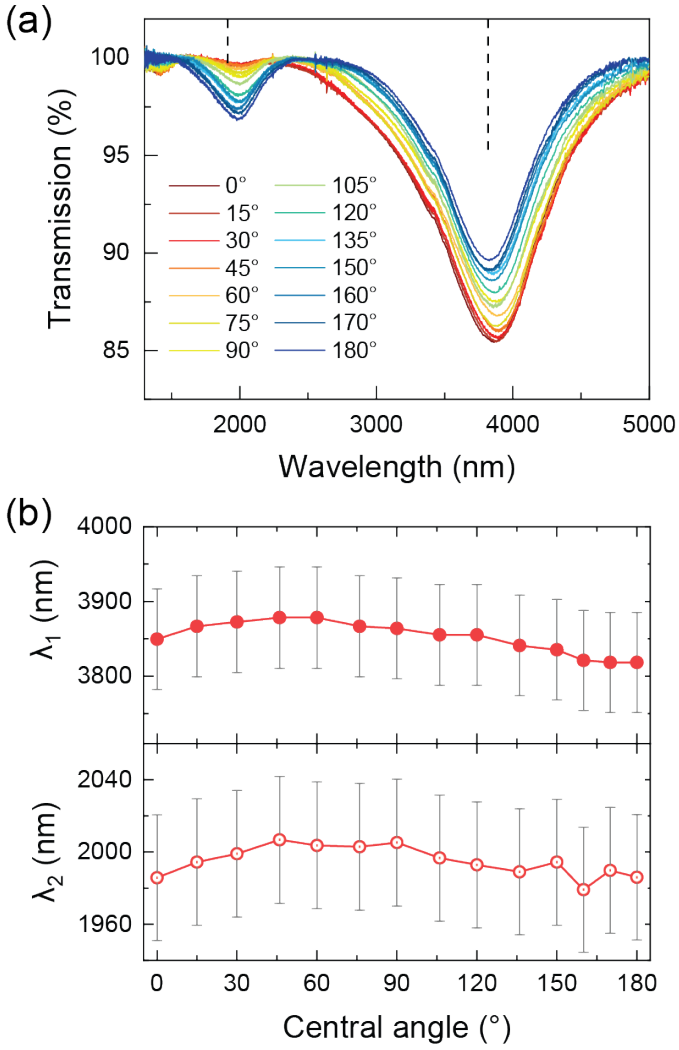

Figure 2.5.3.2 (a) Experimental FTIR transmission spectra of the nanoarcs with L_{mid} = 600 nm, W = 55 nm, t = 55 nm and θ = 0° – 180°. The vertical dash lines illustrate an interval of precisely one octave between two wavelengths: λ_1 of the nanoarcs with θ = 180° at 3818 nm, and $\lambda_1/2$ at 1909 nm. (b) The 1st and 2nd LSPR wavelengths (λ_1 and

λ_2) obtained from the spectra in (a). Error bars (±1.75%) show the anticipated variation range of λ_1 and λ_2 due to fabrication flaws.

While the resonance wavelength does not depend on θ, the resonance intensity varies significantly with θ, as shown by the transmission data in Figure 2.5.3.2 (a). Our FDTD simulation (Figure 2.3.3.1) shows that in longitudinal LSPR modes of nanoarcs, two orthogonal electric dipole orientations are possible. This suggests that the LSPR peak intensity depends not only on the polarizability of the nanoarcs but also on the relative orientation between the oscillating electric dipole of the resonance mode and the polarization of the light. The attenuation of the nanoarcs is maximized when the polarization of the incident light matches the electric dipole orientation; when the two orientations are orthogonal, the attenuation is zero. The orthogonal electric dipoles can be excited separately by probing aligned nanostructures with linearly polarized light. To quantify the relation between the LSPR peak intensities and the central angle, we performed polarization-dependent FTIR transmission measurements.

Polarization-dependent FTIR spectra were collected from 5 series of nanoarcs. The geometric and material parameters of the nanoarcs in the 5 series are summarized in Table 2.5.3.1. Within each series the nanoarcs have fixed L_{mid}, W and t, and various central angles (θ = 0° – 210°). Different series correspond to different substrate materials (Si vs. fused quartz), L_{mid}, or arc thickness. All nanoarcs are patterned into triangular lattice arrays.

Table 2.5.3.1 Geometric and material parameters of the nanoarcs and the lattice parameters

Series	Antenna/ Substrate Material	Rod/Arc Dimensions *	Lattice parameters (a_1, a_2) (μm)
S1	Au/Si	$L600W55t55$ $\theta = 0° – 210°$	(2.3, 2.3)
S2	Al/Si	$L730W60t55$ $\theta = 0° – 180°$	(2.8, 2.8)
Q3	Au/SiO_2	$L600W60t23$ $\theta = 0° – 180°$	(2.5, 3.5)
Q4	Au/SiO_2	$L800W60t23$ $\theta = 0° – 180°$	(2.9, 4.0)
Q5	Au/SiO_2	$L1200W60t23$ $\theta = 0° – 180°$	(3.2, 4.5)

* L: length of nanorod or mid-arc length of nanoarc, W: width, t: thickness, unit: nm. θ: central angle.

These nanoarcs were chosen because their 1st and 2nd LSPR data could be collected simultaneously and without interference from absorption by the substrate, the atmosphere or the optical setup. Polarization-dependent FTIR measurements of the 5 series of nanoarcs were performed with the incident light polarized along the *x'*- or *y'*-axis of the nanoarcs, details of which is also described in Section 2.4.4. The FTIR transmission spectra were converted to extinction spectra via the relation $\alpha(\lambda) = -log_{10}[T(\lambda)]$. The LSPR wavelengths and the extinction of the two LSPR peaks (α_1 and α_2) were determined using the Gaussian-Lorentzian fit described in Section 2.4.6.

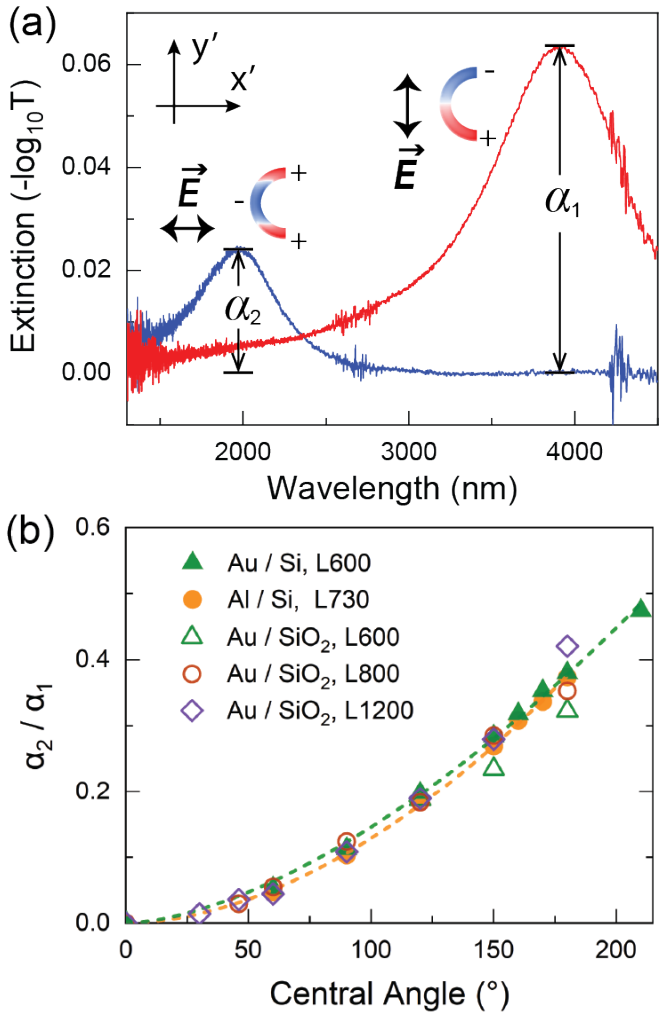

Figure 2.5.3.3 (a) Polarized extinction spectra of gold nanoarcs in Series S1. The blue line data were obtained with *x'*- polarized light and the red line data were obtained with *y'*- polarized light. The illustrations represent the charge accumulation patterns on the surface of the arc for each of the orthogonal polarizations at resonance. (b) The ratio of the extinction by the 2nd and 1st LSPRs of gold (solid green triangles) and aluminum (solid yellow circles) nanoarcs on silicon, as well as gold nanoarcs on quartz (open symbols).

Figure 2.5.3.3 (a) shows two examples of polarization-dependent FTIR extinction spectra $\alpha(\lambda)$ as well as schematics of the charge accumulation patterns of the two LSPR modes. The spectra demonstrate that *y'*-linearly polarized light can only excite odd-order modes, while *x'*-linearly polarized light can only excite even-order modes, in accordance with our FDTD simulation results. The spectroscopic studies of the 5 series of nanoarcs provide information regarding the LSPR wavelengths and the peak

extinctions of the 1st and 2nd LSPR modes. Series S1 and S2 have similar LSPR spectra with λ_1 = 4 μm and λ_2 = 2 μm. For Series Q3 – Q5, λ_1 values are 2.4 μm, 3 μm and 4.4 μm, respectively, and λ_2 values are 1.2 μm, 1.6 μm and 2.3 μm, respectively. For all 5 series, the peak extinction of the 1st LSPR (α_1) decreases as the central angle of the nanoarc increases. The extinction by the 2nd LSPR (α_2) shows the opposite trend. This is because as θ increases the polarizability of the 2nd LSPR mode (which is proportional to the on-resonance extinction) grows, while that of the 1st LSPR mode wanes. These experiments confirm that the central angle θ is instrumental in tuning the relative oscillator strength of the resonances in nanoarcs.

Figure 2.5.3.3 (b) shows the extinction ratio α_2/α_1 as a function of the nanoarc central angle for nanoarc arrays in the 5 series. For Series S1 the extinction ratio α_2/α_1 (solid green triangles) increases up to a value of 0.38 in the range of central angles from 0° to 180° and increases further for arcs with larger central angles. For the other 4 series, the extinction ratios α_2/α_1 are indistinguishable from data of Series S1. Thus, the dependence of α_2/α_1 on θ appears to be universal for high-aspect ratio nanoarcs of various dimensions and materials. The data indicates that, with two intense LSPR features, nanoarcs subtending large central angles are most promising for observing and enhancing effects that rely on coupling between plasmon modes separated by approximately one octave, such as second harmonic generation (to be discussed in more detail in Chapter 4).

Detailed inspection of the values of λ_1 in Figure 2.5.3.2 (b) revealed minor shifts in λ_1 as θ is varied, i.e. the wavelength reaches a maximum value as the central angle approaches 60° and decreases slightly for large central angles. This trend was observed

in full-wave electromagnetic simulations (Figure 2.3.2.1 and Table 8.2.1 in the Appendix) and in measured data in several series of samples with constant L_{mid}, yet in other series this weak effect was masked by statistical deviations in the measurement data (e.g. experimental data in Table 8.2.1). The values of λ_2 did not show any notable trend with respect to θ in the simulations nor in the experiments. We note that a previous computational study reported on the minor blue-shift in λ_1 as the curvature increases in nanoarcs subtending large central angles, from 90° up to at least 270°, until the onset of capacitive coupling between the tips of the arc dramatically red-shifts the resonance. [90]

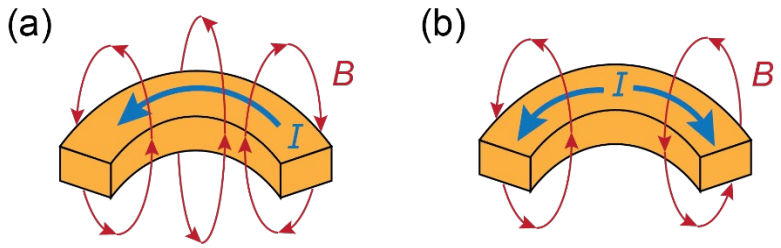

Figure 2.5.3.4 Schematic of the electrical currents I and the induced magnetic field B around a nanoarc upon excitation of the (a) 1st and (b) 2nd LSPR mode.

While the effect of θ on λ_{res} in our nanoarcs is minor, for completeness we have explored this effect. A justification for the different trends in $\lambda_1(\theta)$ and $\lambda_2(\theta)$ can be found from closer inspection of the LSPR modes. As illustrated in Figure 2.5.3.4 (a), the 1st longitudinal LSPR mode in plasmonic nanoarcs involves an oscillatory electrical current in a curved trajectory from tip to tip. Consequently, at the resonance frequency the mode displays simultaneously an in-plane oscillating electric dipole and an out-of-plane oscillating magnetic dipole. [125, 126] In contrast, in the 2nd longitudinal LSPR mode (Figure 2.5.3.4 (b)), the electrical currents oscillate between the tips and the center of the nanoarc. As such, the magnetic fields generated from the two halves of

the nanoarc oscillate out of phase with each other and the magnetic fields are cancelled out in the far field (net magnetic dipole is zero). Therefore the 2nd LSPR mode has only an electric dipole character.

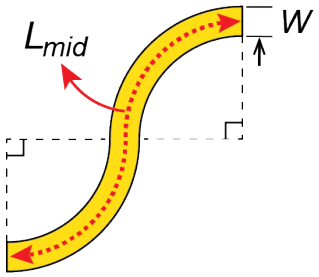

Figure 2.5.3.5 Schematic of the S-shaped nanostructure, with definitions for the mid-arc length L_{mid}, and width W.

The coupling between the magnetic and electric responses may be responsible for a shift in the resonance λ_1 that intensifies as the curvature increases, without shifting λ_2. To test this hypothesis, we compared the 1st longitudinal λ_{res} of nanorods (θ = 0°), nanoarcs (θ = 180°) and S-shaped nanostructures. As illustrated in Figure 2.5.3.5, the centrosymmetric S-shaped nanostructure is composed of two nanoarcs with θ = 90°, and its mid-arc length L_{mid} is twice of the mid-arc length of the composing nanoarc. The S-shaped nanostructures were chosen because they are curved strips, but do not have a net magnetic dipole at the 1st resonance. The gold nanorod, nanoarc and S-shaped nanostructure arrays were fabricated on silicon with dimensions of L_{mid} = 600 nm, W = 50 nm and t = 55 nm. The FTIR spectra and SEM images of these nanostructures are shown in Figure 2.5.3.6. The nanorod arrays were fabricated twice with the same rod dimensions and different lattice parameters on two silicon substrates, which accounts for the different LSPR peak intensities in the two FTIR spectra of nanorods in Figure 2.5.3.6 (a) and (b). In Figure 2.5.3.6 (a), the 1st LSPR wavelength of the nanoarc $\lambda_{1,arc}$ = 3818 nm was slightly offset from that of the nanorod at

$\lambda_{1,rod} = 3850$ nm, whereas in Figure 2.5.3.6 (b), the 1st LSPR peak of the S-shaped nanostructure spectrally overlaps with that of the nanorod ($\lambda_{1,rod} = 3855$ nm, $\lambda_{1,S-shape} = 3863$ nm). These results support the hypothesis that the different trends of λ_1 vs. θ and λ_2 vs. θ in nanoarcs are due to coupling between the magnetic and the electric dipoles. Additionally, the transformation optics analysis has predicted λ_1 will vary with central angle upon the onset of rod-rod coupling in the original space. FTIR spectroscopy on 1D plasmonic nanorod arrays confirmed that the resonance shifts to shorter wavelengths as the unit cell length is reduced to 2.5L or below. The unit cell length for the transformed 1D array is given by $2\pi L / \theta$. Therefore, a similar resonance shift should be observed in the spectra of plasmonic nanoarcs for $\theta > 360°/2.5 = 144°$. Since λ_2 is absent in the spectra of nanorods, transformation optics does not provide additional insight.

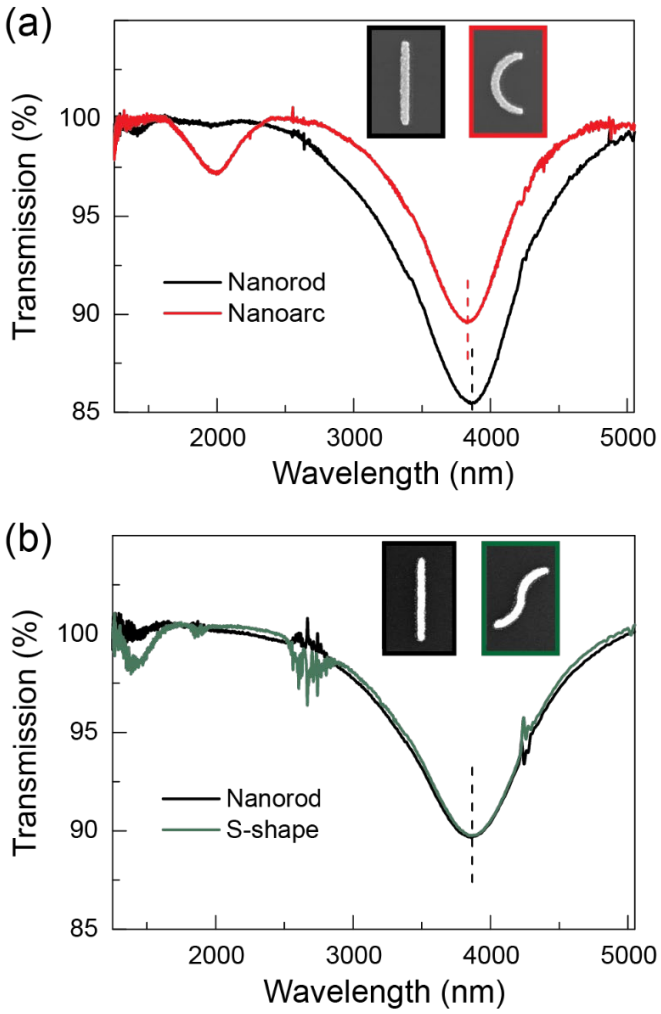

Figure 2.5.3.6 Measured FTIR transmission spectra of nanostructures with L_{mid} = 600 nm, W = 50 and t = 55 nm. (a) Black – nanorod, and red – nanoarc with θ = 180°. (b) Black – nanorod, and green – S-shaped nanostructure. The colored, vertical dashed lines mark the positions of λ_1. The insets display the corresponding SEM images of individual nanostructures.

In conclusion, the central angle θ is instrumental in tuning the relative strength of the resonances in nanoarcs without causing major shifts in the resonance wavelengths. For effects relying on coupling between plasmon modes, nanoarcs subtending large central angles offer two intense LSPR features separated by approximately one octave. In comparison, with plasmonic nanorods the high order longitudinal LSPR mode is substantially weaker than the fundamental mode and is separated from it by approximately two octaves.

2.5.4 Effect of the Mid-arc Length and Material on the LSPR Wavelengths of Nanoarcs

According to the transformation optics analysis in Section 2.2, the LSPR properties of nanorods can directly apply to nanoarcs. Since the LSPR wavelengths (λ_{res}) of nanorods have a linear relation with the rod length (L) [48, 60] and the slope is substrate material-dependent, the LSPR wavelengths of nanoarcs should have a corresponding linear relation with the effective length (i.e. the mid-arc length L_{mid}) of nanoarcs. To verify this analysis, the dependence of the LSPR wavelengths on L_{mid} in nanoarcs was investigated experimentally, using arrays of plasmonic nanoarcs with various values of L_{mid} (180 – 2170 nm) and central angle (θ = 0° – 180°). The effect of the antenna material on the LSPR wavelengths is studied using gold and aluminum. These two metals have different conduction band electron densities (N_e) and plasma frequencies (w_p). The N_e of Al (18.06×10^{22} cm^{-3}) is 3 times higher than the N_e of Au (5.90×10^{22} cm^{-3}) [127]. The w_p of Al is ~15 eV while the w_p of Au is ~9 eV [128]. Consequently, the real values of the permittivity (ε_1) of aluminum in the visible and the infrared are more negative than those of gold. The effect of the substrate material on the LSPR wavelengths is investigated using silicon and quartz. The permittivity of silicon in the infrared is ~12.1 [129] while that of quartz is ~1.45 [117]. In general, a larger substrate permittivity and a less negative metal permittivity result in LSPRs at longer wavelengths.

The gold and aluminum nanoarc arrays were fabricated on silicon and quartz substrates using the methods described in Section 2.4.1 – 2.4.3. FTIR transmission spectra were collected from the nanoarcs arrays using the methods described in Section 2.4.4, and

the LSPR wavelengths and intensities of the nanoarcs were determined using the Gaussian-Lorentzian fit described in Section 2.4.6.

Figure 2.5.4.1 (a) shows the measured 1st and 2nd resonance wavelengths (λ_1 and λ_2) as a function of L_{mid} for aluminum nanoarcs on quartz. The same data is replotted in Figure 2.5.4.1 (b) with different colors representing different central angles. Figure 2.5.4.1 (c) shows the corresponding data for gold nanoarcs on silicon.

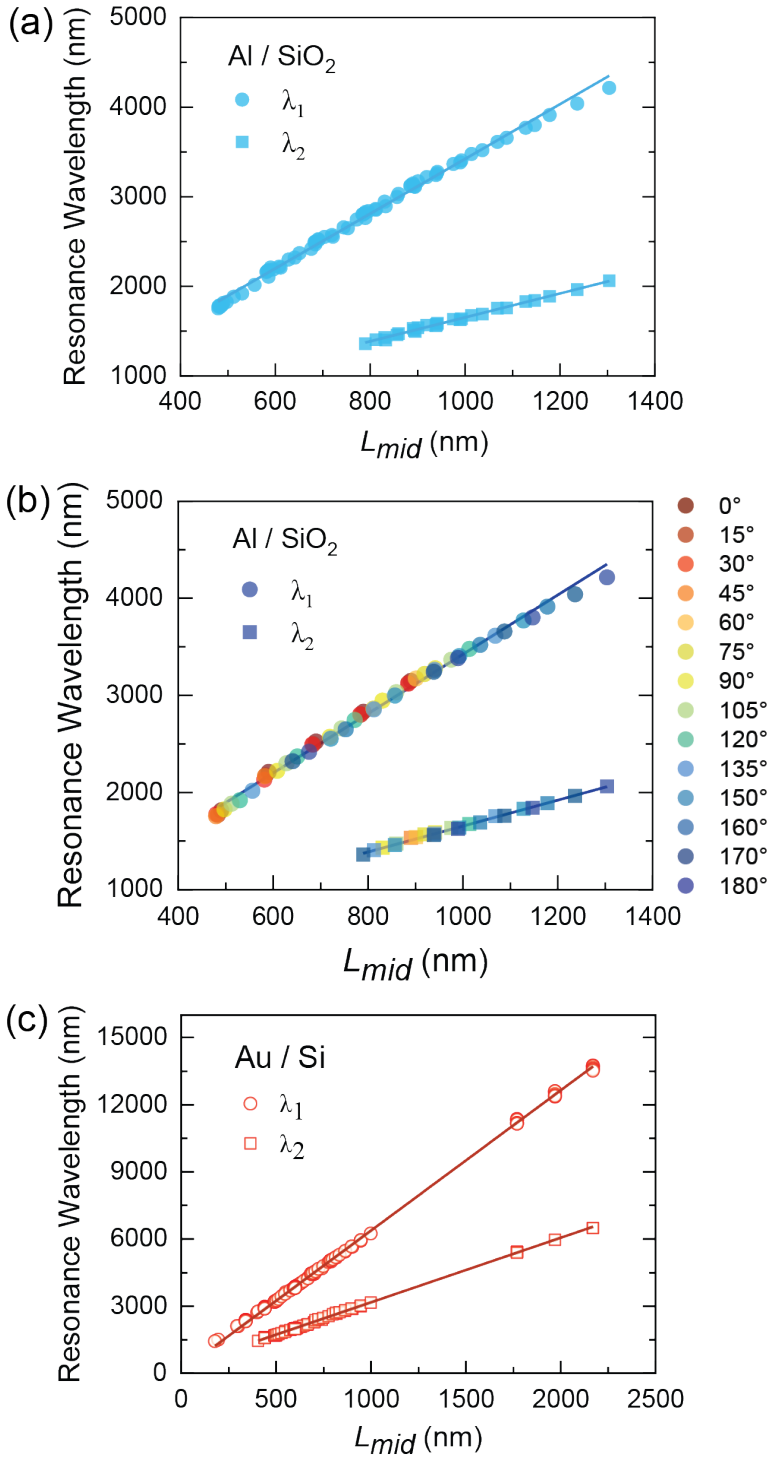

Figure 2.5.4.1 The 1st and 2nd LSPR wavelengths of (a, b) aluminum nanoarcs on quartz with L_{mid} = 460 – 1300 nm, W = 60 nm, t = 55 nm and θ = 0° – 180°, and (c) gold nanoarcs on silicon with L_{mid} =180 – 2170 nm, W = 55 nm, t = 55 nm and θ = 0° – 180°. (b) shows the same data as in (a), but the data are colored differently by angle. Symbols are data from FTIR spectroscopy measurements. Solid lines are linear fits for the data in each series. L_{mid} values are nominal values.

In each plot of Figure 2.5.4.1, a nearly linear relationship between resonance wavelength λ_{res} and L_{mid} is observed for both the 1st and 2nd LSPR modes of the nanoarcs, including all central angles. Based on the transformation optics predictions (Section 2.2), these linear trends should match the linear trends previously observed in multiple experimental studies of plasmonic nanorods; and the available literature on nanorods can be used to predict the LSPR wavelengths of nanoarcs. The dependence of the resonance wavelength λ_{res} on the nanorod length *L* is often explained with a model that considers the nanorod as a Fabry-Perot cavity for standing waves of surface plasmons. [60, 130] This model results in a linear relationship with the slope

$$\frac{d\lambda_{res}}{dL} = \frac{2n_{eff}(\lambda)}{m} \qquad (2.5.4.1)$$

where n_{eff} is the effective refractive index of the metal-dielectric interface, and m is the order of the longitudinal mode (m = 1, 2, 3…). Predicting the value of n_{eff} with analytic models when the nanorod is placed on a semi-infinite dielectric substrate has been a challenging task. [3, 48, 50, 122] Numerical calculations by Berini [131] showed that the propagation constants of surface plasmon polaritons (SPP) in infinite metal strips on the surface of a semi-infinite dielectric substrate depend not only on the permittivities of the metal, the substrate material and air, but also on the mode order, the width and the thickness of the strip. Berini's calculations that considered strips 500nm or wider, and thick enough such that the surface plasmon mode is concentrated in the high-permittivity substrate, resulted in n_{eff} values that are not very different from the values derived from the phase constant of the SPP mode supported by the interface between semi-infinite metallic and dielectric regions, as in Eq. (2.5.4.2).

$$n_{eff}(\omega) \approx \frac{\beta_{SPP}}{k_0} = Re\left[\sqrt{\frac{\varepsilon_M \varepsilon_r}{\varepsilon_M + \varepsilon_r}}\right] \qquad (2.5.4.2)$$

In Eq. (2.5.4.2), β_{SPP} is the phase constant of the SPP mode, $k_0 = \omega/c$ is the wavenumber in free space (ω is the frequency and c is the speed of light in vacuum), ε_M is the complex relative permittivity of the metal and ε_r is the relative permittivity of the high index material (i.e. the substrate). Because of the large negative value of $Re[\varepsilon_M]$ in the spectral range of interest, the right-hand side in Eq. (2.5.4.2) simplifies to $\sqrt{\varepsilon_r}$. This value is used here as a guiding approximation. Berini's model predicts that for the longitudinal surface plasmon modes n_{eff} may increase from this value as the width and thickness of the metal strip are reduced. For quartz, $\sqrt{\varepsilon_r}$ = 1.46. For silicon, $\sqrt{\varepsilon_r}$ = 3.44, however, the presence of a 7-nm native oxide film at the interface prevents intimate contact between the gold and the silicon, and lowers the value of n_{eff} significantly. The value of the slope of the linear fit in Figure 2.5.4.1 (a, b) is 3.06 ± 0.03 for the long wavelength mode (m = 1) and 1.34 ± 0.02 for the short wavelength mode (m = 2). The value of the slope in Figure 2.5.4.1 (c) is 6.27 ± 0.01 for the long wavelength mode and 2.89 ± 0.01 for the short wavelength mode. Notably, the ratio of the slopes is close but not equal to 2 as would be predicted by Eq. (2.5.4.1), and neither of the linear fits passes through the origin. The interval between the frequencies of the 1st and 2nd LSPR modes is not fixed, and is equal to an octave ($\lambda_1/\lambda_2 = 2$) only at a single value of L_{mid} that is material dependent (will be addressed in Section 3.2). In our experiments, the slopes clearly increased when choosing a higher index substrate, in line with Eqs. (2.5.4.1) and (2.5.4.2). Switching the metal from gold to aluminum

did not significantly affect the slope value but shifted the resonances to shorter wavelengths by approximately a constant $\Delta\lambda_{res}$ (Figure 2.5.4.2).

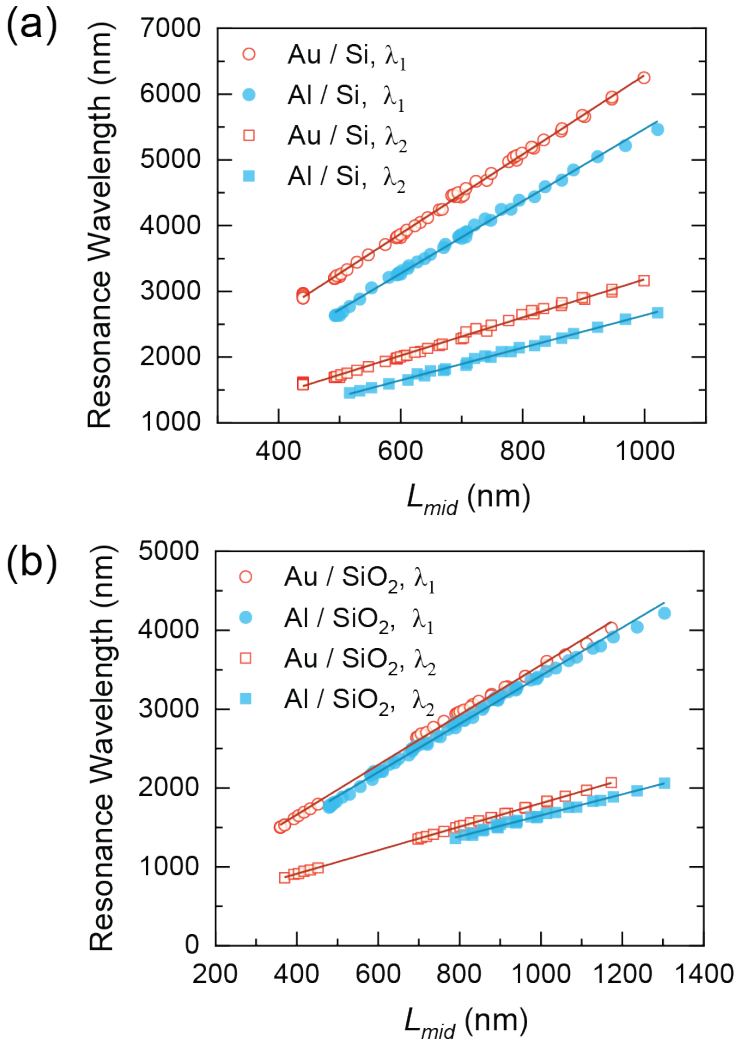

Figure 2.5.4.2 The 1st and 2nd LSPR wavelengths of gold (open red symbols) or aluminum (solid blue symbols) nanoarcs on silicon or quartz substrates. (a) Gold nanoarcs on silicon with L_{mid} = 440 – 1000 nm, W = 55 nm, t = 55 nm and θ = 0° – 180°, and aluminum nanoarcs on silicon with L_{mid} = 490 – 1020 nm, W = 55 nm, t = 55 nm and θ = 0° – 180°. (b) Gold nanoarcs on quartz with L_{mid} = 370 – 1170 nm, W = 60 nm, t = 55 nm and θ = 0° – 180°, and aluminum nanoarcs on quartz with L_{mid} = 460 – 1300 nm, W = 60 nm, t = 55 nm and θ = 0° – 180°. Data points are obtained from measured FTIR spectra. The data for gold nanoarcs on silicon and aluminum nanoarcs on quartz are a subset of the data shown in Figure 2.5.4.1. Solid line is a linear fit for the data in the series. L_{mid} values are nominal values.

The dependence of λ_1 on L_{mid} in nanoarcs can be discerned reliably from data for nanorods. When considering only the data for nanorods (θ = 0°) in Figure 2.5.4.1 (c), the linear fit gives the empirical relation $\lambda_1 = 6.31 \times L + 80$ nm for nanorods with lengths ranging from 440 nm to 2170 nm. The value of λ_1 for the nanoarcs of all central angles can be predicted using this linear relation by setting $L = L_{mid}$. A comparison between the measured $\lambda_1$values and the values predicted by the linear relation shows an average difference of 0.75% and a maximum difference of 2.4%. No similar strategy to predict the values of λ_2 in nanoarcs from data for nanorods can be implemented, since even-order modes in nanorods do not couple to radiation.

In short, we have demonstrated a nearly linear relationship between the LSPR wavelengths of nanoarcs and L_{mid}, the slope of which is substrate-material-dependent and can be very well explained using the theory derived for nanorods. The effect of antenna material (metal) is also investigated. It was found that the antenna material affects the LSPR wavelengths but does not significantly affect the slope of the nearly linear relationship.

2.5.5 Effect of the Mid-arc Length on the LSPR Wavelengths of Thin Nanoarcs

Spectroscopic studies on nanoarcs with *t* = 55 nm have demonstrated the nearly linear relationship between the LSPR wavelengths and the mid-arc length L_{mid} of nanoarcs (Section 2.5.4). Can this relationship be applied to nanoarcs with different thicknesses? To address this question, the spectroscopic study of a series of gold nanoarcs with *t* = 23 nm is discussed in this section. With a thinner thickness the electromagnetic field distribution around the nanoarcs may change upon resonance excitation because of the stronger coupling between the electron oscillations on the top surface and bottom

surface of the nanoarc and because of changes in the relative penetration of the near-field into the surrounding media (air and substrate).

Gold nanoarc arrays were fabricated on silicon and quartz substrates using the methods described in Section 2.4.1 – 2.4.3. The dimensions of the gold nanoarcs on silicon are L_{mid} = 250 – 2100 nm, W = 60 nm, t = 23 nm and θ = 0° – 180°. For gold nanoarcs on quartz, the dimensions of the nanoarcs are L_{mid} = 250 – 1200 nm, W = 60 nm, t = 23 nm and θ = 0° – 180°. FTIR transmission spectra were collected from the nanoarc arrays using the methods described in Section 2.4.4, and the wavelengths and intensities of the LSPR peaks were determined using the Gaussian-Lorentzian fit described in Section 2.4.6.

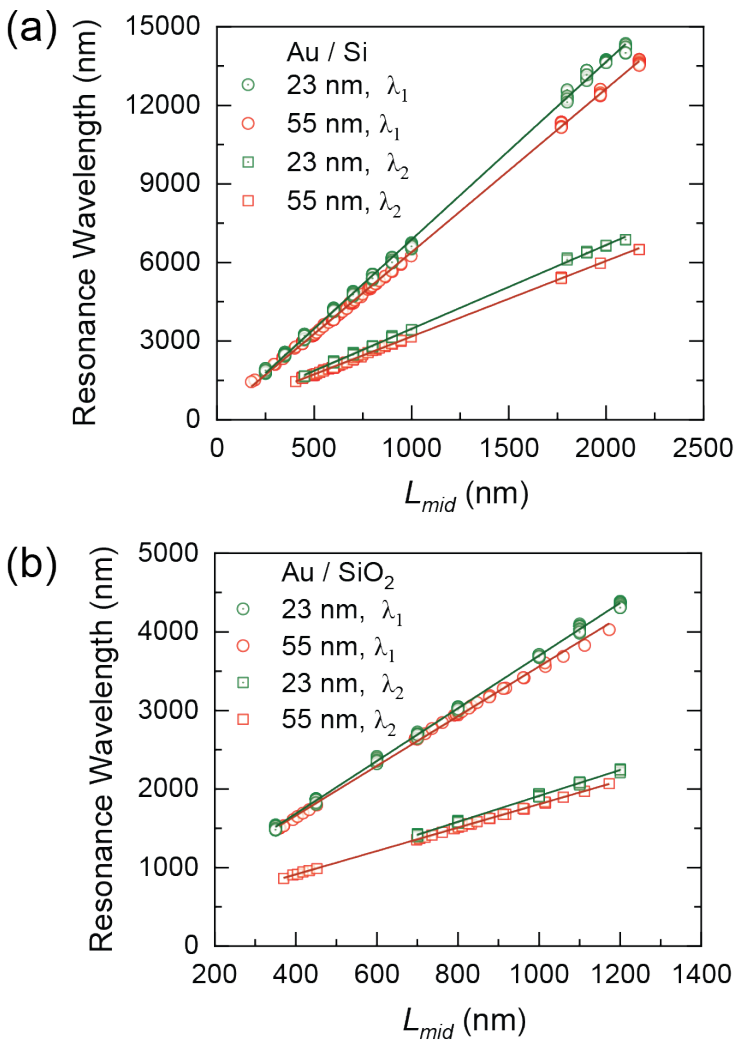

Figure 2.5.5.1 The 1st and 2nd LSPR wavelengths of gold nanoarcs on silicon or quartz substrates. (a) Gold nanoarcs on silicon with t = 23 nm (green) and 55 nm (red), L_{mid} = 180 – 2170 nm, W = 55 nm, and θ = 0° – 180°. (b) Gold nanoarcs on quartz with t = 23 nm (green) and 55 nm (red), L_{mid} = 250 – 1200 nm, W = 60 nm, and θ = 0° – 180°. Data points are obtained from measured FTIR spectra. The data for nanoarcs with 55 nm are same as the data shown in Figures 2.5.4.1 and 2.5.4.2. Solid lines are a linear fit for the data in the series. L_{mid} values are nominal values.

Figure 2.5.5.1 shows the measured 1st and 2nd LSPR wavelengths (λ_1 and λ_2) as a function of L_{mid} for gold nanoarcs with t = 23 nm, together with the data of gold nanoarcs with t = 55 nm. For nanoarcs with high aspect-ratios (L_{mid} > 500 nm), the LSPR wavelengths are larger in nanoarcs with t = 23 nm. In all the data sets there is a nearly linear relationship between λ_{res} and the L_{mid} of the nanoarcs. For nanoarcs on

both silicon (Figure 2.5.5.1 (a)) and quartz substrates (Figure 2.5.5.1 (b)), the value of the slope of the linear fit is approximately 10% larger for nanoarcs with t = 23 nm than nanoarcs with t = 55 nm. The values of the slopes are summarized in Table 2.5.5.1. The larger slope for the thin nanoarcs can be qualitative explained in terms of the effective refractive index ($n_{eff}(\lambda)$ in Eq. 2.5.4.1). As the thickness of the nanoarc is reduced, the field penetration depth into the substrate increases [132, 133]. Consequently, the contribution of the refractive index of the dielectric substrate material is greater in determining the effective refractive index. Therefore, the slope of the linear relationship, which is proportional to $n_{eff}(\lambda)$ according to Eq. 2.5.4.1, becomes larger.

Table 2.5.5.1 The value of the slope of the linear fit

Material	Thickness (nm)	Slope of m = 1 mode	Slope of m = 2 mode
Au/Si	23	6.79 ± 0.02	3.20 ± 0.02
Au/Si	55	6.27 ± 0.02	2.89 ± 0.01
Au/SiO_2	23	3.35 ± 0.01	1.65 ± 0.01
Au/SiO_2	55	3.16 ± 0.03	1.49 ± 0.01

In summary, in nanoarcs with different thicknesses, there is a nearly linear relationship between the LSPR wavelength and L_{mid}, regardless of the curvatures. The value of the slope of the linear fit increases by ~10% when the thickness of the nanoarcs is reduced from t = 55 nm to t = 23 nm.

2.6 Chapter Summary

In this chapter, the tunability of the LSPR wavelength in plasmonic nanoarcs with uniform width profiles was investigated. Using a 2D conformal transformation, the nanoarcs ($0° \leq \theta \leq 180°$) were transformed into nanorods, and vice versa. According to

the conformal transformation, the two types of nanostructures share the same LSPR wavelengths and thus the well-studied plasmonic characteristics of nanorods can be directly applied to predict the plasmonic characteristics of nanoarcs. Through numerical simulations and experiments, we have proven that the effective length L_{mid} is the crucial parameter that determines the LSPR wavelengths of nanoarcs, and the linear dependence of the LSPR wavelength on the length of the nanorod $\lambda_1 = aL + b$ applies with the same slope and intercept values to nanoarcs as $\lambda_1 = aL_{mid} + b$. This holds for both Au nanoarcs on silicon and Al nanoarcs on quartz. Consequently, the fundamental LSPR wavelength of nanoarcs was tuned predictably in the NIR and MIR regimes (1.5 – 13.6 μm, or 730 – 6600 cm^{-1}). This spectral range may be further extended if longer or shorter nanoarcs are fabricated or a substrate with a different refractive index is used. The antenna material also affects the LPSR wavelength/frequency of the nanoarcs. Due to the higher conduction band electron density of aluminum, the plasma resonance frequency of aluminum is higher than that of gold, and the permittivity in the visible and infrared is more negative in aluminum than in gold. Consequently, the LSPRs of aluminum nanoarcs appears at higher frequencies. Adjusting the central angle has a minor effect on the LSPR wavelength, but it changes the attenuation of different-order LSPR modes. The attenuation of the 1st LSPR mode decreases as the central angle increases while the 2nd LSPR mode shows the opposite trend. These results are valid for individual nanoarcs and arrays of nanoarcs with sufficient separation between elements to minimize dipolar coupling. If the distance between adjacent elements in an array is smaller than a threshold value, the dipolar coupling between the elements will shift the fundamental resonance to

shorter wavelengths. The threshold values of the lattice parameters were quantified for centered-rectangular lattices of nanoarcs on silicon and quartz. These results facilitate the design of nanoarcs with desired optical response, paving the way for nanoarcs to be more widely applied as components for photonic technologies.

Chapter 3: Tunability of the Wavelength Interval between the 1st and 2nd LSPRs of Plasmonic Nanoarcs

3.1 Introduction

Light-matter interactions enhanced by multiple LSPRs of nanoantennas have shown exceptional advantages in surface enhanced Raman scattering (SERS) spectroscopy [24, 134] and in second-harmonic generation (SHG) from plasmonic systems [72, 135] compared to those enhanced by a single plasmon resonance. For SERS spectroscopy, multimodal plasmonic nanoantennas with LSPR modes matching both the excitation and the Stokes Raman wavelengths/frequencies have achieved greater SERS enhancement factors [134]. For SHG from plasmonic systems, an improved SHG efficiency has been observed when the 1st and 2nd LSPR wavelengths (λ_1 and λ_2) match the fundamental and second harmonic (SH) wavelengths, respectively, i.e. when the LSPR wavelengths satisfy the octave interval condition $\lambda_1/\lambda_2 = 2$. [72, 135] In this context, the ability to tune the wavelength interval between different-order LSPRs can greatly increase the enhancing power of the plasmonic nanoantennas. Therefore, a design strategy that can systematically tune the wavelength interval is highly desired. Here our focus is on the wavelength interval between the 1st and 2nd LSPRs which will be referred to as the LSPR wavelength interval, or *the LSPR interval* for short.

Previous studies have demonstrated that the LSPR wavelength interval can be tuned in plasmonic dimers [72] and multimers [135, 136] composed of nanoparticles separated by nanometer-sized gaps. For the dimers and multimers, the wavelength interval between different-order LSPR modes is controlled by the geometry of each particle and

the dipolar coupling between adjacent particles, which is manipulated by the gap size. [72, 137-139] Examples of such dimers and multimers are shown in Figure 3.1.1. This approach has proven useful but at the cost of a challenging fabrication process with limited opportunities for scale-up. Alternatively, a more straightforward approach would be to tune the fundamental and higher order LSPR modes in a single nanoantenna. To our knowledge, tuning two LSPRs of a single (i.e. gapless) nanoantenna to achieve the octave interval condition has not been reported before.

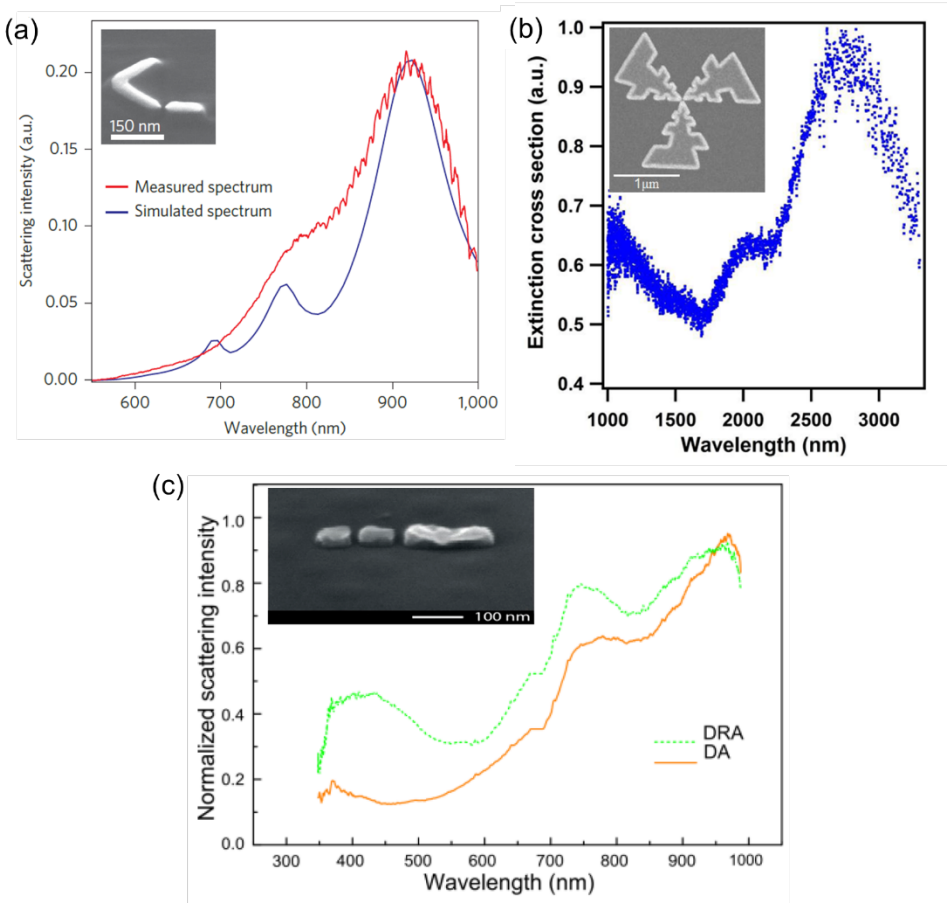

Figure 3.1.1 Plasmonic systems that have been designed and used for enhancement by multiple plasmonic interactions. (a) Gold nanoantenna dimer composed of a V-shaped nanoantenna and a nanorod on a fused silica substrate (reprinted from Ref. [72]). (b) Multi-resonant three-arm trapezoidal silver nanoantenna on a barium fluoride (BaF_2) substrate (reprinted from Ref. [136]). (c) Aluminum double-resonance antenna composed of three nanorods on a fused silica substrate (reprinted from Ref. [135]).

As discussed in Chapter 2, nanoarcs with uniform width profiles, i.e. the distance between the inner and outer edges along the radial direction is constant, can support two strong LSPR modes with the ratio of the resonance wavelengths λ_1/λ_2 close to two (λ_1/λ_2 = 1.73 – 2.09, data will be presented in Section 3.2). In comparison, the nanocrescent geometry studied by Shumaker-Perry et al. [65, 140] was found to have two longitudinal LSPR wavelengths with a generally smaller ratio λ_1/λ_2 of 1.69 – 1.77. The geometries of the nanoarcs and the nanocrescents are similar, but one of the key differences between them is that in nanocrescents the tips are narrower than the center. For both geometries, the 1st and 2nd LSPRs corresponds to orthogonal polarizations (Figure 1.1.4 (b), (e) and Figure 2.3.3.1), and the charge accumulations at resonances are alike: at the 1st LSPR, the charges accumulate around the two tips of the nanoarc/nanocrescent, while at the 2nd LSPR, the charges accumulate around the tips and the center. The difference in the LSPR interval of the two geometries may be attributed to their different width profiles. When a plasmon resonance is excited in a nanocrescent and a nanoarc with similar dimensions, the crescent tips will have more concentrated charges than the arc tips because the crescent tips are narrower. Therefore, the plasmon energy is higher in nanocrescents compared to that of nanoarcs [141, 142], which leads to the different LSPR wavelengths in the two geometries. In addition, due to the difference in the charge distribution at the 1st and 2nd LSPR modes, the two LSPR wavelengths of nanoarcs/nanocrescents are affected differently by the width profile. Therefore, the LSPR interval may be tuned by the width profile in arc-like antennas.

In light of this idea, we have investigated via spectroscopy the ratio λ_1/λ_2 in nanoarcs with different width profiles. The goal is to develop a design strategy to systematically

tune the wavelength interval between the 1st and 2nd LSPR modes in plasmonic nanoarcs. Section 3.2 discusses the ratio λ_1/λ_2 in nanoarcs with a uniform width profile. In Section 3.3 and 3.4, nanoarcs with non-uniform width profiles are studied to identify the parameters that determine the ratio λ_1/λ_2 in nanoarcs.

3.2 Effect of Material and L_{mid} on the Ratio λ_1/λ_2 of Nanoarcs with a Uniform Width Profile

In Chapter 2, we have demonstrated that for nanoarcs with a uniform width profile, the 1st and 2nd LSPR wavelengths (λ_1 and λ_2) vary depending on the materials of the antenna and substrate, and a key geometric parameter: the mid-arc length L_{mid}. Here, the data from Section 2.5.4 are reexamined to investigate the effect of materials and L_{mid} on the ratio of the 1st and 2nd LSPR wavelengths λ_1/λ_2 of nanoarcs.

The FTIR spectroscopy data of nanoarcs with uniform width was presented in Figures 2.5.4.1 and 2.5.4.2 in terms of the relations λ_1 *vs.* L_{mid} and λ_2 *vs*. L_{mid}. The ratio λ_1/λ_2 was calculated using these data and was plotted in Figure 3.2.1 as a function of L_{mid}. The symbols represent the four sets of data obtained from the measured FTIR transmission spectra of gold and aluminum nanoarcs on silicon and quartz substrates. The two dotted lines are a guide to the eye, generated by taking the ratio of the linear fits ($y(L_{mid}) = \frac{a_1 L_{mid}+b_1}{a_2 L_{mid}+b_2}$) of the 1st and 2nd LSPR wavelengths of gold and aluminum nanoarcs on silicon substrates (see Section 2.5.4). The data demonstrates that for nanoarcs on silicon substrates, the ratio λ_1/λ_2 increases with L_{mid}. Specifically, for gold nanoarcs on silicon (circles), λ_1/λ_2 increases from 1.83 to 2.09 as L_{mid} increases from 440 nm to 2170 nm. For aluminum nanoarcs on silicon (diamonds),

λ_1/λ_2 increases from 1.90 to 2.06 as L_{mid} increases from 520 nm to 920 nm. For nanoarcs on quartz substrates, the variation of λ_1/λ_2 as a function of L_{mid} was not clear due to the relatively narrow range of L_{mid}. For gold nanoarcs on quartz (triangles) with fixed L_{mid} = 395 nm (and different central angles), λ_1/λ_2 varies in a relatively large range from 1.73 to 1.81, while for nanoarcs with L_{mid} = 700 – 1170 nm, λ_1/λ_2 barely changes (1.94 – 1.97). For aluminum nanoarcs on quartz (stars) with L_{mid} = 790 – 1300 nm, the ratio λ_1/λ_2 also varies in a limited range of 2.03 – 2.08.

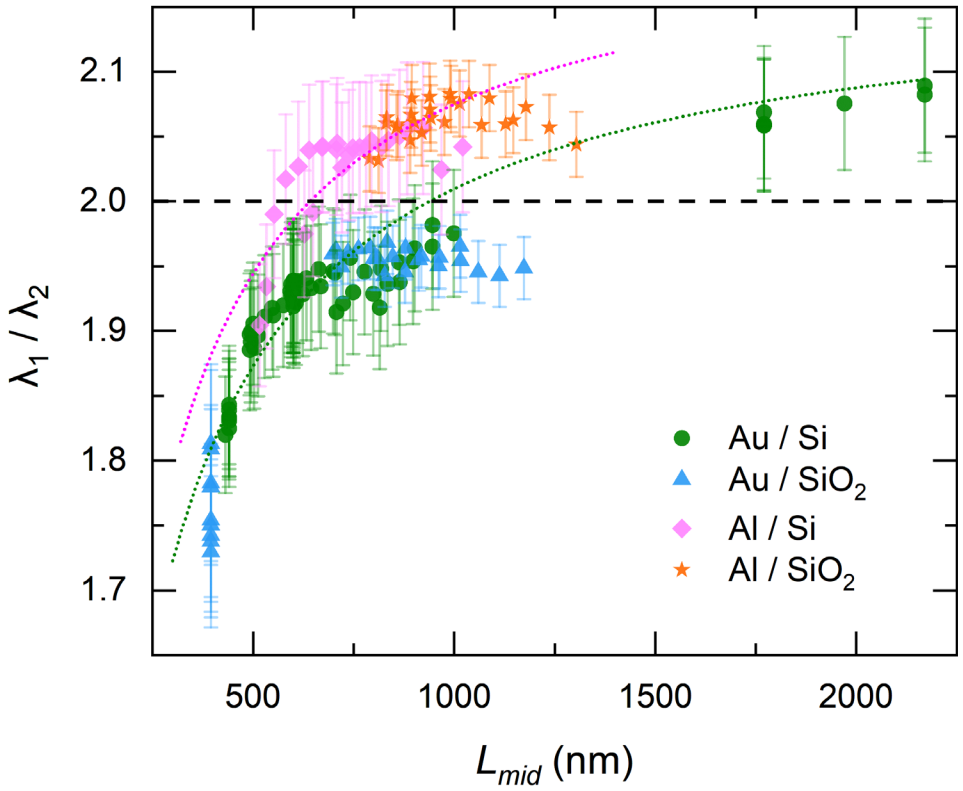

Figure 3.2.1 The ratio between the 1st and 2nd LSPR wavelengths (λ_1/λ_2) as a function of L_{mid} for gold and aluminum nanoarcs on silicon and quartz substrates. Symbols are data obtained from the measured transmission spectra. Dotted lines are the ratio between the linear fits of the 1st and 2nd LSPR wavelengths of Au/Si (green dotted line) and Al/Si (pink dotted line) nanoarcs. Black dash line marks the octave interval condition (λ_1/λ_2 = 2). For Au/Si and Al/Si data, the error bar is ±2.47%. For Au/SiO_2, the error bar is ±2.39%. For Al/SiO_2, the error bar is ±2.34%. The size of the error bars has been estimated based on the statistical deviations of λ_1 and λ_2 determined in Section 2.5.1.

The values of λ_1/λ_2 are larger for aluminum nanoarcs than for gold nanoarcs with similar dimensions (L_{mid} = 550 – 1200 nm). Consequently, aluminum and gold nanoarcs with uniform width achieve the octave interval condition with different L_{mid} values, as marked by the dash line in Figure 3.2.1. The ratio λ_1/λ_2 is ~2 in gold nanoarcs with L_{mid} around 1100 nm, and in aluminum nanoarcs with L_{mid} around 640 nm. Figure 3.2.1 also shows that nanoarcs made on silicon and quartz substrates (i.e., Au/Si vs. Au/SiO_2 and Al/Si vs. Al/SiO_2) show similar λ_1/λ_2 when their dimensions are comparable. In other words, the effect of the substrate material on the ratio λ_1/λ_2 is less significant compared to the effect of the antenna material.

According to the discussion above, with nanoarcs of uniform width the ratio λ_1/λ_2 can be tuned by changing the antenna material and L_{mid} but only to a limited extent, and the octave interval condition is met only for a single L_{mid} per material. To tune the ratio λ_1/λ_2 over a relatively large range, a different strategy is required for adjusting the resonance frequency of each LSPR mode independently.

3.3 The Ratio λ_1/λ_2 in Nanocrescents

To demonstrate that the width profile affects the ratio λ_1/λ_2 in arc-like antennas a plasmonic nanocrescent was examined. The *nanocrescent* is defined here as the trace of an arc-line translated along its axis of symmetry by a distance of *W*, as illustrated Figure 3.3.1 (a). The geometry of the nanocrescent is fully defined by four parameters: height *H* (the chord length of the arc-line), width *W*, central angle θ (the angle subtended by the arc-line), and thickness *t*. The mid-arc length L^*_{mid} of a nanocrescent is defined in a similar way as in the nanoarcs and is equal to the length of the arc-line.

Nanocrescents have parallel terminations at the two ends, in contrast with nanoarcs which have radial terminations. Nominally, the edges of nanocrescents form acute angles at the tips. Resolution limitations of the nanofabrication process lead to rounding of the corners of the elements. Nevertheless, nanocrescents are produced with sharper tips than those of nanoarcs (Figure 3.3.1(b)).

The gold nanocrescent arrays used in the experiments were composed of nanocrescents with dimensions of H = 400 nm, W = 50 nm, t = 55 nm and θ = 90°, 120°, 136°, 150°, and 180°. The arrays were fabricated on a silicon substrate using the methods described in Section 2.4.1 – 2.4.3. As a reference, arrays of gold nanoarcs with the same geometric parameters (H, W, θ and t) were fabricated on the same substrate. These crescent/arc geometries correspond to nominal dimensions of L^*_{mid}= 444, 484, 512, 542 and 628 nm for nanocrescents and L_{mid} = 405, 431, 453, 477 and 550 nm for nanoarcs. All arrays have a triangular lattice with (a_1, a_2) = (1.2, 2.4) μm. FTIR spectra were collected from the nanoarc/nanocrescent arrays using the methods described in Section 2.4.4. Each spectrum showed two attenuation peaks and the LSPR wavelengths were determined using the Gaussian-Lorentzian fit described in Section 2.4.6. After FTIR spectroscopy, SEM imaging (method in Section 2.4.7) was performed to check the dimensions of the nanocrescents and nanoarcs.

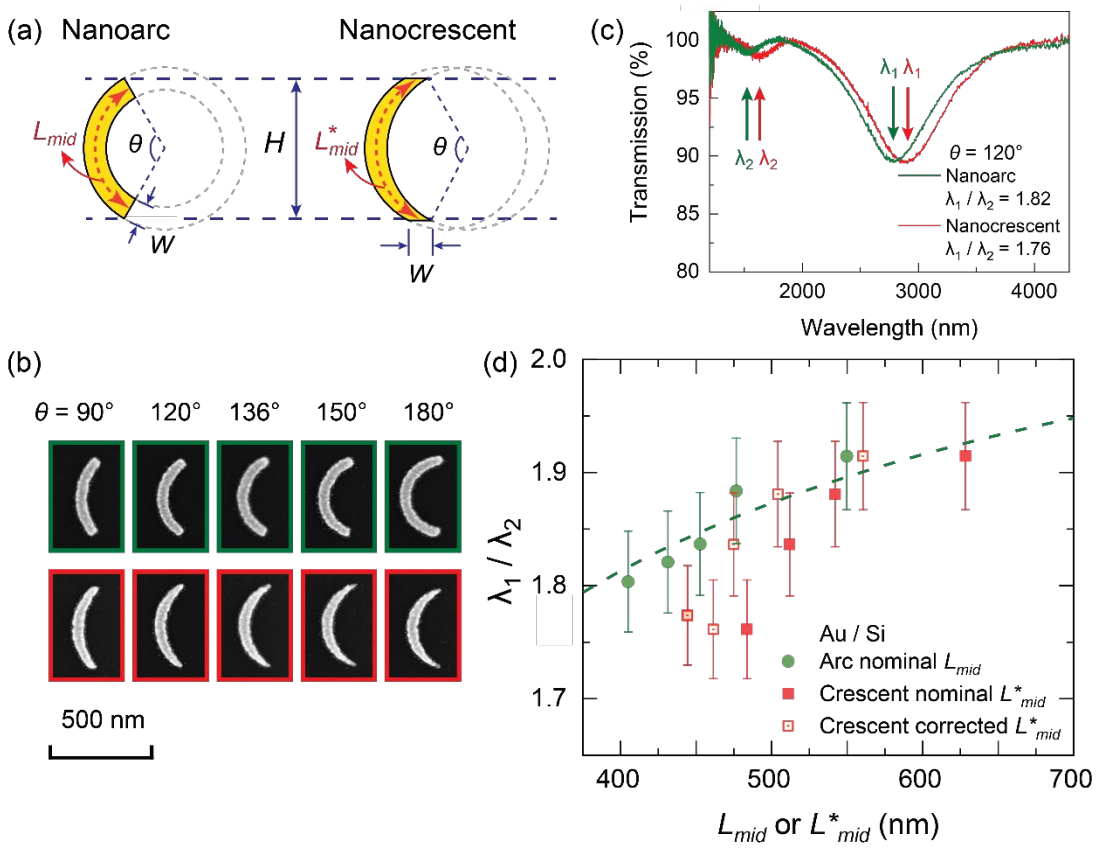

Figure 3.3.1 (a) Schematic of the nanoarc geometry and the nanocrescent geometry, with definitions for the arc/crescent height H, width W, central angle θ and mid-arc length L_{mid} (L^*_{mid}). (b) SEM images of gold nanoarcs (green frames) and nanocrescents (red frames) on silicon with H = 400 nm, W = 50 nm, t = 55 nm and θ = 90°, 120°, 136°, 150° and 180°. (c) FTIR transmission spectra of gold nanoarcs (green) and nanocrescents (red) on silicon with H = 400 nm, W = 50 nm, t = 55 nm and θ = 120°. Arrows indicate the 1st and 2nd LSPR wavelengths. (d) The ratio λ_1/λ_2 as a function of L_{mid} or L^*_{mid} for gold nanoarcs/nanocrescents on silicon substrates. Green circles are the data of nanoarcs with the nominal L_{mid}. Green dash line is the ratio between the linear fits of the 1st and 2nd LSPR wavelengths. The nanoarc data is a subset of the data shown in Figure 3.2.1. Solid and open red squares are the data of nanocrescent with the nominal L^*_{mid} and the corrected L^*_{mid} based on SEM imaging, , respectively. The error bar of ± 2.47% is estimated based on the statistical deviation of λ_1 and λ_2 determined in Section 2.5.1.

The SEM images of the nanoarcs and nanocrescents are shown in Figure 3.3.1 (b). The tips of the nanocrescents are rounded with a radius of ~10 nm due to the limited resolution of the EBL patterning process. As a result, for nanocrescents with large central angles θ = 120° – 180° the mid-arc length was shorter than the nominal L^*_{mid} in

the design by 20 – 70 nm, while for nanocrescents with small central angles $\theta \leq 90°$, the mid-arc length was not affected. The FTIR spectra collected from nanoarcs and nanocrescents with θ = 120° are shown in Figure 3.3.1 (c). Both λ_1 and λ_2 of the nanocrescent are longer than those of the nanoarc, likely because with the same *H*, the L^*_{mid} of the nanocrescent is longer than the L_{mid} of the nanoarc (even after correcting for tip rounding). The nanoarc LSPR wavelengths are λ_1 = 2791 nm and λ_2 = 1532 nm resulting in a ratio of λ_1/λ_2 = 1.82. This value falls on the trend line for Au/Si nanoarcs shown in Figure 3.2.1 and reproduced in Figure 3.3.1 (d), given nominal L_{mid} = 431 nm. For the nanocrescent the two LSPR peaks are centered at λ_1 = 2887 nm and λ_2 = 1637 nm with a ratio of λ_1/λ_2 = 1.76. This ratio would correspond to a nanoarc with L_{mid} of 340 nm, far shorter than the physical dimension of the nanocrescent (corrected L^*_{mid} = 460 nm). Similarly, for the nanocrescent with θ = 90° and corrected L^*_{mid}= 444 nm (same as the nominal L^*_{mid}), the ratio λ_1/λ_2 is much smaller than that of a nanoarcs with the same value of L_{mid} (Figure 3.3.1 (d)). With large nominal mid-arc lengths (L_{mid} or L^*_{mid} > 540 nm) and/or central angles (θ > 136°), the difference between the ratio λ_1/λ_2 of nanocrescents and nanoarcs is not significant. The data in Figure 3.3.1 (d) illustrates that nanocrescents and nanoarcs can have significantly different LSPR intervals and λ_1/λ_2 ratios even when their dimensions are similar. Nanocrescents appear to have smaller λ_1/λ_2 values, particularly when L^*_{mid} is small. This difference in the ratio λ_1/λ_2 is attributed to the modified charge distributions at resonance: with narrower tips in the nanocrescent geometry, the longitudinal LSPRs shift to shorter wavelengths. The impact is stronger on the 1st LSPR mode compared to the 2nd LSPR mode. In the 1st LSPR mode, charge accumulates in the arc tips, where the width in the

nanoarcs and in the nanorods are most dissimilar. In the 2nd LSPR mode, charge accumulates also in the arc middle, an area that has the same width in the nanoarcs and in the nanorods. Since narrowing the tips only shifts the ratio λ_1/λ_2 of the nanocrescents away from the octave interval condition, nanocrescents are not an ideal geometry for achieving the octave interval condition nor for studying the effect of width profile on the LSPR interval. A different strategy is required to tune the width profile of arc-like antennas systematically.

3.4 Nanoarcs with a Non-Uniform Width Profile

In this section, nanoarcs with non-uniform width profiles are studied with the goal of elucidating the relationship between the width profile of the nanoarcs and the interval between the 1st and 2nd LSPR wavelengths. The width profile of the nanoarcs is adjusted by selectively modifying the width at the arc tips (W_{tip}) or the arc center (W_{mid}), the two sites where the charges accumulate upon resonance excitation. The design of the nanoarcs with a non-uniform width, and the methods for sample preparation and characterization are introduced in Section 3.4.1. The FTIR measurement results are discussed in Sections 3.4.2 – 3.4.4.

3.4.1 Methods of Pattern Design, Sample Fabrication and Characterization

Nanoarcs with non-uniform width profiles were designed by applying the geometric transformation of Eqs. (2.2.7) and (2.2.8) to nanorods with a non-uniform width profile. For these nanorods, we have set the parameters of length L, width at tips W_{tip}, and width at center W_{mid}, as shown in Figure 3.4.1.1 (a) and (b). The smooth contour along the long edges of the nanorod was obtained by defining the position-dependent width

of the nanorod as $W(y) = W_{mid} + 2\delta \sin^2(\frac{y}{L}\pi)$ (Figure 3.4.1.1(a)) or as $W(y) = W_{tip} + 2\delta \cos^2(\frac{y}{L}\pi)$ (Figure 3.4.1.1(b)), where δ is the amplitude ($|2\delta| = |W_{mid} - W_{tip}|$) and L is the length of the rod. W_{mid} can be wider or narrower than W_{tip} depending on the sign of δ; both instances were investigated. The non-uniform nanorods were transformed to nanoarcs (Figure 3.4.1.1 (c) and (d)). With the appropriate choice of the nanorod coordinates in the rod-space, W_{mid} of the transformed nanoarc in the arc-space is set to be identical to that of the corresponding nanorod, while W_{tip} of the transformed nanoarc and the original nanorod are slightly different. However, the difference (<1.2 nm in our design) is below the resolution of EBL patterning.

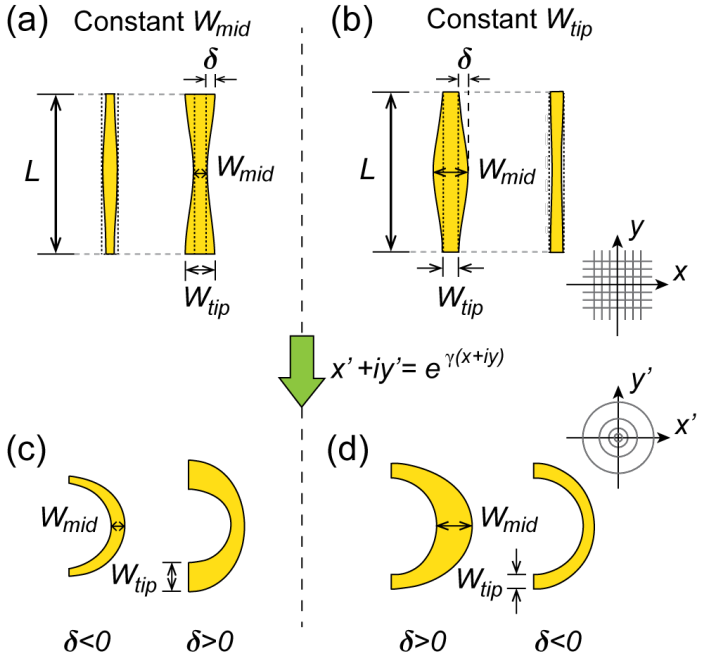

Figure 3.4.1.1 Designing nanoarcs with a non-uniform width profile. (a, b) Nanorods with a non-uniform width are designed by setting the width at the tips $W_{tip} \equiv W$ ($y = \pm L/2$) and the width at the center $W_{mid} \equiv W$ ($y = 0$) to different values, and creating a smooth width profile from tip to tip as $W(y) = W_{mid} + 2\delta\sin^2(\pi y/L)$ or $W(y) = W_{tip} + 2\delta\cos^2(\pi y/L)$. The width profile of a uniform-width rod ($\delta = 0$) is indicated by the dotted

lines. (c, d) The non-uniform nanoarcs are obtained through the conformal transformation of non-uniform nanorods.

For nanoarcs with a non-uniform width profile, the central angle θ given by the relation $\theta = \gamma L$ and the mid-arc length L_{mid} do not have an intuitive physical meaning, and as mentioned, the arc W_{tip} is slightly different from the W_{tip} of the corresponding nanorod. For clarity, we use the dimensions of the *nanorod* as the nominal values to describe the dimensions of the nanoarc. For example, the description "a nanoarc with L = 600 nm, t = 55 nm, W_{tip} = 60 nm, W_{mid} = 50 nm and θ = 90° " is for the nanoarc transformed from a nanorod with these geometric parameters (L = 600 nm, t = 55 nm, W_{tip} = 60 nm, W_{mid} = 50 nm) using the conformal transformation defined by Eqs. (2.2.7) and (2.2.8), with θ in Eq. (2.2.8) being π/2.

Table 3.4.1.1 Antenna material, substrate material and dimensions of the nanoarcs

Group	Material	L (nm)	t (nm)	θ (°)	W_{mid} (nm)	W_{tip} (nm)
S1	Au/Si	600	55	0-180	50	40 – 100
S2	Au/Si	600	55	0-180	70	60 – 130
S3	Au/Si	600	55	0-180	40 – 100	50
S4	Au/Si	600	55	0-180	60 – 130	70
S5	Au/Si	1000	55	0-180	50	40 – 100
S6	Au/Si	1000	55	0-180	40 – 100	50
Q7	Au/SiO_2	1000	55	0-180	50	40 – 100
Q8	Au/SiO_2	1000	55	0-180	40 – 100	50

Eight groups of nanoarc arrays were fabricated using the methods described in Section 2.4.1 – 2.4.3. The dimensions and materials of the nanoarcs and substrates used in the eight groups of arrays are listed in Table 3.4.1.1. Within each group, the nanoarcs were fabricated using the same antenna material and substrate material, and the same values for 3 geometric parameters L, t and W_{tip} or W_{mid}. The different groups correspond to

different width profiles, L, or substrate materials. Based on the analyses of nanoarcs with a uniform width profile presented in Chapter 2, two lengths (L = 600 nm and 1000 nm) were selected because the 1st and 2nd LSPRs of these nanoarcs can be recorded simultaneously by FTIR spectroscopy. The nanoarc arrays have a triangular lattice. The lattice parameters are (a_1, a_2) = (1.6, 3.1) μm for nanoarcs with L = 600 nm, and (a_1, a_2) = (1.8, 4.6) μm for nanoarcs with L = 1000 nm. The lattice parameters are above the threshold values discussed in Section 2.5.2 therefore the nanoarcs are considered as free of inter-particle dipolar coupling.

FTIR spectra were collected from the nanoarc arrays using the methods described in Section 2.4.4 and the LSPR wavelengths and intensities were determined using the Gaussian-Lorentzian fit described in Section 2.4.6. After the FTIR measurements, SEM images were acquired (method in Section 2.4.7) from nanoarcs on silicon to check the dimensions of the nanoarcs.

3.4.2 Effect of W_{tip} on the ratio λ_1/λ_2

The effect of W_{tip} on the ratio of the 1st and 2nd LSPR wavelengths (λ_1/λ_2) of nanoarcs is investigated through spectroscopic study of nanoarcs in Groups S1 and S2.

Figure 3.4.2.1 shows the FTIR transmission spectra measured from nanoarcs in Group S1 with W_{mid} = 50 nm and different W_{tip}. Each panel in Figure 3.4.2.1 shows that for nanoarcs with fixed L, t, θ and W_{mid}, as W_{tip} increases, λ_1 red-shifts and, to a lesser extent, λ_2 blue-shifts. Meanwhile, the attenuation (1-T) of the 1st LSPR mode increases significantly while the attenuation of the 2nd LSPR mode only shows a minor increase. Taking nanoarcs with θ = 180° as an example (Figure 3.4.2.1 (d)), as W_{tip} increases from 40 nm to 110 nm, λ_1 red-shifts by 634nm (from 3636 nm to 4720 nm) while λ_2

blue-shifts by 38nm (from 1978 nm to 1940 nm). As a result, the ratio λ_1/λ_2 increases from 1.84 to 2.20. With increasing W_{tip}, the attenuation of the 1st LSPR mode increases from 11.6% to 18.1% while the attenuation of the 2nd mode only increases from 3.5% to 4.2%. For nanoarcs with the other three central angles (Figure 3.4.2.1 (a)-(c)), the shift of λ_1 caused by the change of W_{tip} increases as central angle increases. Specifically, for arcs with θ = 0°, 90° and 150°, the redshift of λ_1 is 569 nm, 576 nm and 615 nm, respectively. The blueshift of λ_2 is almost constant for nanoarcs with different central angles. For nanoarcs with θ = 90° and 150°, the blueshift of λ_2 is 44 nm and 43 nm, respectively.

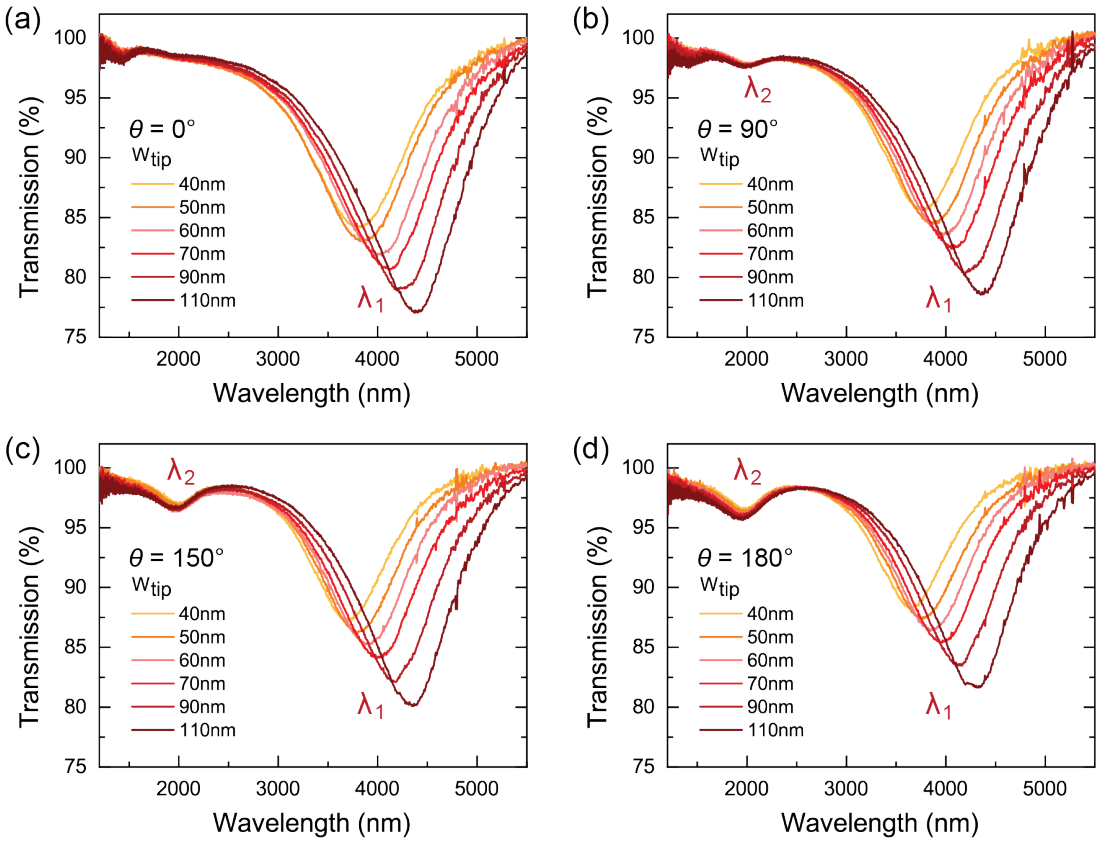

Figure 3.4.2.1 Measured FTIR transmission spectra of gold nanoarcs on silicon with L = 600 nm, t = 55 nm, W_{mid} = 50 nm and W_{tip} = 40 – 110 nm (Group S1). The central angles of the nanoarcs are (a) θ = 0° (nanorods), (b) θ = 90°, (c) θ = 150° and (d) θ = 180°.

Figure 3.4.2.2 shows the ratio λ_1/λ_2 of nanoarcs in Groups S1 and S2. For each group, the ratio λ_1/λ_2 increases monotonically with W_{tip}, and the impact of the central angle on the ratio λ_1/λ_2 is negligible. For nanoarcs with larger W_{mid} (70 nm), the ratios λ_1/λ_2 are smaller.

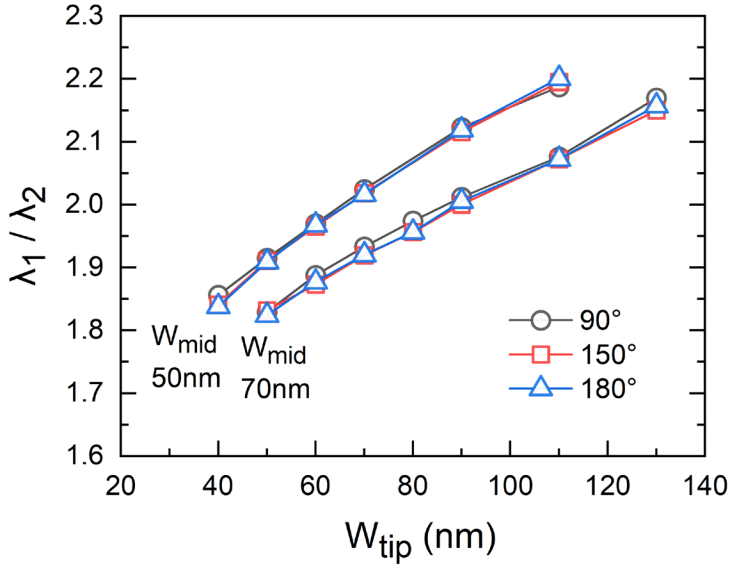

Figure 3.4.2.2 The ratio between the 1st and 2nd LSPR wavelengths (λ_1/λ_2) as a function of W_{tip}. Data were collected from nanoarcs with W_{mid} = 50 nm and W_{mid} = 70 nm (Groups S1 and S2). The nanoarcs had the same L = 600 nm and t = 55 nm, and various central angles θ = 90°, 150°, 180°.

In summary, the data in this section shows that by varying W_{tip}, the 1st LSPR of the nanoarcs can be greatly tuned in wavelength and oscillator strength, while the features of the 2nd LSPR remain almost unchanged. The ratio λ_1/λ_2 increases with W_{tip}.

3.4.3 Effect of W_{mid} on the ratio λ_1/λ_2

In this section, the effect of W_{mid} on the ratio of the 1st and 2nd LSPR wavelengths (λ_1/λ_2) of nanoarcs is investigated through spectroscopy of nanoarcs in Groups S3 and S4.

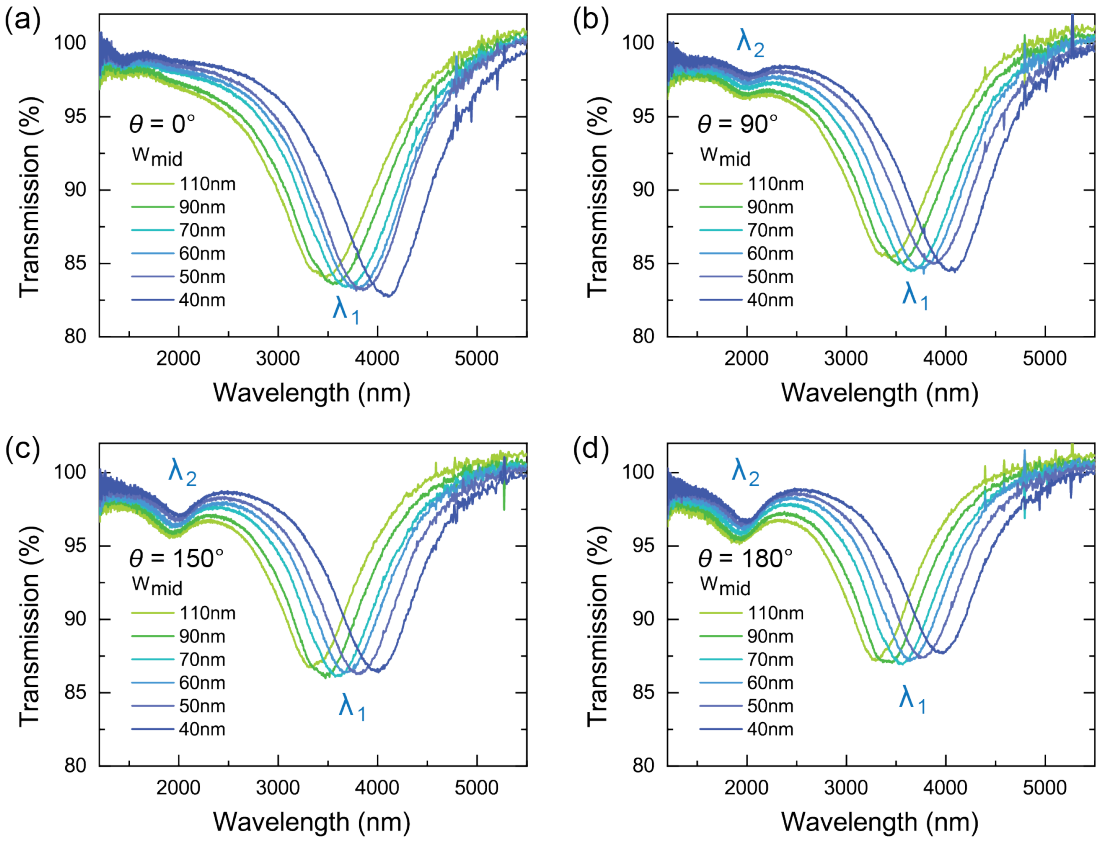

Figure 3.4.3.1 Measured FTIR transmission spectra of gold nanoarcs on silicon with with L = 600 nm, t = 55 nm, W_{tip} = 50 nm and W_{mid} = 40 – 110 nm (Group S3). The central angles of the nanoarcs are (a) θ = 0° (nanorods), (b) θ = 90°, (c) θ = 150° and (d) θ = 180°.

Figure 3.4.3.1 shows the FTIR transmission spectra measured from nanoarcs in Group S3 with W_{tip} = 50 nm and various W_{mid}. Each panel in Figure 3.4.3.1 shows that for nanoarcs with fixed L, t, θ and W_{tip}, as W_{mid} increases, both λ_1 and λ_2 blue-shift. The shift in λ_2 is an order of magnitude less than the shift in λ_1. Varying W_{mid} does not lead to significant changes in the attenuation of the 1st or 2nd LSPR mode. Taking nanoarcs with θ = 180° as an example (Figure 3.4.3.1 (d)), as W_{mid} increases from 40 nm to 110 nm, λ_1 blue-shifts by 664 nm (from 3964 nm to 3301 nm) and λ_2 blue-shifts by 78 nm (from 1988 nm to 1911 nm). As a result, the ratio λ_1/λ_2 decreases from 1.99 to 1.73. Meanwhile, the attenuation of the 1st mode increases from 12.1% to 12.7% and

the attenuation of the 2nd mode increases from 3.3% to 4.7%. The attenuation of nanoarcs with a non-uniform width profile was found to be dependent more on W_{tip} than on W_{mid}. For nanoarcs with the other three central angles, the shifts of λ_1 and λ_2 are similar to that of nanoarcs with $\theta = 180°$. With $\theta = 0°$, 90° and 150° (Figure 3.4.3.1 (a)-(c)), the shift in λ_1 caused by variations in W_{mid} is 639 nm, 646 nm, and 663 nm, respectively. The shift in λ_2 is 46 nm and 58 nm for nanoarcs with $\theta = 90°$ and 150°, respectively.

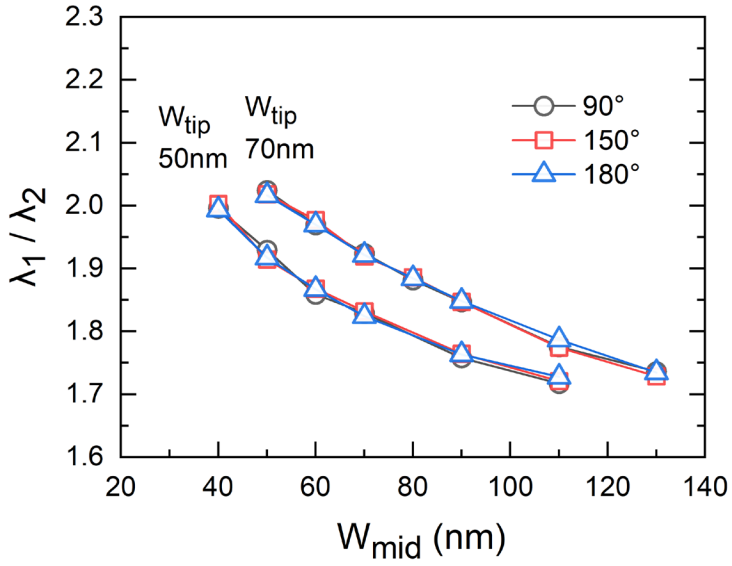

Figure 3.4.3.2 The ratio between the 1st and 2nd LSPR wavelengths (λ_1/λ_2) as a function of W_{mid}. Data were collected from nanoarcs with W_{tip} = 50 nm and W_{tip} = 70 nm (Group S3 and S4). The nanoarcs had the same L = 600 nm and t = 55 nm, and various central angles θ = 90°, 150°, and 180°.

Figure 3.4.3.2 shows the ratio λ_1/λ_2 of nanoarcs in Groups S3 and S4. In each group, the value of W_{tip} is fixed (W_{tip} = 50 nm or 70 nm) and the values of W_{mid} and the central angle are varied. For each group, the ratio λ_1/λ_2 decreases monotonically with W_{mid}. The impact of the central angle on the ratio λ_1/λ_2 is negligible. These results,

together with the data shown in Figure 3.4.2.2, show that both W_{tip} and W_{mid} have strong but opposite impact on the ratio λ_1/λ_2.

3.4.4 Effect of W_{tip} / W_{mid} on the ratio λ_1/λ_2

The data in Figure 3.4.2.2 and Figure 3.4.3.2 (for nanoarcs in Groups S1 – S4) were reexamined by plotting the ratio λ_1/λ_2 as a function of W_{tip}/W_{mid}, instead of the values of W_{tip} or W_{mid}. Since the central angle of the nanoarcs does not affect the ratio λ_1/λ_2, the data of nanoarcs with one central angle, i.e. θ = 180°, is shown in Figure 3.4.4.1 (a). This angle was selected because it could enable two strong LSPRs in nanoarcs (Figures 3.4.2.1(d) and 3.4.3.1(d)).

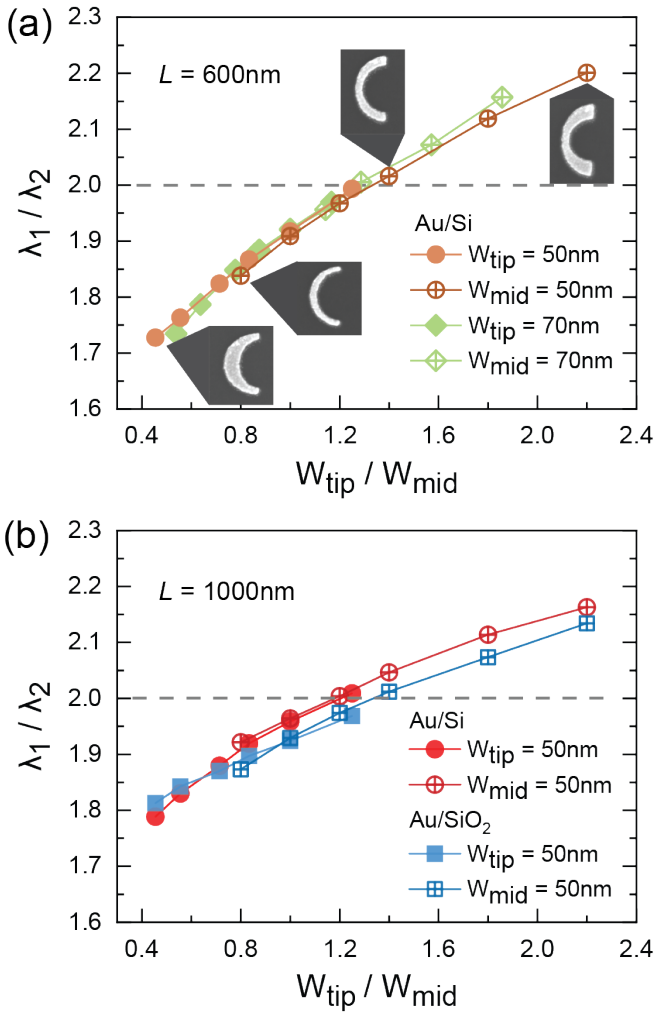

Figure 3.4.4.1 The ratio between the 1st and 2nd LSPR wavelengths (λ_1/λ_2) as a function of the ratio between W_{tip} and W_{mid}. All the data were obtained from nanoarcs described in Table 3.4.1.1 with central angle θ = 180°. (a) Data of nanoarcs in Groups S1 – S4. The 4 insets are SEM images of the nanoarcs corresponding to the indicated data points. (b) Data of nanoarcs in Group S5 – S6 and Q7 – Q8. Solid lines are a guide to the eye. Grey dash lines mark the octave interval condition.

The four sets of data shown in Figure 3.4.4.1 (a) were measured from nanoarcs with constant L, θ and t, and different width profiles. With the ratio λ_1/λ_2 plotted as a function of W_{tip}/W_{mid}, all fours sets of data overlapped, indicating that W_{tip}/W_{mid} is a dominant parameter in determining the value of λ_1/λ_2. The ratio λ_1/λ_2 increases monotonically from 1.73 to 2.20 as W_{tip}/W_{mid} is increased from 0.45 to 2.20. To

further investigate the dependence of λ_1/λ_2 on W_{tip}/W_{mid}, experiments were performed using four more groups of nanoarcs (Groups S5 – S6, Q7 – Q8 in Table 3.4.1.1) with a different L and fabricated on different substrates. The ratio λ_1/λ_2 of these nanoarcs is shown in Figure 3.4.4.1 (b) as a function of W_{tip}/W_{mid}. The trend that λ_1/λ_2 increases monotonically with W_{tip}/W_{mid} is unchanged in the data of nanoarcs with different L (L = 600 and 1000 nm) or on different substrates (Au/Si and Au/SiO_2).

For nanoarcs with L = 1000 nm (Au/Si data in Figure 3.4.4.1 (b)), the ratio λ_1/λ_2 increases monotonically from 1.79 to 2.16 as W_{tip}/W_{mid} is increased from 0.45 to 2.20. For the above mentioned sets of nanoarcs with different L on the same substrate (Au/Si), the λ_1/λ_2 values of the long nanoarcs (L = 1000 nm) are larger than the λ_1/λ_2 values of the short nanoarcs (L = 600 nm) when W_{tip}/W_{mid} is small, and the relation is reversed when W_{tip}/W_{mid} is large. The maximum difference between the ratio λ_1/λ_2 of nanoarcs with L = 600 and 1000 nm is 0.06. By changing the substrate from silicon to quartz (Au/Si and Au/SiO_2 data in Figure 3.4.4.1 (b)), the values of λ_1/λ_2 were modified by less than 0.035. These results indicate that both the length of the nanoarcs and the substrate material affect the ratio λ_1/λ_2, but their impact is less significant compare to that of the parameter W_{tip}/W_{mid}. In all the data sets discussed above, the octave interval condition (λ_1/λ_2 = 2) was achieved with W_{tip}/W_{mid} in the range of 1.20 – 1.40.

In summary, we demonstrated that the 1st and 2nd LSPR wavelengths and their interval can be broadly tuned by the design of nanoarcs with a non-uniform width profile. By adjusting the dominant parameter W_{tip}/W_{mid}, the ratio λ_1/λ_2 of the gold nanoarcs

with L = 600 – 1000 nm on silicon and quartz substrates can be tuned in the range of 1.73 – 2.20, which covers the octave interval condition.

3.5 Chapter Summary

We have investigated the effect of structural and material parameters on the ratio λ_1/λ_2 in nanoarcs with uniform and non-uniform width profiles. For nanoarcs with a uniform width profile, the effects of L_{mid}, antenna material, and substrate material on the ratio λ_1/λ_2 were studied. Among the nanoarcs that have been investigated, aluminum nanoarcs show larger values of λ_1/λ_2 than gold nanoarcs with similar dimensions, and in both cases, the ratio λ_1/λ_2 increases monotonically with L_{mid}. The substrate material has less impact on the ratio λ_1/λ_2 compared to the antenna material.

The study on a nanocrescent geometry with two sharp tips suggested that the width profile is an effective parameter for tuning the LSPR interval. To study the LSPR properties of nanoarcs with non-uniform width profiles in a systematic manner, the 2D conformal transformation described in Chapter 2 was used for transforming nanorods with non-uniform width profiles into nanoarcs ($0° \leq \theta \leq 180°$). This approach helped limit the number of geometric parameters needed for the definition of the width profile to two, W_{tip} and W_{mid}. The FTIR results showed that increasing W_{tip} led to the increase of λ_1/λ_2 while increasing W_{mid} led to the decrease of λ_1/λ_2. The ratio W_{tip}/W_{mid} was found to be a dominant parameter in determining the ratio λ_1/λ_2. By adjusting the value of W_{tip}/W_{mid} from 0.45 to 2.20, the ratio λ_1/λ_2 for gold nanoarcs on silicon with L = 600 nm increased monotonically from 1.73 to 2.20. This range can be potentially expanded if different antenna materials or L are used. The increase in

W_{tip} also led to the increase of the attenuation of the 1st LSPR mode, while increasing W_{mid} did not led to appreciable changes in the attenuation of the 1st or 2nd LSPR mode. Taken together, the work presented in chapters 2 and 3 provides a strategy for finely tuning the LSPR wavelengths and the LSPR wavelength interval in the spectra of plasmonic nanoarcs across the near- and mid-IR regimes, which allows nanoarcs to serve as versatile building blocks for various photonic technologies.

Chapter 4: Harmonics Generation in Plasmonic Nanoarcs

4.1 Introduction

Second-harmonic generation (SHG) is a nonlinear optical phenomenon in which light interacts with a nonlinear medium and generates photons with a doubled frequency [66, 67] (Figure 4.1.1). The materials that allow for this nonlinear phenomena make up the core components of important optical systems such as frequency doubling units in lasers [143]. Harmonics generation is conventionally achieved in bulk nonlinear crystals where the nonlinear conversion efficiency is dependent upon the crystal structure and the satisfaction of the phase matching conditions between the two interacting waves [66]. In recent years, plasmonic nanostructures have been investigated as a new platform for harmonic generation because the local-field enhancement gives rise to strong nonlinear interactions in subwavelength volumes, and when the interaction volume is small the phase matching conditions are no longer as important. The plasmonic metals (Au, Ag, and Al) do not show second-order nonlinearity in bulk because their lattice structures are centrosymmetric. The second harmonic (SH) emission in metallic nanoantennas is allowed by the broken symmetry at the interface between the metal and the dielectric environment and more importantly, by the shape of the nanoantenna when it is designed to be non-centrosymmetric [5, 71]. SHG in plasmonic nanostructures [5, 71, 144, 145] have been extensively explored in order to improve the conversion efficiency and address the need for various optical functionalities including optical switching [146], photodynamic therapy [147], and biosensing [148].

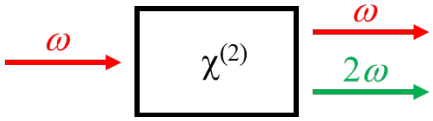

Figure 4.1.1 Diagram of second-harmonic generation.

Previous studies on SHG in U- and V-shaped plasmonic nanoantennas, and dimers and multimers with nanometer-size gaps [27, 31, 72, 73] (see Figure 4.1.2 for examples) have identified two possible approaches to enhance SHG: (i) having a strong fundamental LSPR mode of the nanoantenna in resonance with the excitation wavelength such that the conversion efficiency can be amplified by the field enhancement effect, and (ii) having the nanoantenna in resonance with the SH wavelength so that the generated nonlinear signal can be efficiently radiated to the far-field [71, 72, 149, 150]. In this context, the design of nanoantennas with two LSPRs with tunable resonance wavelengths and oscillator strengths is of great importance for studying the enhancement of SHG in plasmonic systems. Although the LSPR wavelengths can be tuned in the aforementioned nanoantennas by adjusting the dimensions of the particles, the oscillator strength of the LSPRs cannot be manipulated independently, which impedes the understanding of the role of each LSPR in enhancing the nonlinear effects. Plasmonic nanoarcs are well-suited as a platform for the study of SHG in a plasmonic system as their LSPR oscillator strengths and resonance wavelengths can be independently tuned by controlling the geometric parameters. Specifically, as described in Chapters 2 and 3, the oscillator strengths of the 1st and 2nd LSPRs in nanoarcs can be tuned by varying the arc curvature, and the resonance wavelengths can be tuned by adjusting the length and the width profile of the nanoarc.

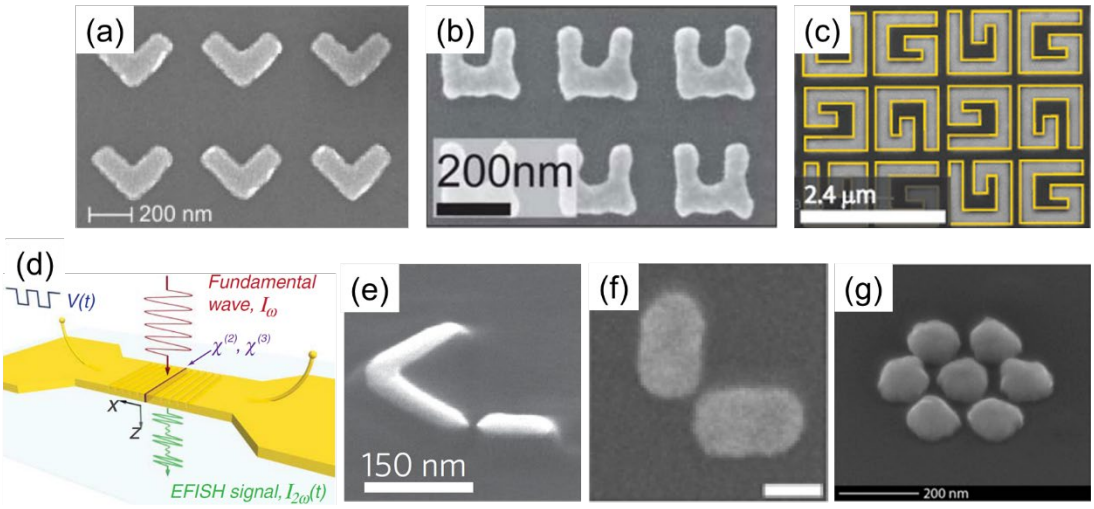

Figure 4.1.2 Examples of plasmonic nanostructures for enhancing second-harmonic generation. (a) V-shaped gold nanoantenna (adapted from Ref. [40]). (b) U-shaped gold nanoantenna (adapted from Ref. [73]). (c) G-shaped chiral gold nanoantenna (adapted from Ref. [151]). (d) Gold nanoslit and grating for electric-field-induced SHG (adapted from Ref. [152]). (e) Gold nanoantenna dimer composed of a V-shaped nanoantenna and a nanorod (adapted from Ref. [72]). (f) L-shaped gold nanoantenna dimer (adapted from Ref. [100]). (g) Silver heptamers (adapted from Ref.[138]).

In this chapter, the LSPR-mediated SHG in plasmonic nanoarcs is investigated. The experimental methods for quantifying the linear optical attenuation in the visible spectra and the SHG signal are introduced in Section 4.2. The experimental characterization of the SHG signal is detailed in Section 4.3. Section 4.4 discusses the effects of the curvature of the nanoarcs and the excitation wavelength on the enhancement of SHG.

The strongly enhanced local electromagnetic field can simultaneously boost SHG and third-harmonic generation (THG) in plasmonic nanoarcs. Since THG is not the focus of this work, the experimental characterization of the THG signal in plasmonic nanoarcs with $\theta = 0°$ (i.e. nanorods) is detailed in Appendix 8.5.

4.2 Experimental Methods

In this section, the experimental systems for linear visible/NIR-light spectroscopy, second-/third-harmonic photometry/spectroscopy, and sample preparation and characterization are introduced. Visible/NIR spectroscopy was used to identify the wavelength of the 2nd LSPR mode of the nanoarcs (around $\lambda = 800$ nm), complementing the use of FTIR spectroscopy as previously described to identify LSPRs. The nonlinear response (SHG and THG) from the nanoarcs was excited using a tunable femtosecond optical parametric oscillator and detected by a NIR photomultiplier tube.

4.2.1 Visible Spectroscopy

Figure 4.2.1.1 depicts the custom-made setup used to measure the visible/NIR transmission spectrum of the plasmonic samples. The light source was a broadband Tungsten-Halogen lamp, whose spectrum covered 360 – 2600 nm (SLS201L, Thorlabs). An optical fiber was used to deliver the light into the coaxial illumination port of the body tube (Part # 1-50487, 12X Zoom, 3 mm Fine Focus, Coax, NAVITAR) which contains a lens (lens 1), a beam splitter, and a zoom module. The light emerging from the tube was focused onto the front surface of the sample by an objective lens (50x Plan NIR, Mitutoyo). The diameter of the focused beam spot was about 30 μm, which is much smaller than the size of the nanoarc arrays (≥ 100 μm × 100 μm) but large enough to ensure that ~500 nanoarcs are illuminated. The transmitted light was filtered by a linear polarizer (LPNIRE100-B, Thorlabs) allowing through only light with polarization parallel to the orientation of the electric dipole of the 2nd LSPR mode, and was focused by lens 2 (LB1471-B, f = 50 mm, Thorlabs) into a compact spectrometer (USB4000, Ocean Optics).

The transmission spectra were obtained by taking the ratio of a background spectrum and a sample spectrum in the software *Oceanview* associated to the spectrometer. The background spectrum was collected from an area on the bare quartz substrate next to the nanoarc array. The sample spectrum was collected from an area within the nanoarc array.

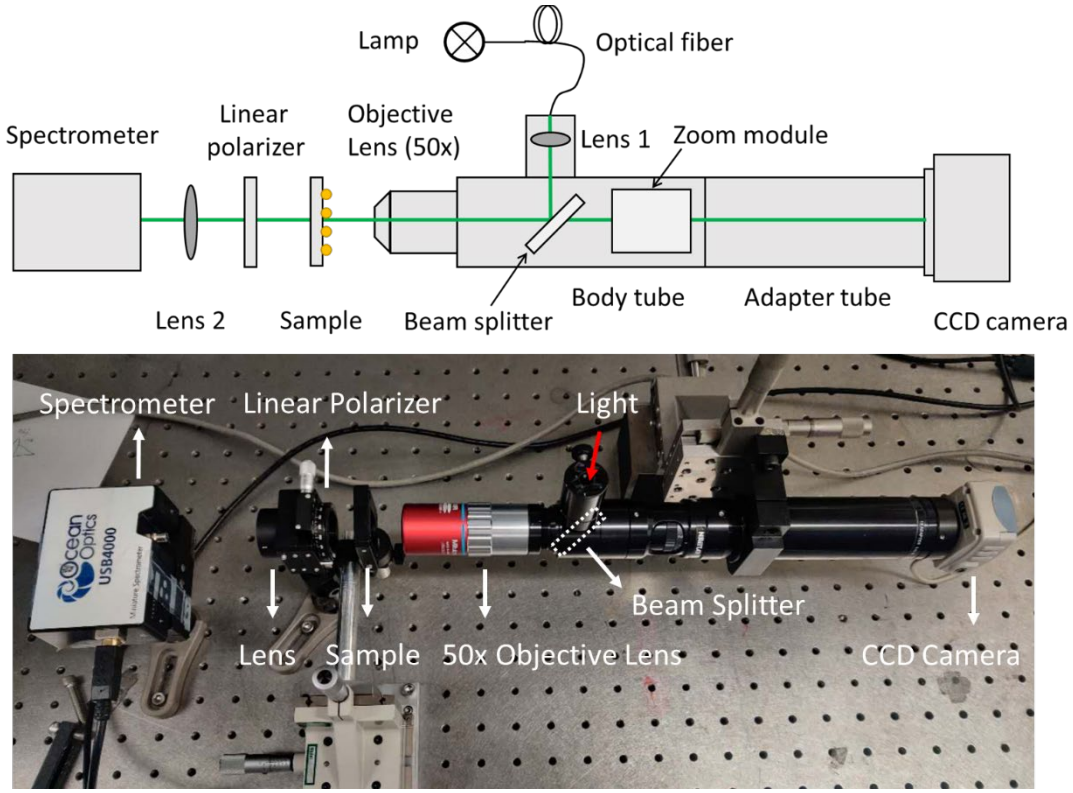

Figure 4.2.1.1 Schematic and photograph of the visible spectroscopy setup.

The illuminated region on the sample was imaged onto a CCD camera (Moticam 1000, 1.3M Pixel, Motic) placed on the remaining port of the body tube. The sample was mounted on a 3-axis-translation stage (462-XYZ-M, Newport) in order to be able to move different regions on the sample to the focal spot.

4.2.2 SHG/THG Photometry and Spectroscopy

The transmitted second-harmonic and third-harmonic signals from the nanoarc arrays were generated and collected using the setup shown in Figure 4.2.2.1. The light source was a femtosecond Ti:sapphire laser (Chameleon, repetition rate 80 MHz, pulse duration ~200 fs, and linewidth ~15 nm, Coherent Inc.) with an optical parametric oscillator (OPO) extension (Chameleon Compact OPO-VIS, wavelength tuning range 340 – 1600 nm, Coherent Inc.). The SHG and THG signals were generated from gold nanoarc arrays on quartz substrates and collected using a photomultiplier tube detector (PMT) (H5784-20, Hamamatsu).

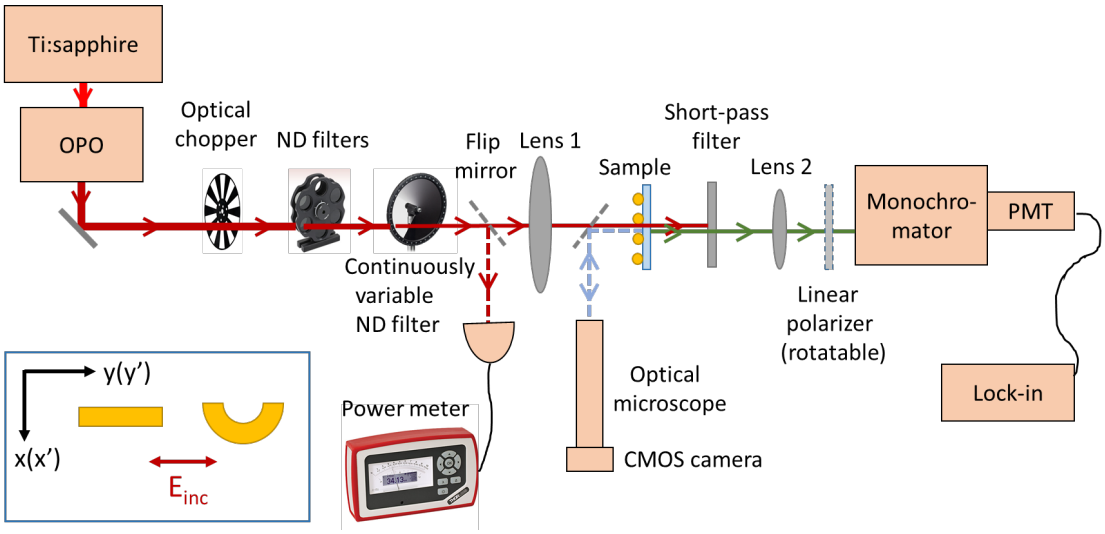

Figure 4.2.2.1 Schematic of the SHG spectroscopy setup. The inset shows the alignment of the frame of individual plasmonic nanoantennas (*x'y'*-coordinate system) with respect to the orientation of the polarization of the incident laser beam (red double-headed arrow) and the frame of the camera (*xy*-coordinate system).

The outcoming beam of the OPO was linearly polarized with the polarization direction parallel to the surface of the table (analyzed by a linear polarizer (LPNIR050, Thorlabs); not shown). The laser beam was mechanically chopped (optical chopper system: MC2000B, blade: MC1F15, Thorlabs) at a frequency of 1010 Hz, which served as the reference frequency of the lock-in amplifier for signal detection. The optical chopping

and lock-in detection ensure that the measurement is responsive only to the portion of the signal caused by the incident illumination, which reduces the effect of background noise and ambient light.

The power of the chopped light was attenuated by three neutral density (ND) filters, two of constant optical density (OD) and one of continuously variable OD. The time-averaged incident laser power was monitored by a thermal power sensor (Analog Handheld Laser Power Meter Console, sensor model S302C, Thorlabs). Because the output power of the OPO varies with the wavelength, the continuously variable neutral density filter was used to keep the incident power on the sample constant when performing excitation-wavelength dependent measurements.

The sample was illuminated by the excitation light at normal incidence. The incident laser beam (excitation light) was focused by lens 1 (f = 100 mm) into a spot with a diameter of ~50 μm. The illuminated area of the sample was imaged by a CMOS camera (EO-1312M-GL LE, Edmund Optics) mounted on an optical microscope.

Sample alignment procedure: Because the infrared excitation beam cannot be detected by the CMOS camera, the alignment between the laser spot and the sample was achieved by the use of a pinhole with a diameter of 40 ± 3 μm (P40D, Thorlabs; not shown). First, the center of the pinhole was aligned with the focal spot by monitoring the laser power transmitted through the pinhole. Then, the pinhole was imaged under the optical microscope, with its position marked in the field of view. After that, the pinhole was replaced by the sample. The marked position was then used to align the region of interest on the sample with the focused laser spot. To maximize the SHG signal, the *y'*-axis of the nanoarcs (shown in the inset of Figure 4.2.2.1) needed to be

aligned with the polarization direction of the excitation light. First, the horizontal axis of the field of view of the optical microscope was aligned parallel to the surface of the optical table. The proper alignment of each sample was achieved by imaging and adjusting the orientation of the corner markers and the alignment markers patterned on the sample.

The light transmitted through the sample was filtered by a short-pass filter (FESH 0900, Thorlabs) to block out the transmitted excitation beam, leaving only the generated light which was then focused by lens 2 (LB1471-B, f = 50 mm, Thorlabs) onto the PMT. The generated light was detected in two configurations: (i) for SHG/THG spectroscopy (to collect the spectrum of the generated light), the PMT was placed after a monochromator (HR-320, ISA Instruments), as shown in Figure 4.2.2.1; or (ii) for SHG photometry (to measure the overall SHG signal intensity), the PMT was placed after a filter (long pass FELH0700 or bandpass FBH800-40, Thorlabs; not shown). This filter was used to block out the THG signal. In both configurations, when analyzing the polarization of the SH emission, an additional linear polarizer (LPNIRE100-B, Thorlabs) was inserted in between lens 2 and the PMT.

The HR-320 monochromator was calibrated using a halogen lamp (Hg-1 Mercury Argon calibration light source, Ocean Optics) with spectral lines at 436 nm, 546 nm, 577 nm, 697 nm, 707 nm, 727 nm, 738 nm, 750 nm, 764 nm, and 772 nm. The optical grating of the monochromator, which controls the wavelength range and the resolution of the spectrum recorded by the PMT, was driven by a step motor. At every angle of the optical grating, the voltage output signal from the PMT was recorded by a lock-in amplifier (SR830, Stanford Research Systems) whose settings were kept the same in

all the experiments: integration time = 100 ms, filter slope = 18 dB/octave. A home-built Matlab program was used to control the movement of the step motor, therefore, angle of the optical grating, and record simultaneously the output of the lock-in amplifier at every movement.

The SHG/THG spectra were obtained by applying the mathematical correction to the output of the lock-in amplifier (V_{LIA})

$$I_{SHG}(\lambda) or\ I_{THG}(\lambda) = \frac{V_{LIA}(\lambda)}{\eta_{gain}\eta_{sv}(\lambda)T_{filter}(\lambda)T_{lens}(\lambda)} \qquad (4.2.2.1)$$

where η_{gain} is the PMT gain, $\eta_{sv}(\lambda)$ is the PMT sensitivity, $T_{filter}(\lambda)$ is the transmission of the short-pass filter or the product of the transmission of the short-pass filter and the linear polarizer in the case when the linear polarizer was used, and $T_{lens}(\lambda)$ is the transmission of lens 2 (AR coated). The values assigned to the correction factors, i.e., the parameters in the denominator in Eq. (4.2.2.1), are reported in Appendix 8.3.

In SHG photometry, the output of the lock-in amplifier (V_{LIA}) corresponds to an overall light intensity integrated over the linewidth of the SHG spectra. To estimate the SHG signal intensity, the values of V_{LIA} were corrected using Eq. (4.2.2.2)

$$I_{SHG} = \frac{V_{LIA}}{\eta_{gain}\bar{\eta}_{sv}\bar{T}_{filter}\bar{T}_{lens}} \qquad (4.2.2.2)$$

where η_{gain} is the PMT gain, $\bar{\eta}_{sv}$, $\bar{T}_{filter}$ and $\bar{T}_{lens}$ are the averages of the PMT sensitivity, the transmission of the short-pass filter (or the product of the transmission of the short-pass filter and the linear polarizer in the case when the linear polarizer was used), and the transmission of lens 2, respectively. The average values were calculated

using the data of each correction factor (presented in Appendix 8.3) in the range of the FWHM (8 nm, see Section 4.3.1) of the SHG signal.

In addition, η_{gain} is a function of the control voltage of the PMT which was kept constant in each set of experiments. When measuring the SHG spectra, the control voltage was 0.493±0.002 V, corresponding to a PMT gain of 16800±500; when measuring the SHG signal intensity, the control voltage was 0.464±0.002 V, corresponding to a PMT gain of 11000±330. The values are obtained from the manufacturer specifications.

4.2.3 Sample Fabrication and Characterization

The gold nanoarc arrays used in second-harmonic photometry/spectroscopy were fabricated on quartz substrates using the methods described in Section 2.4.1 – 2.4.3. Two groups of nanoarcs were used in the measurement: nanoarcs with a uniform width profile and arc dimensions of L_{mid} = 395 nm, W = 60 nm, t = 55 nm, and θ = 0° – 210°; and nanoarcs with a non-uniform with profile and arc dimensions of L = 360 nm, W_{mid} = 50 nm, W_{tip} = 70 nm ($W_{tip}/W_{mid} = 1.4$), t = 55 nm, and θ = 90 – 210°. The lengths (L_{mid} and L) were selected because the 1st LSPR wavelength of these nanoarcs were predicted to be within the OPO wavelength tuning range, according to the analyses presented in Chapters 2 and 3. The area of the nanoarc arrays was 100 μm×100 μm or 200 μm×200 μm with nanoarcs arranged in a triangular lattice. For the two arrays of nanoarcs with a uniform width profile, the lattice parameters were (a_1, a_2) = (1.2, 2.4) μm and (0.64, 1.5) μm. For the arrays of nanoarcs with a non-uniform width profile, the lattice parameters were fixed with (a_1, a_2) = (1.2, 2.4) μm to maintain a constant element density. The arrays with (a_1, a_2) = (1.2, 2.4) μm are free of inter-particle dipolar

coupling according to the analysis presented in Section 2.5.2, while the values of (a_1, a_2) = (0.64, 1.5) μm are below the threshold values of the lattice parameters therefore dipolar coupling is expected between the neighboring elements in the array. The pattern also includes corner marks (50 μm long, 15 μm wide) and alignment marks (cross shape, arm length 190 μm, arm width 5 μm) which are used to align the sample.

FTIR and visible transmission spectra were collected (using the methods described in Section 2.4.4 and Section 4.2.1, respectively) from the nanoarc arrays before and after the SHG/THG photometry/spectroscopy measurements to determine the 1st and 2nd LSPR wavelengths. The wavelengths of the LSPR peaks in each spectrum were determined using the Gaussian-Lorentz fit method described in Section 2.4.6.

Since SEM imaging is not applicable to nanostructures fabricated on quartz, AFM imaging were used to check the dimensions of the nanoarcs and the completeness of the pattern. AFM imaging was performed using the MFP-3D system (Asylum; see Section 2.4.8) with AFM probes Arrow NCR (f = 285 kHz, k = 42 N/m, NanoWorld).

SHG/THG spectroscopy was performed using the setup described in Section 4.2.2 (with the monochromator). The excitation wavelength was set to 1580 nm or swept across an IR spectral range near the 1st LSPR wavelength of the nanoarcs (1500 – 1590 nm, in steps of 10 nm). When measuring the dependence of the SHG intensity on the incident laser power, the laser power was varied from 29.6 mW to 184.5 mW. When measuring the polarization angle of the SHG signal, the incident laser power was fixed at 79.4 mW. These power values were measured without the chopper; the laser power ultimately reaching the sample during the SHG experiments was half of these values. The spectra of the generated light were collected in the range of 775 – 805 nm and 515

– 535 nm for SHG and THG spectroscopy, respectively. The peak shape parameters, including the peak center, peak intensity, and the FWHM of the SHG/THG spectra, were extracted by fitting a Gaussian function to the spectra using the method described in Section 2.4.6 (the amplitude of the Lorentzian function was set to 0).

SHG photometry was performed using the second configuration described in Section 4.2.2 (with a filter instead of the monochromator in front of the PMT). The excitation wavelength was set to 1580 nm or was swept across an IR spectral range near the 1st LSPR wavelength of the nanoarcs (1400 – 1600 nm). With fixed excitation wavelength, a bandpass filter (FBH800-40, transmits light in the range of 780 – 820 nm, Thorlabs) was placed in front of the PMT. When scanning the excitation wavelength, a longpass filter (FELH0700, Thorlabs) was used to transmit light with wavelength longer than 700 nm. When measuring the dependence of the SHG signal intensity on the incident laser power, the laser power was varied from 1.05 mW to 42.8 mW. When measuring the polarization of the SHG signal, the incident laser power was fixed at 23.9 mW. The powers were measured without the chopper; the laser power ultimately reaching the sample during the SHG experiments was half of these values.

4.3 Characterization of SHG in Plasmonic Nanoarcs

Confirming that the signal emerging from the plasmonic nanoarcs has characteristics consistent with the SHG process is an important preliminary task. The SHG signal has the following two characteristics: (i) the center wavelength of the generated light is one half of the excitation wavelength, and (ii) the power of the generated light scales quadratically with the power of the excitation light. Therefore, the characterization and

the confirmation of the generated light includes quantifying the center wavelength and the signal intensity as a function of the incident laser power.

The polarization of the SH (2ω) emission provides insights into the generation process. In prior studies of the U-shaped [27] and V-shaped [153] nanoantennas, it was observed that the polarization of SH (2ω) light was parallel to the axis of symmetry of the nanoantenna. Since the symmetry of nanoarcs, U- and V-shaped nanoantennas is the same, it is expected that the polarization of SH (2ω) light from nanoarcs is also parallel to their axis of symmetry (i.e., the *x'*-axis).

4.3.1 Central Wavelength and Peak Intensity of the Generated Light

The characterization of SHG was performed using a nanoarc array with nominal arc dimensions L_{mid} = 395 nm, W = 60 nm, t = 55 nm and central angle θ = 150°. The sample was selected out of the series of nanoarc arrays with L_{mid} = 395 and central angle θ = 0 – 180° reported on in Sections 2.3.2 and 8.2, designed to manifest the fundamental LSPR within the wavelength tuning range of the OPO, i.e. less than 1600 nm. Nanoarcs with shorter mid-arc lengths are challenging to fabricate reproducibly on quartz. The central angle of 150° was selected because it could enable two strong light-plasmon interactions in the nanoarc and because of strong emission at the SH wavelength observed in a preliminary study. The area of the array was 200 μm by 200 μm, and the lattice parameters were (a_1, a_2) = (1.2, 2.4) μm. The 1st and 2nd LSPR wavelengths of the nanoarcs before the nonlinear measurement were λ_1 = 1603 nm and λ_2 = 920 nm, respectively (the spectrum was reported in Figure 2.3.2.1 (d)).

The spectra collected in the SHG spectroscopy measurement for various incident laser powers are shown in Figure 4.3.1.1 (a). The peak intensity and FWHM extracted from

the spectra are shown in Figure 4.3.1.1 (b) and (c), respectively. As expected for SHG, the peak in the spectra of the generated light was centered at 790 nm (Figure 4.3.1.1 (a)), i.e. at one half of the excitation wavelength (1580 nm). As shown in Figure 4.3.1.1 (b), the peak intensity scales as the square of the incident power, that is, under a log-log scale, the data points matched well with a straight line with a slope of two, as expected for SHG; the least-squares regression line for log(SHG peak intensity) *vs.* log(laser power) had a slope of 2.20±0.03. The SHG signal intensity vs. incident laser power was also measured by SHG photometry, and the results (Appendix 8.4) confirm the quadratic relation. As shown in Figure 4.3.1.1(c), the FWHM values were nearly constant for all the SHG spectra with an average of 7.9 nm. The FWHM of the SHG signal is determined by the linewidth of the laser source (15 nm) and the spectral resolution of the monochromator (0.5 nm), both of which are independent of the incident power. The FWHM value was used to set the linewidth of the SHG signal (8 nm) measured by SHG photometry in Section 4.4.2.

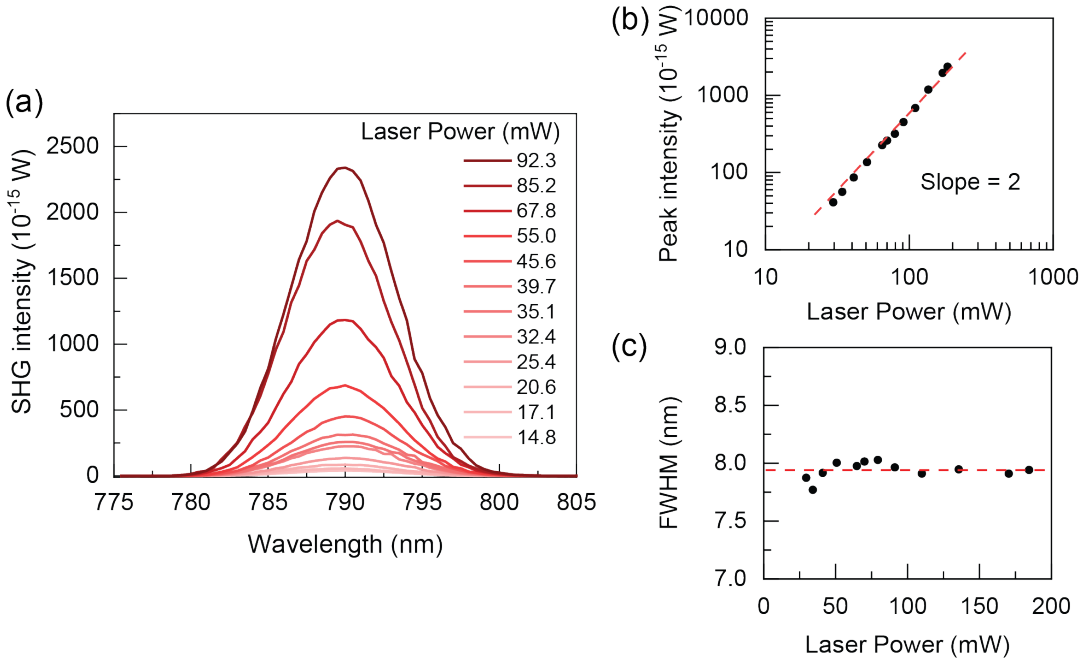

Figure 4.3.1.1 Second harmonic generation (SHG) from gold nanoarcs on a quartz substrate with L_{mid} = 395 nm, W = 60 nm, t = 55 nm and θ = 150°. (a) SHG spectra collected with different incident laser powers. (b) SHG peak intensity as a function of the incident laser power under a log-log scale. The red dash line with a slope of two is a guide to the eye. (c) FWHM of the SHG spectra as a function of incident laser power. The dash line marks the average value.

The features of the spectra of the generated light (wavelength, intensity and FWHM) strongly indicate that the detection in our experiment is sensitive and selective to the SHG process. Moreover, it was confirmed that when the bare substrate (i.e. in an area free of nanoarcs) was illuminated by the incident laser, there was no measurable SHG signal. This observation helps exclude the possibility that the measured signal was generated by the quartz substrate or any part of the optical train.

4.3.2 Polarization of the SH (2ω) light from nanoarcs

The polarization of the SH (2ω) light was investigated using the array with L_{mid} = 395 nm and θ = 150° used in the SHG central wavelength characterization (Section 4.3.1). The polarization was analyzed by rotating the analyzer (linear polarizer) following the sample (Figure 4.2.2.1) and recording the resulting SH signal as a function of the angle of the analyzer. The 0° of the analyzer was defined such that the transmission axis of the analyzer was aligned with the y'-axis of the nanoarcs, which coincide with the polarization direction of the incident light, as shown in the inset of Figure 4.3.2.1. The SHG spectra were recorded as the polarizer was manually rotated by 360° in steps of 10°.

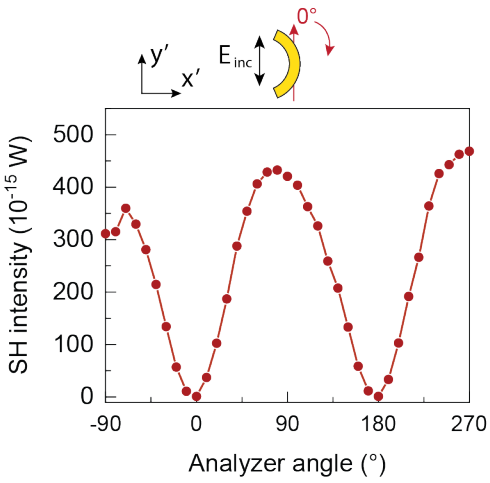

Figure 4.3.2.1 Peak intensity of the measured SHG spectra as a function of the analyzer angle. At 0°, the analyzer blocks the light polarized parallel to the *x'*-axis of the nanoarc.

In Figure 4.3.2.1, the peak intensity of the SHG light was plotted as a function of the angle of the analyzer. At 0°, the SH intensity was at its minimum, close to 0 W. As the angle of the analyzer increased, the SH intensity varied in a periodic manner and reached the maxima at 90° and at 270°. These results indicate that the SH emission is linearly polarized along the *x'*-axis of the nanoarcs, orthogonal to the polarization of the incident light. Due to the property of the linear polarizer, the SHG intensities corresponding to two analyzer angles separated by 180° were expected to be the same. However, the peak values of the SH intensity increased slightly with increasing analyzer angle (from -90° to 90° to 270°), which is suspected to have been caused by the exposure to the laser. The measurements were performed with the analyzer angle varying from -90° to 270° over a period of 8 hours. The data corresponding to larger analyzer angles were collected after longer laser exposure time and an increase in the SHG intensity was observed with time. A tentative explanation for this phenomenon is

the possible change in the morphology of the nanoarcs, caused by laser-induced annealing of the material, resulted in the increase of the SHG intensity.

In short, the data demonstrates that the SH emission from the plasmonic nanoarcs is linearly polarized with the polarization direction parallel to the *x'*-axis of the nanoarcs. This direction coincides with the electric dipole orientation associated with the 2nd LSPR mode, which is the mode closest in frequency to the SH emission.

4.4 Effect of Central Angle and Excitation Wavelength on SHG in Plasmonic Nanoarcs

In this section, the impact of two parameters, the curvature of the nanoarcs and the excitation wavelength, on the SHG intensity is investigated. The SHG efficiency in plasmonic nanoantennas depends on the enhancement of the electromagnetic field confined around the nanoantenna. The field enhancement is related to the oscillator strength of the LSPR mode [5, 27, 71]. A higher SHG efficiency is expected when the light-plasmon interactions are strong at the excitation wavelength and the SH wavelength [27]. In plasmonic nanoarcs, the oscillator strengths of the 1st and 2nd LSPRs can be tuned simultaneously in opposite manner by varying the curvature, which allows the study of the relative importance of the 1st and 2nd LSPRs in terms of SH enhancement. With the frequency interval between the two LSPRs in nanoarcs tuned to be slightly off from one octave, the light-plasmon interaction at the two LSPRs can be probed independently by varying the excitation wavelength. The analysis of the SHG efficiency under different excitation wavelengths helps further clarify the role of the 1st and 2nd LSPRs in mediating SH enhancement. With the knowledge of the impact

of the two LSPRs in SH enhancement, an optimum design and optimal illumination conditions can be identified for generating strong SH light in plasmonic nanoarcs.

The SHG measurements were carried out using nanoarcs with uniform and non-uniform width profiles. The main difference between the two types of nanoarcs is the interval between their 1st and 2nd LSPR wavelengths, which determines whether the two LSPRs can be simultaneously on-resonance with the excitation light and the SH emission light. Here, the ratio λ_1/λ_2 is closer to two for the nanoarcs with a non-uniform width profile. Nanoarcs with a non-uniform width profile were used to study the dependence of the SHG intensity on both the curvature of nanoarcs and the excitation wavelength. Nanoarcs with a uniform width profile were used to study the dependence of SHG intensity on the excitation wavelength.

4.4.1 Nanoarcs with a Non-uniform Width Profile

The nanoarcs with a non-uniform profile were designed with different central angles θ = 90 – 210°, and fixed L = 360 nm, W_{mid} = 50 nm, W_{tip} = 70 nm ($W_{tip}/W_{mid} = 1.4$), and t = 55 nm. The large central angles allow nanoarcs to support two strong plasmon resonances. The length and the width profile were selected (based on the conclusions of Chapter 3) such that the 1st LSPR wavelength (λ_1) was within the wavelength tuning range of the OPO and the ratio λ_1/λ_2 was close to two. The nanoarcs were arranged in a triangular lattice with (a_1, a_2) = (1.2, 2.4) μm, and the size of the array was 100 μm by 100 μm. The sample was imaged by AFM and the complete arrays (with no missing elements) was observed on the sample. Representative AFM images are shown in Figure 4.4.1.1 for nanoarcs with L = 360 nm, W_{mid} = 50 nm, W_{tip} = 70 nm, t = 55 nm and θ = 150°. The width (W_{mid} and W_{tip}) of the nanoarcs in the AFM images are larger

than the actual size by ~50 nm which is expected because the AFM tip has a typical radius of ~10 nm.

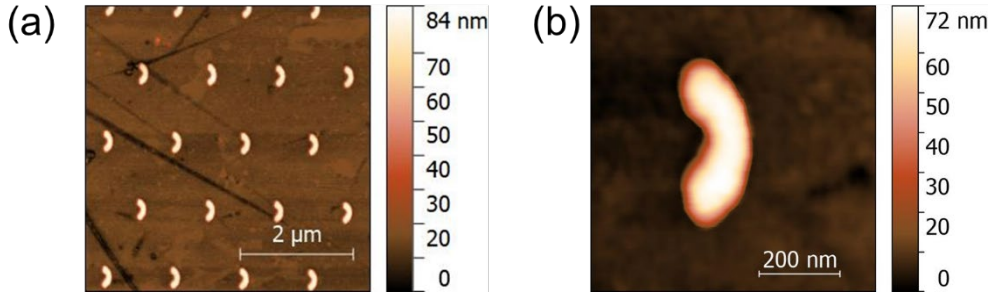

Figure 4.4.1.1 AFM images of the nanoarcs on quartz substrate with L = 360 nm, W_{mid} = 50 nm, W_{tip} = 70 nm, t = 55 nm and θ = 150°. (a) An array of nanoarcs. (b) A single nanoarc.

FTIR and visible transmission spectra of the nanoarcs were collected before and after the SHG spectroscopy measurements. These measurements revealed that the LSPR wavelengths (λ_1 and λ_2) had blue-shifted due to the laser exposure: λ_1 blue-shifted by 57 – 78 nm, and λ_2 blue-shifted by 31 – 49 nm. Therefore, to better represent the LSPR properties of nanoarcs during the SH emission process, the FTIR and visible transmission spectra measured after the SHG measurement (Figure 4.4.1.2) were used in the analysis. The LSPR wavelengths and the attenuation (1-T) of the two LSPR modes varied with the central angle. As θ increased from 90° to 210°, λ_1 blue-shifted from 1488 nm to 1416 nm, and the attenuation of the 1st mode decreased from 19.2% to 16.0%; λ_2 varied in the range of 785 – 795 nm and the attenuation of the 2nd mode increased from 4.6% to 12.0%. The ratio λ_1/λ_2 varied with central angle from 1.87 to 1.78, i.e., it was always smaller than 2. Figure 4.4.1.2 illustrates the near-fulfilment of the double resonance condition: The range of the excitation wavelength (1500 – 1590 nm) used in the SHG measurement and the corresponding SH wavelength range (750 – 795 nm) are highlighted in Figure 4.4.1.2 as shaded areas. All the excitation

wavelengths were on the long wavelength side with respect to the 1st LSPR peak, while the SH wavelengths were close to the center of the 2nd LSPR peak.

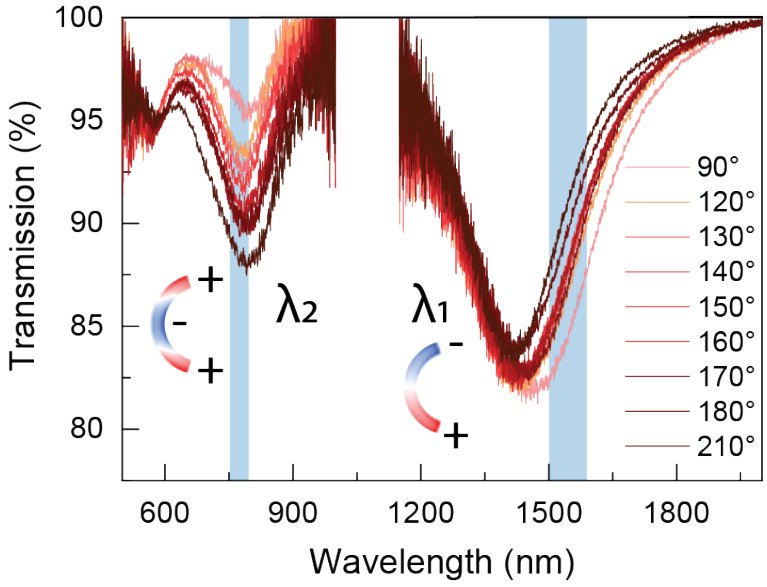

Figure 4.4.1.2 The visible transmission spectra and FTIR transmission spectra measured after the SHG measurements for gold nanoarcs on quartz with L = 360 nm, W_{mid} = 50 nm, W_{tip} = 70 nm, t = 55 nm, and central angle θ = 90 – 210°. The shaded areas in the near-IR and visible show the range of the SHG excitation wavelength and the range of the SH wavelength, respectively.

The SHG spectra were collected from nanoarcs with different central angles using the SHG spectroscopy setup described in Section 4.2.2 (with the monochromator). The average power of the chopped excitation light was fixed at 30.0±0.2 mW. During SHG measurement, it was observed that the SHG intensity first increased upon laser illumination and then reached a steady-state value which was invariant afterwards. All the SHG results reported in this work were the steady-state values.

Figure 4.4.1.3 shows the SHG spectra measured from nanoarcs with eight different central angles, and each panel present the spectra collected with various excitation wavelengths. For each nanoarc array, the SHG intensity varied with the excitation wavelength, and the specific wavelength at which the SHG intensity reached the

maximum value was denoted as the optimum excitation wavelength $\lambda_{Opt.Ex.}$. For nanoarcs with different central angles, $\lambda_{Opt.Ex.}$ were at different wavelengths and the maximum SHG intensity varied. Figure 4.4.1.4 plots the optimal excitation wavelength $\lambda_{Opt.Ex.}$ in comparison to the 1st LSPR wavelength λ_1 and twice the value of the 2nd LSPR wavelength $2\lambda_2$.

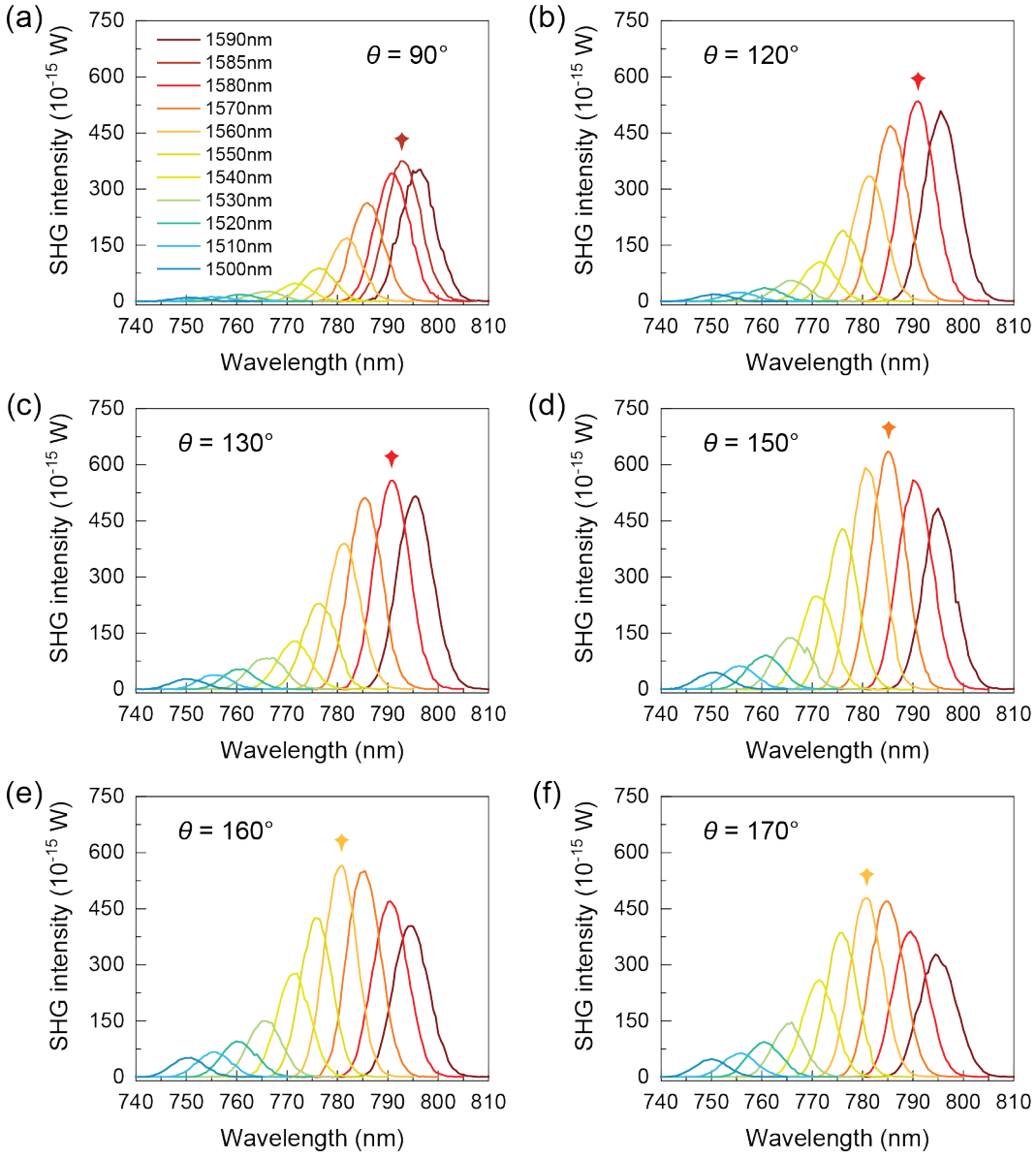

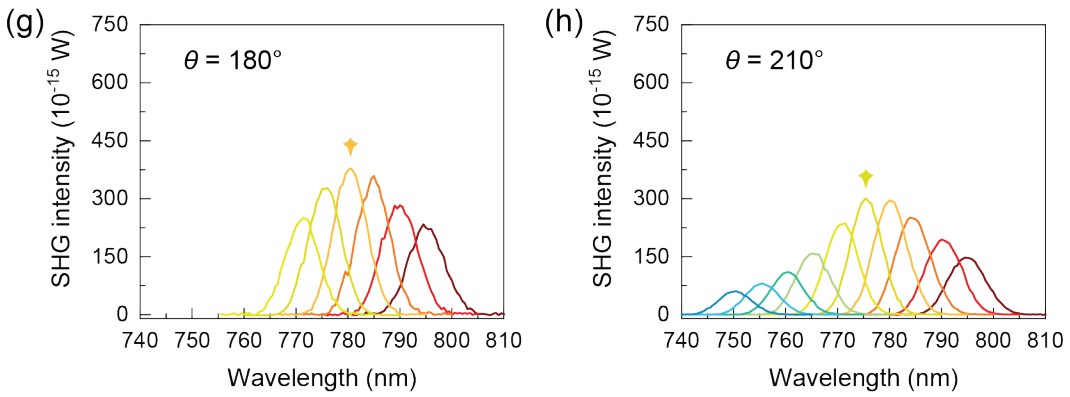

Figure 4.4.1.3 The SHG spectra of nanoarcs with central angles θ = 90° – 210°. The nanoarcs are made of gold on quartz with dimensions of L = 360 nm, W_{mid} = 50 nm, W_{tip} = 70 nm, t = 55 nm. The center of the excitation wavelength is in the range of 1500 – 1590 nm, therefore, the center of the SHG spectra is in 750 – 795 nm. The arrows indicate the spectra with the maximum SHG intensity in each panel.

Since λ_1/λ_2 is smaller than 2, the wavelengths associated with SHG (the excitation and SH wavelengths) cannot match both LSPR wavelengths (λ_1 and λ_2) simultaneously. It is expected that $\lambda_{Opt.Ex.}$ will match better with one of two LSPR wavelengths. Figure 4.4.1.4 shows that for all the central angles investigated, $\lambda_{Opt.Ex.}$ is red-shifted compared to λ_1, and $\lambda_{Opt.Ex.}$ matches or is slightly blue-shifted with respect to $2\lambda_2$. These results indicate that the light-plasmon interaction at the 2nd LSPR is more important for SH enhancement in this group of nanoarcs. Since the FWHM of the 1st LSPR peak is more than 300 nm, $\lambda_{Opt.Ex.}$ falls within the linewidth of the 1st LSPR peak (Figure 4.4.1.2), meaning that the 1st LSPR mode could still play a role in enhancing SHG. When the central angle is large (e.g. θ = 210°), the oscillator strength of the 2nd LSPR mode is (relatively) strong while that of the 1st LSPR mode is (relatively) weak, which makes the 1st LSPR mode a limiting factor in SH enhancement. Therefore, as the central angle increases, $\lambda_{Opt.Ex.}$ shifts closer to λ_1 to

achieve a stronger light-plasmon interaction. This trend is apparent in Figure 4.4.1.4 as a decrease in $\lambda_{Opt.Ex.}$ with the central angle.

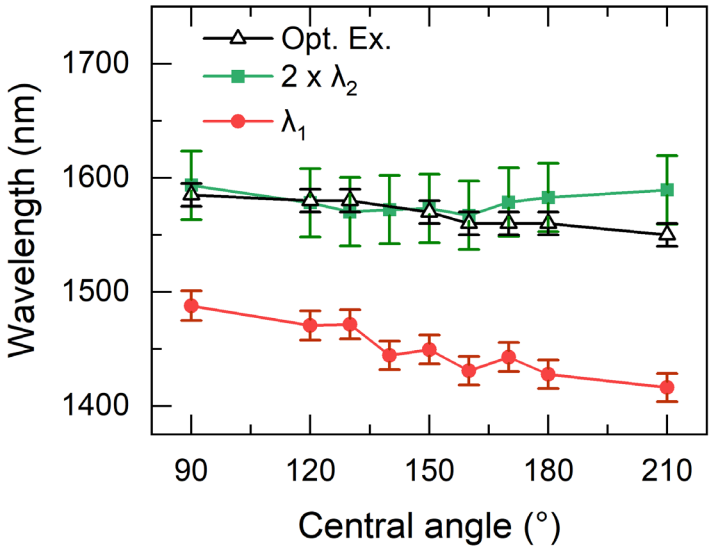

Figure 4.4.1.4 The 1st LSPR wavelength (λ_1) and twice the 2nd LSPR wavelength ($2\lambda_2$) of the nanoarcs after the SHG measurement, and the optimum excitation wavelength $\lambda_{Opt.Ex.}$. For λ_1, the error bar ± 0.87% is determined using the statistical deviation of the resonance wavelengths of nanostructures fabricated on quartz. For $2\lambda_2$, the error bar ±30 nm is estimated based on twice of the variation of λ_2 obtained from different visible spectra measured from the same array. For the optimum excitation wavelength, the error bar ± 10 nm is determined based on the step size in the SHG measurement.

To investigate the impact of the central angle on the SHG intensity, the maximum SHG intensities obtained from nanoarcs with different central angles were compared. The maximum SHG intensity was defined as the peak intensity of the spectra excited by $\lambda_{Opt.Ex.}$. The spectra indicated by the arrows in Figure 4.4.1.3 were replotted in Figure 4.4.1.5 (a), and the corresponding maximum SHG intensities were summarized in Figure 4.4.1.5 (b). The maximum SHG intensity increased as θ increased from 90° to 150° and then decreased as θ further increased to 210°. This trend can be qualitatively correlated to the dependence of the oscillator strength of the two LSPRs on central angle. Specifically, as the central angle increases, the oscillator strength at the

excitation wavelength (near the 1st LSPR mode) decreases, while that at the SH wavelength (near the 2nd LSPR mode) increases (Figure 4.4.1.2). Consequently, the two light-plasmon interactions that give rise to the enhancement of SHG are affected by the central angle in opposite manner, resulting in the non-monotonic variation in the maximum SHG intensity.

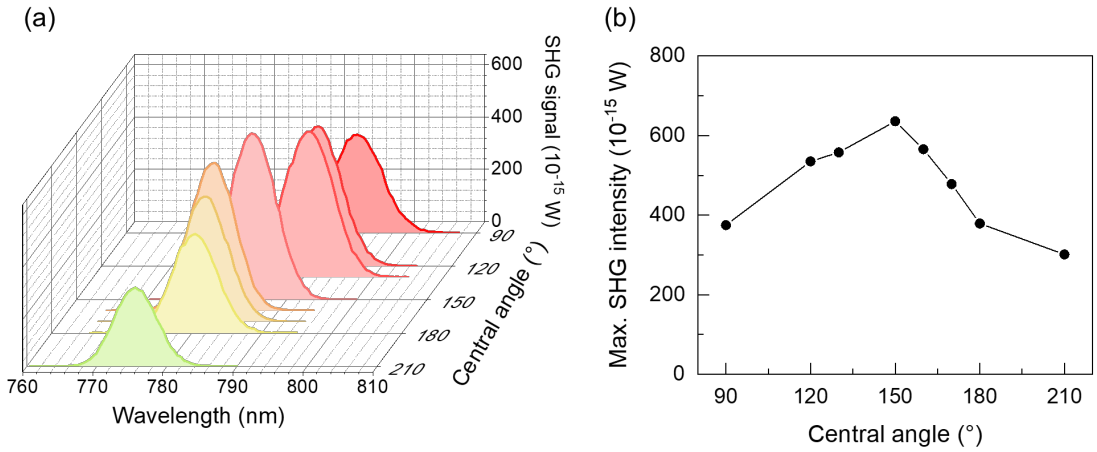

Figure 4.4.1.5 (a) SHG spectra of nanoarcs with different central angles generated by the optimal excitation wavelengths. (b)The maximum SHG intensity as a function of the central angle of the nanoarc.

In summary, we have investigated the impact of two important factors, the excitation wavelength and the central angle of the nanoarcs, on the intensity of SH signal generated with plasmonic nanoarcs with a non-uniform width profile. With λ_1/λ_2 in the range of 1.78 – 1.87, the optimum excitation wavelength ($\lambda_{Opt.Ex.}$) was found to be close to $2\lambda_2$. The maximum SHG efficiency was achieved in nanoarcs with a central angle of 150°.

4.4.2 Nanoarcs with a Uniform Width Profile

Nanoarcs with a uniform width profile were also used in the study of the effect of the excitation wavelength on the SHG intensity. Two arrays with a triangular lattice were

composed of the same nanoarcs with arc dimensions L_{mid} = 395 nm, W = 50 nm, θ = 150° and t = 55 nm. The lattice parameters of the two arrays were (a_1, a_2) = (1.2, 2.4) μm and (0.64, 1.5) μm, i.e. the planar density of nanoarcs in the high-density array was 3 times that of the low-density array. The nanoarcs in the high-density array are expected to couple to neighboring elements.

FTIR and visible transmission spectra of the nanoarcs were collected before and after the SHG photometry measurements to identify the 1st and 2nd LSPR wavelengths. After the laser exposure, the 1st LSPR wavelength of the low-density array blue-shifted by ~20 nm, and that of the high-density array blue-shifted by ~10 nm. The 2nd LSPR wavelength of the two arrays blue-shifted by ~20 nm. The extinction ($-\log_{10}T$) spectra of the two arrays measured after the SHG photometry measurements are shown in Figure 4.4.2.1 (black and grey curves). The low-density array has its 1st LSPR at a wavelength of 1580 nm, while in the high-density array the coupling between adjacent nanoarcs blue-shifts the peak to 1515 nm. The 2nd LSPR wavelength of 900 nm does not shift as a result of the change in density and the coupling between nanoarcs. Consequently, the ratio λ_1/λ_2 is 1.72 and 1.64 for the low- and high-density arrays, respectively, smaller than the ratio λ_1/λ_2 of nanoarcs with L = 360 nm and $W_{tip}/W_{mid} = 1.4$ reported in Section 4.4.1. In terms of the intensity, the higher element density increases the extinction of the 1st and 2nd LSPR mode by a factor of 3.3 – 4.

SHG photometry was performed on both arrays using the setup described in Section 4.2.2 with the PMT placed after a long-pass filter. The excitation wavelength was swept across 1400 – 1600 nm, and the power of the excitation light was fixed at 9.0±0.1 mW.

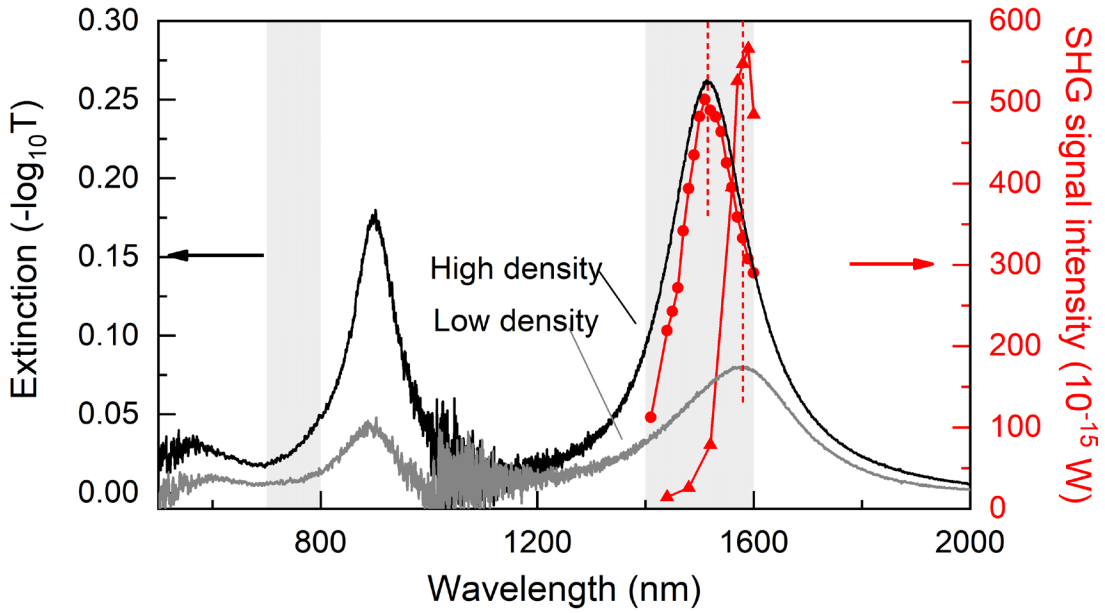

Figure 4.4.2.1 The extinction spectra (black and gray lines) and the SHG signal intensity (red spot and triangles) of gold nanoarcs (L_{mid} = 395 nm, W = 60 nm, θ = 150° and t = 55 nm) in arrays with low and high densities. The two dash lines mark λ_1 of the two arrays at 1515 nm and 1580 nm. The shaded areas in the near-IR and visible show the range of the SHG excitation wavelength and the range of the SH wavelength, respectively.

Due to the small ratio λ_1/λ_2, the SHG excitation wavelength and SH emission wavelength cannot match the two plasmon resonances simultaneously, i.e., when one of the LSPR is on-resonance, the other one will be completely out-of-resonance. In the SHG photometry measurement, the excitation wavelength overlapped with the 1st LSPR wavelength while the emitted SH light was completely out-of-resonance with respect to the 2nd LSPR. Figure 4.4.2.1 shows that the optimal excitation wavelengths $\lambda_{Opt.Ex.}$ are at 1590±10 nm and 1510±10 nm for the low- and high-density array, respectively, which match the extinction peak of the 1st LSPR modes in both cases. Another SHG spectroscopy measurement on the low-density array (data not shown) demonstrated that a longer excitation wavelength of 1800 nm, which is close to $2\lambda_2$, generate weaker SHG light compared to that with a excitation wavelength of 1550 nm

or 1600 nm. Therefore, for the two arrays studied here, it is more important to excite the light-plasmon interaction at the 1st LSPR than the 2nd LSPR in order to enhance the SHG signal. This trend is different from that shown in Figure 4.4.4 where $\lambda_{Opt.Ex.}$ was near $2\lambda_2$. The difference in the two sets of data suggests that the relative importance of the coupling to the 1st and 2nd LSPRs in enhancing SHG signal is related to the ratio λ_1/λ_2. When the ratio λ_1/λ_2 is close to 2 (examples in Section 4.4.1), the coupling of the emitted SH light to the 2nd LSPR is of more importance; while with λ_1/λ_2 much smaller than 2 (examples in this section), the coupling of the excitation light to the 1st mode is more important. Interestingly, the SHG signal intensity did not correlate with the element density: the array with a three-fold higher density of nanoarcs generated an even weaker SHG signal. The reasons could be (i) the coupling between nanoarcs enhances a competing relaxation pathway, and (ii) the smaller ratio λ_1/λ_2 diminishes the coupling of the emitted SH light to the 2nd LSPR mode.

In summary, we have investigated the impact of the excitation wavelength on the intensity of SH signal generated with plasmonic nanoarcs with a uniform width profile arranged in low- and high-density arrays with λ_1/λ_2 values of 1.72 and 1.64, respectively. The optimum excitation wavelength ($\lambda_{Opt.Ex.}$) was found to be close to λ_1. The SHG efficiency is even lower in the high-density array where the nanoarcs are coupled than in the low-density array where the nanoarcs are not coupled.

4.5 Chapter Summary

SHG signal was measured from gold nanoarc arrays on quartz substrates. The SH emission from nanoarcs is linearly polarized along the direction of the electric dipole

of the 2nd LSPR mode. The dependence of the maximum SHG efficiency on the excitation wavelength and the curvature (central angle) of the nanoarcs was investigated. With the 1st and 2nd LSPR wavelengths (λ_1 and λ_2) at approximately fixed positions and the ratio λ_1/λ_2 in the range of 1.78 – 1.87, both the excitation wavelength and the SH wavelength fell within the spectral linewidths of the 1st and 2nd LSPR modes, respectively. In this case, the SHG intensity was observed to be strongest when the excitation wavelength matched twice the 2nd LSPR wavelength ($2\lambda_2$), and the optimum excitation wavelength slightly shifted towards λ_1 as the central angle increased. When the ratio λ_1/λ_2 was 1.64 and 1.72, the two LSPR modes could not couple to the excitation and the SH emission light simultaneously, in which case the optimum excitation wavelength tracked the 1st LSPR wavelength (λ_1). These results indicate that the two LSPRs play an important role in enhancing the nonlinear interaction, and the relative importance of the light-plasmon interactions at the two LSPRs in enhancing SHG signal varies with the interval between the two LSPR modes. In addition, since the curvature of the nanoarcs affects the oscillator strengths of the two LSPRs, the SHG efficiency varies with the curvature. The maximum SHG efficiency was found in nanoarcs with θ = 150° when the ratio λ_1/λ_2 was close to 2 (1.78 – 1.87). In the prior studies of SHG in U-shaped antennas measured with various excitation wavelengths [29, 154], the optimum excitation wavelength was found to be geometry-dependent and it either matched with λ_1 or was longer than λ_1 but shorter than $2\,\lambda_2$ (for nanostructures with $\lambda_1/\lambda_2 < 2$). In those studies, the individual contributions of the 1st and 2nd LSPRs in enhancing SHG were not clear due to the lack of capability of tuning the two LSRP wavelengths and oscillator strengths

independently. This challenge was overcome in plasmonic nanoarcs, and consequently, the studies on nanoarcs can identify the role of the 1st and the 2nd LSPRs in SH enhancement. The results of this chapter provide insight into plasmon-mediated enhancement of SHG in plasmonic nanoantennas and for optimizing a plasmonic structure to a specific application.

Chapter 5: Surface Enhanced Infrared Absorption with Plasmonic Nanoarcs

5.1 Introduction

When localized surface plasmon resonances are excited in plasmonic nanoantennas, a strongly enhanced electromagnetic field is generated in a subwavelength volume around the plasmonic nanoantennas [155]. The intense electromagnetic field enables strong interactions between the surface plasmons, and the vibrational modes of molecules found in the close vicinity of the nanoantennas. [1, 75, 156] These interactions lead to enhanced light absorption/scattering by the molecules, which forms the basis of surface-enhanced infrared absorption spectroscopy (SEIRA) [75] and surface-enhanced Raman scattering spectroscopy (SERS) [157]. These novel techniques make it possible to realize ultra-sensitive chemical sensing. [1, 157] The SEIRA effect has been explored with various nanoantenna shapes (Figure 5.1.1), including nanorods [80, 85, 86, 158], nanocrosses [159], split-ring resonators [160, 161], nanoslits [82, 162, 163], and plasmonic multimers [164, 165]. For most of the nanoantennas designed for SEIRA, only the fundamental LSPR mode with the strongest attenuation is utilized to enhance the signal of molecular vibrations, and all the higher order LSPR modes are ignored because of their weak interaction with light, making the benefit of SEIRA not fully exploited. In previous work, a dual-band plasmonic nanocross antenna has been reported to simultaneously enhance the signals of two molecular vibrational modes (Figure 5.1.1 (c)). [159] However, the two LSPRs of the nanocross were tuned by varying the antenna arm lengths and the LSPR

wavelengths are hard to predict without a significant amount of numerical simulations. Moreover, the plasmonic nanocrosses are densely packed and there could be dipolar coupling between adjacent elements, which poses additional complications in predicting the LSPR frequencies and interpreting the signal enhancement.

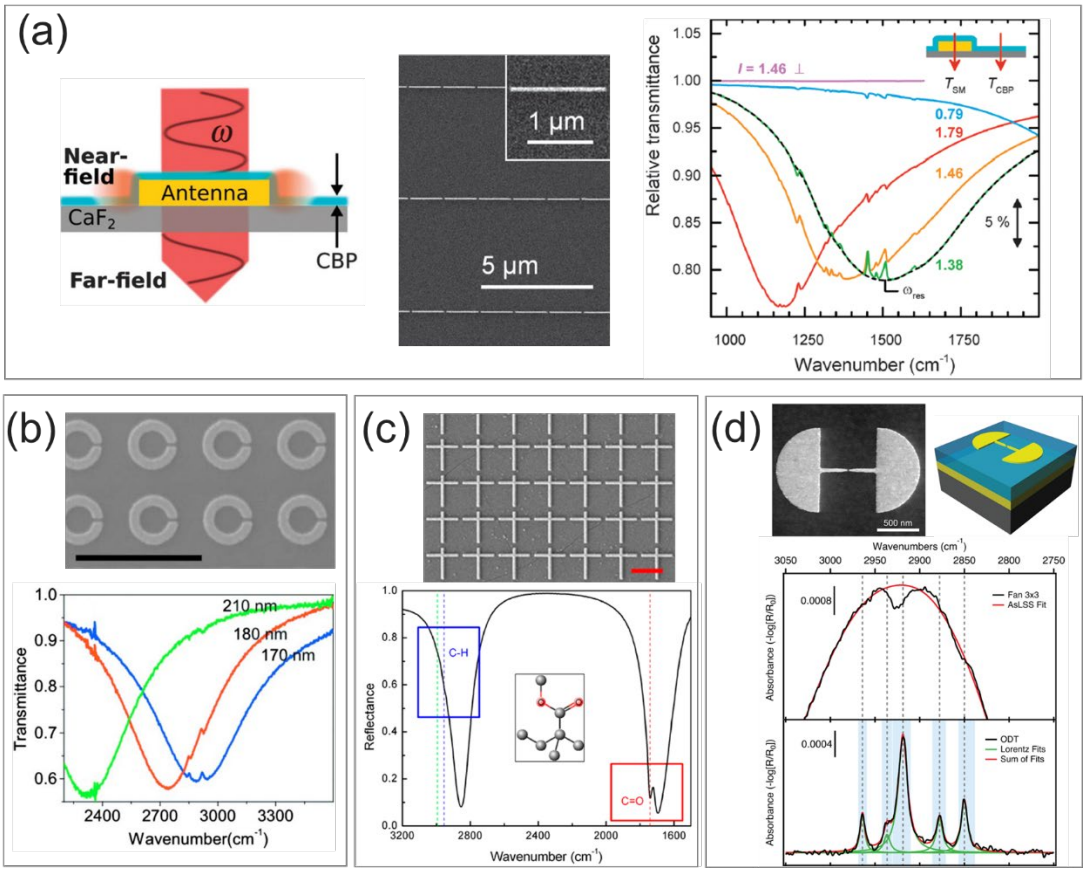

Figure 5.1.1 Schematics, SEM images and transmission/reflectance/extinction spectra of selected plasmonic nanoantennas used for SEIRA. (a) Gold nanorods covered with a layer of 4,4′-bis(N-carbazolyl)-1,1′-biphenyl (CBP) on a CaF_2 substrate. Adapted from Ref. [86]. (b) Gold split-ring resonators covered with a monolayer of 1-octadecanthiol (ODT) on an indium tin oxide coated quartz substrate. Adapted from Ref. [160]. (c) Gold nanocross antenna covered with a thin PMMA film. The nanoantenna is placed on top of a 3-layer substrate composed of a MgF_2 spacer, a thin Ag film and a silicon substrate. Adapted from Ref. [159]. (d) Fan-shaped gold nanoantenna dimer covered with a monolayer of octadecanethiol (ODT). The nanoantenna is placed on top of a 3-layer substrate composed of a SiO_2 spacer, a thin Ag film and a silicon substrate. Adapted from Ref. [82].

Here we report a study of SEIRA in plasmonic nanoarcs, with the goal of determining the enhancement effect of different order LSPR modes. As presented in Chapter 2, plasmonic nanoarcs with a uniform width can support two strong LSPRs whose resonance wavelengths can be tuned predictably in the near- and mid-IR regime. A series of nanoarcs with two tunable LSPRs is ideal for multiband SEIRA. We perform FTIR transmission spectroscopy of plasmonic nanoarcs to determine the enhancement of the signal of molecular vibrations of three analytes: polymethyl methacrylate (PMMA), native oxide of silicon (SiO_2), and 4-aminothiophenol (4-ATP). The analytes are attached to the nanoarcs by depositing the metallic nanoarcs on top of a thin analyte film or by a self-assembly process. The LSPRs of the nanoarcs are tuned in an IR-region across the vibrational fingerprint of each analyte. The enhanced signal of molecular vibrations are characterized by quantifying the SEIRA signal extracted from the FTIR spectrum. The studies with PMMA and SiO_2 in Sections 5.3 and 5.4, respectively, focus on understanding the line shape of the SEIRA signal. In Section 5.5, 4-ATP is used to compare the SEIRA effect by the 1st and 2nd LSPRs of nanoarcs and by nanoarcs patterned in arrays with different element densities.

5.2 Method of SEIRA signal quantification

The SEIRA signal is an enhanced vibrational mode signal which is induced by the coupling between a broadband plasmon resonance and narrow-band molecular vibration excitation. This section introduces the methods for extracting the SEIRA signal from the FTIR spectra and quantifying the intensity of the SEIRA signal.

The SEIRA signal is revealed in the transmission spectrum as a change in the attenuation of the LSPR peak around the spectral region of the vibrational bands [1, 86,

166] (see Figure 5.1.1 for examples). To extract the SEIRA signal, the attenuation corresponding to the LSPR peak of nanoarcs without molecules needs to be excluded from the spectrum (Figure 5.1.1 (a) and (d)). This is achieved here by creating a baseline that approximates the hypothetical LSPR peak and subtracting the baseline from the spectrum.

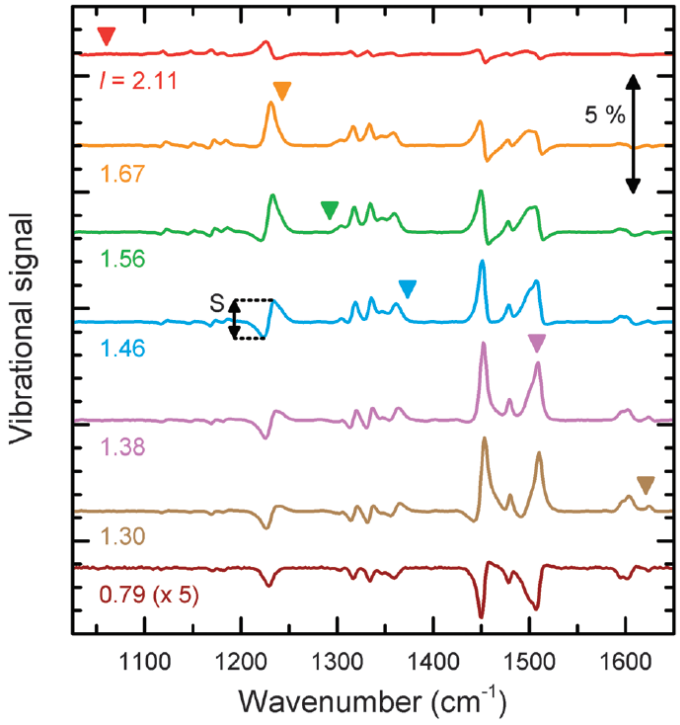

Figure 5.2.1 The SEIRA spectra of a thin film of 4,4′-bis(N-carbazolyl)-1,1′-biphenyl (CBP). The triangles mark the LSPR peak positions. Adapted from Ref. [86].

The SEIRA signal typically shows an asymmetric spectral line shape, and the line shape varies as the frequency of the LSPR mode (ω_{res}) is tuned across the molecular vibrational mode (ω_{vib}) (see the example in Figure 5.2.1). According to Fano's theory [166], this characteristic asymmetric line shape is described by the Fano-function

$$f_{FANO}(\varepsilon) = \frac{(q+\varepsilon)^2}{1+\varepsilon^2} \quad (5.2.1)$$

where q is the asymmetry factor and ε is a function of frequency,

$$\varepsilon = \frac{2(\omega - \omega_{vib})}{\Gamma} \quad (5.2.2)$$

where ω is the frequency, ω_{vib} and Γ are the vibrational frequency and the spectral linewidth of the molecular vibrational mode.

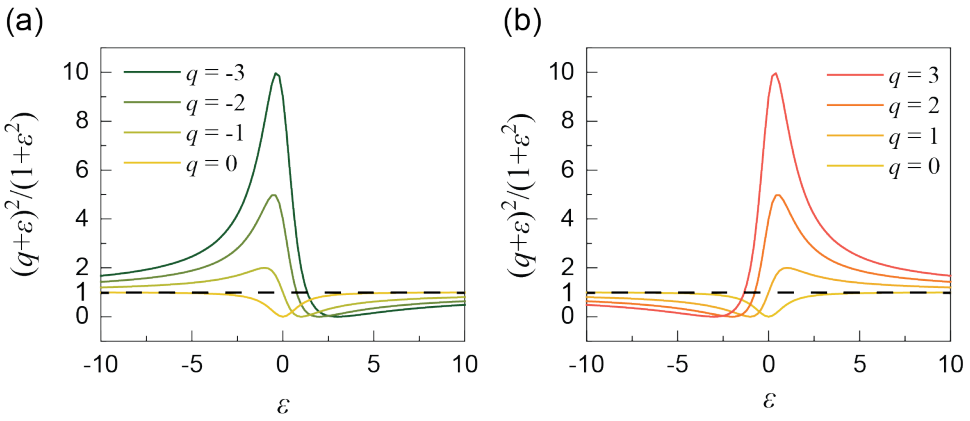

Figure 5.2.2 The line shapes of the Fano resonance with different values of q. (a) $q \leq 0$. (b) $q \geq 0$.

The line shape of the Fano-function with selected q values is shown in Figure 5.2.2. The curves in panel (a) and panel (b) with the same absolute q values are symmetric with respect to $\varepsilon = 0$. The Fano function describes the asymmetric line shape, but it has two features that do not agree well with the features of the SEIRA signal: (i) The Fano function converges to $f_{FANO}(\varepsilon) = 1$ instead of 0 when $|\varepsilon|$ approaches infinity. (ii) The amplitude of the function, i.e. the difference between the maximum and the minimum of the peak, is q^2+1. Pucci [86] et. al. demonstrated the SEIRA line shape to be well-described by the modified Fano-function

$$f(\omega) = \frac{S}{q^2+1}\left(\frac{(2(\omega - \omega_{vib}) + q\Gamma)^2}{4(\omega - \omega_{vib})^2 + \Gamma^2} - 1\right) \quad (5.2.3)$$

where S is an amplitude. The modified function converges to $f(\varepsilon) = 0$ when $|\varepsilon|$ approaches infinity. The amplitude S corresponds to the amplitude of the SEIRA signal.

The method we used to quantify of the SEIRA signal includes 4 steps:

(1) Measuring the FTIR transmission spectrum $T_{FTIR}(\omega)$ of nanoarcs with molecules attached;

(2) Using the Gaussian-Lorentzian fit described in Section 2.4.6 or a 5th degree polynomial function (following the same fitting procedure described in Section 2.5.1) to fit a baseline $T_{baseline}(\omega)$ to the transmission spectra in a range containing the molecular signal and to determine the LSPR frequency ω_{res};

(3) Extracting the SEIRA spectrum from the experimental spectrum $T_{SEIRA}(\omega) = T_{baseline}(\omega) - T_{FTIR}(\omega)$; and

(4) Fitting the modified Fano-function $f(\omega)$ to the SEIRA spectrum using a built-in function of Matlab, "*lsqcurvefit*", to obtain the line shape parameters *S*, q, and Γ of the SEIRA signal.

5.3 Coupling between LSPR and a Molecular Vibrational Mode of PMMA

We investigated the SEIRA signal of polymethyl methacrylate (PMMA) enhanced by nanoarcs with different L_{mid} through spectroscopic studies. PMMA is a photoresist used in e-beam lithography (EBL) processes. Ideally, it would be fully removed by a photoresist stripper before completion of the fabrication. In practice, however, the PMMA film may not completely dissolve, leaving a small amount of residue on the sample surface. As such, when the plasmon resonances are excited in nanoantennas fabricated by EBL, the strong electromagnetic field around the nanoantennas interacts with the molecular vibrations of PMMA and boost the vibrational mode signal. PMMA is used here as a standard material for investigating the interaction between plasmonic nanoarcs and the molecules in their immediate vicinity since PMMA is a widely used

polymer, it is easy to apply on a surface, and its IR and SEIRA spectra have been documented. Previous studies have demonstrated that the vibrational mode of PMMA at 1734 cm^{-1}, associated to the C=O symmetrical stretch [167], can be enhanced by plasmonic nanorods, nanocrosses, and nano-grooves [80, 159, 168]. Here, we study the enhancement of this vibrational mode signal using a series of plasmonic nanoarcs with different L_{mid}.

The gold nanoarcs arrays were fabricated on a diamond substrate (~5 mm × 5 mm × 1 mm, WD Lab Grown Diamonds) using the same methods for fabricating nanostructures on quartz described in Section 2.4.1 – 2.4.3. Diamond substrates were chosen because diamond is transparent in the spectral range near the vibrational mode of PMMA at 1734 cm^{-1}. In order to tune the 1st LSPR frequency of the nanoarcs across the vibrational frequency of PMMA, the nanoarcs were design with L_{mid} in the range of 900 – 1600 nm, and the other geometric parameters were fixed (width W = 50 nm, thickness t = 55 nm and central angle $\theta = 90°$). These L_{mid} values were selected based on the conclusions from Section 2.5.4 that the 1st LSRP wavelength (inversely proportional to the LSPR frequency) of nanoarcs increases linearly with L_{mid}, and the slope is determined by the refractive index of the substrate (Eq. (2.5.4.2)). When estimating the LSPR wavelength, the refractive index of diamond was obtained from Ref. [169], and the intercept of the linear trend was set to 0. Each array was 100 μm by 100 μm in size and the nanoarcs were arranged in a triangular lattice with a constant metal coverage rate of R_m = 1.88%. The constant R_m across the arrays ensured that the same amount of PMMA was attached to the illuminated nanoarcs, even though the number of illuminated nanoarcs

may vary. This allows for a direct comparison of the magnitude of the signal enhancement through the SEIRA effect in nanoarcs with different L_{mid}.

FTIR transmission spectra were collected from the nanoarc arrays using the methods described in Section 2.4.4. In the FTIR measurement, the background spectrum was obtained from a spot on the bare diamond substrate next to the nanoarc arrays. With the assumption that the PMMA residue is distributed uniformly on the substrate and on the arrays, the unenhanced signal of PMMA, i.e. signal of PMMA on the substrate, is cancelled out in the transmission spectra. The LSPR wavelengths were determined using the Gaussian-Lorentzian fit described in Section 2.4.6. The SEIRA signal was quantified using the method described in Section 5.2, with the use of a 5^{th} degree polynomial in Step (2). For creating the baseline, the spectral data in the range of 1500 – 1700 cm^{-1} and 1760 – 1850 cm^{-1} used in the fitting. The data in the range of 1700 – 1760 cm^{-1} were affected by the molecular vibrations, therefore, they were not considered. The Fano-function was fitted to the SEIRA spectra in the range of 1680 – 1780 cm^{-1}.

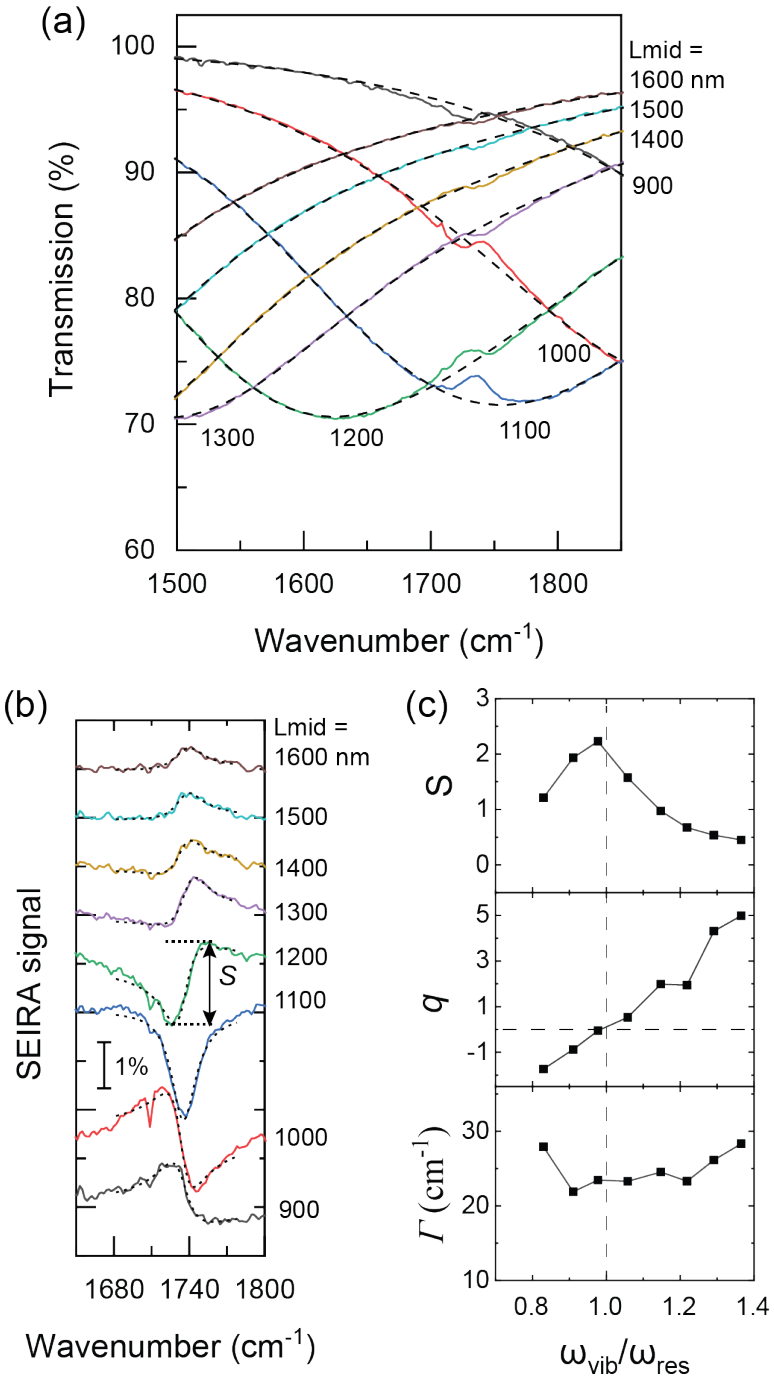

Figure 5.3.1 (a) FTIR transmission spectra of gold nanoarcs with different L_{mid} (900 – 1600 nm) on a diamond substrate. Black dash lines represent fitted baselines. (b) SEIRA spectra (solid curves) of the seven nanoarc arrays shown in (a). The spectra are shifted vertically for clarity. The signal amplitude S is the peak-to-peak value as labelled in the figure. The modified Fano-function, Eq. 5.2.3, was fitted to the SEIRA spectra and the peak shape parameters obtained from the fitting curves (dashed lines in (b)) are shown in (c) as a function of the frequency ratio $\omega_{vib} / \omega_{res}$.

Figure 5.3.1 (a) shows the FTIR transmission spectra of nanoarcs with different L_{mid} (solid lines) and the corresponding baselines (dash lines). The 1st LSPR peak of the nanoarcs spectrally overlaps with the vibrational band of PMMA at 1734 cm^{-1}. The extracted SEIRA spectra are shown in Figure 5.3.1 (b) (solid curves) together with the best fits to the modified Fano-function of Eq. 5.2.3 (dash lines). In Figure 5.3.1 (c), the line shape parameters of the Fano-function, including the signal amplitude *S*, the asymmetry factor q and the linewidth Γ, are plotted as a function of the ratio between the molecular vibrational mode frequency and the LSPR frequency $\omega_{vib}/\omega_{res}$. The amplitude *S* increases as the plasmon resonance frequency approaches the molecular vibrational frequency. The asymmetry factor q increases monotonically with the frequency ratio. When $\omega_{vib}/\omega_{res}$ is close to 1, the value of q approaches 0, which corresponds to a symmetric Fano line shape. According to Fano's theory [86, 166], q = 0 corresponds to the maximum coupling between the plasmon mode and the molecular vibration, therefore the enhancement of the vibrational signal should be greatest. This is consistent with the observation that the maximum of *S* appears at $\omega_{vib}/\omega_{res}$ around 1. In addition, Fano's theory suggests that large $|q|$ values correspond to weak coupling, thus the corresponding signal amplitude *S* is expected to be small, which is also observed in Figure 5.3.1 (c). The linewidth Γ of the vibrational mode does not show a dependence on the frequency ratio $\omega_{vib}/\omega_{res}$, indicating that SEIRA analysis is a proper approach for measuring the linewidth of molecular vibrations without needing a large quantity of sample.

In summary, the SEIRA effect on the vibrational mode of PMMA at 1734 cm^{-1} was investigated with nanoarcs whose 1st LSPR frequency was tuned across the vibrational

mode frequency. The signal amplitude of the SEIRA spectra is maximized when the plasmon frequency approximately matches the vibrational mode frequency.

5.4 Coupling between LSPR and Phonons of SiO_2

In this section, the coupling of the 1st LSPR mode of nanoarcs and the phonons of the thin native oxide layer on silicon is investigated. Silicon substrate typically has a few-nanometer-thick native oxide layer on its surface [170]. This layer can be removed by buffered oxide etch (BOE) solution, but it can grow back in a few hours if the substrate is exposed to air. The presence of this stable oxide layer allows for the study of the phonons and vibrational modes in SiO_2 film. According to the literature [1, 85], the phonon modes of SiO_2 include the surface phonon polariton (SPhP) mode at the air-silica interface with ω_{SPhP} = 1191cm^{-1} (8396 nm), the interface phonon polariton (IPhP) mode at the silica-silicon interface with ω_{IPhP} = 1094 cm^{-1} (9141 nm), and the longitudinal optical (LO) mode with ω_{LO} =1247 cm^{-1} (8019 nm). Previous studies on gold nanorods [85] and split-ring resonators [161] have demonstrate that, when the LSPR mode of a gold nanoantenna spectrally overlaps with the phonon modes of a thin SiO_2 film, a strong interaction between the surface plasmons and the phonons will occur, leading to the emergence of the phonon (vibration)-induced transparency in the spectra.

To study the evolution of the transparency window, we fabricated gold nanoarcs with different L_{mid} on a silicon substrate with a native silicon oxide layer. The thickness of the native oxide layer was 11+/-0.8 nm, as determined by ellipsometry. The L_{mid} of the nanoarcs were varied in the range of 350 nm to 2240 nm such that the 1st LSPR frequency was tuned from 750 cm^{-1} to 4300 cm^{-1}, a frequency range that includes the

phonon/vibrational modes of SiO_2. The other geometric parameters of the nanoarcs were fixed: width W = 150 nm, thickness t = 55 nm and central angle θ = 90°. The arrays of the nanoarcs had a square lattice and the lattice parameters a_1 and a_2 ($a_1 = a_2$) were selected to achieve a constant metal coverage rate R_m = 2.7%. FTIR transmission spectra were collected from the nanoarc arrays using the methods described in Section 2.4.4.

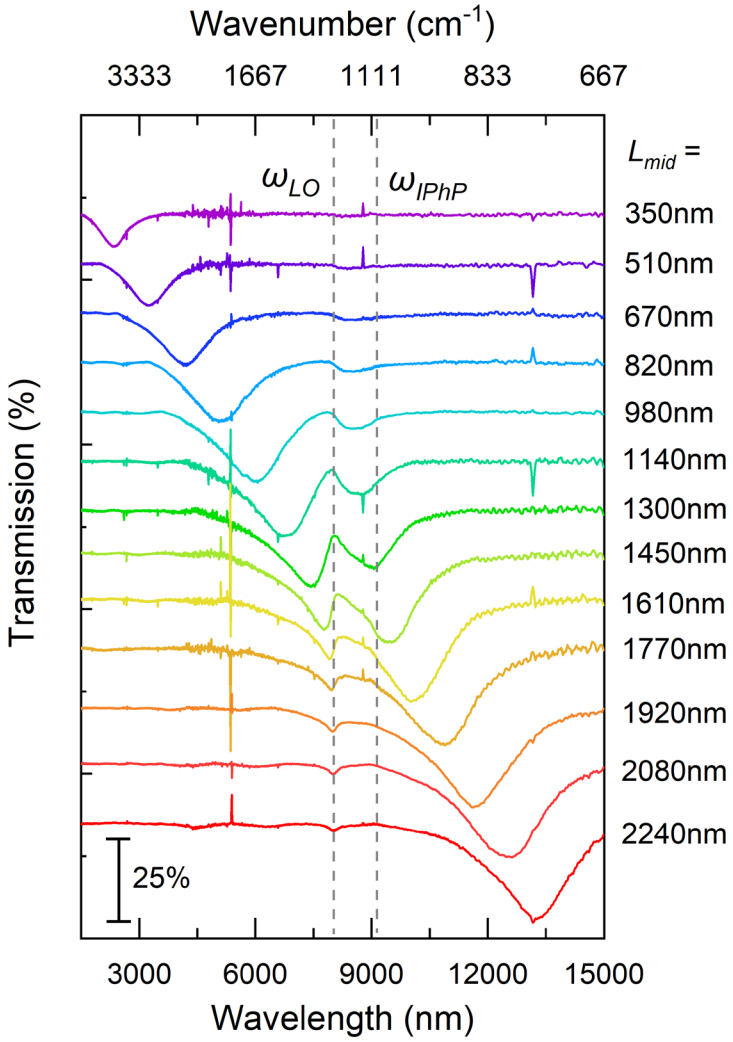

Figure 5.4.1 Transmission spectra of gold nanoarcs on a silicon substrate with L_{mid} = 350 – 2240 nm, W = 150nm and t = 55 nm. The spectra are shifted vertically for clarity. Dash lines mark the positions of the LO mode at ω_{LO} = 1247 cm^{-1} and the interface phonon polariton mode at ω_{IPhP} = 1094 cm^{-1}.

The FTIR transmission spectra of the nanoarc arrays are shown in Figure 5.4.1.When $L_{mid} \leq 510$ nm, the LSPR frequency is much higher than that of the LO mode, and the attenuation (1-T) by SiO_2 reduces the transmission by no more than 0.4%. As L_{mid} increases from 510 nm to 980 nm, the LSPR frequency approaches the LO frequency, and the attenuation by SiO_2 is enhanced to 5.3% by an off-resonance interaction with the surface plasmons. Further increasing L_{mid} from 1140 nm to 1770 nm leads to an apparent reduction of plasmon attenuation (also known as the transparency window [158, 171]), due to the spectral overlap between the LSPR mode and the two phonon modes. Neubrech et.al. attributed this phenomenon to the cancellation of the electric field in the out-of-plane (z) direction. [85] Within the spectral range bounded by the two phonon frequencies, the z-component of the electric fields confined in the SiO_2 layer and on top of the plasmonic nanoantenna have a phase difference of π and cancel each other out, resulting in a coupled mode with low attenuation. This phenomenon is of great importance as it shows that the phonon modes of ultrathin films can be detected through the coupling to surface plasmon modes. In this example, the transparency window may have a 14.5% transmission difference peak-to-valley, compared to the 0.4% transmission difference for the unenhanced SiO_2 film. The SEIRA effect could be applied in surface sensing applications such as monitoring phase transitions in an ultrathin film.

Interestingly, as the plasmon resonance is tuned to even lower frequencies with L_{mid} increasing from 1920 nm to 2240 nm, the LO mode continues to be observed with an enhanced amplitude in the spectra, indicating that the phonon modes and plasmon modes were hybridized even though the plasmon modes was strongly detuned.

In short, when the LSPR mode is detuned from the phonon modes, the coupling between the two is weak. When the LSPR mode approaches the phonon modes in frequency, the coupling between the two becomes stronger and the spectral line shape of the coupled mode varies. When the frequency of the LSPR mode matches that of the phonon modes, the coupling induces a transparency window in the LSPR-dominated spectra.

5.5 Comparative Study of SEIRA by the 1st and the 2nd LSPRs of Plasmonic Nanoarcs

The SEIRA effects by the 1st and the 2nd LSPRs of plasmonic nanoarcs were compared through spectroscopic studies. The thiol molecule, 4-aminothiolphenol (4-ATP), was used in this study as the analyte, because it adsorbs to the surface of gold and forms a self-assembled monolayer [172, 173]. Previous studies have shown that the vibrational modes of 4-ATP at 1490 cm^{-1} and 1590 cm^{-1}, which are assigned to the νCC + δCH, and νCC vibrations, respectively [174, 175], could be detected by surface enhanced spectroscopy. [172, 176] These two vibrational modes are used here as the fingerprint of 4-ATP.

5.5.1 The Design of the Nanoarc Arrays for SEIRA

Five groups of nanoarc arrays were used in the study of the enhancement of the vibrational mode signal at 1490 cm^{-1}, as listed in Table 5.5.1.1. Within each group, the nanoarc arrays have the same metal coverage rate R_m, while the arrays consist of nanoarcs with different L_{mid}. Different groups correspond to different R_m values or different ranges of L_{mid}. The values of L_{mid} were selected to tune the frequency of the 1st or 2nd LSPR (m = 1 or 2) of the nanoarcs across the vibrational frequency of 4-ATP,

based on the analyses for gold nanoarcs on silicon substrates in Section 2.5.4. The constant R_m in each group of nanoarcs ensured that the same number of 4-ATP molecules were attached to the illuminated nanoarcs, even though the number of illuminated nanoarcs may vary. This allows for a direct comparison of the magnitude of the signal enhancement through the SEIRA effect in nanoarcs with different L_{mid}. Different R_m corresponds to different element densities, in other words, different number of molecules that are illuminated by the incident light. Also, arrays with different R_m have distinct lattice parameters which result in different strengths of dipolar coupling between neighboring nanoarcs.

Table 5.5.1.1 Geometric parameters and the metal coverage rates of the 5 groups of nanoarc arrays

Group	Arc Dimensions*	R_m
m1R$_m$2.2	***L*380 – *L*1270** *W*50*t*55*θ*90	2.2%
m1R$_m$4.4	***L*380 – *L*1270** *W*50*t*55*θ*90	4.4%
m2R$_m$1.1	***L*1830 – *L*2570** *W*50*t*55*θ*90	1.1%
m2R$_m$2.2	***L*1830 – *L*2570** *W*50*t*55*θ*90	2.2%
m2R$_m$4.4	***L*1830 – *L*2570** *W*50*t*55*θ*90	4.4%

* L: mid-arc length of nanoarc, W: width, t: thickness, unit: nm. θ: central angle, unit: °.

The nanoarcs were patterned into triangular lattices with lattice parameters (a_1, a_2) as shown in Figure 5.5.1.1 (a). Examples of nanoarcs in the 5 groups are shown in Figure 5.5.1.1 (b) – (f). Three R_m values were used in this study: 1.1%, 2.2% and 4.4%. For arrays composed of the same nanoarc with different R_m, the ratio a_1/a_2 was fixed. With larger R_m the nanoarcs become coupled since one or more lattice parameters (a_1, a_2) or distance parameters (d_1, d_2, d_3) fell below the corresponding threshold value. The

dipolar coupling shifts the LSPRs to higher frequencies (Section 2.5.3). With the lattice parameters used in these designs the shift was expected to be less than 200 cm^{-1}. As a result, the LSPR frequencies of the nanoarcs still overlapped with the fingerprint region of 4-ATP.

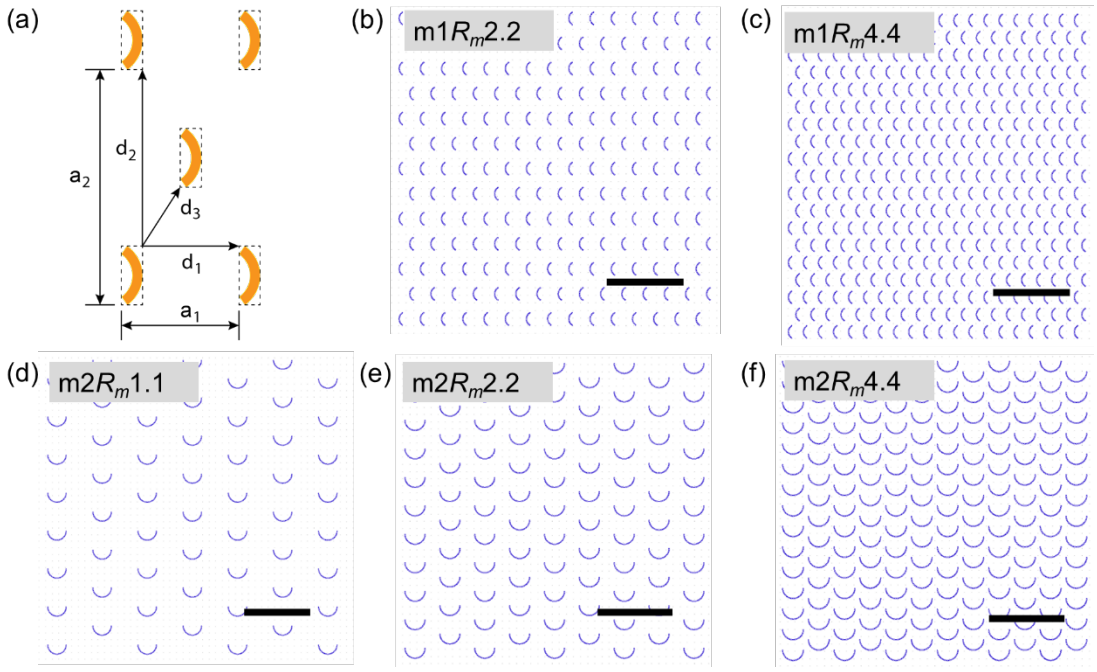

Figure 5.5.1.1 The design of nanoarcs in triangular lattices with different metal coverage rates R_m. (a) The definitions of the lattice parameters (a_1, a_2) and the distance parameters (d_1, d_2, d_3). (b, c) CAD pattern of nanoarc arrays with R_m = 2.2% and 4.4%, and L_{mid} = 1000 nm, W = 50 nm and θ = 90°. (d – f) CAD pattern of nanoarc arrays with R_m = 1.1%, 2.2% and 4.4%, respectively, and L_{mid} = 2210 nm, W = 50 nm and θ = 90°. Scale bar is 5 μm.

5.5.2 Methods of Sample Cleaning, Molecule Adsorption, and Characterization

The gold nanoarc arrays were fabricated on silicon substrates using the methods described in Section 2.4.1 – 2.4.3. After the fabrication process, the samples were cleaned to remove the residual photoresists such that the 4-ATP molecules could attach to the gold surface. In this section, the methods of sample cleaning, 4-ATP molecule adsorption and characterization are introduced.

As demonstrated in Section 5.3, the lift-off process could not completely remove the PMMA film used as EBL resist. A preliminary experiment has shown that the PMMA residue could prevent thiol molecules from attaching to the nanoarcs. To remove the PMMA residue, the samples were cleaned by oxygen plasma (Branson 3000 Barrel Resist Stripper). The sample was exposed to oxygen plasma with a gas pressure of 1 Torr and a power of 100 W in the "forward" mode for 1min. The exposure to oxygen plasma also facilitates the growth of an oxide on the silicon substrate. A thick oxide layer will strongly reduce the optical transmission at the phonon bands of SiO_2 (1100 – 1250 cm^{-1}) as discussed in Section 5.4, which is not ideal for this study. Therefore, the silicon oxide layer on the sample was etched by soaking in buffered oxide etchant (BOE 6:1, consisting of a 6:1 volume ratio of 40% ammonium fluoride to 49% hydrofluoric acid, both in aqueous solutions) for 30s. The sample was then rinsed repeatedly with DI water until the sample surface appeared to be hydrophobic. After that, the sample was dried under a flow of nitrogen.

The 4-ATP molecule adsorption was done by soaking the sample in a 50 mM solution of 4-ATP (97%, Sigma-Aldrich) in ethanol for ~12 hours. Subsequently, the sample was cleaned by soaking in DI water, and was dried in air.

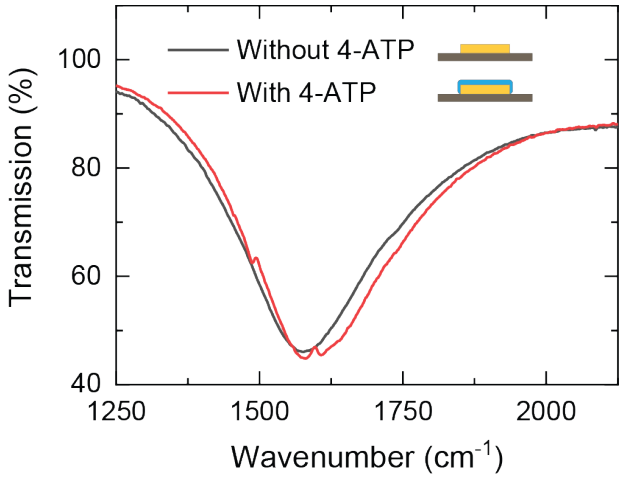

Figure 5.5.2.1 FTIR transmission spectra of gold nanoarcs with and without 4-ATP. The dimensions of the nanoarcs are L_{mid} = 2120 nm, W = 50 nm, t = 55 nm, θ = 180° and R_m = 4.4%.

Polarization-dependent FTIR transmission spectra were collected from the nanoarc arrays using the methods described in Section 2.4.4. When investigating the SEIRA effect by the 1st LSPR (Section 5.5.3) or 2nd LSPR (Section 5.5.4), the incident light was linearly polarized along the *y'*-axis or *x'*-axis of the nanoarcs, respectively. As an example, Figure 5.5.2.1 shows two spectra of nanoarcs with and without 4-ATP. The spectra were collected from two substrates with the same gold nanoarc pattern. Both substrates were cleaned by oxygen plasma and etched by BOE. The spectrum of nanoarcs with 4-ATP shows enhanced vibrational peaks around 1492 cm^{-1} and 1590 cm^{-1}, and the LSPR peak is blue-shifted compared to the peak in the spectrum of nanoarcs without 4-ATP.

The wavelengths of the LSPR peaks were determined using the Gaussian-Lorentzian fit described in Section 2.4.6. The SEIRA spectra were extracted from the FTIR spectra. The modified Fano-function was fitted to the SEIRA spectra in the range of 1480 – 1500 cm^{-1}, in order to model the SEIRA signal corresponding to the νCC + δCH combination band. The line shape parameters (S, q, and Γ) of the modified Fano-

function were quantified using the method described in Section 5.2, with the use of the Gaussian-Lorentzian fit in Step (2).

5.5.3 SEIRA effect of the 1st LSPR mode

The enhancement of the vibrational mode of 4-ATP by the 1st LSPR of plasmonic nanoarcs was investigated using nanoarcs in Groups m1R_m2.2 and m1R_m4.4.

The upper panel of Figure 5.5.3.1 shows the FTIR spectrum and the molecular structure of 4-ATP. The lower panel shows the FTIR spectra of nanoarcs with a monolayer of 4-ATP. As planned, the 1st LSPR frequencies of the nanoarcs bracket the frequencies of the vibrational bands of 4-ATP. When the nanoarc LSPR is detuned from the vibrational mode (for nanoarcs with L_{mid} = 380 nm), the signal of the vibrational modes is below the detection limit. When the LSPR peak overlaps with the vibrational mode bands, the signal of the vibration modes at 1492 cm^{-1} and 1590 cm^{-1} are enhanced. The calculated baselines of the LSPR peaks are indicated in the lower panel of Figure 5.5.3.1 by the dash lines.

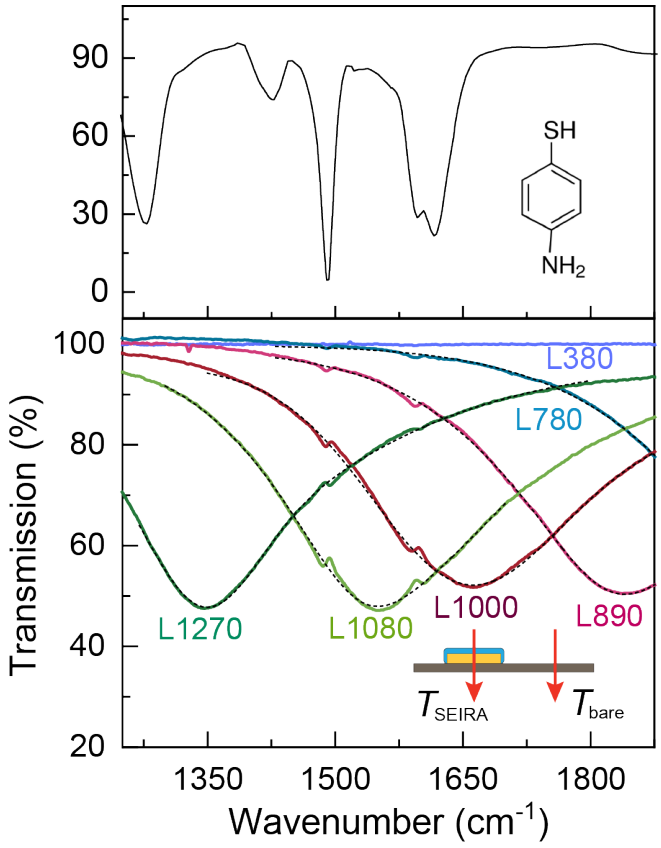

Figure 5.5.3.1 Upper panel: FTIR transmission spectra and structure of 4-ATP (Data from Sigma-Aldrich database [177]). Lower panel: FTIR transmission spectra of nanoarcs with different L_{mid} (380 – 1270 nm) and constant R_m = 2.2% coated with 4-ATP. Dash lines are the baselines fitted to the LSPR peaks. Inset: The background transmission spectrum was measured at a location on the bare substrate (without gold and 4-ATP) away from the nanoarc array.

The dependence of the SEIRA spectra around the vibrational mode of 4-ATP at 1492 cm^{-1} on the nanoarc L_{mid}, and thus on the nanoarc LSPR frequency, is tracked in Figure 5.5.3.2 (a) and (b) for nanoarcs arrays with R_m = 2.2% and 4.4%, respectively. Also shown are the best fits of the SEIRA spectra to the modified Fano-function of Eq. 5.2.3 (dash lines). Figure 5.5.3.2 (c) shows the line shape parameters obtained from the fit, including the asymmetry factor q and the linewidth Γ, as well as the normalize amplitude S*. The number of 4-ATP molecules attached to the nanoarc arrays with R_m = 4.4% is nominally twice of that attached to the arrays with R_m = 2.2%. To compare

the SEIRA signal enhancement by the two series of nanoarcs, the amplitude *S* obtained from the fit was normalized with respect to the metal coverage rate R_m, i.e., the normalized amplitude *S** is $S/(100R_m)$, i.e. *S*/2.2 or *S*/4.4.

For the two series of nanoarc arrays with different R_m, the normalized amplitude *S** reaches the maximum when the LSPR frequency (ω_{res}) is slightly higher than the molecular vibrational frequency (ω_{vib}). Specifically, for nanoarc arrays with R_m = 2.2%, the maximum $S^*_{m1Rm2.2}$ is 1.63% and it corresponds to a frequency ratio of ω_{vib} / ω_{res} = 0.96. For arrays with R_m = 4.4%, $S^*_{m1Rm4.4}$ reaches the maximum (0.62%) when ω_{vib} / ω_{res} = 0.88. This phenomenon is in accordance with the observation by Neubrech et al. from the SEIRA signal of a thin CBP film over gold nanorods. [86] To explain why the maximum in *S** corresponds to a frequency ratio smaller than 1, these researchers adopted a model of a driven and damped harmonic oscillator [178] which illustrated the maximum intensity of the near-field appears at a lower frequency than that of the far-field extinction maximum, i.e. $\omega_{res,\ near\text{-}field} < \omega_{res,\ far\text{-}field}$. Since the molecules that are probed are in the near-field of the nanoarcs and the enhancement of the molecular vibration scales with the near-field intensity, it is expected that the maximum enhancement appears at $\omega_{vib} = \omega_{res,\ near\text{-}field} < \omega_{res,\ far\text{-}field}$. If this idea is accepted, the fact that in our experiments the maximum of $S^*_{m1Rm4.4}$ occurs at a smaller frequency ratio suggests that the dipolar coupling between the nanoarcs in dense arrays blue-shifts the near-field resonances even more than the far-field resonances. The maximum value of the normalized SEIRA signal amplitude *S** is lower in the arrays with higher metal coverage rate, indicating that the stronger dipolar coupling deteriorates the SEIRA effect.

The asymmetry factor q generally increases with the frequency ratio $\omega_{vib}/\omega_{res}$. For both series of nanoarcs, the value of q approaches 0 when $\omega_{vib}/\omega_{res}$ is close to 1, indicating that $q = 0$ does not necessarily correspond to the strongest SEIRA signal enhancement, especially when there is strong dipolar coupling between nanoantennas.

The linewidth Γ of the vibrational mode, at ~9 cm^{-1}, does not show a strong dependence on the frequency ratio $\omega_{vib}/\omega_{res}$. It is reasonable that the linewidth of a molecular vibration is narrower than that of a vibration in PMMA which is a polymer.

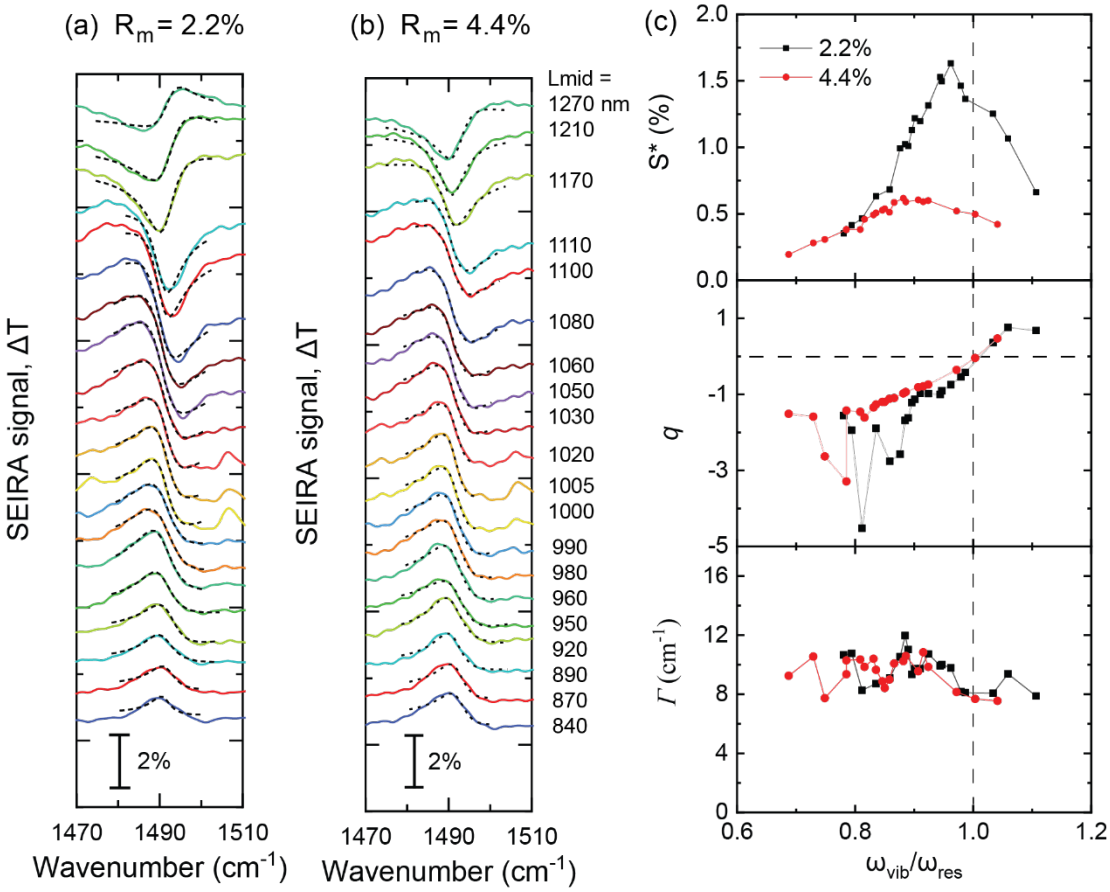

Figure 5.5.3.2 (a, b) SEIRA spectra (ΔT, solid lines) of 4-ATP enhanced by the fundamental LSPR mode of nanoarcs with different L_{mid}, and the corresponding fitting curves (dash lines). (a) Nanoarc arrays with R_m = 2.2%. (b) Nanoarc arrays with R_m = 4.4%. (c) The normalized SEIRA signal amplitude S*, asymmetry factor q and the linewidth Γ.

In summary, for nanoarc arrays that are affected by dipolar coupling, the SEIRA signal enhanced by the 1st LSPR of the nanoarcs is maximized when the far-field LSPR frequency is slightly higher than the molecular vibration frequency. Increasing the element density of the arrays lowers the SEIRA signal amplitude. This observation is evidence for the negative effect of dipolar coupling on the enhancement of the electric near-field by LSPRs.

5.5.4 SEIRA effect of the 2nd LSPR mode

The enhancement of the vibrational mode signal of 4-ATP by the 2nd LSPR of plasmonic nanoarcs was investigated using nanoarcs in Groups $m2R_m1.1$, $m2R_m2.2$ and $m2R_m4.4$.

With metal coverage rates of 1.1% and 2.2%, the spectra of the nanoarc arrays show the resonance frequency of the 2nd LSPR almost in the same position, indicating that the nanoarcs are not coupled in these two series of arrays, while for arrays with R_m = 4.4%, the 2nd LSPRs are at shorter wavelengths, indicating that the nanoarcs are coupled.

The SEIRA spectra around the vibrational mode of 4-ATP at 1492 cm^{-1} and the corresponding fitting curves are shown in Figure 5.5.4.1 for nanoarc arrays with R_m = 1.1%, 2.2% and 4.4%, respectively. The line shape parameters obtained from the fitting curves, including the asymmetry factor q and the linewidth Γ, and the normalized amplitude S^* are shown in Figure 5.5.4.2.

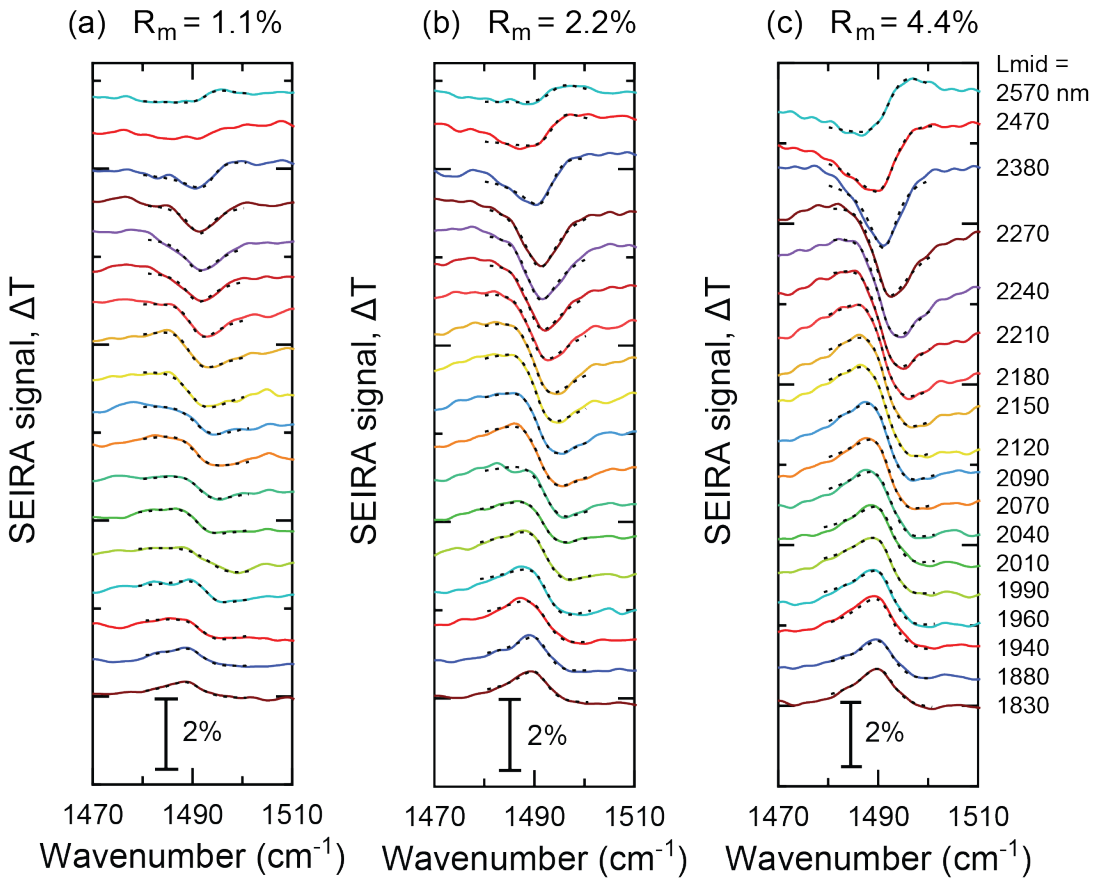

Figure 5.5.4.1 SEIRA spectra (ΔT, solid lines) of 4-ATP enhanced by the 2nd LSPR mode of nanoarcs with different L_{mid}, and the corresponding fitting curves (dash lines). (a) R_m = 1.1%. (b) R_m = 2.2%. (c) R_m = 4.4%.

For the three series of nanoarc arrays with different R_m, the normalized amplitude S^* (Figure 5.5.4.2 (a)) increases as the far-field plasmon resonance frequency approaches the molecular vibration frequency, and reach the maximum when $\omega_{vib} / \omega_{res}$ = 0.96, which is consistent with the results in Section 5.5.3. The maximum amplitudes are $S^*_{m2Rm1.1} = S^*_{m2Rm2.2}$= 0.91%, $S^*_{m2Rm4.4}$ = 0.68%. These data confirm that when there is no dipolar coupling between nanoarcs S^* values are fixed, while the stronger dipolar coupling induced by a smaller distance between the nanoantennas reduces the SEIRA effect. The maximum S^* in these three series ($S^*_{m2Rm1.1} = S^*_{m2Rm2.2}$ = 0.91%) is smaller than the maximum S^* obtained from the SEIRA signal enhanced by the 1st

LSPR of the nanoarcs ($S^*_{m1Rm2.2}$ =1.63%), indicating that the 1st LSPR mode of the nanoarcs is more effective in enhancing the molecular vibrations. With the same metal coverage rates, $S_{m2Rm2.2}$ is smaller than $S_{m1Rm2.2}$, but $S_{m2Rm4.4}$ is larger than $S_{m1Rm4.4}$, suggesting that the enhancement by the 2nd LSPR can be stronger than that of the 1st LSPR when there is strong dipolar coupling between nanoarcs. The data suggest that, to obtain the maximum SEIRA signal amplitude *S*, a nanoarc arrays should be designed with the 1st LSPR frequency tuned to be slightly higher than the molecular vibrational frequency, with the lattice parameters of the array at their threshold values to maximize analyte/antenna density while avoiding the deleterious effects of strong dipolar coupling. The 2nd LSPR is also effective for SEIRA signal enhancement. When using the 2nd LSPR for SEIRA, the LSPR frequency should also be slightly higher than the molecular vibrational frequency to maximize the SEIRA signal amplitude *S*; increasing the element density contributes to the amplitude *S*, even beyond the onset of dipolar coupling. Further studies are needed to quantify the optimum lattice parameters (or R_m) of nanoarc arrays that give rise to the maximum SEIRA enhancement.

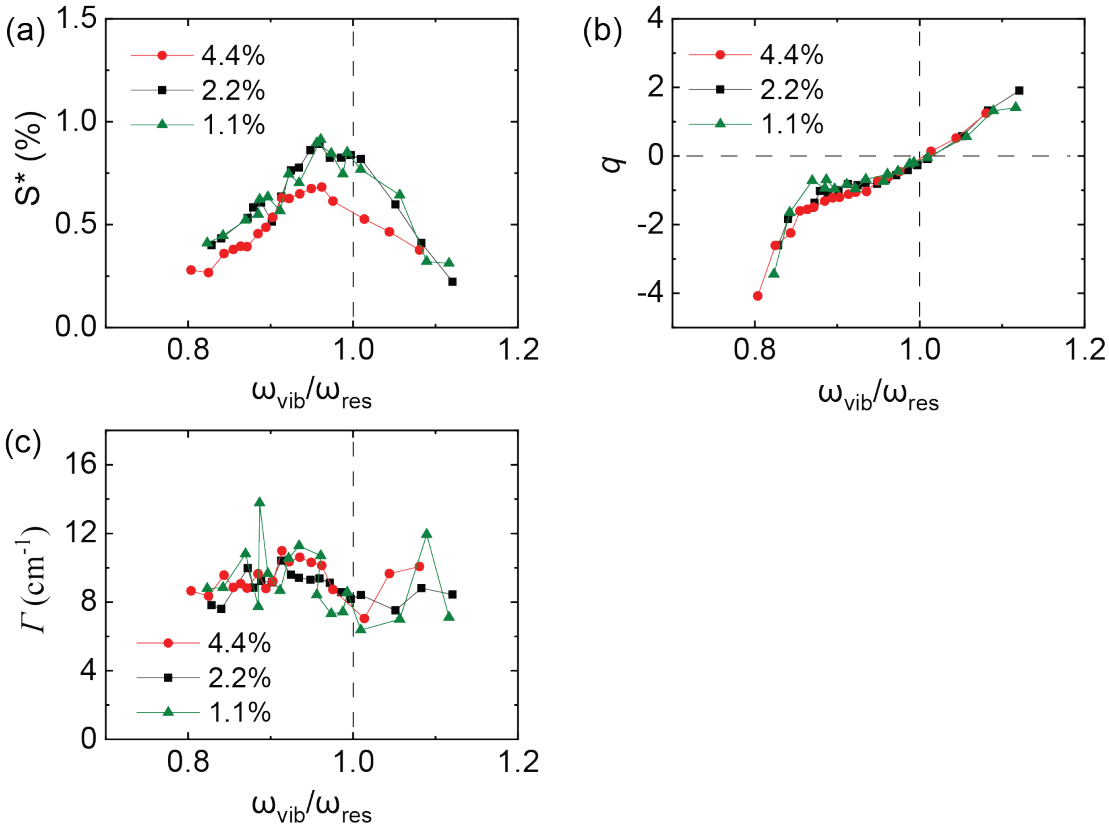

Figure 5.5.4.2 (a) The normalized vibrational signal amplitude S^*, (b) the asymmetry factor q and (c) the linewidth Γ extracted from the modified Fano-functions fitted to the SEIRA spectra in Figure 5.5.4.1.

The asymmetry factor q increases with the frequency ratio and the q values of the three series are almost identical, similar to what was observed from Figure 5.5.3.2. The linewidth Γ of the vibrational mode does not show a dependence on the frequency ratio $\omega_{vib} / \omega_{res}$ nor on the order of the LSPR mode.

In summary, the 2nd LSPR mode of nanoarcs is effective in enhancing molecular vibrational signals. The SEIRA signal enhancement is maximized when the far-field LSPR frequency is slightly higher than the molecular vibration frequency. In the absence of dipolar coupling between nanoarcs, the total SEIRA signal amplitude S increases with element density. Dipolar coupling has a negative effect on the enhancement of molecular vibrational signals, placing an upper bound on the optimum

element density. The results may be further improved by optimizing the central angle of the nanoarcs.

5.6 Chapter Summary

We have demonstrated the detection of thin-films and a molecular monolayer using plasmonic nanoarcs featuring two strong longitudinal LSPRs. By varying the L_{mid} of the nanoarcs, the resonance frequencies of the 1st or 2nd LSPR modes were tuned across broad frequency ranges to enhance the molecular vibrational modes of a thin film of PMMA, the native oxide layer on the surface of silicon, and a self-assembled monolayer of 4-aminothiolphenol (4-ATP) molecules.

For the native oxide of silicon, the coupling between the plasmon mode and the phonon modes results in a transparency window, the shape of which varies as the plasmon mode scans across the phonon bands of SiO_2.

The coupling between the LSPR modes of the nanoarcs and the narrow-band vibrational modes of PMMA and 4-ATP results in a SEIRA signal with the Fano line shape in the transmission spectra. Both the 1st and 2nd LSPRs are effective for SEIRA. The SEIRA signal amplitude is maximized when the far-field LSPR frequency is slightly higher than the vibrational mode frequency ($\omega_{vib} / \omega_{res} = 0.88 – 0.98$). When there is no dipolar coupling between nanoarcs, the maximum SEIRA signal amplitude increases as the element density increases. The dipolar coupling has a negative effect on the enhancement of molecular vibrational signals. Plasmonic nanoarcs could enable dual-band SEIRA spectroscopy, and hold promise for multiplexed chemical sensing and cost-effective biomedical applications.

Chapter 6: Other experiments

This chapter reports the results of three smaller studies, two of which focus on the LSPRs of plasmonic dimers and tetramers composed of nanorods, nanocrescents or nanoarcs, and a third on surface-enhanced Raman scattering (SERS) with optical fibers coated by gold nanoparticles. The spectroscopic measurements of plasmonic dimers and tetramers provide preliminary data for understanding the dipolar coupling between plasmonic nanoantennas when the gap between adjacent elements is a few tens of nanometers. With the SERS-active optical fiber, remote Raman detection is realized with high sensitivity.

6.1 Dipolar Coupling in Plasmonic Dimers

The near-field coupling in plasmonic dimers with nanometer-sized gaps modifies the electromagnetic field distribution around the nanoantennas, especially near the narrow gap. [179] The near-field coupling can potentially enhance the electromagnetic field intensity [180], therefore, plasmonic dimers hold the promise of boosting nonlinear interactions and improving the sensitivity of surface enhanced sensing techniques. In addition, the modification of the electromagnetic field distribution may alter the LSPR frequencies compared to those of the plasmonic monomers, providing tunability with respect to the spectral position of the LSPR peaks. Here, we have investigated the spectral shift caused by the dipolar coupling in a homodimer (rod-rod) and in a heterodimer (rod-crescent). The nanocrescent geometry has been defined in Figure 3.3.1 (a). Different from nanoarcs whose inner radius is smaller than their outer radius, a nanocrescent has identical inner and outer radii and the terminations at the tips are

parallel to each other. We designed four arrays composed of nanorod monomers, nanocrescent monomers, homodimers (rod-rod) and heterodimers (rod-crescent). All the nanorods have the same dimensions of length L = 400 nm, width W = 50 nm, and thickness t = 55 nm. All the nanocrescents have dimensions of height H = 400 nm, width W = 50 nm, thickness t = 55 nm, and central angle θ = 120°. For both the homodimer and heterodimer, the two elements in a dimer have parallel $y(y')$-axes and the gap size is 50 nm (narrowest gap), as shown in the insets of Figure 6.1.1. The two monomer arrays have a triangular lattice with lattice parameters (a_1, a_2) = (1.2, 2.4) μm. The two dimer arrays have a rectangular lattice with lattice parameters (a_1, a_2) = (1.2, 2.4) μm. Therefore, the four arrays have identical element densities.

The gold nanoantenna arrays were fabricated on silicon substrates using the methods described in Section 2.4.1 – 2.4.3. FTIR spectra were collected from the arrays using the methods described in Section 2.4.4. After FTIR spectroscopy, SEM imaging (method described in Section 2.4.7) was performed to check the dimensions of the nanoantennas.

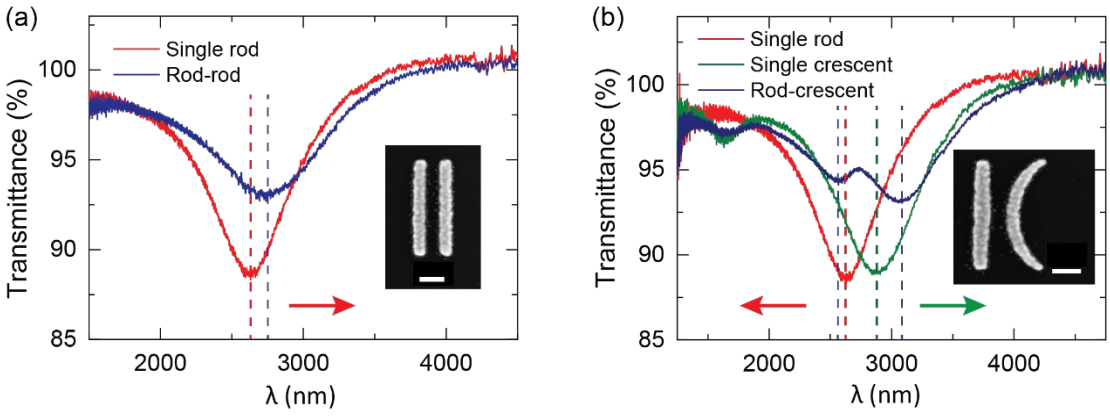

Figure 6.1.1 FTIR spectra of the (a) homodimer and (b) the heterodimer and their corresponding monomers. Dash lines mark the peak positions in each spectrum. Insets are SEM images of the two types of dimers. The scale bar is 100 nm.

The FTIR spectra of the plasmonic dimers and the corresponding monomers are compared in Figure 6.1.1. The rod-rod homodimer displays a single LSPR peak in the spectrum, while the spectrum of the rod-crescent heterodimer consists of two peaks. In the homodimer, the coupling interactions redshift the LSPR peak of the nanorod monomer. In Section 2.5.4 we reported on the blueshift of the LSPR with the decrease in array lattice parameters, i.e. with increased coupling between nanoantennas. The opposite LSPR wavelength shifts here and in Section 2.5.4 are caused by the different nature of the coupling between the nanoantennas. At short range, the evanescent field interactions dominate, while at the long range, the radiative field interactions dominate. [50] For the heterodimer, however, the effect of coupling is to shift the fundamental LSPR modes of the two monomers in opposite directions. The fundamental LSPR mode of the nanorod which occurs at a shorter wavelength than that of the nanocrescent shifts to an even shorter wavelength while the fundamental LSPR mode of the nanocrescent shifts to a longer wavelength, as indicated by the arrows in Figure 6.1.1 (b). In contrast, the 2nd LSPR peak of the nanocrescent appears at the same spectral position in the spectrum of the heterodimer.

A plasmon hybridization theory [181] has been previously proposed to explain this plasmon coupling effect, the principle of which is illustrated in Figure 6.1.2. When two nanoantennas with different resonance frequencies are placed close to each other, the electron oscillations will be coupled and create two new modes with frequency shift in opposite directions, same as what we have observed in the above experiment.

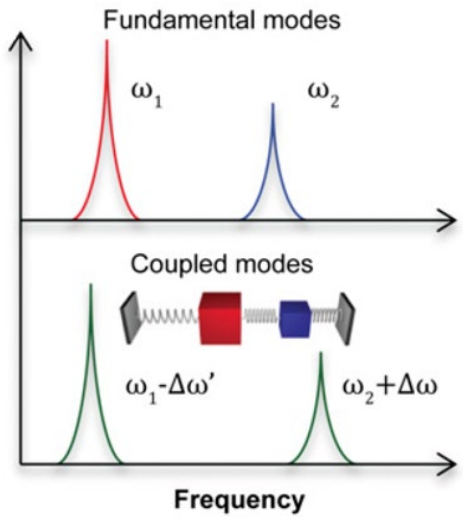

Figure 6.1.2 Illustration of two fundamental modes of monomers and the frequency shifts in the dimer due to the coupling. Adapted from reference [181].

The hybridization of the plasmon modes in homodimers and heterodimers can be used for optimizing their LSPR properties. The strong coupling between the nanoantennas and the modified electromagnetic field around the plasmonic dimer have potential applications in developing plasmonic sensors and nonlinear optical devices.

6.2 Statistical Analysis of the Variation of the Resonance Wavelength of Plasmonic Tetramers due to Fabrication Flaws

As demonstrated in Section 6.1, when the gap between the plasmonic nanoantennas is on the order of tens of nanometers, there will be strong near field coupling between the monomers, which shifts the LSPR wavelengths. Because the near field coupling strength is related to the gap size [180], on one hand, the gap size could be an effective parameter for tuning the LSPR wavelength of plasmonic multimers, but on the other hand, smaller gaps add more challenges to the fabrication process. In particular, they could cause deviations in the LSPR peak positions due to the sensitivity of the resonance to the gap size. To quantify the wavelength deviations caused by the

fabrication flaws in plasmonic multimers with nanometer-sized gaps, small arrays of nano-pinwheels (Figure 6.2.1) were replicated multiple times on a single substrate and the FTIR spectra of the small arrays were measured to find the maximum (λ_{max}), minimum (λ_{min}) and the average (λ_{avg}) LSPR wavelengths. These values were used to determine the deviation of the resonance wavelength, defined as ((λ_{max} - λ_{min})/ λ_{avg}).

The plasmonic nano-pinwheels (tetramers) are composed of 4 gold nanoarcs with H = 600 nm, W = 50 nm, t = 55 nm and θ = 90°. The geometry of the nano-pinwheel and the definition of the gap size are illustrated in Figure 6.2.1 (a). Two values of the gap size (20 nm and 25 nm) were selected because with these gap sizes there will be near-field coupling between the composing nanoarcs and these nano-pinwheels can be fabricated with a high success rate using the available equipment. Each array contains three nominally identical nano-pinwheels arranged in a triangular lattice with (a_1, a_2) = (2.0, 4.0) μm.

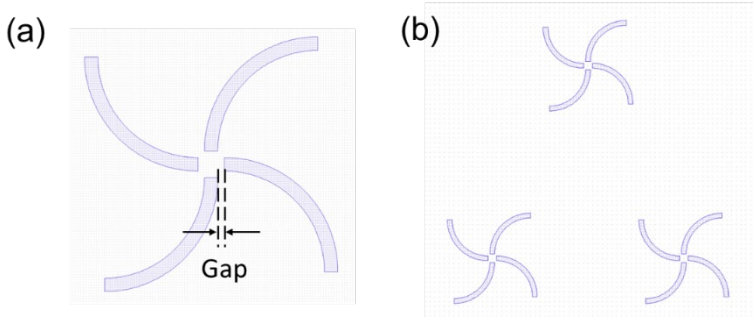

Figure 6.2.1 CAD patterns of (a) a nano-pinwheel and (b) an array that contains 3 nano-pinwheels. The definition of the gap is shown in panel (a).

Each gold nano-pinwheel array was replicated 49 times using the fabrication methods described in Section 2.4.1 – 2.4.3. FTIR spectra were collected from each array using the methods described in Section 2.4.4. The LSPR wavelengths and intensities were determined by a fit to a 7th degree polynomial function (method in Section 2.5.1).

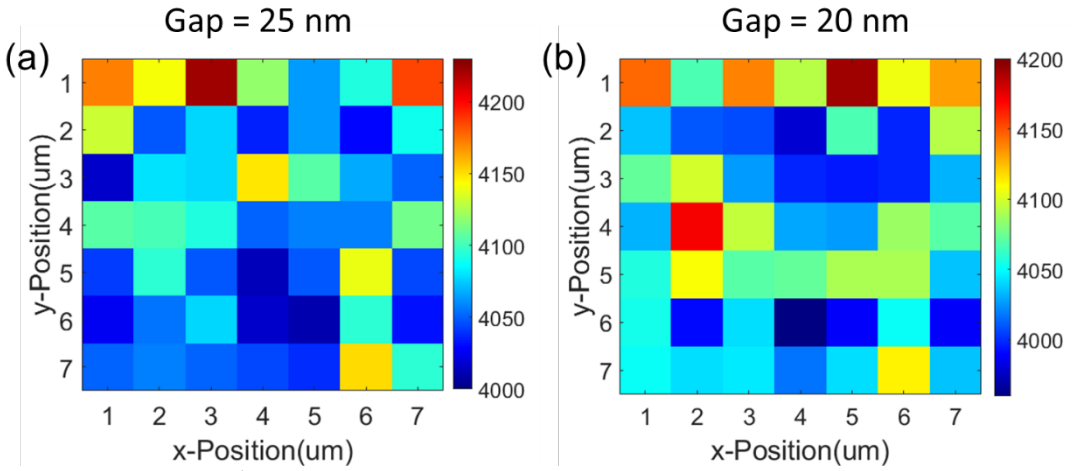

Figure 6.2.2 The 1st LSPR wavelength of gold nano-pinwheels on silicon. Each plot shows a 7-by-7 matrix. Each square in the matrix represents a small array containing 3 nano-pinwheels. The color of the square corresponds to the LSPR wavelength. The gap sizes of the nano-pinwheels are (a) 25 nm and (b) 20 nm.

Figure 6.2.2 presents the LSPR wavelengths of gold nano-pinwheels on quartz, represented by color. Panels (a) and (b) show the 1st LSPR wavelengths of nano-pinwheels with gap = (20 nm, 25 nm), respectively. Similar to the case of arrays of individual plasmonic nanoarcs (see Section 2.5.1), the LSPR wavelength varies across the arrays, despite all 49 arrays being replicas. These variations provide us a measure of the uncertainty caused by the fabrication flaws. In each panel of Figure 6.2.2, the arrays whose LSPR wavelength deviates far from the mean value appear in random positions (bluer or redder squares), suggesting there is no systematic error in the fabrication process or data processing. The maximum (λ_{max}), minimum (λ_{min}), average value (λ_{avg}) and the deviation ((λ_{max} - λ_{min})/ λ_{avg}) are summarized in Table 6.2.1, together with the data of the composing monomer (data from Section 2.5.1).

Nano-pinwheels demonstrate larger deviations of λ_1 compared to that of the monomer, and the deviation of λ_1 is larger in nano-pinwheels with a smaller gap. The fabrication flaws related to the EBL of nano-pinwheels induce variations in the effective mid-arc length of the constituent nanoarcs but more importantly in the effective gap size

between the nanoarcs of the tetramer. The strength of the evanescent field interactions is highly sensitive to the gap size, subsequently, the variations in the gap size can induce much more significant changes in the LSPR wavelength than those induced by the variation in the antenna length. Because of the non-linear nature of the dependence of the near-field interactions on the gap size, the impact of the uncertainty in the gap size on the LSPR wavelength is more significant in nano-pinwheels with the small gap.

Table 6.2.1 The maximum, minimum, average, and maximum deviation of the LSPR wavelengths of gold nanoarcs on quartz and silicon substrates (based on 49 replicas).

Antenna/ Substrate Material	Geometry	Gap size (nm)	λ_{max} (nm)	λ_{min} (nm)	λ_{avg} (nm)	Deviation $(\lambda_{max} - \lambda_{min})/ \lambda_{avg}$
Au/Si	Monomer	>1000	4409	4257	4336	**3.5%**
	Tetramer	25	4223	4010	4078	**5.2%**
	Tetramer	20	4192	3958	4056	**5.8%**

The near-field coupling between nanoarcs in the nano-pinwheel blue-shifts the LSPR wavelengths (λ_{max}, λ_{min}, and λ_{avg}) and the shift is more significant in the nano-pinwheels with the smaller gap. This shift is opposite to the red-shift induced by the near-field coupling in plasmonic rod-rod homodimers (Section 6.1), which is likely because of the different relative orientations of the composing elements and the electric dipoles generated in them upon resonance excitation (parallel dipoles in the homodimer and orthogonal dipoles in the tetramer), and the different interactions of the evanescent fields.

6.3 SERS with Optical Fibers

Surface-enhance Raman spectroscopy (SERS) is an important technique for highly sensitive chemical sensing with an enhancement factor as high as $10^{10} – 10^{14}$ [182-184]. It remains an active topic of research to further improve the sensitivity of Raman

spectroscopy, especially with *in-situ* remote sensors [185, 186]. In this work, an optical-fiber based SERS sensor was developed so that remote chemical detection was realized. The fiber tip was functionalized using the method developed by Rabin group which combines block copolymer templating and self-assembly methods to coat large-area substrates with an ordered, tunable array of gold nanoparticles. [187]

The fabrication process is as follows:

(1) Solution preparation

Polystyrene-b-poly(4-vinylpyridine) (PS-b-P4VP, used without further purification, Polymer Source Inc.) with 47k-b-10k molecular weight was dissolved in propylene glycol methyl ether acetate (PGMEA, CAS: 108-65-6) with 0.75 wt% at 80°C. The polymer formed a slightly cloudy solution.

(2) Optical fiber preparation

- Typically, a multimode silica fiber, 0.22 NA, low-OH with a core diameter of 105 μm and a coating diameter of 250 μm was used (FG105LCA, Thorlabs).
- Remove the cladding/coating near the tip of the optical fiber with a fiber stripping tool (T06S13, Thorlabs).
- Put the optical fiber through the center of the SMA connector (10125A, Thorlabs) and fix the fiber with hot-melt adhesive (Crystalbond™ 509, Ted Pella).
- On the front surface of the SMA connector, clip the optical fiber (FG105LCA, Thorlabs) with a Ruby Fiber Scribe (S90R, Thorlabs) so that the fiber tip is on the same plane as the surface of the SMA connector.

- Connect the SMA connector to a polishing disk (D50-SMA, Thorlabs) and polish it on fiber polishing films (LF1D, LF3D, LF6D and LF30D, Thorlabs).
- Check the fiber tip under a fiber inspection scope (FS201, Thorlabs) to make sure there is no large scratch.

(3) Spin coating

The 0.75 wt% PS-b-P4VP was spin coated on the fiber tip with spinning rate 2000 rpm, ramp time 1s and spin time 30s. The SMA connector and the fiber were held in a home-made holder that fitted on the spin coater and encapsulated the loose end of the fiber.

(4) THF vapor exposure

The optical fiber was placed on a curved stainless-steel mesh in a petri dish with a few drops of tetrahydrofuran (THF). The stainless-steel mesh prevents the THF from contacting the optical fiber. The uncovered petri dish was placed in a desiccator. A vail containing 5 vol.% ethanol and 95 vol.% of THF was also placed in the desiccator. The purpose of the solvent vial is to slow down the evaporation of the THF inside the petri dish. The ethanol can improve the mobility of the P4VP block and empirically can help the formation of a smooth surface. The vapor annealing was allowed to take place for 24 hours.

(5) Dibromobutane cross-linking

The polymer films were put in an uncovered petri dish inside of a desiccator. A vial of 1,4-dibromobutane (DBB) is also put in the desiccator. The desiccator was covered and put in an oven at 70°C for 4 hours for cross-linking.

After cross linking, the fiber tip was washed with hexane and then dried under a flow of nitrogen.

(6) Gold nanoparticle attachment

The fiber tip was then soaked in a gold colloid solution overnight. 15 nm diameter gold nanoparticles (#15704-20, Ted Pella) were found to be the most effective. After soaking, the fiber tip was washed with HPLC grade water and was dried under a flow of nitrogen. The overgrowth of the gold nanoparticles was achieved by soaking the fiber tip in a solution of $HAuCl_4$.

A sketch of the fabrication process is shown in Figure 6.3.1.

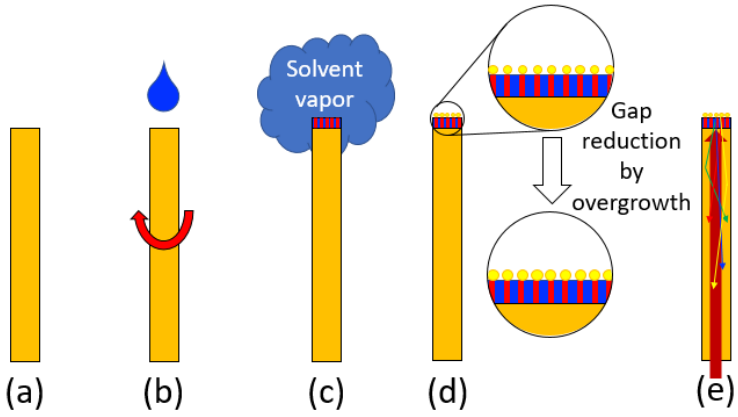

Figure 6.3.1 Fabrication process of gold nanoparticle patterns on the tip of an optical fiber. (a) Fiber preparation. Both tips of the optical fiber were polished and cleaned. (b) Holding the fiber in a special holder, a polymer (PS-b-P4VP) film was spin-coated on the fiber tip. (c) The fiber was annealed in THF (tetrahydrofuran) vapor to form a nanopattern on the fiber tip. (d) Gold nanoparticles were attached to the nanopattern and the gap size between the nanoparticles was controled by the over-growth time. (5) SERS measurement with the optical fiber.

Using this fabrication method, gold nanoparticles were self-assembled on a PS-b-P4VP block copolymer film on the polished end of an optical fiber. The gap size between nanoparticles, which determines the SERS activity, was controlled by the overgrowth time. The well-organized gold nanoparticle array was characterized using SEM and AFM by Dr. Xin Zhang (Figure 6.3.2).

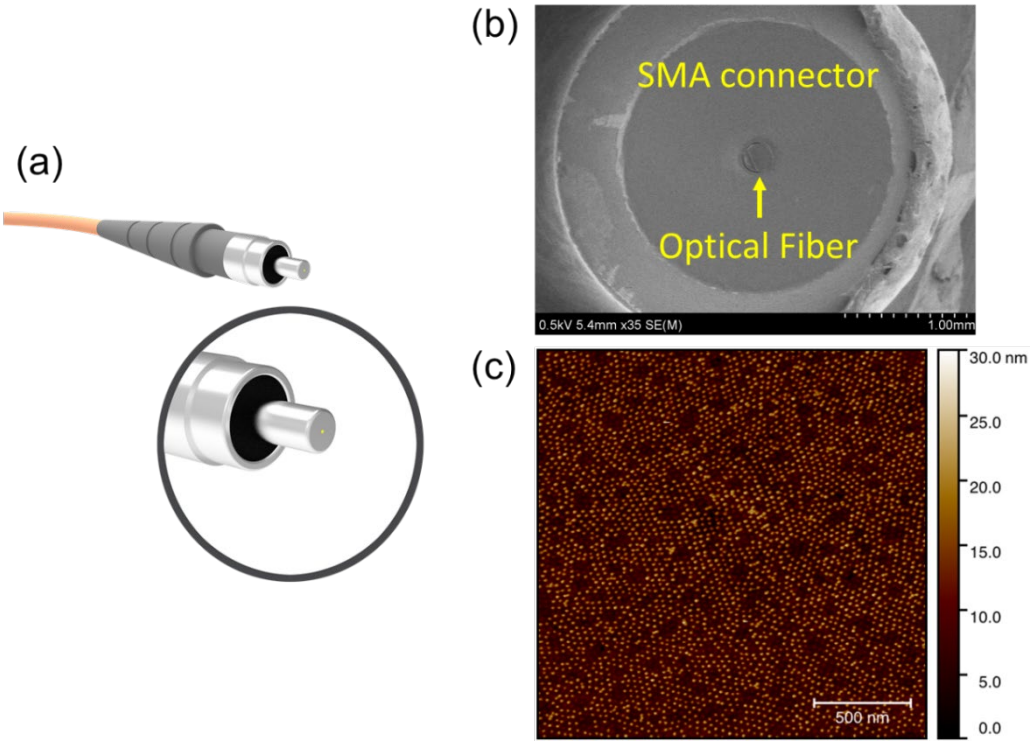

Figure 6.3.2 (a) Illustration of an optical fiber in a SMA holder. The tip of the fiber is coated with gold nanoparticles. (b) SEM image of the fiber tip in a SMA holder.(c) AFM image of the gold nanoparticle array on the fiber tip.

This functionalized optical fiber was utilized for the detection of the SERS signal of 4-aminothiophenol (4-ATP). The incident laser (633 nm) was guided through the optical fiber and excited the surface plasmons of the gold nanoparticle array. The nanoparticle-carrying fiber tip was submerged in a solution of the molecules. The strong electromagnetic field generated by the LSPR interacts with the minute amount of molecules attached on the gold nanoparticles on the coated tip. The light scattered from the molecule-coated nanoparticles was collected in the near-field through the same optical fiber into the spectrometer (Horiba Jobin-Yvon LabRAM HR-VIS) for analyzing the SERS signal. Using this method, a monolayer of 4-aminothiophenol was detected through the optical fiber after background signal subtraction, with an

enhancement factor of ~2×10^4 (Figure 6.3.3). This fiber-coupled SERS detector offers great opportunities for *in-situ*, remote and high-throughput Raman sensing.

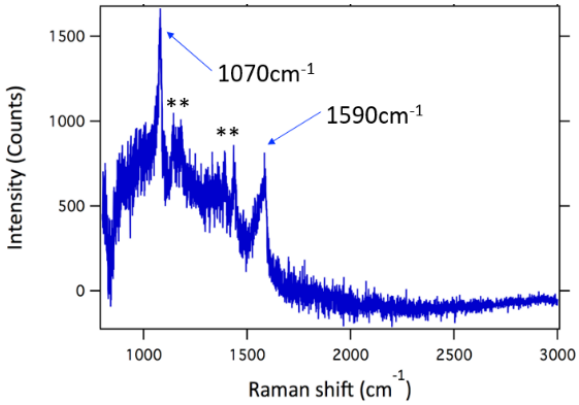

Figure 6.3.3 Raman spectrum of 200 mM 4-aminothiophenol in 1,5-pentanediol detected by the fiber-couped SERS detector after background subtraction.

Chapter 7: Conclusion and Future Work

7.1 Conclusion

Plasmonic nanoantennas are a building block for light manipulation at the nanoscale. In these nanoantennas, the localized surface plasmon resonances (LSPRs) driven by an incoming light will generate a strong electromagnetic (EM) field in subwavelength volumes and creates sharp light scattering/absorption peaks in the visible and IR spectra. The light-plasmon interactions can give rise to an enhancement of harmonics generation, making plasmonic nanoantennas an ideal platform for nonlinear optical frequency conversion in the nanoscale. In addition, the LSPRs can coupled to other emitters and strongly modify their emission properties, therefore, plasmonic nanoantennas has been widely adopted in ultra-sensitive chemical sensing techniques, such as surface enhanced infrared absorption (SEIRA) and surface enhanced Raman scattering (SERS). To accommodate the needs of various applications, it is important to tune the LSPR features of the plasmonic nanoantennas in a predictable manner.

In this work, the tunability of the LSPRs of plasmonic nanorod and nanoarc antennas were systematically investigated, and semi-quantitative relationships between the LSPR wavelengths and intensities of these nanoantennas and their geometric and material parameters were established. These relationships provide a framework for designing nanoarcs with desired LSPR features and have been adopted in improving the performance of nanoarcs in the applications of second harmonic generation (SHG) and SEIRA.

We focused our efforts on plasmonic nanoarc antennas because they can support both odd- and even-order longitudinal LSPRs and allow the excitation of an out-of-plane magnetic dipole. These outstanding features make nanoarcs a versatile plasmonics building block. The properties of the LSPRs of nanoarcs were elucidated with the help of a 2D conformal transformation which links a column of nanorods in the original space to a nanoarc in the transformed space, and vice versa. The 2D conformal transformation conserves the in-plane permittivity and permeability tensors of the two spaces therefore the LSPR frequencies of the corresponding nanostructures in the two spaces were expected to be the same. The transformation optics analysis also predicted that the nearly linear dependence of the LSPR wavelength on the length of nanorods should be applicable to nanoarcs. These predictions of the transformation optics analysis were proven by numerical simulations and FTIR transmission spectroscopy. The wavelengths of the fundamental LSPR mode in a nanorod and a series of nanoarcs transformed from the nanorod were found to be almost identical. Importantly, it was observed in experiments that a length parameter, L_{mid}, was the key geometric parameter that dominates the resonance wavelengths of the nanoarcs. Akin the linear relationship between LSPR wavelength and the rod length observed in nanorods, a linear relationship was observed between L_{mid} and the LSPR wavelengths of nanoarcs, the slope of which depended on the refractive index of the substrate and the order of the LSPR mode. Furthermore, in plasmonic nanoarcs, the extinction cross-sections of different order LSPR modes were controlled by the central angle (curvature).

We then concentrated on the tunability of the wavelength interval between the 1st and 2nd LSPRs of nanoarcs. It was observed that for nanoarcs with a uniform width profile,

the ratio of the 1st and 2nd LSPR wavelengths relies on the material of the nanoantenna and L_{mid}, while the impact of the substrate is minor. Specifically, the ratio λ_1/λ_2 generally increases with L_{mid} and, with a fixed L_{mid}, the value of λ_1/λ_2 is larger in nanoantennas made of aluminum than those made of gold. In order to tune the ratio λ_1/λ_2 in a relatively large range, the width profiles of the nanoarcs were adjusted. This idea was inspired by the observation that nanocrescents with two tips narrower than the center had a smaller ratio λ_1/λ_2 than that of nanoarcs with same mid-arc length but a uniform width. The effect of the non-uniform width profile on the LSPR interval was investigated using nanoarcs with different W_{tip}/W_{mid}. It was found that λ_1/λ_2 of nanoarcs increased monotonically with W_{tip}/W_{mid}, and the octave interval condition was achieved when W_{tip}/W_{mid} = 1.20 – 1.40 for nanoarcs with L = 600 – 1000 nm. This finding demonstrates the width profile provides additional flexibility for finely tuning the LSPR wavelengths and the LSPR wavelength interval, in addition to the flexibility provided by materials, L_{mid} and the central angle.

The newly found relationships were then utilized as guidelines for improving the performance of nanoarcs in two representative applications, SHG and SEIRA. The study of SHG in plasmonic nanoarcs demonstrated that the light-plasmon interactions at both the fundamental and the 2nd order LSPR mode play an important role in improving SHG efficiency, and the relative importance of the two LSPRs in enhancing SHG is dependent on the LSPR interval. The curvature of the nanoarcs also affects the SHG efficiency, likely by determining the oscillator strengths of the two LSPRs. The maximum SHG efficiency was observed in nanoarcs with central angle θ = 150° when the ratio λ_1/λ_2 was close to two.

The SEIRA spectroscopy of a thin film of polymer, an oxide layer, and a thiol monolayer was performed using plasmonic nanoarcs. By varying the L_{mid} of the nanoarcs, the 1st and 2nd LSPR wavelengths were tuned across the vibrational bands of different molecules, and the enhancement of the vibrational mode signals was varied. The maximum vibrational signal intensity was obtained when the ratio of the molecular vibrational frequency and the LSPR frequency was ~0.88 – 0.98. Moreover, for low-density arrays without dipolar coupling between nanoarcs, the vibrational mode signal intensity increased with the element density. However, for high-density arrays with dipolar coupling between nanoarcs, the normalized vibrational signal intensity decreased as the element density increased. To optimize the SEIRA effect, the lattice parameters need to be selected such that the element density is high while the neighboring nanoarcs in the array are not strongly coupled.

The near-field coupling effect in plasmonic dimers and tetramers was briefly studied using homodimers composed of two identical nanorods, heterodimers composed of a nanorod and a nanocrescent, and tetramers composed of four identical nanoarcs. With the gap size as small as a few tens of nanometers, the dipolar coupling between nanoantennas was found to shift the LSPR peaks with respect to those of the monomers. Beyond the applications of plasmonic nanoantennas mentioned above, we also developed a plasmonic system for surface-enhanced Raman scattering (SERS). An optical fiber-based remote Raman sensor was developed by making one of the fiber tips SERS-active. Using this remote sensor, the SERS signal of a monolayer of thiol molecules was detected with an enhancement factor of $10^4 – 10^5$.

7.2 Future Work

Based on the work presented in this thesis, future directions of the investigation on plasmonic nanoarcs could include probing the near-field optical properties of the nanoarcs and utilizing plasmonic multimers composed of nanoarcs for ultra-sensitive chemical sensing.

While the optical properties of the nanoarcs in the far-field were examined using visible and FTIR spectroscopy, the near-field optical response of nanoarcs was not fully elucidated. The near-field properties can possibly help explain the mechanism of the nonlinear conversion in nanoarcs and the coupling between molecular vibrations and surface plasmons. The near-field optical intensity distribution can be characterized by scattering-type near-field scanning optical microscopy (sNSOM). By employing a metal-coated AFM tip to confine light to a sub-wavelength volume, sNSOM can probe the light elastically scattered from the AFM tip simultaneously with topography (Figure 7.2.1), with a spatial resolution beyond the diffraction limit.

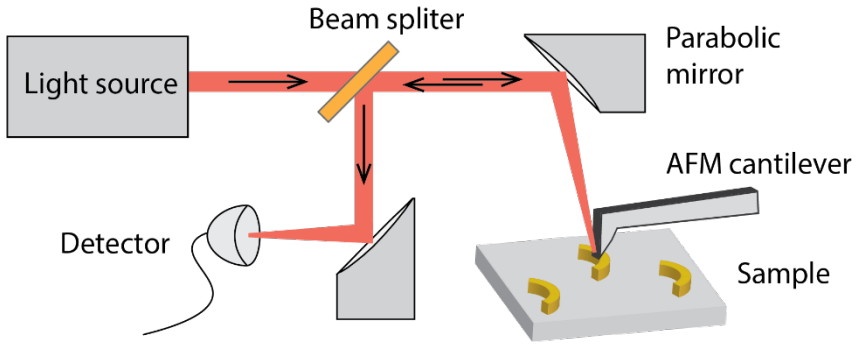

Figure 7.2.1 Schematic of an sNSOM setup.

Because of the strong optical near-field interaction between the AFM tip and the nanoarc, the elastically scattered light contains information regarding the local LSPR properties. The map of the scattered light reveals the electric field distribution on the

surface of the nanoarc upon the interaction with the plasmon of the AFM tip. Figure 7.2.2 shows AFM images and near-field optical amplitude images of gold nanoarcs measured by a sNSOM system (Neaspec), with a Pt-coated AFM tip (Arrow NCPt, Oxford Instrument) and a 1550 nm laser (model EXS1520-2101, EXALOS). The regions with high amplitude of the optical signal in the near-field images (bright areas) are interpreted as regions that interact strongly with the plasmon excited on the AFM tip.

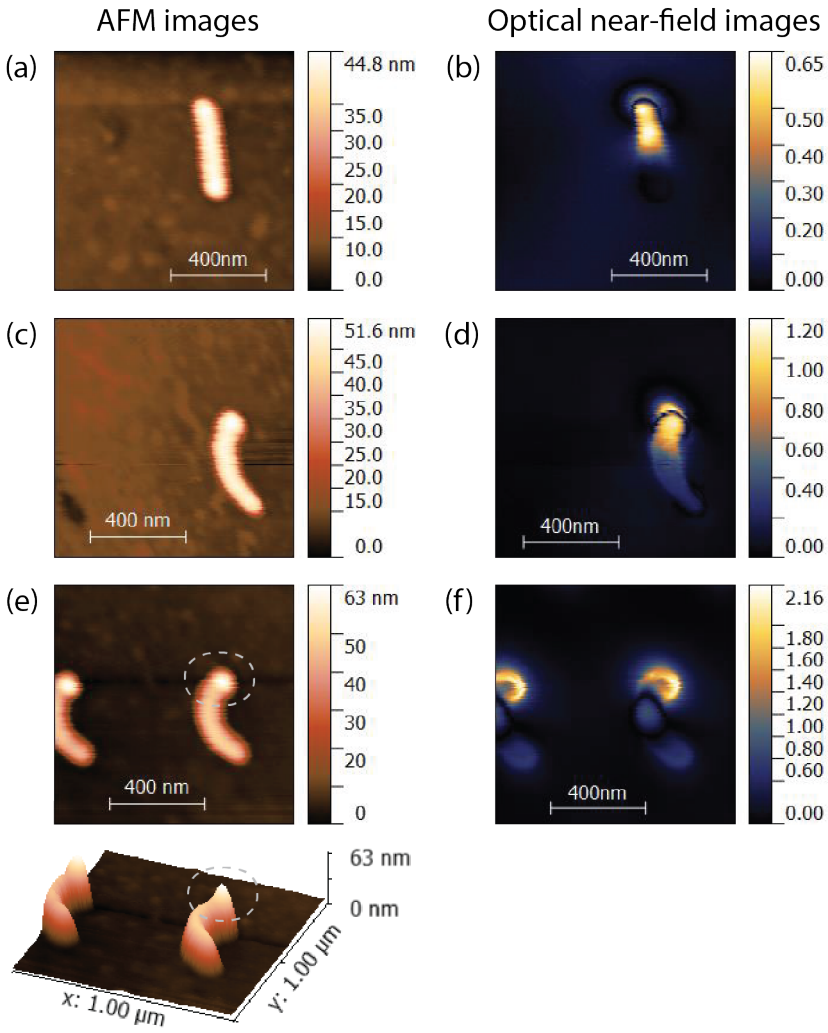

Figure 7.2.2 AFM images and corresponding optical near-field images (optical signal amplitude) of nanoarcs with L_{mid} = 395 nm, W = 60 nm and (a, b) θ = 0°, (c, d) θ = 130°, (e, f) θ = 150°. A 3D topography image of the nanoarcs with θ = 150° is also shown in (e). The images drifted in the horizontal direction during the AFM scanning.

A second future direction is to investigate multimers composed of nanoarcs, such as nano-pinwheels (Figure 7.2.3). These multimers can potentially change the polarization status of the incident beam and generate chiral plasmonic fields, holding promise for chiroptical applications. The optical properties of nanoarc multimers can be predicted based on the known properties of the monomers and the dipolar coupling effect. The combination of nanoarc multimers and 3D nanostructures (humps or pits) on a dielectric substrate could potentially enable the detection of the absolute configuration of molecules.

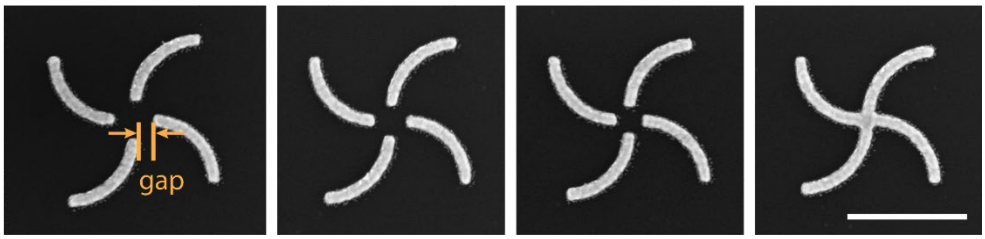

Figure 7.2.3 SEM images of nano-pinwheels composed of nanoarcs with H = 400 nm, W = 50 nm, t = 55 nm and θ = 90°.The gap sizes are (a) 50 nm, (b) 35 nm, (c) 25 nm and (d) 0 nm. The scale bar is 500 nm.

In conclusion, metallic nanoantennas have enabled novel optical phenomena such as surface enhanced Raman scattering / infrared absorption, nonlinear wave mixing, and quantum emission, which have already or will boost the development of nano-optics. Currently, the full control over the radiative properties of nanoantennas and emitter-nanoantenna interactions remains one of the biggest challenges. With the advancement of fabrication techniques, theoretical models, and innovative design strategies of plasmonic nanoantennas, it is foreseen that this challenge will be overcome and integrated optical devices with high performance will be broadly adopted in many areas of research.

8. Appendices

Appendix 8.1. Prove the Transformation $\zeta' = e^{\gamma\zeta}$ is Conformal

A 2D transformation is conformal if it satisfies the Cauchy-Riemann equations[102] with nonzero derivatives,

$$\frac{\partial x'}{\partial x} = \frac{\partial y'}{\partial y} \quad (8.1)$$

$$\frac{\partial x'}{\partial y} = -\frac{\partial y'}{\partial x} \quad (8.2)$$

where x and y are the coordinates in the original plane and x' and y' are the coordinates in the transformed plane.

In this section, we prove that the 2D coordinate transformation $\zeta' = e^{\gamma\zeta}$ that was applied to transform rods to arcs is a conformal transformation. Subsequently, we calculate the permittivity tensor in the transformed (arc) space with the assumption that the material in the original (rod) space is isotropic and non-magnetic to show how the permittivity is affected by the transformation.

A nanorod of length *L* and width *W* is mapped to a nanoarc through the 2D coordinate transformation,

$$\zeta' = e^{\gamma\zeta} \quad (8.3)$$

with the complex number notations $\zeta = x + iy$ for the original (rod) plane and $\zeta' = x' + iy'$ for the transformed (arc) plane. Therefore, the Cartesian coordinates in the two spaces are related by

$$x' = e^{\gamma x}\cos(\gamma y) \quad (8.4)$$

$$y' = e^{\gamma x}\sin(\gamma y) \quad (8.5)$$

$$z' = z \qquad (8.6)$$

where the parameter γ sets the central angle θ (in radians) subtended by the resulting arc via the relation

$$\gamma = \frac{\theta}{L} \qquad (8.7)$$

The Jacobian matrix (Λ) of this transformation is

$$\Lambda \equiv \begin{bmatrix} \frac{\partial x'}{\partial x} & \frac{\partial x'}{\partial y} & \\ \frac{\partial y'}{\partial x} & \frac{\partial y'}{\partial y} & \\ & & \frac{\partial z'}{\partial z} \end{bmatrix} = \begin{bmatrix} \gamma e^{\gamma x}\cos(\gamma y) & -\gamma e^{\gamma x}\sin(\gamma y) & \\ \gamma e^{\gamma x}\sin(\gamma y) & \gamma e^{\gamma x}\cos(\gamma y) & \\ & & 1 \end{bmatrix} \qquad (8.8)$$

The Jacobian matrix in Eq. (8.8) satisfies the Cauchy-Riemann equations, therefore, the transformation $\zeta' = e^{\gamma\zeta}$ is a 2D conformal transformation.

The permittivity tensor (ε') and the permeability tensor (μ') in the transformed space are related to the permittivity (ε) and permeability tensors (μ) in the original space by [103, 106]

$$\varepsilon' = [\det(\Lambda)]^{-1}\Lambda\varepsilon\Lambda^T \qquad (8.9)$$

$$\mu' = [\det(\Lambda)]^{-1}\Lambda\mu\Lambda^T \qquad (8.10)$$

Eq. (8.9) can be written element-wise as

$$\varepsilon'_{11} = [\det(\Lambda)]^{-1}(\Lambda_{11}\Lambda_{11}\varepsilon_{11} + \Lambda_{11}\Lambda_{12}\varepsilon_{12} + \Lambda_{12}\Lambda_{11}\varepsilon_{21} + \Lambda_{12}\Lambda_{12}\varepsilon_{22}) \qquad (8.11)$$

$$\varepsilon'_{12} = [\det(\Lambda)]^{-1}(\Lambda_{11}\Lambda_{21}\varepsilon_{11} + \Lambda_{11}\Lambda_{22}\varepsilon_{12} + \Lambda_{12}\Lambda_{21}\varepsilon_{21} + \Lambda_{12}\Lambda_{22}\varepsilon_{22}) \qquad (8.12)$$

$$\varepsilon'_{13} = [\det(\Lambda)]^{-1}(\Lambda_{11}\varepsilon_{13} + \Lambda_{12}\varepsilon_{23}) \qquad (8.13)$$

$$\varepsilon'_{21} = [\det(\Lambda)]^{-1}(\Lambda_{21}\Lambda_{11}\varepsilon_{11} + \Lambda_{21}\Lambda_{12}\varepsilon_{12} + \Lambda_{22}\Lambda_{11}\varepsilon_{21} + \Lambda_{22}\Lambda_{12}\varepsilon_{22}) \qquad (8.14)$$

$$\varepsilon'_{22} = [\det(\Lambda)]^{-1}(\Lambda_{21}\Lambda_{21}\varepsilon_{11} + \Lambda_{21}\Lambda_{22}\varepsilon_{12} + \Lambda_{22}\Lambda_{21}\varepsilon_{21} + \Lambda_{22}\Lambda_{22}\varepsilon_{22}) \qquad (8.15)$$

$$\varepsilon'_{23} = [\det(\Lambda)]^{-1}(\Lambda_{21}\varepsilon_{13} + \Lambda_{22}\varepsilon_{23}) \qquad (8.16)$$

$$\varepsilon'_{31} = [\det(\Lambda)]^{-1}(\Lambda_{11}\varepsilon_{31} + \Lambda_{22}\varepsilon_{32}) \quad (8.17)$$

$$\varepsilon'_{32} = [\det(\Lambda)]^{-1}(\Lambda_{21}\varepsilon_{31} + \Lambda_{22}\varepsilon_{32}) \quad (8.18)$$

$$\varepsilon'_{33} = [\det(\Lambda)]^{-1}\varepsilon_{33} \quad (8.19)$$

where the determinant of the Jacobian matrix is

$$\det(\Lambda) = \gamma^2 e^{2\gamma x} \quad (8.20)$$

For isotropic and non-magnetic materials, such as the metals used in the experiments for the antenna material (Au, Al), the permittivity tensor (ε) in the original (rod) space is

$$\varepsilon = \varepsilon_m I = \begin{bmatrix} \varepsilon_m & & \\ & \varepsilon_m & \\ & & \varepsilon_m \end{bmatrix} \quad (8.21)$$

where I is the identity matrix.

Using the expressions for ε_{ij} and $\det(\Lambda)$ in Eqs. (8.11) – (8.19) the elements of ε' can be expressed as

$$\varepsilon'_{11} = \cos^2(\gamma y)\varepsilon_m + \sin^2(\gamma y)\varepsilon_m = \varepsilon_m \quad (8.22)$$

$$\varepsilon'_{22} = \sin^2(\gamma y)\varepsilon_m + \cos^2(\gamma y)\varepsilon_m = \varepsilon_m \quad (8.23)$$

$$\varepsilon'_{33} = \frac{\varepsilon_{33}}{\det(\Lambda)} = \frac{\varepsilon_m}{\gamma^2 e^{2\gamma x}} \quad (8.24)$$

$$\varepsilon'_{12} = \varepsilon'_{21} = \varepsilon'_{13} = \varepsilon'_{31} = \varepsilon'_{23} = \varepsilon'_{32} = 0 \quad (8.25)$$

i.e., the permittivity tensor (ε') in the transformed space is

$$\varepsilon' = \begin{bmatrix} \varepsilon_m & & \\ & \varepsilon_m & \\ & & \frac{\varepsilon_m}{\gamma^2 e^{2\gamma x}} \end{bmatrix} \quad (8.26)$$

Similarly, with the permeability tensor (μ) in the original (rod) space being the identity matrix ($\mu = I$), the permeability tensor (μ') in the transformed (arc) space is

$$\mu = \begin{bmatrix} 1 & & \\ & 1 & \\ & & \frac{1}{\gamma^2 e^{2\gamma x}} \end{bmatrix} \qquad (8.27)$$

Therefore, the 2D conformal transformation $\zeta' = e^{\gamma\zeta}$ only preserves the in-plane (*x'y'*-plane) components of the permittivity and permeability tensors, and the material is uniaxial in the transformed (arc) space. The permittivity (permeability) along the out-of-plane direction (*z*'-axis) in the transformed (arc) space depends upon the central angle θ, the length of the rod L and the *x*-coordinate.

Appendix 8.2. Resonance Wavelength of Gold Nanoarcs on Quartz: Simulation vs. Experiment

Table 8.2.1 shows the data plotted in Figure 2.3.2.1 (d).

Table 8.2.1 Calculated and measured 1st and 2nd LSPR wavelength of gold nanoarcs on quartz with L_{mid} = 395 nm.

θ (°)	$\sigma_{ext} = \sigma_{scat} + \sigma_{abs}$		Measured	
	λ_1 (nm)	λ_2 (nm)	λ_1 (nm)	λ_2 (nm)
0	1653 ± 4	-	1639 ± 15	-
30	1657	-	1634	-
46	1660	-	1637	-
60	1660	-	1628	-
90	1657	921 ± 2	1621	894 ± 20
120	1653	920	1616	908
130	1643	919	1608	902
140	1643	917	1605	915
150	1639	920	1603	920
160	1639	919	1598	913
170	1632	918	1597	919
180	1626	919	1600	925

*In the simulations, W = 62 nm and t = 50 nm; in the experiments, W = 60 nm and t = 55 nm.

Appendix 8.3. Correction Factors for the SHG/THG Measurement

The SHG/THG spectra ($I_{SHG}(\lambda)$ and $I_{THG}(\lambda)$) in Chapter 4 were obtained by

$$I_{SHG}(\lambda)\ or\ I_{THG}(\lambda) = \frac{V_{LIA}(\lambda)}{\eta_{gain}\eta_{sv}(\lambda)T_{filter}(\lambda)T_{lens}(\lambda)}$$

where V_{LIA} is the output voltage of the lock-in amplifier, η_{gain} η_{gain} is the PMT gain ($\eta_{gain}$is a function of the control voltage), $\eta_{sv}(\lambda)$ is the PMT sensitivity, $T_{filter}(\lambda)$ is the transmission of the short-pass filter (or the product of the transmission of the short-pass filter and that of the linear polarizer for the cases when the linear polarizer was used), and $T_{lens}(\lambda)$ is the transmission of the AR coated lens. The values of the correction factors are provided in Figure 8.3.1.

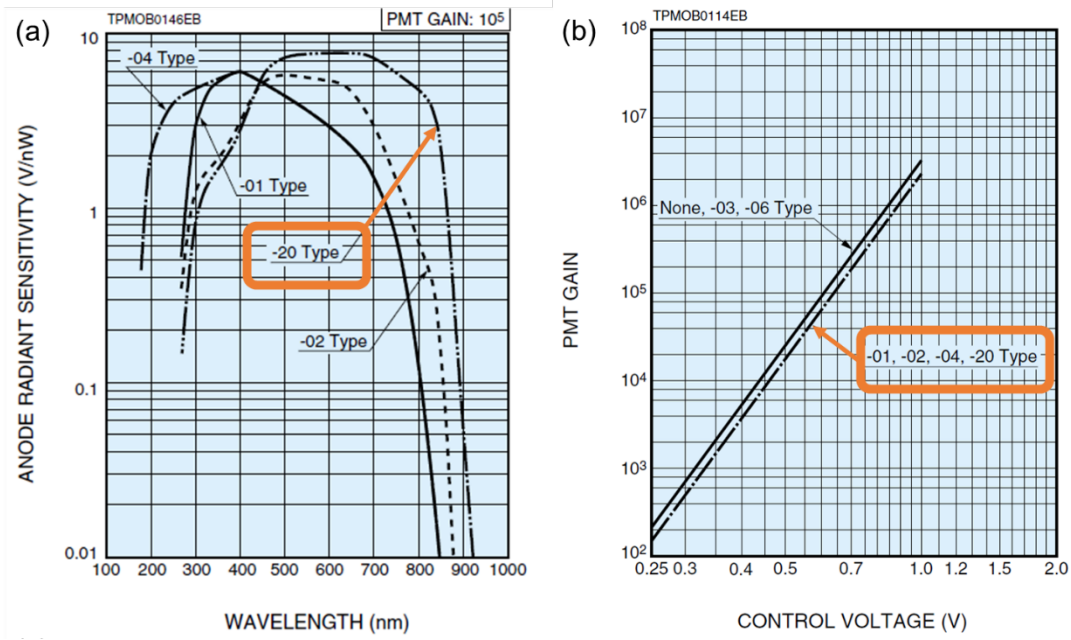

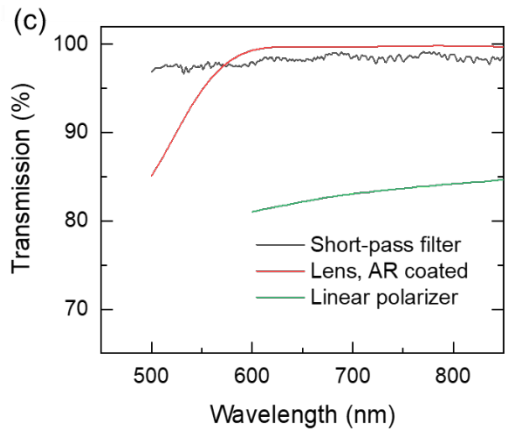

Figure 8.3.1 (a) The PMT sensitivity $\eta_{sv}(\lambda)$ and (b) the PMT gain $\eta_{gain}(V)$. Data was obtained from Ref [188]. (c) The transmission of the short-pass filter (FESH 0900, Thorlabs), the AR coated lens (LB1471-B, Thorlabs), and the linear polarizer (LPNIRE-B, Thorlabs). Data was obtained from Refs. [189-191].

Appendix 8.4. SHG Polarization and Power Dependence Measurement

In this section, the SHG signal measured with SHG photometry (the 2nd configuration described in Section 4.2.2) is reported.

The nanoarc array used in this measurement was the same array used in Section 4.3. The dimensions of the nanoarcs were L_{mid} = 395 nm, W = 60 nm, t = 55 nm, and θ = 150°. In the SHG photometry measurement, the excitation wavelength was fixed at 1580 nm. A bandpass filter (FBH800-40, Thorlabs) was used to set 780 – 820 nm as the range of the signal being collected. The generated light in this range was collected by the PMT whose output was recorded by the lock-in amplifier (V_{LIA}). The value of V_{LIA} was used to represent the intensity of the SHG signal. Due to the lack of accurate conversion factors, the SHG signal is reported as a percentage of the maximum value of V_{LIA} in a series of related measurements, i.e. normalized to the range of 0 – 100.

Figure 8.4.1 (a) shows the normalized SHG signal intensity as a function of the incident laser power. As expected for SHG, the intensity of the generated light closely scales with the square of the incident power (the least square linear regression of the data had a slope of 1.99 ± 0.01). Figure 8.4.1 (b) shows the normalized signal intensity as a function of the polarizer angle. The polarization of the SH emission is directed along the *x'*-axis of the nanoarc, rotated by 90° compared to the polarization of the incident light. These results are consistent with the results of the measurement performed using the SHG spectroscopy configuration on the same sample (Section 4.3.1 and 4.3.2).

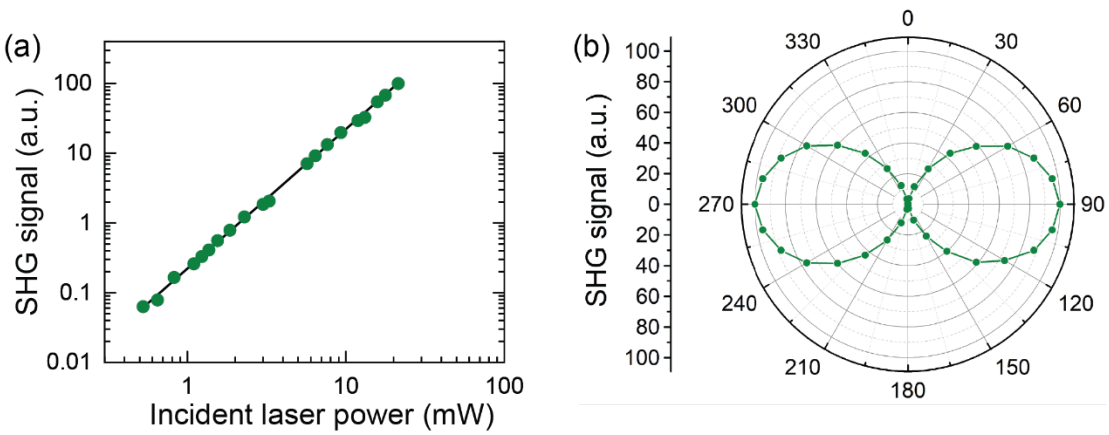

Figure 8.4.1 (a) Normalized SHG signal intensity as a function of the incident laser power. The black line with a slope of 2 is a guide to the eye. (b) Measured polarization of the SHG emission represented as a polar diagram. 0° corresponds to the direction parallel to the *y'*-axis of the nanoarc.

Appendix 8.5. Characterization of THG in Plasmonic Nanorods

When arrays of gold nanorods on quartz were irradiated by femtosecond IR laser pulses, emission of shorter wavelength light was detected. The signals generated by the plasmonic nanorods were characterized to confirm that they correspond to emission via the process of third-harmonic generation (THG). The THG signal has the following two characteristics: (i) the central wavelength of the generated light is a third of the excitation wavelength, and (ii) the power of the generated light scales cubically with the power of the excitation light. Therefore, the characterization of the generated light includes quantifying the central wavelength and measuring the peak intensity as a function of the incident laser power. The characterization of THG was performed using nanorods ($\theta = 0°$) with L_{mid} = 395 nm, W = 60 nm, t = 55 nm. The sample was selected out of the series of nanoarc arrays with L_{mid} = 395 and central angle θ = 0 – 180° reported on in Sections 2.3.2 and 8.2, designed to manifest the fundamental LSPR within the wavelength tuning range of the OPO, i.e. less than 1600 nm. The central angle of 0° was selected because it could enable two strong light-plasmon interactions separated by approximately two octaves in the nanorod. The area of the array was 200 μm by 200 μm, and the lattice parameters were (a_1, a_2) = (1.2, 2.4) μm.

The fabrication and characterization (collecting FTIR/visible transmission spectra, and recording THG spectra with different incident laser powers) methods were the same as the methods used for SHG characterization with nanoarcs (θ = 150°) in Section 4.3, except that the THG spectra were collected in the wavelength range of 515 – 535 nm.

The FTIR and visible transmission spectra of the nanorod array are shown in Figure 2.3.2.1 (d). The 1st LSPR wavelength of the nanorod was at λ_1 = 1638 nm, and the 3rd

LSPR wavelength was approximately at λ_3 = 560 nm. The spectra collected in the THG spectroscopy measurement for various incident laser powers are shown in Figure 8.5.1 (a). The peak intensity and FWHM extracted from the spectra are shown in Figure 8.5.1 (b) and (c), respectively. As expected for THG, the peak in the spectra of the generated light was centered at 526 nm (Figure 8.5.1 (a)), i.e. at one third of the excitation wavelength (1580 nm). As shown in Figure 8.5.1 (b), the peak intensity scales as the cube of the incident power, that is, under a log-log scale, the data points matched well with a straight line with a slope of three, as expected for THG; the least-squares regression line for log(THG peak intensity) *vs.* log(laser power) had a slope of 3.28±0.04. As shown in Figure 8.5.1 (c), the FWHM values were nearly constant for all the THG spectra with an average of 4.6 nm.

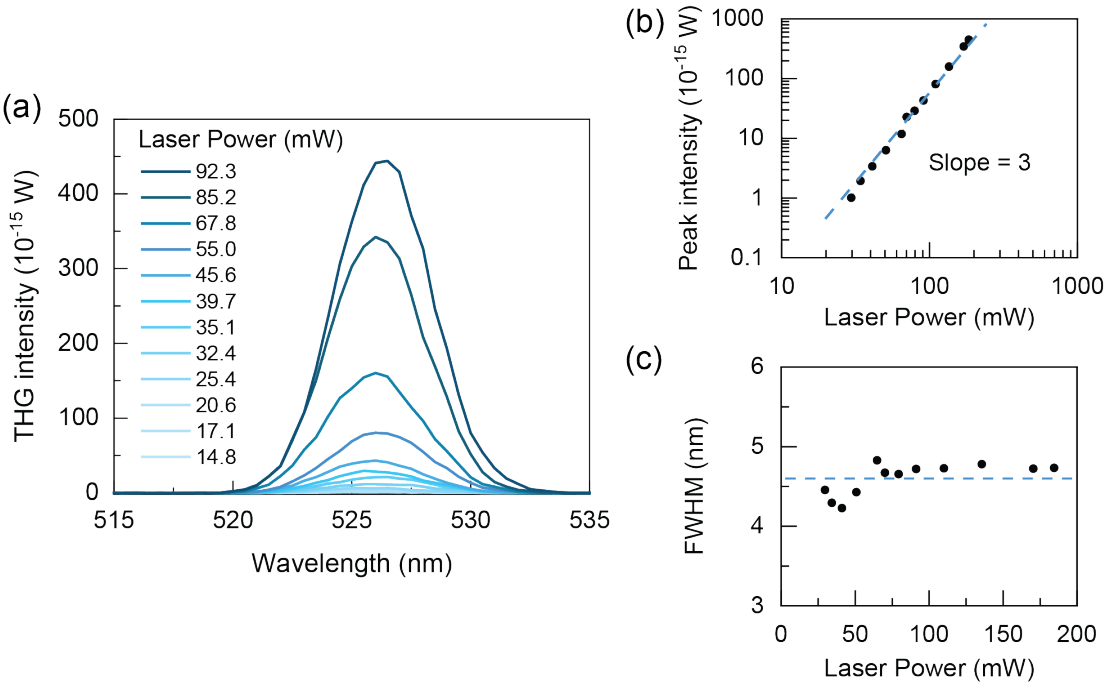

Figure 8.5.1 Third harmonic generation from gold nanorods on quartz substrate with L_{mid} = 395 nm, W = 60 nm, t = 55 nm and θ = 0°. (a) THG spectra measured with different incident laser powers. (b) THG peak intensity as a function of the incident laser power. The blue dash line with a slope of 3 is a guide to the eye. (c) FWHM of the THG spectra as a function of incident laser power. The dash line marks the average value.

The features of the spectra of the generated light (wavelength, intensity and FWHM) strongly indicate that the detection in our experiment is sensitive and selective to the THG process.

Bibliography

[1] F. Neubrech, C. Huck, K. Weber, A. Pucci, and H. Giessen, "Surface-Enhanced Infrared Spectroscopy Using Resonant Nanoantennas," Chem. Rev. **117**, 5110-5145 (2017).

[2] K. A. Willets, and R. P. Van Duyne, "Localized surface plasmon resonance spectroscopy and sensing," Annu. Rev. Phys. Chem. **58**, 267-297 (2007).

[3] K. M. Mayer, and J. H. Hafner, "Localized surface plasmon resonance sensors," Chemical Reviews **111**, 3828-3857 (2011).

[4] X. Zhang, Y. L. Chen, R.-S. Liu, and D. P. Tsai, "Plasmonic photocatalysis," Reports on Progress in Physics **76**, 046401 (2013).

[5] M. Kauranen, and A. V. Zayats, "Nonlinear plasmonics," Nat. Photonics **6**, 737 (2012).

[6] M. Mesch, B. Metzger, M. Hentschel, and H. Giessen, "Nonlinear plasmonic sensing," Nano Lett. **16**, 3155-3159 (2016).

[7] W. L. Barnes, A. Dereux, and T. W. Ebbesen, "Surface plasmon subwavelength optics," Nature **424**, 824–830 (2003).

[8] E. Ozbay, "Plasmonics: merging photonics and electronics at nanoscale dimensions," Science **311**, 189-193 (2006).

[9] M. Schnell, A. Garcia-Etxarri, A. J. Huber, K. Crozier, J. Aizpurua, and R. Hillenbrand, "Controlling the near-field oscillations of loaded plasmonic nanoantennas," Nat. Photonics **3**, 287 (2009).

[10] A. Bouhelier, J. Renger, M. Beversluis, and L. Novotny, "Plasmon-coupled tip-enhanced near-field optical microscopy," J. Microsc. **210**, 220-224 (2003).

[11] P. K. Jain, X. Huang, I. H. El-Sayed, and M. A. El-Sayed, "Review of some interesting surface plasmon resonance-enhanced properties of noble metal nanoparticles and their applications to biosystems," Plasmonics **2**, 107-118 (2007).

[12] K.-S. Lee, and M. A. El-Sayed, "Gold and silver nanoparticles in sensing and imaging: sensitivity of plasmon response to size, shape, and metal composition," The Journal of Physical Chemistry B **110**, 19220-19225 (2006).

[13] M. W. Knight, L. Liu, Y. Wang, L. Brown, S. Mukherjee, N. S. King, H. O. Everitt, P. Nordlander, and N. J. Halas, "Aluminum plasmonic nanoantennas," Nano Lett. **12**, 6000-6004 (2012).

[14] I. Zoric, M. Zach, B. Kasemo, and C. Langhammer, "Gold, platinum, and aluminum nanodisk plasmons: material independence, subradiance, and damping mechanisms," ACS Nano **5**, 2535-2546 (2011).

[15] S. A. Maier, *Plasmonics: fundamentals and applications* (Springer Science & Business Media, 2007).

[16] T. Coenen, F. Bernal Arango, A. Femius Koenderink, and A. Polman, "Directional emission from a single plasmonic scatterer," Nat. Commun. **5** (2014).

[17] A. Akimov, A. Mukherjee, C. Yu, D. Chang, A. Zibrov, P. Hemmer, H. Park, and M. Lukin, "Generation of single optical plasmons in metallic nanowires coupled to quantum dots," Nature **450**, 402-406 (2007).

[18] A. V. Kabashin, P. Evans, S. Pastkovsky, W. Hendren, G. A. Wurtz, R. Atkinson, R. Pollard, V. A. Podolskiy, and A. V. Zayats, "Plasmonic nanorod metamaterials for biosensing," Nat. Mater. **8**, 867-871 (2009).

[19] T. K. Sau, and C. J. Murphy, "Seeded high yield synthesis of short Au nanorods in aqueous solution," Langmuir **20**, 6414-6420 (2004).
[20] G. W. Bryant, F. J. Garcia de Abajo, and J. Aizpurua, "Mapping the plasmon resonances of metallic nanoantennas," Nano Letters **8**, 631-636 (2008).
[21] J. S. Shumaker-Parry, H. Rochholz, and M. Kreiter, "Fabrication of crescent-shaped optical antennas," Adv. Mater. **17**, 2131-2134 (2005).
[22] L. Y. Wu, B. M. Ross, and L. P. Lee, "Optical properties of the crescent-shaped nanohole antenna," Nano Lett. **9**, 1956-1961 (2009).
[23] A. W. Clark, A. K. Sheridan, A. Glidle, D. R. S. Cumming, and J. M. Cooper, "Tuneable visible resonances in crescent shaped nano-split-ring resonators," Appl. Phys. Lett. **91**, 093109 (2007).
[24] A. W. Clark, A. Glidle, D. R. S. Cumming, and J. M. Cooper, "Plasmonic split-ring resonators as dichroic nanophotonic DNA biosensors," J. Am. Chem. Soc. **131**, 17615-17619 (2009).
[25] A. W. Clark, and J. M. Cooper, "Nanogap ring antennae as plasmonically coupled SERRS substrates," Small **7**, 119-125 (2011).
[26] A. Huber, B. Deutsch, L. Novotny, and R. Hillenbrand, "Focusing of surface phonon polaritons," Appl. Phys. Lett. **92**, 203104 (2008).
[27] M. W. Klein, C. Enkrich, M. Wegener, and S. Linden, "Second-harmonic generation from magnetic metamaterials," Science **313**, 502-504 (2006).
[28] R. Marques, J. Martel, F. Mesa, and F. Medina, "Left-handed-media simulation and transmission of EM waves in subwavelength split-ring-resonator-loaded metallic waveguides," Phys. Rev. Lett. **89**, 183901 (2002).
[29] F. B. P. Niesler, N. Feth, S. Linden, and M. Wegener, "Second-harmonic optical spectroscopy on split-ring-resonator arrays," Opt. Lett. **36**, 1533-1535 (2011).
[30] C. Rockstuhl, F. Lederer, C. Etrich, T. Zentgraf, J. Kuhl, and H. Giessen, "On the reinterpretation of resonances in split-ring-resonators at normal incidence," Opt. Express **14**, 8827-8836 (2006).
[31] R. Czaplicki, H. Husu, R. Siikanen, J. Mäkitalo, M. Kauranen, J. Laukkanen, J. Lehtolahti, and M. Kuittinen, "Enhancement of second-harmonic generation from metal nanoparticles by passive elements," Phys. Rev. Lett. **110**, 093902 (2013).
[32] J. Lee, M. Tymchenko, C. Argyropoulos, P.-Y. Chen, F. Lu, F. Demmerle, G. Boehm, M.-C. Amann, A. Alu, and M. A. Belkin, "Giant nonlinear response from plasmonic metasurfaces coupled to intersubband transitions," Nature **511**, 65 (2014).
[33] C. Ciracì, E. Poutrina, M. Scalora, and D. R. Smith, "Second-harmonic generation in metallic nanoparticles: Clarification of the role of the surface," Phys. Rev. B **86**, 115451 (2012).
[34] C. Yi, P. D. Dongare, M.-N. Su, W. Wang, D. Chakraborty, F. Wen, W.-S. Chang, J. E. Sader, P. Nordlander, and N. J. Halas, "Vibrational coupling in plasmonic molecules," Proc. Natl. Acad. Sci. U. S. A. **114**, 11621–11626 (2017).
[35] M. Decker, M. Ruther, C. E. Kriegler, J. Zhou, C. M. Soukoulis, S. Linden, and M. Wegener, "Strong optical activity from twisted-cross photonic metamaterials," Opt. Lett. **34**, 2501-2503 (2009).
[36] M. Schnell, P. Sarriugarte, T. Neuman, A. B. Khanikaev, G. Shvets, J. Aizpurua, and R. Hillenbrand, "Real-space mapping of the chiral near-field distributions in spiral antennas and planar metasurfaces," Nano Lett. **16**, 663-670 (2015).

[37] Q. Yu, P. Guan, D. Qin, G. Golden, and P. M. Wallace, "Inverted size-dependence of surface-enhanced Raman scattering on gold nanohole and nanodisk arrays," Nano Lett. **8**, 1923-1928 (2008).
[38] R. Adato, A. A. Yanik, C.-H. Wu, G. Shvets, and H. Altug, "Radiative engineering of plasmon lifetimes in embedded nanoantenna arrays," Opt. Express **18**, 4526-4537 (2010).
[39] R. Bukasov, T. A. Ali, P. Nordlander, and J. S. Shumaker-Parry, "Probing the Plasmonic Near-Field of Gold Nanocrescent Antennas," ACS Nano **4**, 6639-6650 (2010).
[40] R. Czaplicki, A. Kiviniemi, J. Laukkanen, J. Lehtolahti, M. Kuittinen, and M. Kauranen, "Surface lattice resonances in second-harmonic generation from metasurfaces," Opt. Lett. **41**, 2684-2687 (2016).
[41] S. E. Lohse, and C. J. Murphy, "The quest for shape control: a history of gold nanorod synthesis," Chem. Mater. **25**, 1250-1261 (2013).
[42] N. R. Jana, L. Gearheart, and C. J. Murphy, "Wet chemical synthesis of high aspect ratio cylindrical gold nanorods," Journal of Physical Chemistry B **105**, 4065-4067 (2001).
[43] X. Ye, L. Jin, H. Caglayan, J. Chen, G. Xing, C. Zheng, V. Doan-Nguyen, Y. Kang, N. Engheta, C. R. Kagan, and C. B. Murray, "Improved Size-Tunable Synthesis of Monodisperse Gold Nanorods through the Use of Aromatic Additives," ACS Nano **6**, 2804-2817 (2012).
[44] X. Ye, L. Jin, H. Caglayan, J. Chen, G. Xing, C. Zheng, V. Doan-Nguyen, Y. Kang, N. Engheta, and C. R. Kagan, "Improved size-tunable synthesis of monodisperse gold nanorods through the use of aromatic additives," ACS Nano **6**, 2804-2817 (2012).
[45] G. A. Wurtz, R. Pollard, W. Hendren, G. P. Wiederrecht, D. J. Gosztola, V. A. Podolskiy, and A. V. Zayats, "Designed ultrafast optical nonlinearity in a plasmonic nanorod metamaterial enhanced by nonlocality," Nat. Nanotechnol. **6**, 107 (2011).
[46] J. R. Krenn, G. Schider, W. Rechberger, B. Lamprecht, A. Leitner, F. R. Aussenegg, and J. C. Weeber, "Design of multipolar plasmon excitations in silver nanoparticles," Appl. Phys. Lett. **77**, 3379-3381 (2000).
[47] G. Schider, J. R. Krenn, A. Hohenau, H. Ditlbacher, A. Leitner, F. R. Aussenegg, W. L. Schaich, I. Puscasu, B. Monacelli, and G. Boreman, "Plasmon dispersion relation of Au and Ag nanowires," Phys. Rev. B **68**, 155427 (2003).
[48] F. Neubrech, T. Kolb, R. Lovrincic, G. Fahsold, A. Pucci, J. Aizpurua, T. W. Cornelius, M. E. Toimil-Molares, R. Neumann, and S. Karim, "Resonances of individual metal nanowires in the infrared," Appl. Phys. Lett. **89**, 253104 (2006).
[49] R. Adato, A. A. Yanik, C.-H. Wu, G. Shvets, and H. Altug, "Radiative engineering of plasmon lifetimes in embedded nanoantenna arrays," Opt. Express **18**, 4526-4537 (2010).
[50] B. S. Simpkins, J. P. Long, O. J. Glembocki, J. Guo, J. D. Caldwell, and J. C. Owrutsky, "Pitch-dependent resonances and near-field coupling in infrared nanoantenna arrays," Opt. Express **20**, 27725-27739 (2012).
[51] F. Neubrech, D. Weber, R. Lovrincic, A. Pucci, M. Lopes, T. Toury, and M. L. de La Chapelle, "Resonances of individual lithographic gold nanowires in the infrared," Appl. Phys. Lett. **93**, 163105 (2008).

[52] B. Nikoobakht, and M. A. El-Sayed, "Preparation and Growth Mechanism of Gold Nanorods (NRs) Using Seed-Mediated Growth Method," Chem. Mater. **15**, 1957-1962 (2003).
[53] S. Zhang, Z. Ye, Y. Wang, Y. Park, G. Bartal, M. Mrejen, X. Yin, and X. Zhang, "Anti-Hermitian Plasmon Coupling of an Array of Gold Thin-Film Antennas for Controlling Light at the Nanoscale," Phys. Rev. Lett. **109**, 193902 (2012).
[54] S. T. Shibu Joseph, B. I. Ipe, P. Pramod, and K. G. Thomas, "Gold Nanorods to Nanochains: Mechanistic Investigations on Their Longitudinal Assembly Using α,ω-Alkanedithiols and Interplasmon Coupling," J. Phys. Chem. B **110**, 150-157 (2006).
[55] J. Yao, Z. Liu, Y. Liu, Y. Wang, C. Sun, G. Bartal, A. M. Stacy, and X. Zhang, "Optical Negative Refraction in Bulk Metamaterials of Nanowires," Science **321**, 930-930 (2008).
[56] R. Adato, A. A. Yanik, J. J. Amsden, D. L. Kaplan, F. G. Omenetto, M. K. Hong, S. Erramilli, and H. Altug, "Ultra-sensitive vibrational spectroscopy of protein monolayers with plasmonic nanoantenna arrays," Proc. Natl. Acad. Sci. U. S. A. **106**, 19227-19232 (2009).
[57] J. Li, H. Guo, and Z.-Y. Li, "Microscopic and macroscopic manipulation of gold nanorod and its hybrid nanostructures," Photonics Research **1**, 28-41 (2013).
[58] L. Novotny, and N. Van Hulst, "Antennas for light," Nat. Photonics **5**, 83-90 (2011).
[59] S.-S. Chang, C.-W. Shih, C.-D. Chen, W.-C. Lai, and C. R. C. Wang, "The Shape Transition of Gold Nanorods," Langmuir **15**, 701-709 (1999).
[60] L. Novotny, "Effective wavelength scaling for optical antennas," Phys. Rev. Lett. **98**, 266802 (2007).
[61] Y.-W. Huang, W. T. Chen, W.-Y. Tsai, P. C. Wu, C.-M. Wang, G. Sun, and D. P. Tsai, "Aluminum plasmonic multicolor meta-hologram," Nano Lett. **15**, 3122-3127 (2015).
[62] L.-J. Black, Y. Wang, C. H. de Groot, A. Arbouet, and O. L. Muskens, "Optimal Polarization Conversion in Coupled Dimer Plasmonic Nanoantennas for Metasurfaces," ACS Nano **8**, 6390-6399 (2014).
[63] M. Zeisberger, H. Schneidewind, U. Huebner, J. Popp, and M. A. Schmidt, "Nanoboomerang-based inverse metasurfaces—A promising path towards ultrathin photonic devices for transmission operation," APL Photonics **2**, 036102 (2017).
[64] C. T. Cooper, M. Rodriguez, S. Blair, and J. S. Shumaker-Parry, "Mid-Infrared Localized Plasmons through Structural Control of Gold and Silver Nanocrescents," J. Phys. Chem. C **119**, 11826-11832 (2015).
[65] C. T. Cooper, M. Rodriguez, S. Blair, and J. S. Shumaker-Parry, "Polarization Anisotropy of Multiple Localized Plasmon Resonance Modes in Noble Metal Nanocrescents," J. Phys. Chem. C **118**, 1167-1173 (2014).
[66] R. W. Boyd, *Nonlinear optics* (Elsevier, 2003).
[67] P. E. Powers, and J. W. Haus, *Fundamentals of nonlinear optics* (CRC press, 2017).
[68] E. P. A. Franken, A. E. Hill, C. W. e. Peters, and G. Weinreich, "Generation of optical harmonics," Phys. Rev. Lett. **7**, 118 (1961).
[69] J. Martorell, R. Vilaseca, and R. Corbalan, "Second harmonic generation in a photonic crystal," Appl. Phys. Lett. **70**, 702-704 (1997).
[70] D. Wei, C. Wang, H. Wang, X. Hu, D. Wei, X. Fang, Y. Zhang, D. Wu, Y. Hu, and J. Li, "Experimental demonstration of a three-dimensional lithium niobate nonlinear photonic crystal," Nat. Photonics **12**, 596-600 (2018).

[71] J. Butet, P.-F. Brevet, and O. J. F. Martin, "Optical Second Harmonic Generation in Plasmonic Nanostructures: From Fundamental Principles to Advanced Applications," ACS Nano **9**, 10545-10562 (2015).
[72] M. Celebrano, X. Wu, M. Baselli, S. Großmann, P. Biagioni, A. Locatelli, C. De Angelis, G. Cerullo, R. Osellame, and B. Hecht, "Mode matching in multiresonant plasmonic nanoantennas for enhanced second harmonic generation," Nat. Nanotechnol. **10**, 412 (2015).
[73] N. Feth, S. Linden, M. W. Klein, M. Decker, F. B. P. Niesler, Y. Zeng, W. Hoyer, J. Liu, S. W. Koch, and J. V. Moloney, "Second-harmonic generation from complementary split-ring resonators," Opt. Lett. **33**, 1975-1977 (2008).
[74] R. Adato, A. A. Yanik, J. J. Amsden, D. L. Kaplan, F. G. Omenetto, M. K. Hong, S. Erramilli, and H. Altug, "Ultra-sensitive vibrational spectroscopy of protein monolayers with plasmonic nanoantenna arrays," Proceedings of the National Academy of Sciences **106**, 19227-19232 (2009).
[75] M. Osawa, "Surface-enhanced infrared absorption," in *Near-field optics and surface plasmon polaritons*(Springer, 2001), pp. 163-187.
[76] J. Chalmers, and P. Griffiths, *Handbook of Vibrational Spectroscopy, 5 volumes set* (Wiley, 2002).
[77] E. Petryayeva, and U. J. Krull, "Localized surface plasmon resonance: nanostructures, bioassays and biosensing—a review," Anal. Chim. Acta **706**, 8-24 (2011).
[78] F. Le, D. W. Brandl, Y. A. Urzhumov, H. Wang, J. Kundu, N. J. Halas, J. Aizpurua, and P. Nordlander, "Metallic nanoparticle arrays: a common substrate for both surface-enhanced Raman scattering and surface-enhanced infrared absorption," ACS Nano **2**, 707-718 (2008).
[79] Y. Jin, Y. Pennec, and B. Djafari-Rouhani, "Acoustic analogue of electromagnetically induced transparency and Autler–Townes splitting in pillared metasurfaces," J. Phys. D: Appl. Phys. **51**, 494004 (2018).
[80] R. Adato, A. Artar, S. Erramilli, and H. Altug, "Engineered absorption enhancement and induced transparency in coupled molecular and plasmonic resonator systems," Nano Lett. **13**, 2584-2591 (2013).
[81] T. B. Hoang, G. M. Akselrod, and M. H. Mikkelsen, "Ultrafast room-temperature single photon emission from quantum dots coupled to plasmonic nanocavities," Nano Lett. **16**, 270-275 (2016).
[82] L. V. Brown, X. Yang, K. Zhao, B. Y. Zheng, P. Nordlander, and N. J. Halas, "Fan-shaped gold nanoantennas above reflective substrates for surface-enhanced infrared absorption (SEIRA)," Nano Lett. **15**, 1272-1280 (2015).
[83] O. Khatib, H. A. Bechtel, M. C. Martin, M. B. Raschke, and G. L. Carr, "Far infrared synchrotron near-field nanoimaging and nanospectroscopy," ACS Photonics **5**, 2773-2779 (2018).
[84] J. W. Zubrick, *The organic chem lab survival manual: a student's guide to techniques* (John Wiley & Sons, 2020).
[85] C. Huck, J. Vogt, T. Neuman, T. Nagao, R. Hillenbrand, J. Aizpurua, A. Pucci, and F. Neubrech, "Strong coupling between phonon-polaritons and plasmonic nanorods," Opt. Express **24**, 25528-25539 (2016).

[86] J. Vogt, C. Huck, F. Neubrech, A. Toma, D. Gerbert, and A. Pucci, "Impact of the plasmonic near-and far-field resonance-energy shift on the enhancement of infrared vibrational signals," Phys. Chem. Chem. Phys. **17**, 21169-21175 (2015).
[87] W.-Y. Tsai, J.-S. Huang, and C.-B. Huang, "Selective trapping or rotation of isotropic dielectric microparticles by optical near field in a plasmonic archimedes spiral," Nano Lett. **14**, 547-552 (2014).
[88] C. Kelly, R. Tullius, A. J. Lapthorn, N. Gadegaard, G. Cooke, L. D. Barron, A. S. Karimullah, V. M. Rotello, and M. Kadodwala, "Chiral plasmonic fields probe structural order of biointerfaces," J. Am. Chem. Soc. **140**, 8509-8517 (2018).
[89] L. Zeng, L. Wu, L. Liu, and X. Jiang, "Analyzing structural properties of heterogeneous cardiolipin-bound cytochrome c and their regulation by surface-enhanced infrared absorption spectroscopy," Anal. Chem. **88**, 11727-11733 (2016).
[90] A. Pors, M. Willatzen, O. Albrektsen, and S. I. Bozhevolnyi, "From plasmonic nanoantennas to split-ring resonators: tuning scattering strength," J. Opt. Soc. Am. B **27**, 1680-1687 (2010).
[91] F. Monticone, and A. Alù, "The quest for optical magnetism: from split-ring resonators to plasmonic nanoparticles and nanoclusters," J. Mater. Chem. C **2**, 9059-9072 (2014).
[92] S. M. Hein, and H. Giessen, "Tailoring Magnetic Dipole Emission with Plasmonic Split-Ring Resonators," Phys. Rev. Lett. **111**, 026803 (2013).
[93] J. Zhou, T. Koschny, and C. M. Soukoulis, "Magnetic and electric excitations in split ring resonators," Opt. Express **15**, 17881-17890 (2007).
[94] M. Hentschel, M. Schäferling, X. Duan, H. Giessen, and N. Liu, "Chiral plasmonics," Sci. Adv. **3**, e1602735 (2017).
[95] R. Blanchard, "Modeling nanoscale V-shaped antennas for the design of optical phased arrays," Phys. Rev. B **85**, 155457 (2012).
[96] J. Sung, M. Sukharev, E. M. Hicks, R. P. Van Duyne, T. Seideman, and K. G. Spears, "Nanoparticle Spectroscopy: Birefringence in Two-Dimensional Arrays of L-Shaped Silver Nanoparticles," J. Phys. Chem. C **112**, 3252-3260 (2008).
[97] M. Sukharev, J. Sung, K. G. Spears, and T. Seideman, "Optical properties of metal nanoparticles with no center of inversion symmetry: Observation of volume plasmons," Phys. Rev. B **76**, 184302 (2007).
[98] R. Bukasov, and J. S. Shumaker-Parry, "Highly Tunable Infrared Extinction Properties of Gold Nanocrescents," Nano Lett. **7**, 1113-1118 (2007).
[99] R. Bukasov, T. A. Ali, P. Nordlander, and J. S. Shumaker-Parry, "Probing the Plasmonic Near-Field of Gold Nanocrescent Antennas," ACS Nano **4**, 6639-6650 (2010).
[100] L.-J. Black, P. R. Wiecha, Y. Wang, C. H. de Groot, V. Paillard, C. Girard, O. L. Muskens, and A. Arbouet, "Tailoring Second-Harmonic Generation in Single L-Shaped Plasmonic Nanoantennas from the Capacitive to Conductive Coupling Regime," ACS Photonics **2**, 1592-1601 (2015).
[101] J. B. Pendry, A. Aubry, D. R. Smith, and S. A. Maier, "Transformation optics and subwavelength control of light," Science **337**, 549-552 (2012).
[102] U. Leonhardt, and T. G. Philbin, "Transformation optics and the geometry of light," in *Progress in Optics*(Elsevier, 2009), pp. 69-152.
[103] J. Zhang, J. B. Pendry, and Y. Luo, "Transformation optics from macroscopic to nanoscale regimes: a review," Advanced Photonics **1**, 014001 (2019).

[104] N. B. Kundtz, D. R. Smith, and J. B. Pendry, "Electromagnetic design with transformation optics," Proceedings of the IEEE **99**, 1622-1633 (2010).
[105] L. Xu, and H. Chen, "Conformal transformation optics," Nat. Photonics **9**, 15 (2015).
[106] Z. Nehari, *Conformal mapping* (Courier Corporation, 2012).
[107] R. Schinzinger, and P. A. Laura, *Conformal mapping: methods and applications* (Courier Corporation, 2012).
[108] M. Heiblum, and J. Harris, "Analysis of curved optical waveguides by conformal transformation," IEEE J. Quantum Electron. **11**, 75-83 (1975).
[109] K.-i. Maeda, "Towards the Einstein-Hilbert action via conformal transformation," Phys. Rev. D **39**, 3159 (1989).
[110] M. Kraft, Y. Luo, S. A. Maier, and J. B. Pendry, "Designing plasmonic gratings with transformation optics," Phys. Rev. X **5**, 031029 (2015).
[111] J. B. Pendry, and S. A. Ramakrishna, "Near-field lenses in two dimensions," J. Phys.: Condens. Matter **14**, 8463 (2002).
[112] J. B. Pendry, "Perfect cylindrical lenses," Opt. Express **11**, 755-760 (2003).
[113] J. P. Turpin, A. T. Massoud, Z. H. Jiang, P. L. Werner, and D. H. Werner, "Conformal mappings to achieve simple material parameters for transformation optics devices," Opt. Express **18**, 244-252 (2010).
[114] D. E. Merewether, R. Fisher, and F. W. Smith, "On implementing a numeric Huygen's source scheme in a finite difference program to illuminate scattering bodies," IEEE Trans. Nucl. Sci. **27**, 1829-1833 (1980).
[115] T. Brintlinger, A. A. Herzing, J. P. Long, I. Vurgaftman, R. Stroud, and B. S. Simpkins, "Optical dark-field and electron energy loss imaging and spectroscopy of symmetry-forbidden modes in loaded nanogap antennas," ACS Nano **9**, 6222-6232 (2015).
[116] M. Husnik, M. W. Klein, N. Feth, M. König, J. Niegemann, K. Busch, S. Linden, and M. Wegener, "Absolute extinction cross-section of individual magnetic split-ring resonators," Nat. Photonics **2**, 614-617 (2008).
[117] I. H. Malitson, "Interspecimen comparison of the refractive index of fused silica," J. Opt. Soc. Am. **55**, 1205-1209 (1965).
[118] T. O'Haver, "A Pragmatic Introduction to Signal Processing (Essay)," Software is available at https://terpconnect.umd.edu/~toh/spectrum/InteractivePeakFitter.htm.
[119] R. Taylor, A. Pénicaud, and N. J. Tower, "Matrix isolation of fullerene-derived CO2 at ambient temperature," Chem. Phys. Lett. **295**, 481-486 (1998).
[120] B. Lamprecht, G. Schider, R. Lechner, H. Ditlbacher, J. R. Krenn, A. Leitner, and F. R. Aussenegg, "Metal nanoparticle gratings: influence of dipolar particle interaction on the plasmon resonance," Phys. Rev. Lett. **84**, 4721 (2000).
[121] M. Meier, A. Wokaun, and P. F. Liao, "Enhanced fields on rough surfaces: dipolar interactions among particles of sizes exceeding the Rayleigh limit," JOSA B **2**, 931-949 (1985).
[122] D. Weber, P. Albella, P. Alonso-González, F. Neubrech, H. Gui, T. Nagao, R. Hillenbrand, J. Aizpurua, and A. Pucci, "Longitudinal and transverse coupling in infrared gold nanoantenna arrays: long range versus short range interaction regimes," Opt. Express **19**, 15047 (2011).
[123] F. Neubrech, A. Garcia-Etxarri, D. Weber, J. Bochterle, H. Shen, M. Lamy De La Chapelle, G. W. Bryant, J. Aizpurua, and A. Pucci, "Defect-induced activation of

symmetry forbidden infrared resonances in individual metallic nanorods," Appl. Phys. Lett. **96**, 213111 (2010).
[124] G. Laurent, N. Félidj, J. Aubard, G. Lévi, J. R. Krenn, A. Hohenau, G. Schider, A. Leitner, and F. R. Aussenegg, "Evidence of multipolar excitations in surface enhanced Raman scattering," Phys. Rev. B **71**, 045430 (2005).
[125] N. Kumar, A. C. Strikwerda, K. Fan, X. Zhang, R. D. Averitt, P. C. M. Planken, and A. J. L. Adam, "THz near-field Faraday imaging in hybrid metamaterials," Opt. Express **20**, 11277-11287 (2012).
[126] A. Bitzer, H. Merbold, A. Thoman, T. Feurer, H. Helm, and M. Walther, "Terahertz near-field imaging of electric and magnetic resonances of a planar metamaterial," Opt. Express **17**, 3826-3834 (2009).
[127] C. Kittel, P. McEuen, and P. McEuen, *Introduction to solid state physics* (Wiley New York, 1996).
[128] M. A. Ordal, R. J. Bell, R. W. Alexander, L. L. Long, and M. R. Querry, "Optical properties of fourteen metals in the infrared and far infrared: Al, Co, Cu, Au, Fe, Pb, Mo, Ni, Pd, Pt, Ag, Ti, V, and W," Appl. Opt. **24**, 4493-4499 (1985).
[129] D. T. Pierce, and W. E. Spicer, "Electronic structure of amorphous Si from photoemission and optical studies," Phys. Rev. B **5**, 3017 (1972).
[130] E. Cubukcu, and F. Capasso, "Optical nanorod antennas as dispersive one-dimensional Fabry–Pérot resonators for surface plasmons," Appl. Phys. Lett. **95**, 201101 (2009).
[131] P. Berini, "Plasmon-polariton waves guided by thin lossy metal films of finite width: Bound modes of asymmetric structures," Phys. Rev. B **63**, 125417 (2001).
[132] P. Berini, "Plasmon-polariton waves guided by thin lossy metal films of finite width: Bound modes of asymmetric structures," Phys. Rev. B **63** (2001).
[133] V. M. Agranovich, *Surface polaritons* (Elsevier, 2012).
[134] Y. Chu, M. G. Banaee, and K. B. Crozier, "Double-resonance plasmon substrates for surface-enhanced Raman scattering with enhancement at excitation and stokes frequencies," ACS Nano **4**, 2804-2810 (2010).
[135] K. Thyagarajan, S. Rivier, A. Lovera, and O. J. F. Martin, "Enhanced second-harmonic generation from double resonant plasmonic antennae," Opt. Express **20**, 12860-12865 (2012).
[136] H. Aouani, M. Navarro-Cia, M. Rahmani, T. P. H. Sidiropoulos, M. Hong, R. F. Oulton, and S. A. Maier, "Multiresonant broadband optical antennas as efficient tunable nanosources of second harmonic light," Nano Lett. **12**, 4997-5002 (2012).
[137] H. Harutyunyan, G. Volpe, R. Quidant, and L. Novotny, "Enhancing the nonlinear optical response using multifrequency gold-nanowire antennas," Phys. Rev. Lett. **108**, 217403 (2012).
[138] K. Thyagarajan, J. Butet, and O. J. F. Martin, "Augmenting second harmonic generation using Fano resonances in plasmonic systems," Nano Lett. **13**, 1847-1851 (2013).
[139] K. Y. Yang, J. Butet, C. Yan, G. D. Bernasconi, and O. J. F. Martin, "Enhancement Mechanisms of the Second Harmonic Generation from Double Resonant Aluminum Nanostructures," ACS Photonics **4**, 1522-1530 (2017).
[140] R. Bukasov, and J. S. Shumaker-Parry, "Highly Tunable Infrared Extinction Properties of Gold Nanocrescents," Nano Lett. **7**, 1113-1118 (2007).

[141] X. Zhu, X. Zhuo, Q. Li, Z. Yang, and J. Wang, "Gold nanobipyramid-supported silver nanostructures with narrow plasmon linewidths and improved chemical stability," Adv. Funct. Mater. **26**, 341-352 (2016).
[142] M. Grzelczak, A. Sánchez-Iglesias, B. Rodríguez-González, R. Alvarez-Puebla, J. Pérez-Juste, and L. M. Liz-Marzán, "Influence of iodide ions on the growth of gold nanorods: tuning tip curvature and surface plasmon resonance," Adv. Funct. Mater. **18**, 3780-3786 (2008).
[143] T. Brabec, and F. Krausz, "Intense few-cycle laser fields: Frontiers of nonlinear optics," Reviews of Modern Physics **72**, 545 (2000).
[144] E. Rahimi, and R. Gordon, "Nonlinear plasmonic metasurfaces," Advanced Optical Materials **6**, 1800274 (2018).
[145] N. C. Panoiu, W. E. I. Sha, D. Y. Lei, and G. C. Li, "Nonlinear optics in plasmonic nanostructures," Journal of Optics **20**, 083001 (2018).
[146] F. F. Lu, T. Li, X. P. Hu, Q. Q. Cheng, S. N. Zhu, and Y. Y. Zhu, "Efficient second-harmonic generation in nonlinear plasmonic waveguide," Opt. Lett. **36**, 3371-3373 (2011).
[147] A. V. Kachynski, A. Pliss, A. N. Kuzmin, T. Y. Ohulchanskyy, A. Baev, J. Qu, and P. N. Prasad, "Photodynamic therapy by in situ nonlinear photon conversion," Nat. Photonics **8**, 455 (2014).
[148] E. Di Fabrizio, S. Schlücker, J. Wenger, R. Regmi, H. Rigneault, G. Calafiore, M. West, S. Cabrini, M. Fleischer, and N. F. Van Hulst, "Roadmap on biosensing and photonics with advanced nano-optical methods," Journal of Optics **18**, 063003 (2016).
[149] C. Ciracì, E. Poutrina, M. Scalora, and D. R. Smith, "Origin of second-harmonic generation enhancement in optical split-ring resonators," Phys. Rev. B **85**, 201403 (2012).
[150] M. W. Klein, M. Wegener, N. Feth, and S. Linden, "Experiments on second-and third-harmonic generation from magnetic metamaterials: erratum," Opt. Express **16**, 8055-8055 (2008).
[151] V. Valev, N. Smisdom, A. Silhanek, B. De Clercq, W. Gillijns, M. Ameloot, V. Moshchalkov, and T. Verbiest, "Plasmonic ratchet wheels: switching circular dichroism by arranging chiral nanostructures," Nano Lett. **9**, 3945-3948 (2009).
[152] W. Cai, A. P. Vasudev, and M. L. Brongersma, "Electrically controlled nonlinear generation of light with plasmonics," Science **333**, 1720-1723 (2011).
[153] R. Czaplicki, M. Zdanowicz, K. Koskinen, J. Laukkanen, M. Kuittinen, and M. Kauranen, "Dipole limit in second-harmonic generation from arrays of gold nanoparticles," Opt. Express **19**, 26866-26871 (2011).
[154] S. Linden, F. B. P. Niesler, J. Förstner, Y. Grynko, T. Meier, and M. Wegener, "Collective effects in second-harmonic generation from split-ring-resonator arrays," Phys. Rev. Lett. **109**, 015502 (2012).
[155] V. Giannini, A. I. Fernández-Domínguez, S. C. Heck, and S. A. Maier, "Plasmonic nanoantennas: fundamentals and their use in controlling the radiative properties of nanoemitters," Chem. Rev. **111**, 3888-3912 (2011).
[156] R. F. Aroca, D. J. Ross, and C. Domingo, "Surface-enhanced infrared spectroscopy," Appl. Spectrosc. **58**, 324A-338A (2004).
[157] P. L. Stiles, J. A. Dieringer, N. C. Shah, and R. P. Van Duyne, "Surface-enhanced Raman spectroscopy," Annu. Rev. Anal. Chem. **1**, 601-626 (2008).

[158] F. Neubrech, A. Pucci, T. W. Cornelius, S. Karim, A. García-Etxarri, and J. Aizpurua, "Resonant plasmonic and vibrational coupling in a tailored nanoantenna for infrared detection," Phys. Rev. Lett. **101**, 157403 (2008).
[159] K. Chen, R. Adato, and H. Altug, "Dual-band perfect absorber for multispectral plasmon-enhanced infrared spectroscopy," ACS Nano **6**, 7998-8006 (2012).
[160] E. Cubukcu, S. Zhang, Y.-S. Park, G. Bartal, and X. Zhang, "Split ring resonator sensors for infrared detection of single molecular monolayers," Appl. Phys. Lett. **95**, 043113 (2009).
[161] D. J. Shelton, I. Brener, J. C. Ginn, M. B. Sinclair, D. W. Peters, K. R. Coffey, and G. D. Boreman, "Strong coupling between nanoscale metamaterials and phonons," Nano Lett. **11**, 2104-2108 (2011).
[162] C. Huck, J. Vogt, M. Sendner, D. Hengstler, F. Neubrech, and A. Pucci, "Plasmonic enhancement of infrared vibrational signals: nanoslits versus nanorods," ACS Photonics **2**, 1489-1497 (2015).
[163] C. Huck, F. Neubrech, J. Vogt, A. Toma, D. Gerbert, J. Katzmann, T. Härtling, and A. Pucci, "Surface-enhanced infrared spectroscopy using nanometer-sized gaps," ACS Nano **8**, 4908-4914 (2014).
[164] B. Cerjan, X. Yang, P. Nordlander, and N. J. Halas, "Asymmetric aluminum antennas for self-calibrating surface-enhanced infrared absorption spectroscopy," ACS Photonics **3**, 354-360 (2016).
[165] I. M. Pryce, K. Aydin, Y. A. Kelaita, R. M. Briggs, and H. A. Atwater, "Highly strained compliant optical metamaterials with large frequency tunability," Nano Lett. **10**, 4222-4227 (2010).
[166] U. Fano, "Effects of configuration interaction on intensities and phase shifts," Physical Review **124**, 1866 (1961).
[167] S. Ramesh, and K. N. Bing, "Conductivity, mechanical and thermal studies on poly (methyl methacrylate)-based polymer electrolytes complexed with lithium tetraborate and propylene carbonate," J. Mater. Eng. Perform. **21**, 89-94 (2012).
[168] Y. Chang, J. Yao, X. Wu, D. Wu, and X. Liu, "Strong and weak couplings in molecular vibration–plasmon hybrid structures," Opt. Express **27**, 1479-1487 (2019).
[169] D. F. Edwards, and E. Ochoa, "Infrared refractive index of diamond," JOSA **71**, 607-608 (1981).
[170] H. R. Philipp, and E. A. Taft, "An optical characterization of native oxides and thin thermal oxides on silicon," J. Appl. Phys. **53**, 5224-5229 (1982).
[171] H. Yan, T. Low, F. Guinea, F. Xia, and P. Avouris, "Tunable phonon-induced transparency in bilayer graphene nanoribbons," Nano Lett. **14**, 4581-4586 (2014).
[172] X. Hu, T. Wang, L. Wang, and S. Dong, "Surface-enhanced Raman scattering of 4-aminothiophenol self-assembled monolayers in sandwich structure with nanoparticle shape dependence: off-surface plasmon resonance condition," J. Phys. Chem. C **111**, 6962-6969 (2007).
[173] Y. Xue, X. Li, H. Li, and W. Zhang, "Quantifying thiol–gold interactions towards the efficient strength control," Nat. Commun. **5**, 1-9 (2014).
[174] J. Mirza, I. Martens, M. Grüßer, D. Bizzotto, R. Schuster, and J. Lipkowski, "Gold nanorod arrays: excitation of transverse plasmon modes and surface-enhanced Raman applications," J. Phys. Chem. C **120**, 16246-16253 (2016).

[175] Q. Li, Y. Wang, Y. Li, Y. Park, Y. Chen, X. Wang, B. Zhao, W. Ruan, and Y. M. Jung, "Identification of native charge-transfer status of p-aminothiolphenol adsorbed on noble metallic substrates by surface-enhanced infrared absorption (SEIRA) spectroscopy," Spectrochimica Acta Part A: Molecular and Biomolecular Spectroscopy **204**, 532-536 (2018).
[176] J. Zheng, Y. Zhou, X. Li, Y. Ji, T. Lu, and R. Gu, "Surface-enhanced Raman scattering of 4-aminothiophenol in assemblies of nanosized particles and the macroscopic surface of silver," Langmuir **19**, 632-636 (2003).
[177] Sigma Aldrich Corporation, "FTIR spectrum of condensed phase PMMA", Millipore Sigma (2020), https://www.sigmaaldrich.com/spectra/ftir/FTIR002075.PDF.
[178] J. Zuloaga, and P. Nordlander, "On the energy shift between near-field and far-field peak intensities in localized plasmon systems," Nano Lett. **11**, 1280-1283 (2011).
[179] N. Liu, and H. Giessen, "Coupling effects in optical metamaterials," Angewandte Chemie International Edition **49**, 9838-9852 (2010).
[180] C.-Y. Tsai, J.-W. Lin, C.-Y. Wu, P.-T. Lin, T.-W. Lu, and P.-T. Lee, "Plasmonic coupling in gold nanoring dimers: observation of coupled bonding mode," Nano Lett. **12**, 1648-1654 (2012).
[181] C. Yi, P. D. Dongare, M.-N. Su, W. Wang, D. Chakraborty, F. Wen, W.-S. Chang, J. E. Sader, P. Nordlander, and N. J. Halas, "Vibrational coupling in plasmonic molecules," Proceedings of the National Academy of Sciences, 201712418 (2017).
[182] H. M. Lee, S. M. Jin, H. M. Kim, and Y. D. Suh, "Single-molecule surface-enhanced Raman spectroscopy: a perspective on the current status," Phys. Chem. Chem. Phys. **15**, 5276-5287 (2013).
[183] Y. Sharma, and A. Dhawan, "Plasmonic “nano-fingers on nanowires” as SERS substrates," Opt. Lett. **41**, 2085-2088 (2016).
[184] A. Hakonen, K. Wu, M. S. Schmidt, P. O. Andersson, A. Boisen, and T. Rindzevicius, "Detecting forensic substances using commercially available SERS substrates and handheld Raman spectrometers," Talanta **189**, 649-652 (2018).
[185] P.-C. Peng, H.-Y. Tseng, and S. Chi, "Long-distance FBG sensor system using a linear-cavity fiber Raman laser scheme," IEEE Photonics Technology Letters **16**, 575-577 (2004).
[186] Y.-G. Han, T. Tran, S.-H. Kim, and S. B. Lee, "Multiwavelength Raman-fiber-laser-based long-distance remote sensor for simultaneous measurement of strain and temperature," Opt. Lett. **30**, 1282-1284 (2005).
[187] W. Lee, S. Y. Lee, R. M. Briber, and O. Rabin, "Self-assembled SERS substrates with tunable surface plasmon resonances," Adv. Funct. Mater. **21**, 3424-3429 (2011).
[188] Hamamatsu Corporation, "Metal package PMT Photosensor Modules H5784 Series", H5784-20 Datasheet (2020), https://www.alldatasheet.com/datasheet-pdf/pdf/62585/HAMAMATSU/H5784-20.html.
[189] Thorlabs Inc., "N-BK7 Bi-Convex Lenses (AR Coating: 650 - 1050 nm)", https://www.thorlabs.com/newgrouppage9.cfm?objectgroup_id=4849.
[190] Thorlabs Inc., "Ø25.0 mm Premium Shortpass Filter, Cut-Off Wavelength: 900 nm", https://www.thorlabs.com/newgrouppage9.cfm?objectgroup_id=6082.
[191] Thorlabs Inc., "Economy Film Polarizers, 600 - 1100 nm, LPNIRE100-B", https://www.thorlabs.com/newgrouppage9.cfm?objectgroup_id=4984&pn=LPNIRE100-B#7211.